The Computer-Aided Design and Analysis of Impulse Magnetizing Fixtures.

Geraint Wyn Jewell

A Thesis submitted for the degree of PhD, in the Department of Electronic and Electrical Engineering, University of Sheffield.

August 1992.

SUMMARY

The magnetization of the permanent magnet components is a key enabling technology in the production of permanent magnet based electromagnetic devices. Although recent advances in the properties of rare-earth magnets, offer considerable scope for enhanced device performance, in order to realise such improvements, the permanent magnet must be magnetized to saturation. This is a considerably more onerous requirement for the rare-earth materials as compared to the more established permanent magnet materials, particularly if the preferred production route of single step, multipole magnetization of either the part or fully assembled device is to be employed.

To enable accurate design of magnetizing systems for such demanding applications, an integrated computer-aided design methodology has been developed. It is based on both analytical and finite element field calculation techniques, and spans the entire design synthesis from initial specification through to the assessment of the performance of the final device into which the magnetized magnet is incorporated. Particular attention is directed towards the role of eddy-currents during the impulse magnetization, and to this end a transient, electric circuit coupled finite element simulation is described.

A case study is presented on the relative merits of magnetizing the anisotropic NdFeB magnet of a brushless D.C motor at various stages during the motor production. A further case study on the magnetization of an isotropic bonded NdFeB multipole rotor highlights the additional considerations that arise in the design of magnetizing fixtures for isotropic materials. Finally, the utility of the methodology in designing a limited range of axial multipole fixtures is demonstrated with a case study on a fine pole-pitch axially magnetized ring magnet.

Acknowledgements

I would like to express my gratitude to the following:

Professor David Howe for his supervision

Philips Components for their support, both technical and financial.

SERC for the award of a CASE studentship.

My colleagues in the Machines and Drives Group.

Table of Contents

CHAPTER1

INTRODUCTION

1.1 RARE-EARTH MAGNET MATERIALS

Recent advances in rare-earth based permanent magnet materials have resulted in greatly enhanced magnetic properties compared to the more established materials such as ceramic ferrites and alnicos. These improved magnetic properties offer considerable scope for miniaturisation and efficiency improvements in many permanent magnet devices. However, in order to realise these advantages, the permanent magnet of an actual device is required to be fully saturated during its initial magnetization, a requirement which is considerably more difficult to achieve for the rare-earth materials than for previous types of magnet. Although the level of magnetizing field strength required to ensure full saturation of rare-earth based permanent magnets can be readily generated in dipole solenoids, their realisation in complex multipole magnetizing fixtures is considerably more onerous. Multipole magnetization of either the magnet alone or of an in-situ magnet is often highly desirable in the production of a permanent magnet device. Indeed, in recent market projections [1.1] the difficulties associated with in-situ magnetization are cited as being one of the principal barriers to the market growth of NdFeB magnets. These difficulties are due principally to existing limitations in the design of the impulse magnetizing fixtures rather than being due to inherent limitations in the available technologies. Therefore, a reliable design methodology for this key enabling technology in device realisation is critical if the benefits of the improved magnet material properties are to be fully realised.

There has been rapid progress in permanent magnet materials since the 1960s with an almost exponential increase in the energy density, fig 1.1, and a dramatic improvement in the remanence, coercivity and linearity of the demagnetization curve,

fig 1.2. The development of rare-earth permanent magnets was initiated by Strnat et al [1.2] in the mid 1960s with the discovery of the high magnetic properties of the $RECo_5$ alloys, the most important material in this group being $SmCo_5$. In the early 1970s the RE_2CO_{17} alloys were developed, of which the Samarium based alloy was again the most technically and economically significant. However, materials based on Samarium and Cobalt suffer from expensive raw material costs which have limited their penetration into cost-sensitive markets, particularly since the long term price stability of cobalt is susceptible to the strategic nature of the world reserves. Nevertheless, they still maintain a significant share of the overall rare-earth magnet market (39% by value in 1991), and hold a dominant position in the military and aerospace sectors.

A major advance, in terms of both magnetic properties and economic viability, was the commercialisation of NdFeB by Sumitomo Special Metals Company and General Motors Corporation in 1983. The cost savings were related to the elimination of cobalt and the use of Neodymium which is far more abundant than Samarium in typical rare-earth ores, e.g the 1989 mean cost of high purity Samarium and Neodymium metals supplied by Rhone-Poulenc for magnet production were $175 and $20 per kilogram respectively [1.1]. Although the magnetic properties and cost per kg of NdFeB are superior to those for the SmCo magnets, the inferior temperature and corrosion resistance are inhibiting its penetration into the military and aerospace market sectors, where reliability and high temperature peformance tend to override cost considerations.

In 1990, the various grades of NdFeB accounted for 17.4% of the world permanent magnet market by value [1.1]. Although this represents a reasonable degree of market penetration, it is not reflective of the greatly improved magnetic properties of NdFeB compared to the established materials such as sintered and bonded ceramic ferrites which had market shares of 36.6% and 19.6% respectively. Indeed, its market

share is currently only twice that of the Alnico materials, whose magnetic properties per unit cost are so inferior that they are almost obsolete from a technical point of view, although the resistance to change within the manufacturing industry and their use in specialist instrumentation applications lead to their continued use.

The principal limiting factor preventing further market penetration of NdFeB magnets is their relatively high cost compared to ferrites. Typical costs per kilogram of the various generic magnet materials are shown in fig 1.3. Although the cost of bulk materials is a useful guide to their relative economic merits, the fraction of the finished magnet cost which is attributable to the raw materials decreases as the magnet size is reduced. This is due to the relatively fixed cost of the machining to the final tolerances. The machining cost of a magnet weighing a few grams may well add up to 200% of the magnet production cost [1.3]. This results in a dramatic narrowing of the price differential in small magnets, although issues such as protective coatings can add to the cost of rare-earth magnets [1.4]. Hence it is presently in the small magnets sector of the market in which NdFeB is most often used as an alternative to ferrite materials.

Whereas bonded magnets can be moulded directly to the final dimensional tolerance, either by compression or injection moulding or by extrusion, anisotropic shrinkage of magnets during sintering is not sufficiently reproducible to sinter directly to the final dimensional tolerance. Hence the finishing cost of sintered magnets is considerably higher than for bonded magnets [1.3]. This provides further scope for much of the price differential between sintered ferrite and bonded NdFeB to be absorbed even in moderately large magnets, particularly for geometries which are difficult to machine e.g arc segments. The viability of using bonded NdFeB magnets in applications which presently employ sintered ferrite is further enhanced by effecting production simplifications e.g injection moulding of a magnet ring directly onto a motor core and shaft to produce an integrated magnetic component. However, these produc-

tion simplifications usually require the use of bonded magnets with a reduced powder to polymer ratio and hence diluted magnetic properties. Nevertheless, extremely flexible bonded materials can be produced in large sheets with magnetic properties which are still superior to those of the best grades of sinted ferrite. Indeed, it is estimated that at present 50% of the bonded NdFeB which is produced, is a direct replacement for sintered ferrite in a wide range of cost-sensitive applications[1.5].

In summary, although rare-earth magnet materials offer considerable improvements in magnetic properties, their present relatively high cost usually limits their use to applications in which there is a viable premium in terms of miniaturisation and efficiency, or an improved power to weight ratio or other preformance factor. Nevertheless, the continual reduction in price, which is being driven by increased competition and improved production routes will lead to further penetration of NdFeB magnets into market sectors which are presently dominated by ceramic ferrites.

1.2 PROPERTIES OF NdFeB

The normal demagnetization characteristics for the different generic types of permanent magnet material are shown in fig 1.2, and highlight the improved magnetic properties of sintered NdFeB compared to the more established materials such as the Ceramic Ferrites, Alnicos and Samarium Cobalt alloys. Of particular relevance to the use of NdFeB magnets in electrical machines is the linearity of the demagnetization curve, which often extends throughout the 2nd quadrant and affords a high degree of demagnetization withstand for a given magnet thickness. This linearity ensures that NdFeB materials are unconditionally air-stable at room temperature, i.e there is no irreversible loss in magnet flux under magnetic open-circuit conditions irrespective of the magnet geometry. The magnetic properties of NdFeB magnets are continually being improved by refinements to the production route and by compositional variations to enhance specific properties e.g the addition of cobalt, vanadium and dysprosium etc.

The maximum energy product of current commercially available NdFeB magnets is approximately 356 kJ/m^3 (45 MGOe) [1.6].

The effect of temperature on the demagnetization characteristic of a typical commercial grade of sintered NdFeB is shown in fig 1.4. A comparison with the average reversible temperature coefficients of remanence and coercivity of other generic material types, fig 1.5, illustrates the increased thermal sensitivity of the properties of NdFeB. As well as leading to a reduction in the coercivity and remanence, the squareness of the intrinsic demagnetization characteristic also degrades severely with temperature. As a result, the knee in the normal demagnetization characteristic, i.e the point at which it departs from a linear slope, moves further into the second quadrant. Thus, at elevated temperatures NdFeB is significantly more susceptible to irreversible demagnetization and extreme care is necessary in the design of magnetic circuits.

The problem of the poor elevated temperature performance of NdFeB magnets has been addressed to an extent by the development of higher temperature grades, obtained by doping or substitution of the constiuent elements of the standard grades. For example, large increases in the intrinsic coercivity of NdFeB can be effected by substitution with dysprosium or molybdenum [1.7], although at room temperature this is not reflected in an improved normal coercivity. As the temperature is increased the coercivity of the material decreases at a similar rate to that of the undoped material. However, since the room temperature coercivity is significantly higher the coercivity and the position of the knee at a given elevated temperature are improved, thus extending the working temperature range of the material. Although doping does not address the fundamental problem of the poor temperature coefficents of coercivity and remanence, it is commonly used to produce high temperature grades of materials. The magnetic properties for a number of commercial high temperature grades of NdFeB at

150°C are shown in fig 1.6.

NdFeB magnets, particularly the sintered grades, are sensitive to corrosion even in non-extreme environments. One method of overcoming this problem is the application of a thin protective coating to the magnet as a final stage in the production. Coatings based on vapour deposited aluminium(10μm thick), plated nickel (15μm thick), and epoxy resins(25μm) have been commercialised and shown to give greatly improved long term stability[1.8]. However, although the coating of magnets has extended the long term stability in experimental assessments, their reliability in a production environment relies on maintaining the integrity of the coating, since even microscopic surface damage during device assembly can cause corrosion. This, coupled with the additional production cost associated with the coating process, make an improvement in the intrinsic corrosion resistance a more favourable target. However, although material grades with improved intrinsic corrosion resistance have been realised by substitution of small percentages of Vanadium [1.9], the majority of magnets used in corrosion sensitive applications are presently supplied with coatings.

1.3 MAGNETIZATION.

A schematic showing the change in the operating point of a permanent magnet during its intial magnetization is shown in fig 1.7. For convenience, the magnet is assumed to have a single operating point, whereas in practice there will be a spread of operating points within the magnet, the spread being dependant on the geometry and the demagnetization characteristic of the magnet. In an unmagnetized magnet the magnetic moments of the individual domains are randomly oriented with a resultant zero net moment for the bulk magnet.

The application of a magnetizing field to the unmagnetized magnet causes a gradual alignment of the domain moments and the working point of the magnet is

driven along the initial magnetization curve from point A to point B.

On removal of the magnetizing field the working point of the magnet recoils along a different locus to a point C in the second quadrant which is determined by the open-circuit load-line and the level of magnetizing field to which it was exposed. For a given grade of material there is a minimum saturating field strength which must be applied in order to develop the full hysteresis loop of the material. Failure to achieve this saturating field leads to the magnet recoiling along a minor loop with a consequent reduction in the remanence, coercivity, and 2nd quadrant linearity. Once the magnet has been magnetized, the operating point may move up and down the hysteresis loop, either by the application of an external field or by a change in reluctance of the magnetic circuit. However, if the operating point moves beyond the linear region of the demagnetization characteristic then on removal of the demagnetizing field the magnet will recoil to a different open-circuit working point, with a resultant irreversible loss in the magnet flux. This irreversible loss can only be recovered by re-magnetizing the permanent magnet.

1.4 DEMAGNETIZATION

The demagnetization of a magnetized magnet can be effected either by heating the magnet above its Curie temperature or by exposing it to a decaying alternating magnetic field. Complete thermal demagnetization can be readily achieved for sintered NdFeB magnets since their low Curie temperature (typically 320^{o}C) is below the temperature at which permanent metallurgical damage occurs. However, polymer bonded isotropic NdFeB magnets cannot be thermally demagnetized since the temperature required to ensure complete demagnetization is well beyond that at which the commercially used polymer binding agents are stable. Exposure of a magnet to a decaying alternating field, such as that illustrated in fig 1.8, can be used in cases where thermal demagnetization is not practical. With the application of such a field waveform

the magnet is successively demagnetized in alternating directions and the working point cycles around an ever decreasing hysteresis loop which spirals in towards the completely demagnetized state. To ensure complete demagnetization, the decay envelope of the waveform must be sufficiently long with respect to the frequency of the sinusoidal variation to ensure that the reduction in magnitude between successive pulses is sufficiently small so as to allow at least partial reversal of the magnetization.

1.5 ROLE OF ANISOTROPY IN MAGNETIZATION

An anisotropic material such as sintered NdFeB has a preferred direction of magnetization. Typical initial magnetization curves in the preferred and non-preferred directions for a well aligned anisotropic permanent magnet are shown in fig 1.9 The magnetizing field which must be applied to reach the same level of polarization in the non-preferred direction is the anisotropy field of the material, H_A. It should be noted, however, that even though the same level of polarization can be reached in the first quadrant by the application of a field in excess of the anisotropy field, the subsequent recoil characteristic is vastly different in the two orientations. The rare-earth based permanent magnets exhibit very strong anisotropy e.g NdFeB has an anisotropy field of 6.36 MA/m (8.0 T) at room temperature [1.10].

In an idealised fully aligned magnet there will be a component of remanent magnetism only in the preferred direction irrespective of the orientation of the magnetizing field providing of course that it has a component in the preferred direction. Nevertheless in anisotropic materials, such as sintered NdFeB, it is important to achieve good alignment between the applied magnetizing field and the preferred axis of magnetization if saturation of the entire magnet volume is to be achieved for the minimum magnetizing mmf. Failure to achieve this alignment results in an increase in the mmf required to saturate the magnet since at any point in the magnet only the component of the magnetizing field which is parallel to the preferred direction is useful

in achieving saturation in the preferred direction. However, even in cases where there is very poor alignment almost complete saturation in the preferred direction of magnetization can be achieved, albeit at the expense of a very high applied mmf requirement. The orientation of the remanent magnetism in such a case will be a very good approximation to the required preferred orientation, although in practical magnets there is inevitably a remanent magnetism in the nominally non-preferred direction due to imperfections in the granular structure and the degree of alignment which can be achieved during the production of the magnet.

In isotropic materials, such as polymer bonded NdFeB, the magnetization in the material is parallel to the applied magnetizing field. Hence, any deviation of the magnetizing field from the desired direction will result in a corresponding deviation in the resultant remanent magnetism.

1.6 ROLE OF COERCIVITY MECHANISMS IN MAGNETIZATION

Coercivity in permanent magnets is essentially controlled by one of two mechanisms, either domain wall pinnning (e.g isotropic melt-spun NdFeB) or domain nucleation (e.g anisotropic sintered NdFeB) [1.11]. Although a full consideration of these microscopic phenomena is outside the scope of this thesis, their macroscopic consequences are of great importance in the design of magnetizing systems. The mechanism which controls the coercivity determines both the shape of the initial magnetization curve and the magnetizing field strength which must be applied within the magnet to ensure saturation. Typical initial magnetization and demagnetization curves for both nucleation and pinning type materials are shown in fig 1.10. The magnetization curve for a pinning type material has a distinct initial knee, below which the application of a magnetizing field produces negligible residual remanence or coercivity in the magnet i.e the characteristic is approximately reversible in this initial

region. For a nucleation material , however, the characteristic is immediately strongly irreversible and has a significantly higher initial permeability, e.g sintered NdFeB (RES270) and isotropic bonded NdFeB (Bremag10N) have maximum relative permeabilities of 19.5 and 1.65 respectively.

The dependance of the remanence and coercivity on the level of the applied magnetizing field for typical nucleation and pinning type materials is shown in fig 1.11. In nucleation type materials the remanence is developed very rapidly as a function of the applied magnetizing field, and near full remanence is obtained for magnetizing fields significantly lower than those required to obtain the full coercivity. In a pinning type material, however, the remanence is developed gradually, and full remanence is achieved at magnetizing fields similar to those required to achieve the maximum coercivity and the maximum energy product. The application of ever increasing magnetizing fields will eventually lead to the attainment of the maximum possible remanence, coercivity and energy product for the material, i.e the fully saturated values. However, the rate at which these limiting values are approached with an increasing magnetizing field differs greatly between nucleation and pinning controlled materials. Fig 1.12 and 1.13 shows the published dependancies of the demagnetization characteristics of a pinning controlled isotropic NdFeB[1.11] and a nucleation controlled $SmCo_5$[1.12] on the level of initial magnetizing field.

In the case of nucleation type materials the limiting properties are achieved with field levels which are realisable in a production enviroment. In pinning type materials the application of fields far in excess of those which are practically achievable in a production enviroment can produce discernable improvements in the demagnetization characteristic. However, the relatively small incremental improvements which can be produced in pinning type materials as the saturation values are approached are often not justifiable in terms of the increased magnetizer energy required to produce the large

increase in magnetizing field e.g the outer characteristic of fig 1.12 is produced following magnetization with a field strength of 8750 kA/m which corresponds to a flux density in the magnet of 11.8 T. Thus a compromise material characteristic is usually aimed for, being somewhat below the limiting value in order to reduce the magnetizing field requirement to a manageable level. Hence a direct comparison of the magnetizing field required to achieve the absolute maximum energy products for nucleation and type pinnning materials is of limited use in determining the relative difficulties of their magnetization in practice.

A more practically based comparison to compare the magnetizing field required to produce 90% of the limiting value, since for both coercivity mechanisms the incremental slope of the energy product increase with respect to the magnetizing field as the 90% level is approached is usually sufficient to justify the additional magnetizer energy requirements. The magnetizing field strength required to obtain 90% of the maximum energy product for a range of materials is shown in fig 1.14, from which it can be seen that the required magnetizing fields are significantly lower for nucleation materials than for pinning materials.

1.7 MAGNET PRODUCTION ROUTES

The two principal production routes for NdFeB magnets are the rapid solidification process(also commonly known as melt spinning or rapid quenching) developed by General Motors Corporation and the more conventional powder sinter process developed by Sumitomo Special Metals Company, although alternative production routes based on processes such as mechanical alloying are gradually evolving [1.13]. The relative merits of these alternative production routes and possible modifications to reduce the cost of finished magnets are well documented [1.14],[1.15],[1.16]. The following discussion will, therefore, be limited to those aspects of production which play a role in determining the magnetization requirements.

Powder sinter production route

The production route for anisotropic sintered NdFeB magnets is depicted in the flowchart of fig 1.15. A stoichiometric composition of the consituent elements is induction melted to from an ingot which has a random orientation of grain easy axes. This ingot is then reduced to fine powder particles which typically have a diameter of the order of 2μm [1.17]. The reduction of the ingot to powder is effected either by a two stage mechanical crushing/milling process or by Hydrogen decrepitation follwed by jet milling [1.18]. To obtain useful magnetic properties these grains must then be aligned in a magnetic field to produce a net preferred axis prior to the pressing of the magnet. The aligned powder is then either die-pressed or isostatically pressed to form the so-called green compacts which are subsequently sintered. The sintered magnet is then machined to the final tolerance and any required corrosion resistant coating applied.

Aligning process

Small blocks, disks, ring magnets and arc segments are usually field aligned during the die-pressing process by using a ferromagnetic punch. A schematic of a typical aligning and pressing system is shown in fig 1.16. The field coils of the punch are normally supplied from a d.c source but pulsed sources such as half-cycle or capacitor-discharge magnetizers can also be utilised, providing the pulse duration is sufficiently long to overcome eddy current problems in the steel structure, and are of a similar duration to the finite pressing period. However, although it is a convenient single stage process, it does suffer from the drawback of limited field capability, particularly for d.c sources.

To produce fields in excess of the saturation flux density of typical steel, i.e 1.8

to 2T, requires a disproportionate increase in the field current and hence losses in the excitation coils. However, even in cases where the onerous supply demands for high fields can be met, the extreme saturation of the punch can result in the field distribution departing from the required aligning field distribution. The limited field which can be applied to align the magnetic powder in typical die-pressing equipment often results in less than ideal alignment and hence a dilution in the magnetic properties of the finished magnet. The dependance of the magnetic properties of $SmCo_5$ (Philips Components RES190) on the magnitude of the aligning field is shown in fig 1.17. Although equivalent data for NdFeB was not obtainable, the similar coercivity mechanisms of $SmCo_5$ and sintered NdFeB suggest that the behaviour of anisotropic NdFeB is likely to be similar.

The dilution in properties which result from failing to achieve ideal alignment are, however, often regarded as being acceptable, thereby easing the production process and hence reducing cost. Uniaxial pressing in a ferromagnetic punch also introduces inhomogeneities into the magnet, a factor that is reflected in the variation of the electrical conductivity for different orientations to the pressing direction [1.19]. Improved magnetic properties can be achieved from anisotropic sintered magnets with pulsed field alignment and isostatic pressing in which a long cylindrical flexible polymer sheath is filled with the milled powder which is then aligned in the bore of an air-cored solenoid supplied from a capacitor-discharge magnetizer. By using this method, very uniform fields, which are often in excess of 5T, can be applied, resulting in near ideal alignment. The aligned powder in the sheath is then pressed in an oil bath, such that pressure is applied uniformly in all directions. The green compact is then sintered in a similar manner to the die-pressed compacts, and the resulting magnet is used as stock for cutting into blocks and discs. A relatively small isostatically pressed sample of sintered NdFeB is shown in fig 1.18.

The rapid solidification route

A schematic of the rapid solidification equipment used to manufacture isotropic NdFeB powder is shown in fig 1.19. The constituent alloy elements are induction melted in a quartz glass crucible and then drawn from the nozzle onto a water cooled rotating copper wheel. The molten alloy cools rapidly to form a thin ribbon, which typically has a thickness in the range 30μm - 50μm and a width of 1.5mm. Typical cooling rates for optimal magnet properties are of the order of 10^6 K/s. There are three alternative methods for the subsequent fabrication of bulk magnets from these ribbons, viz cold pressing in a polymer medium, hot pressing and die-upset forging [1.20]. Room temperature intrinsic demagnetization curves of magnets produced by these three alternative processing methods are shown in fig 1.20.

Although improved properties can be achieved by hot pressing and die-upset forging, the isotropic polymer bonded grades are presently the most important commercial grades [1.5]. The bulk magnetic properties of polymer bonded NdFeB magnets based on isotropic magnetic ribbon can be controlled by varying the powder to polymer ratio. The isotropic powder produced commercially by General Motors Corporation for polymer bonding has a specified remanence of 0.69T and an intrinsic coercivity of 1190 kA/m [1.12]. Thus almost fully dense bonded magnets with a high powder content of 85% or so, exhibit magnetic properties close to those of the powder itself, e.g Magnet Applications Ltd. produce a grade with Br =0.64T (Bremag 10N), whereas mechanically flexible materials with a higher polymer content can have correspondingly diluted magnetic properties, e.g Br = 0.47T (Dynacast PBN1). The magnetic properties of the powder itself and hence the magnetizing field strength required to ensure saturation is unaffected by the proportion of polymer loading. However the total mmf which must be produced by the fixture winding to achieve this field strength in the magnet is

affected by the loading because of its effect on the bulk magnetic properties and hence permeability.

1.8 ROLE OF MAGNETIZATION IN THE PRODUCTION OF A PERMANENT MAGNET DEVICE.

The magnetization process is often treated as the last consideration in the design and production of a permanent magnet device. Indeed, the pivotal role of magnetization in device realisation is often completely overlooked. There are a number of stages during the production of a permanent magnet device at which the magnetization can be carried out. This can be illustrated by considering the production of a brushless d.c motor with a multipole rare-earth permanent magnet rotor:

1. Two-pole sub-component level magnetization.

In this method each magnet pole is magnetized separately and the multipole magnet is assembled from simple two-pole magnetized magnet sections. However, this is an unattractive method in production, particularly if a high pole number is required. Nevertheless, it is useful for initial prototyping since a standard solenoid magnetizing fixture can be used.

2. Multipole component level magnetization.

In this method the multipole magnet is magnetized in a single step using an assembly specific magnetizing fixture. The magnet may be a single piece of material or constructed from a number of discrete un-magnetized magnets.

3. Sub-assembly magnetization e.g assembled multipole rotor

In this method the fully assembled rotor is magnetized with the required multipole field pattern in an assembly specific magnetizing fixture.

4. Post-assembly magnetization e.g fully assembled motor.

In this method the motor is completely assembled and subsequently magnetized by inserting it into a motor specific magnetizing fixture. Alternatively it may be possible to use the windings of the motor itself for magnetization, but this is generally limited to machines that are specifically designed for high current and low voltage operation, as will be discussed in chapter 4.

The difficulty associated with the various magnetization processes increases in progressing from 1 to 4, both in terms of the energy required for magnetization, and the design of the assembly specific fixture. However, from a production point of view, eliminating the handling of magnetized magnets is highly desirable.

1.9 MAGNETIZATION PATTERNS

The most basic magnetization configuration is a simple dipole, which can be readily produced for a wide range of magnet dimensions and geometries by a single general purpose solenoid fixture. A selection of multipole magnetization field patterns which can be applied to both an isotropic or suitably aligned anisotropic magnets are shown in fig 1.21.

1.10 MAGNETIZING EQUIPMENT.

D.C Electromagnets

Iron-yoked D.C electromagnets are limited to magnetizing materials such as ferrites and alnicos with simple two-pole field configurations. For such materials the magnetizing field strength required to ensure near full properties can be achieved in the airgap of an electromagnet without excessive saturation of the iron-yoke. The airgap field which is developed as a function of current and pole spacing for a typical

commercial electromagnet is shown in fig 1.22. The major problem with d.c electromagnets is the much larger total energy dissipation, and hence temperature rise, which results from producing fields with a relatively long duration compared to pulsed magnetizing systems.

Superconducting Solenoids

Liquid helium cooled superconducting solenoids capable of producing flux-densities up to 15T are an established but expensive technology. However, the emergence of ceramic superconducting materials with critical temperatures suitable for liquid nitrogen cooling offer scope for superconducting solenoids to enter the magnet produtión environment, where the rapid magnetization of two-pole magnets by passing them through a static field produced by a superconducting magnet could emerge as a viable option. However, for multipole magnetization, superconducting fixtures are of little utility since they have a limited critical current densitiy e.g the latest laboratory scale state-of-the-art silver sheathed Bismuth based superconducting wire has critical current densities of 110 A/mm^2 at 77K and $1kA/mm^2$ at 4.2K [1.21]. The case studies of chapters 4,5 and 6 will demonstrate that the current density required in multipole magnetization fixtures is typically at least $5kA/mm^2$, and can in some cases be as high as 30 KA/mm^2.

Permanent Magnet Magnetizer

For materials such as Alnicos and certain grades of bonded and sintered ceramic ferrites, the field level required for saturation is within the range which can be produced by focussing the field produced by another magnetized permanent magnet by a suitably designed iron-yoked magnetic circuit. The circuit can include low grade steel components, e.g mild steel, in regions where the iron yoke can be dimensioned to limit the flux density to less than 1.6T, whilst higher grade magnetic steels, usually of high cobalt

content, can be used for flux focussing beyond 1.6 T. This method is useful when the flux density required in the airgap does not exceed 2.3T or so (typical saturation flux density of high cobalt content alloys e.g Permendure 49). Outside the active magnetizing region, the field should decay gradually so as not to distort the magnetization of the magnet as it is withdrawn from the fixture. This requires a consideration of the full three-dimensional nature of the field distribution. Since the field is present continuously, precautions must also be taken to ensure that there is no contamination of the active region by ferrous debris, and that safety measures for the handling of the magnet assemblies are enforced .

Fig 1.23 shows a sintered NdFeB based fixture for magnetizing a fully assembled 2-pole 5-slot brushed d.c motor equipped with a bonded ferrite magnet (Ferriflex3). The saturation polarization of 0.23T and the saturation magnetizing field strength of 800 kA/m correspond to a flux density in the magnet of only 1.23T to ensure saturation. The field distribution in the fixture predicted by a magnetostatic finite element field solution is shown in fig 1.24. The field produced by the fixture is sufficient to ensure saturation of the magnet despite the fact that the motor back-iron shunts the magnetizing flux and the fixture has large leakage flux. Although the fixture is not optimised it serves to show that this method of magnetization is feasible. An improvement in the fixture design, with a subsequent reduction in magnet volume, could be achieved by refining the shape of the focussing circuit near the motor.

Half-cycle magnetizers

One method of producing a unidirectional pulsed field is to isolate one half cycle from the AC mains by a suitable control circuit, such as that shown in fig 1.25. However, half-cycle magnetizers have a limited peak current capability due to the source impedance of the mains supply. Nevertheless, by using a suitable pulse trans-

former peak currents of up to 60,000A are obtainable. With a 50Hz supply, the fixed pulse duration of 10ms imposes a constraint on the peak current that can flow for a given total energy dissipation, since the joule heating over a half cycle determines the maximum current which can flow through a given wire diameter for a given temperature rise. By assuming that the transient current which flows is sinusoidal, a reasonable approximation for most multipole fixtures since the limited space forces the fixture to be comparatively resistive, the total energy dissipated per unit length of the conductor is given by:

$$E = \int_0^{0.01} i(t)^2 r(t)\, dt \qquad (1.1)$$

where

r is the resistance per unit length.

For a maximum temperature rise of 200°C the resistance increases by approximately 80%. The integral of equation 1.1 can be simplified if r is taken to be the average value r' over the pulse period, i.e the resistance per unit length at 120°C (i.e 100°C rise above a 20°C ambient).

$$\Delta E = \frac{0.01\, I_p^2\, r'}{2} \qquad (1.2)$$

where

Ip = Peak current (A)

The resulting temperature rise for a conductor of a given cross-sectional area Ac is then

$$\Delta T = \frac{0.01\, I_p^2\, r'}{2\, A_c^2\, D_{Cu}\, C_h} \qquad (1.3)$$

where

D_{cu} = Density of copper ($8900 kgm^{-3}$)

C_h = Specific heat capacity of copper ($385\ J\ Kg^{-1}\ K^{-1}$).

Thus, substituting the relevant constants for a 200°C temperature rise gives:

$$I_p = \sqrt{5.735\, A_c^2\, 10^{18}} \tag{1.4}$$

Calculated values of peak current for a range of conductor diameters are shown in fig 1.26. The relatively low currents compared to those achievable with capacitor-discharge systems demonstrate the limitations of half-cycle equipment particularly in small multipole fixtures in which small conductor cross-sections are required.

Capactior-discharge magnetizers

Capacitor-discharge magnetizer systems can be much more powerful than both half-cycle equipment and d.c electromagnets, and are by far the most dominant technology used for the magnetization of rare-earth permanent magnets. In capacitor-discharge magnetization a bank of capacitors is charged over a period of a few seconds and the stored energy is subsequently discharged into a suitably designed magnetizing fixture. The resulting current pulse length can typically be varied from a few μs to tens of ms by varying the capacitance and the fixture inductance. Thus the method offers much greater flexibility than fixed duration half-cycle equipment since much higher currents can flow through small cross-sectional area conductors for the same total dissipation. The magnetizer and the fixture can be represented by the equivalent circuit of fig 1.27.

Neglecting the effect of temperature on the resistance of the fixture and the internal resistance of the magnetizer, the fixture current during the period in which the clamping device is not conducting can be calculated from the governing second-order differential equation of the system, viz:

$$L\frac{d^2i}{dt} + R\frac{di}{dt} + \frac{i}{C} = 0 \tag{1.5}$$

The form of the analytical solution is dependant on the damping of the circuit. For the overdamped and underdamped cases the corresponding solutions to equation (1.5) are:

Underdamped, i.e $R < 2\sqrt{(\frac{L}{C})}$

$$i(t) = \frac{V_o}{\omega L} e^{-\sigma t} \sin(\omega t) \tag{1.6}$$

where

R=Total circuit resistance

L = Total circuit inductance

C = Total circuit capacitance

where

$$\sigma = \sqrt{\frac{R}{2L}}$$

$$\omega = \sqrt{(\frac{1}{LC} - \frac{R^2}{4L^2})}$$

Overdamped, i.e $R > 2\sqrt{(\frac{L}{C})}$

$$i(t) = \frac{V_o}{L(\lambda_1 - \lambda_2)} (e^{-\lambda_1 t} - e^{-\lambda_2 t}) \tag{1.7}$$

where

$$\lambda_1 = -\frac{R}{2L} + \sqrt{\left(\frac{R^2}{4L^2} - \frac{1}{LC}\right)}$$

$$\lambda_2 = -\frac{R}{2L} - \sqrt{\left(\frac{R^2}{4L^2} - \frac{1}{LC}\right)}$$

The most efficient energy transfer is obtained with an underdamped circuit and hence wherever possible the fixture design should be designed to produce an underdamped system. In order to produce a unidirectional current pulse, a clamping device is connected in parallel with the fixture. When the voltage across this clamping device becomes negative, it conducts, and the fixture current decays exponentially according to:

$$i(t) = I_o e^{-\frac{Rt}{L}} \qquad (1.8)$$

Capacitors

The capacitors are usually one of three types, viz electrolytic, metal-foil paper, and oil filled. Electrolytic capacitors are suitable for use up to approximately 500V e.g the low voltage unit shown fig 1.28 has two 410V capacitors connected in series between the positive and ground busbars. Since they are unipolar, they are not generally suitable for producing oscillatory demagnetizing waveforms, although certain high quality electrolytic capacitors can withstand occasional significant reverse voltages without breakdown. Magnetizers based on electrolytic capcitors are suitable for long time constant pulses, but are often unsuitable for fixtures having small cross-sectional area conductors due to excessive fixture heating. There are long term stability problems with the dielectric to an extent that after several weeks of inactivity, the dielectric layer must be reformed by increasing the voltage to the working voltage in a series of steps

over a few hours.

Metal-foil paper capacitors are bipolar and typically have voltage ratings of several thousand volts. They are commonly used in commercial magnetizers rated up to 3kV, and are particularly suitable for short duration pulses. Oil-filled capacitors have higher voltage ratings than metal-foil paper capacitors and are useful for producing the very fast large magnitude pulses, which are often required in magnetizing fixtures employing small cross sectional area conductors. Neither metal-foil paper nor oil-filled capacitors suffer significant wear and stability problems.

The internal impedance of a magnetizer, which consists of the inductance and resistance of the capacitors, switching devices and the connection leads, can play a crucial role in determining the performance of a fixture, particularly when geometrical constraints limit the number of turns that can used to such an extent that the impedance of the fixture may be comparable to that of the magnetizer. Electrolytic capacitors have higher internal impedances than metal foil and oil-filled capacitors. The internal impedance of the capacitors can vary due to ageing, temperature rise, voltage stress and duty cycle, particularly for electrolytic capacitors. Therefore, whilst they are capable of producing long duration pulses, in other respects electrolytic capacitor performance is vastly inferior to metal-foil and oil-filled capacitors. Nevertheless they are still widely used since the capital cost per unit of stored energy is typically half that of the other capacitor types.

The two experimental magnetizers which were used in the design studies described in chapters 4,5 and 6 are shown in fig 1.28. Both have a facility for varying the capacitance, a feature which is not generally available on production magnetizers. Although the high voltage magnetizer is capable of being used at 5kV, for the purpose of the design studies, its maximum voltage was specified as 3kV, since this is more

representative of high voltage magnetizers which are used in production environments [1.22][1.23]. The magnetizers of fig 1.28 are equipped with ignitron series switches, which although inferior to thyristors in terms of the on-state voltage drop and switching drive requirements, offer a degree of robustness to occasional overload which cannot be matched by semiconductor devices. The clamping devices are a semiconductor diode for the low-voltage magnetizer and an ignitron for the high voltage magnetizer.

The internal impedances of the magnetizers of fig 1.28 were estimated from short-circuit tests with subsequent substitution of the measured peak current and time to peak in the appropriate equation which governs the current during the non-conducting state of the diode. The variation of the internal impedance for the two experimental magnetizers as a function of their connected capacitance are shown in figs 1.29 and 1.30. By short-circuiting the terminals of the magnetizer with a set of leads which are representative of those used to connect to fixtures, the impedance of the fixture connection leads is included in the internal impedance of the magnetizer, thus simplifying the calculation of the magnetizing fixture impedance.

1.11 MAGNETIZING FIXTURES FOR CAPACITOR DISCHARGE SYSTEMS

The most general purpose form of magnetizing fixture is the solenoid coil depicted in fig 1.31, which is used for magnetizing dipole magnets . The dimensional constraints, e.g volume available for the conductors, are not generally of paramount importance, and hence very efficient coils utilising large cross-sectional area conductors can be constructed. Solenoid coils capable of producing up to 60T are used in fundamental materials research [1.24], this limitation being imposed by conductor material mechanical limitations rather than by electromagnetic or thermal considerations. There are numerous topologies of multipole fixtures. However, they can be divided into 3 principal categories, viz circular radial-field, circular axial-field and planar axial-field.

Schematics of multipole magnetizing fixtures of each of these types are shown in fig 1.32. The very high currents and flux densities associated with the pulsed magnetization of rare-earth magnets produce extreme mechanical stresses within the fixture structure. Therefore, considerable attention must be paid to the mechanical design and construction of the fixture.

Construction usually involves the machining of fixture formers from cast resin or composite materials, the winding of the fixture from a single continuous conductor, the encapsulation of the winding in a resin (usually under vacuum for production fixtures), and the use of glass fibre or composite materials for encasing the fixture.

Thermal considerations are also important since in a production enviroment the time between successive impulses must usually be minimised. In general, the two limiting parameters on cycle time are the energy dissipated in the fixture and the duration of the capacitor re-charging period. For a given cooling arrangement and a non-regenerative magnetizer, in which all the stored energy is disspated in the fixture, switching devices and connection leads, the cycle time is minimised by minimising the magnetizer stored energy. However, as well as the need to minimise the cycle time, other thermal considerations such as insulation degradation and the effect of localised elevated temperatures on the structural integrity of a fixture should be considered. Since the fixture heating during the impulse period is a good approximation to an adiabatic process, a complex cooling arrangement, although useful in quickly removing the dissipated energy, does not influence the maximum instantaneous temperatures in the fixture windings and the winding insulation.

Commercially available enamelled conductors are available with a continous temperature rating of approximately 200^{o}C, whilst Aluminium oxide coated silver conductors are available with a continous temperature rating of 870^{o}C [1.25]. Although

these offer considerable scope in fine-pole pitch fixture design, providing that the magnet can be thermally insulated from the conductors, their prohibitive cost prevented their consideration in the investigations reported in this thesis.

Further, although the fixtures analysed in this thesis are all based on circular cross-section conductors, the design methodology which is developed is equally applicable to fixtures based on rectangular cross-section conductors.

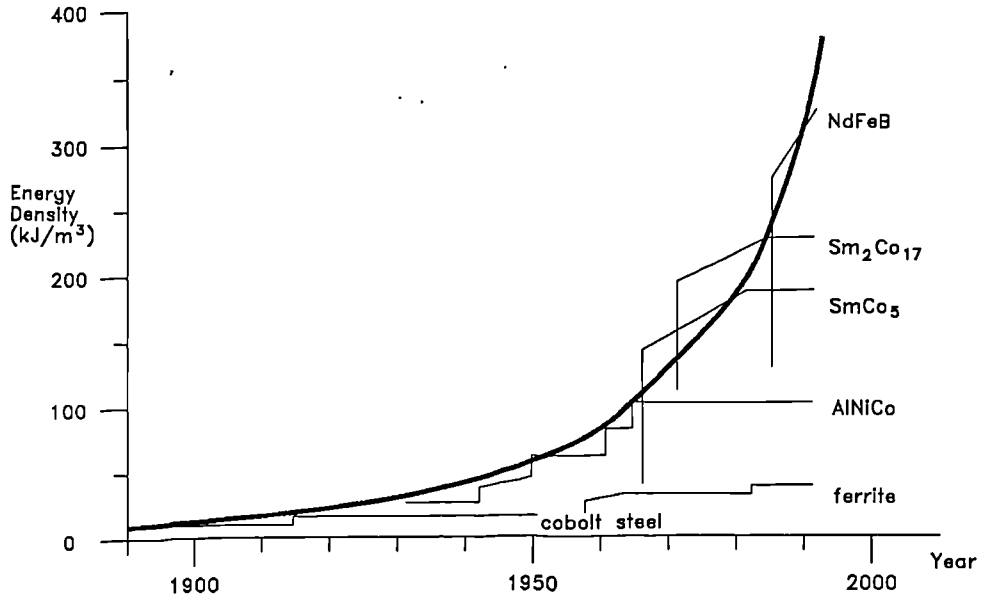

Fig. 1.1 Increase in maximum energy product of permanent magnets.

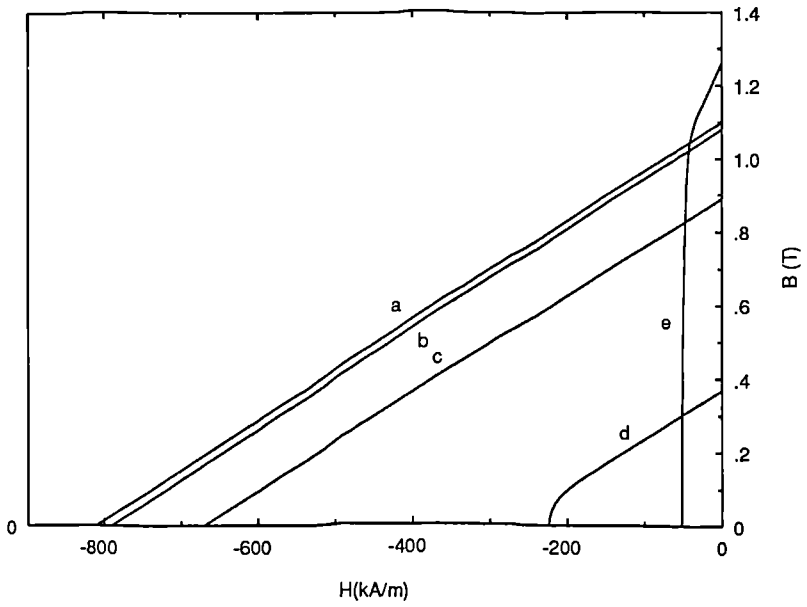

a-Sintered NdFeB (Philips Components RES270)
b-Sintered Sm_2Co_{17} (Vacuumschmelze Vacodym 255HR)
c-Sintered $SmCo_5$ (Philips Components RES190)
d-Sintered Ceramic Ferrite (Philips Components FXD330)
e-Cast Alnico (Philips Components Ticonal 600)

Fig. 1.2 Normal demagnetization characteristics for commercial grades of the major permanent magnet types.

Material	Average selling price per kg in 1991
Bonded Ferrite	$3.80
Sintered Ferrite	$3.70
Cast Alnico	$39.50
Bonded NdFeB	$165.00
Sintered NdFeB	$209.00
Sintered SmCo	$437.00

(Source: Gorham Advanced Materials Institute)

Fig. 1.3 Typical costs per kilogram for the various generic permanent magnet materials.

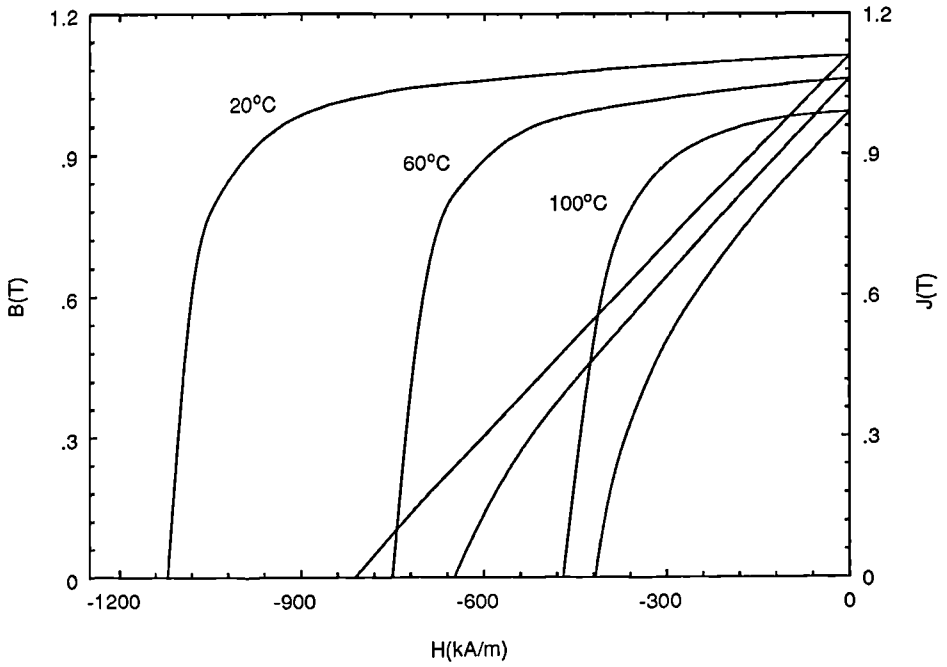

Fig. 1.4. Effect of temperature on the normal and intrinsic demagnetization curves of sintered NdFeB (Philips Components RES270).

Material	τ_{B_r} (% / °C)	$\tau_{H_{ci}}$ (% / °C)
Alnico	-0.02	-0.02
Ferrite	-0.2	+0.35
SmCo	-0.04	-0.05
NdFeB	-0.1 to -0.15	-0.3 to -0.6

Fig 1.5. Typical reversible temperature coefficents of remanence (τ_{B_r}) and coercivity ($\tau_{H_{ci}}$) for various generic permanent magnet materials.

Manufacturer	Grade	H_{ci} (kA/m)	B_r(T)
Outukumpo	Neorem 27SH	450	0.9
Sumitomo	Neomax 30 SH	640	1.0
Crucible	Crumax 301	640	0.9
Philips	RES 257	625	0.9
Vacuumschmelze	Vacodym 400HR	600	0.95
Ugimag	Ugistab 250 XH	650	0.95

Fig. 1.6 Intrinsic coercivity (H_{ci}) and remanence (B_r) at 150°C for a commercial high temperature grades of sintered NdFeB.

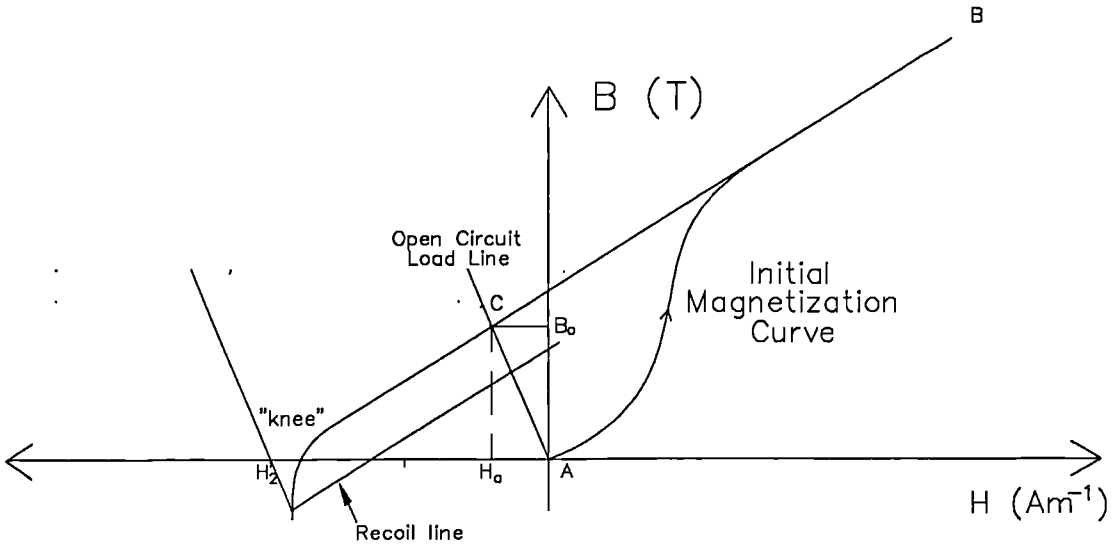

Fig. 1.7 Schematic of the change in operating point of a permanent magnet during magnetization

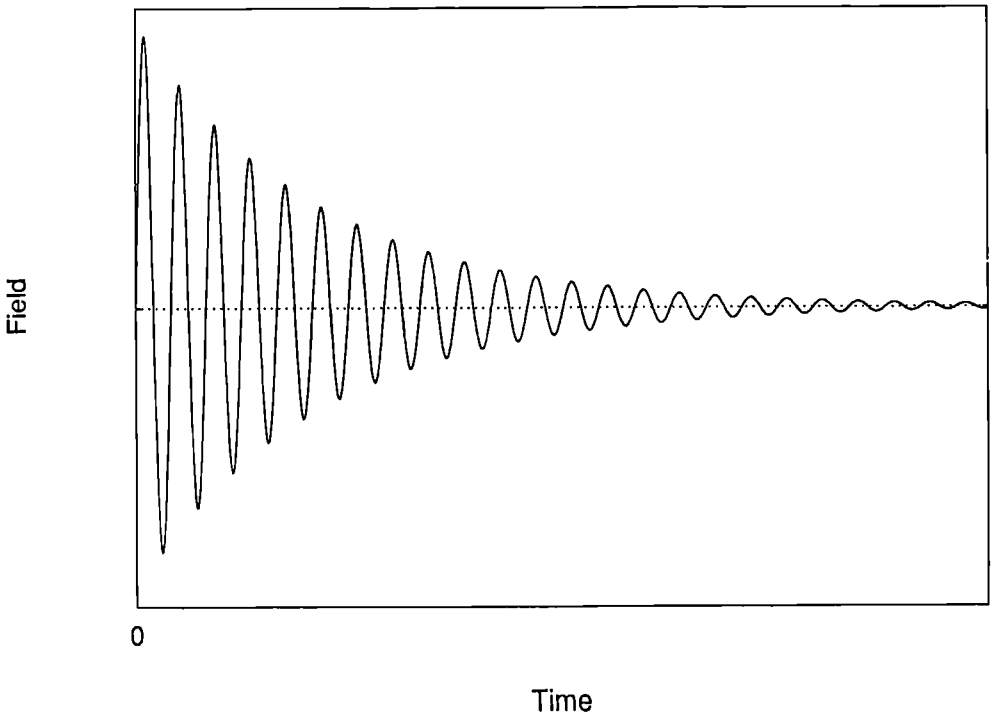

Fig. 1.8 Typical decaying alternating field for the demagnetization of a permanent magnet

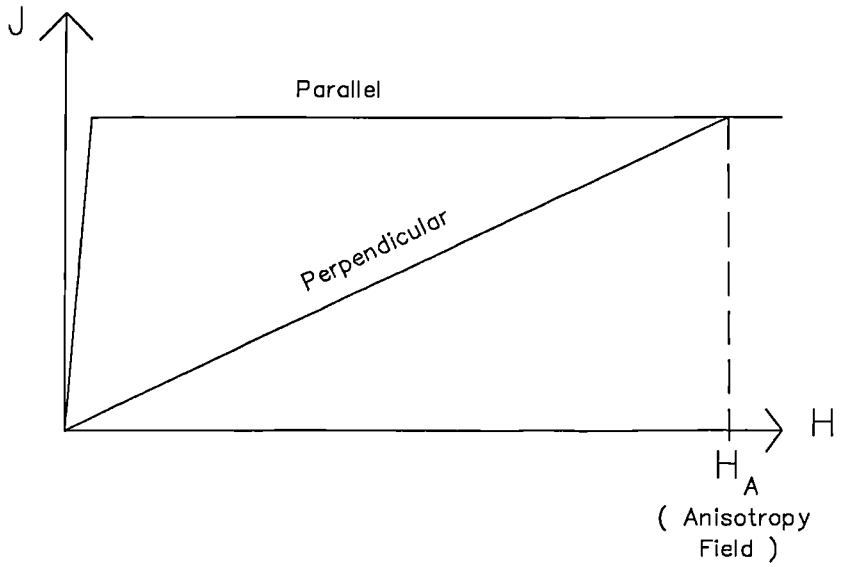

Fig. 1.9 Schematic initial magnetization curves parallel and perpendicular to the preferred axis of magnetization of a well aligned permanent magnet.

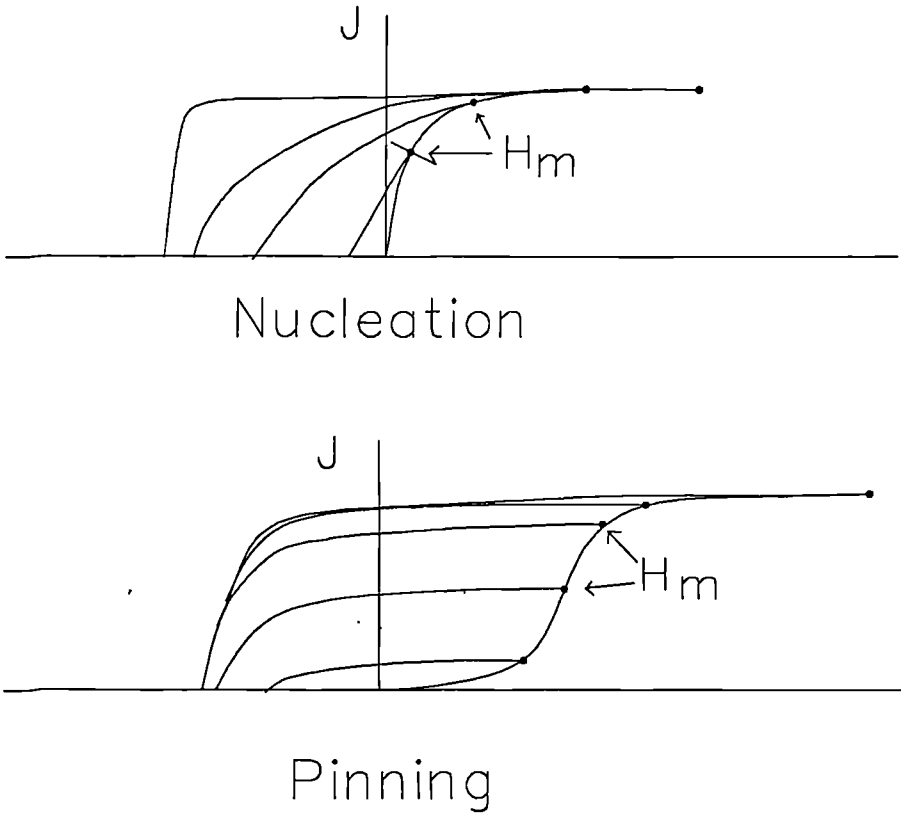

Fig. 1.10 Typical initial magnetization and demagnetization curves for nucleation and pinning coercivity mechanism materials.

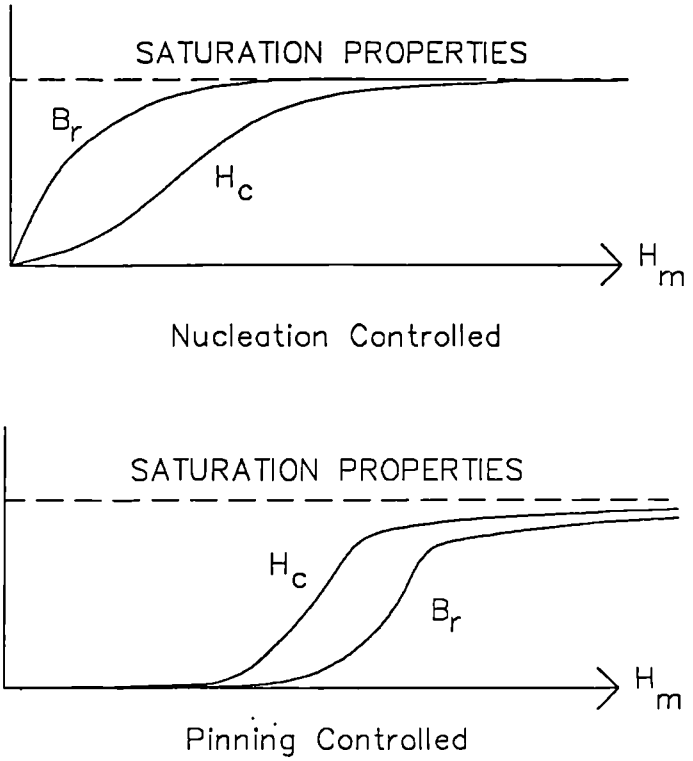

Fig. 1.11 Dependance of remanence and coercivity on the level of magnetizing field for a nucleation and pinning type materials.

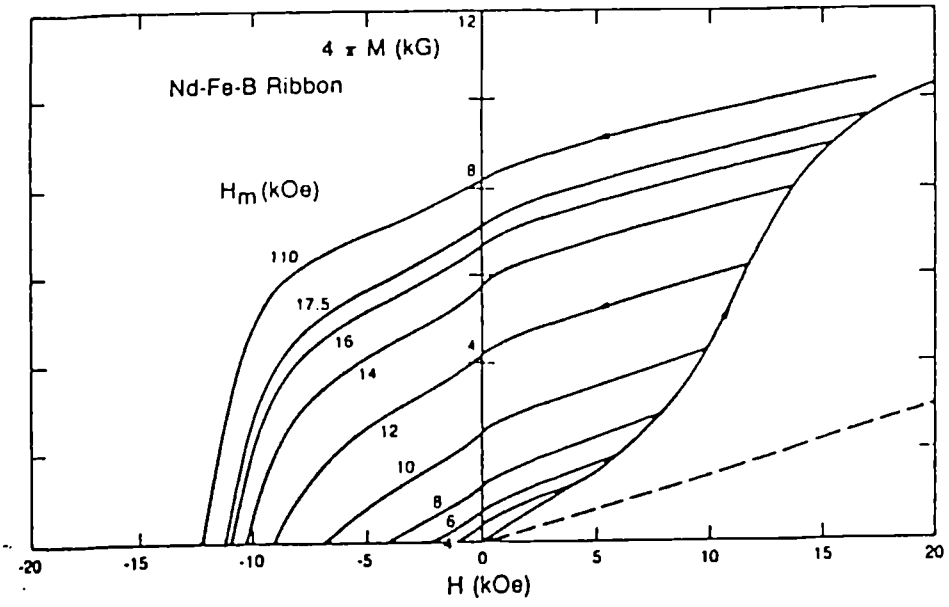

Fig. 1.12 Initial magnetization and demagnetization curves for melt-spun NdFeB ribbons for a range of magnetizing fields H_m (Source: F.E Pinkerton)

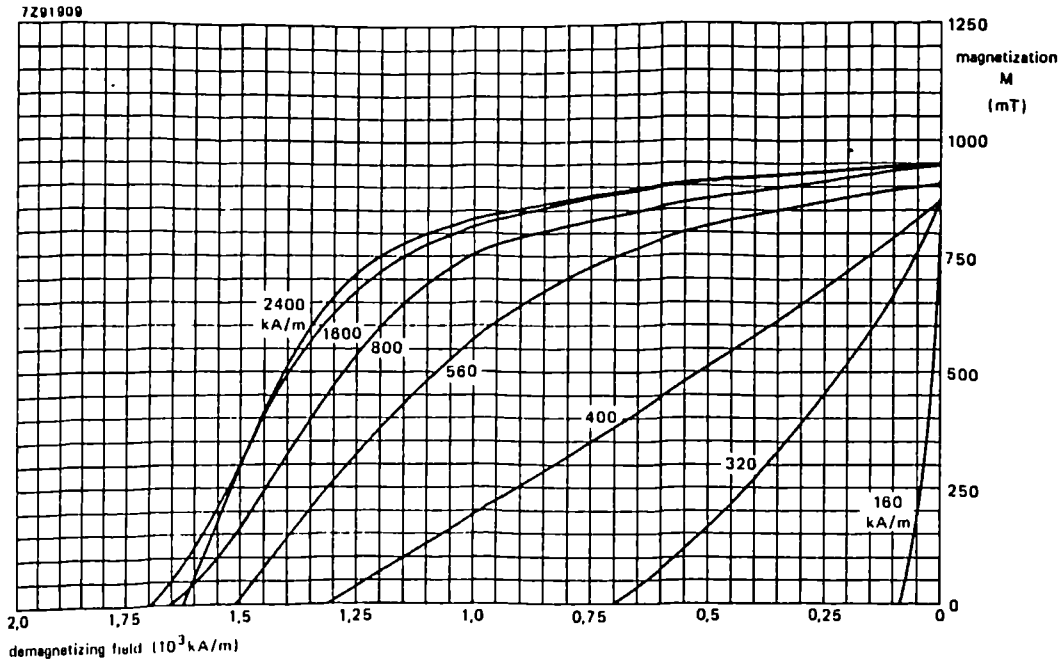

Fig. 1.13 Dependance of demagnetization curves on initial magnetizing field for $SmCo_5$ (Philips Components RES190) (Source: J Ormerod)

Material	Magnetizing field strength (kA/m)	Coercivity Mechanism
$SmCo_5$	1200	Nucleation
Sm_2Co_{17}	2200	Pinning
Sintered NdFeB	1100	Nucleation
Isotropic NdFeB(MQ1)	2300	Pinning

Fig 1.14 Magnetizing field required to obtain 90% of the maximum possible energy product

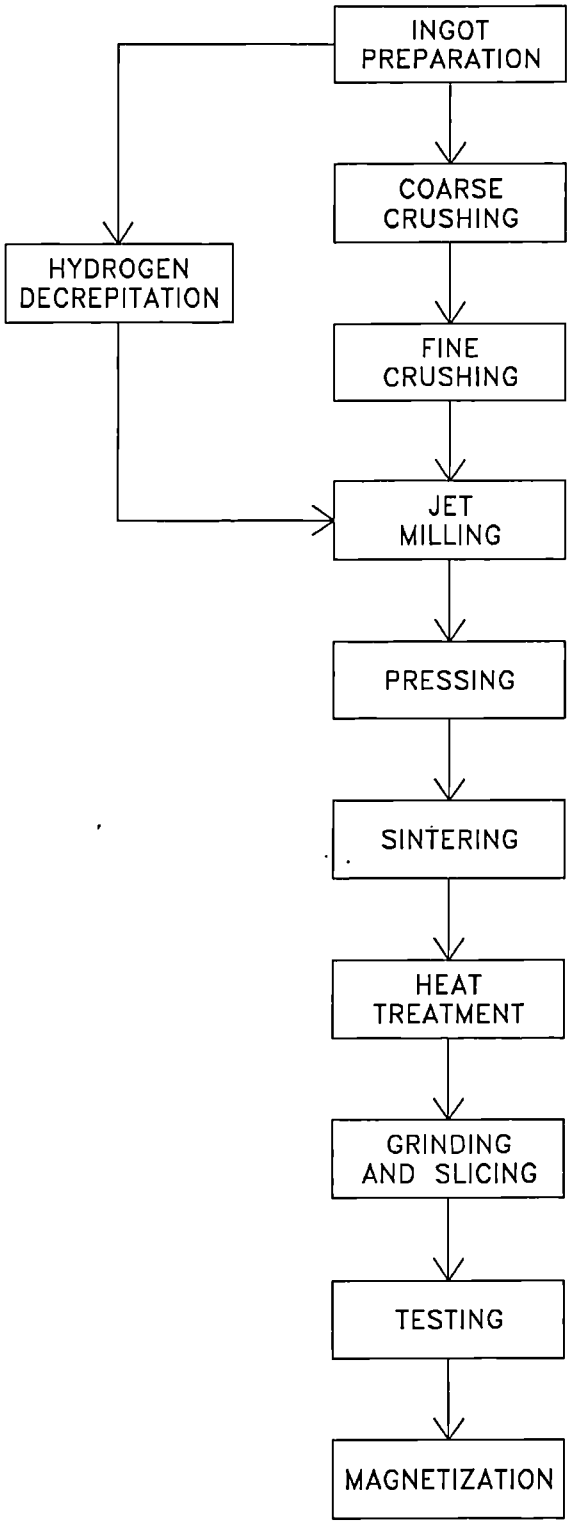

Fig. 1.15 Production routes for anisotropic sintered NdFeB.

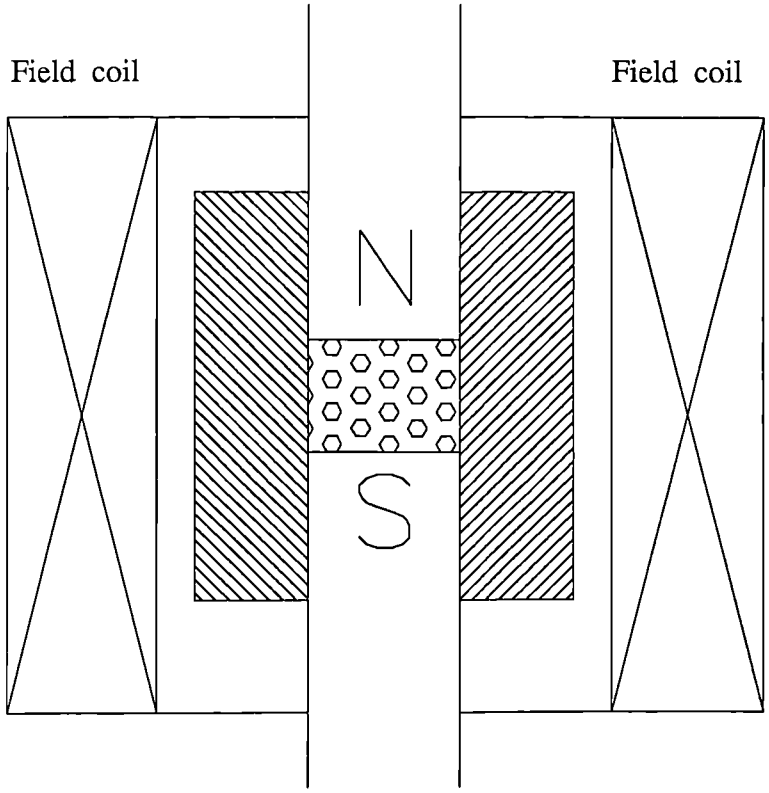

Fig. 1.16 Schematic of a die press and field aligning coils.

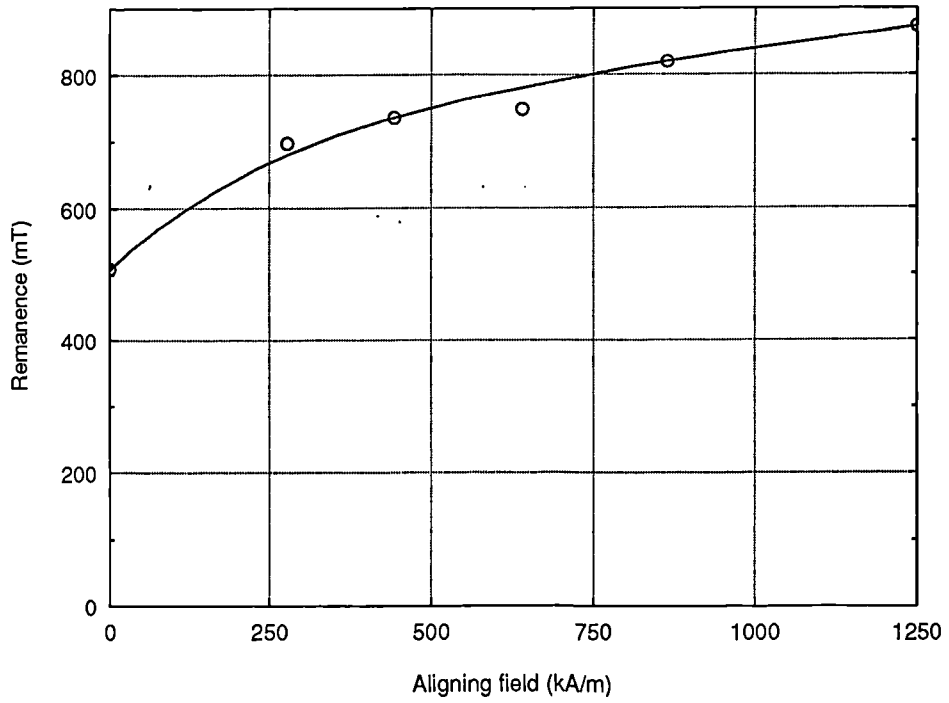

Fig. 1.17 Dependance of the magnetic properties of $SmCo_5$ (Philips Components RES190) on the magnitude of the aligning field. (Source: J. Ormerod)

Fig. 1.18 Isostatically pressed sample of sintered NdFeB (Philips Components RES300).

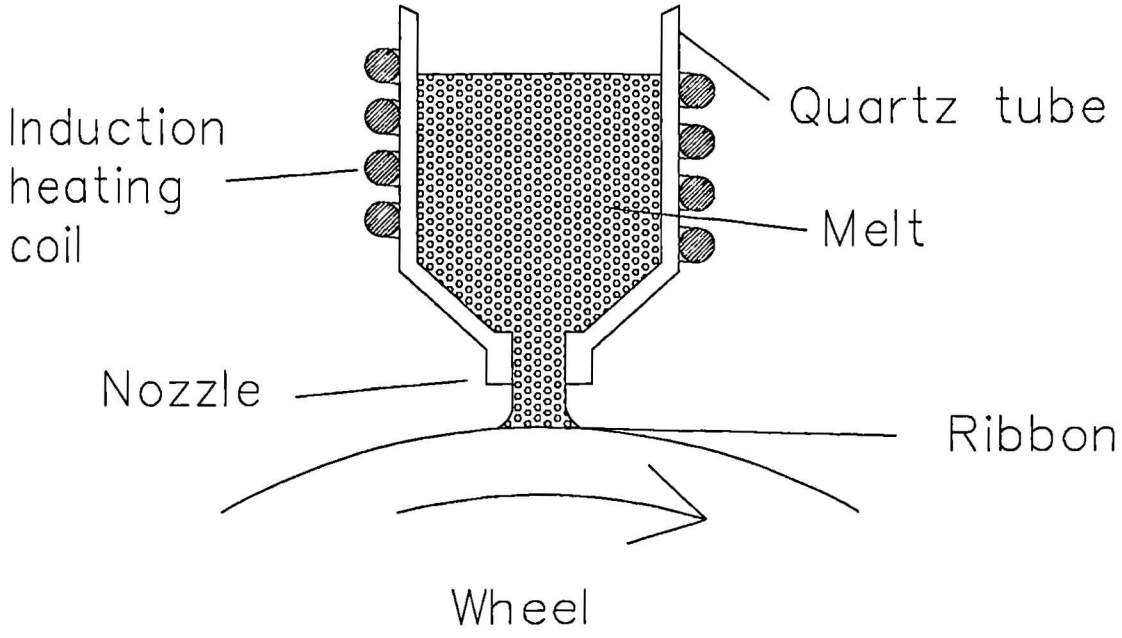

Fig. 1.19 Schematic representation of the rapid solidification process for the manufacture of isotropic NdFeB powder.

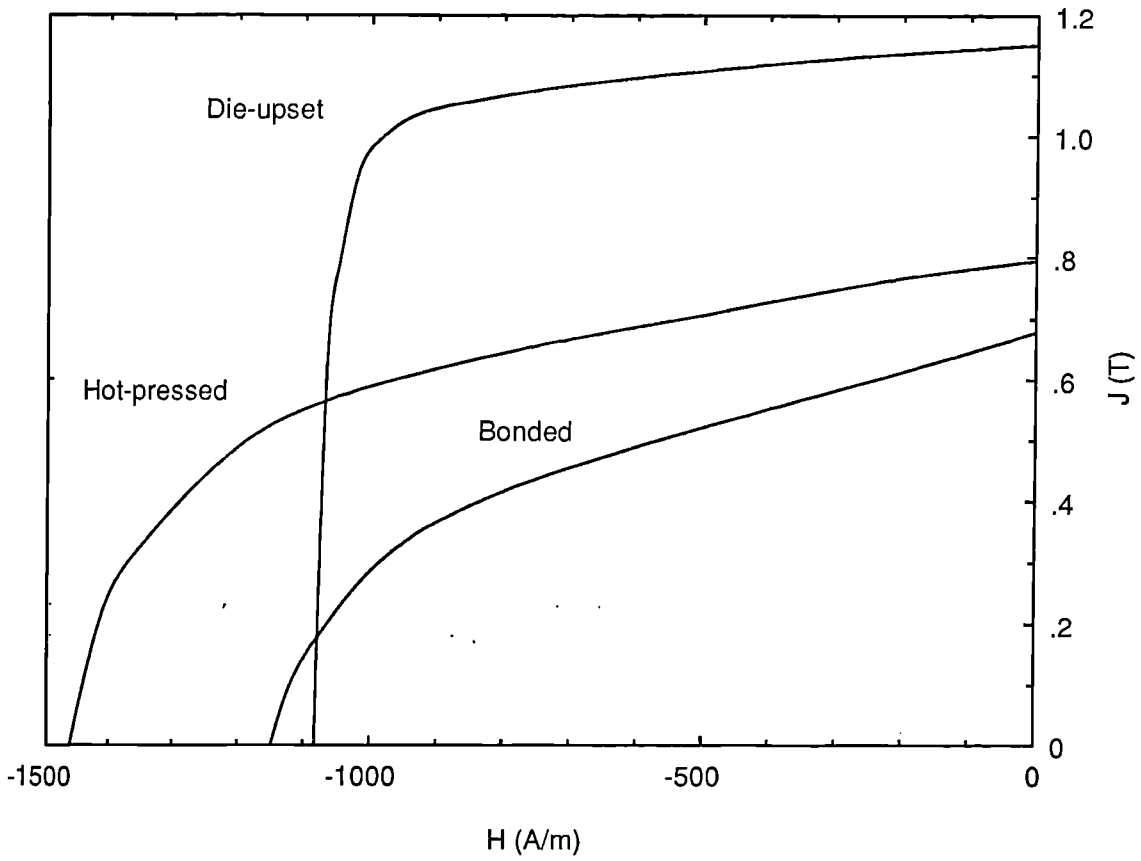

Fig 1.20 Room temperature demagnetization curves of bonded, hot pressed and die upset NdFeB magnets prepared from melt spun ribbons.

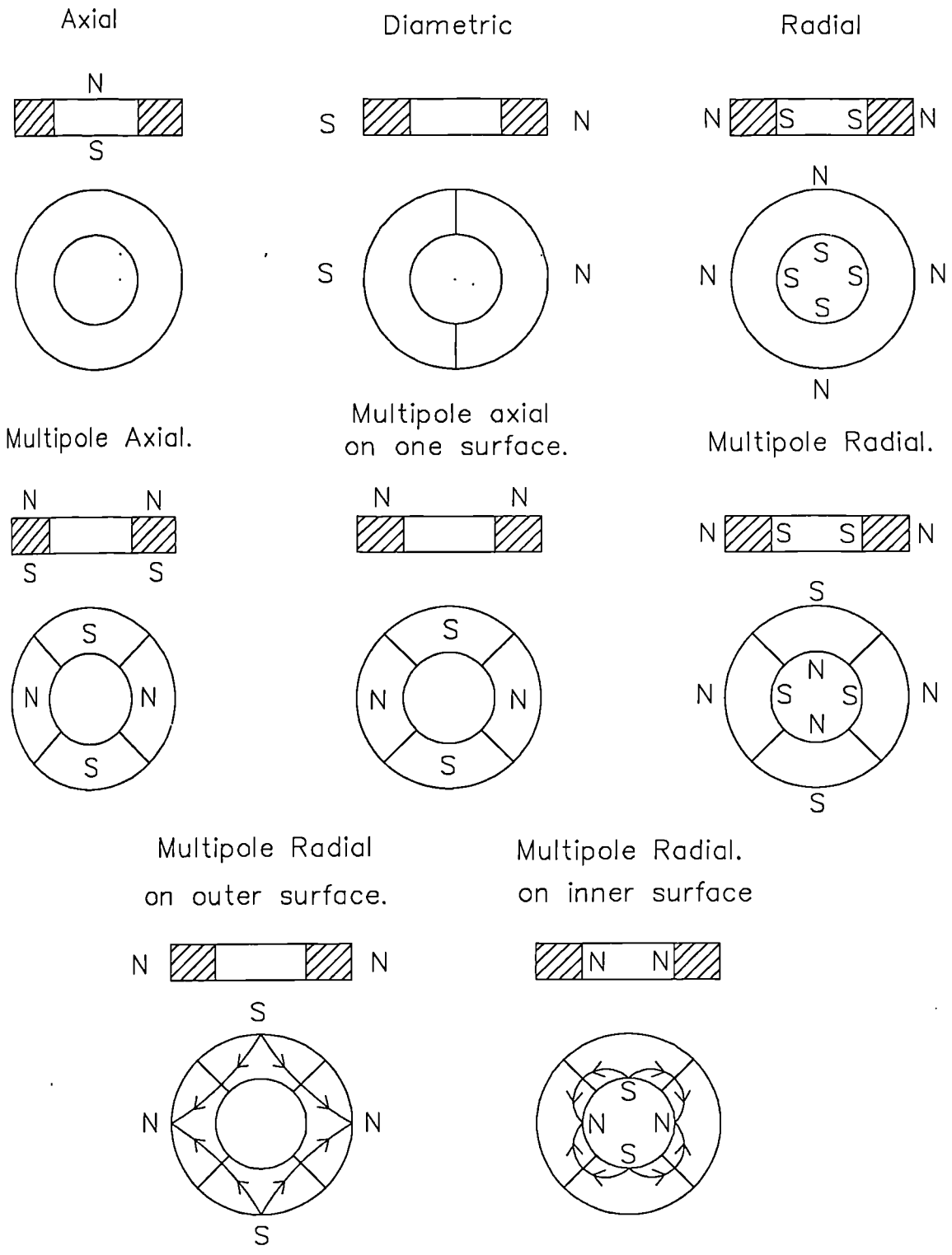

Fig. 1.21 Alternative magnetization patterns.

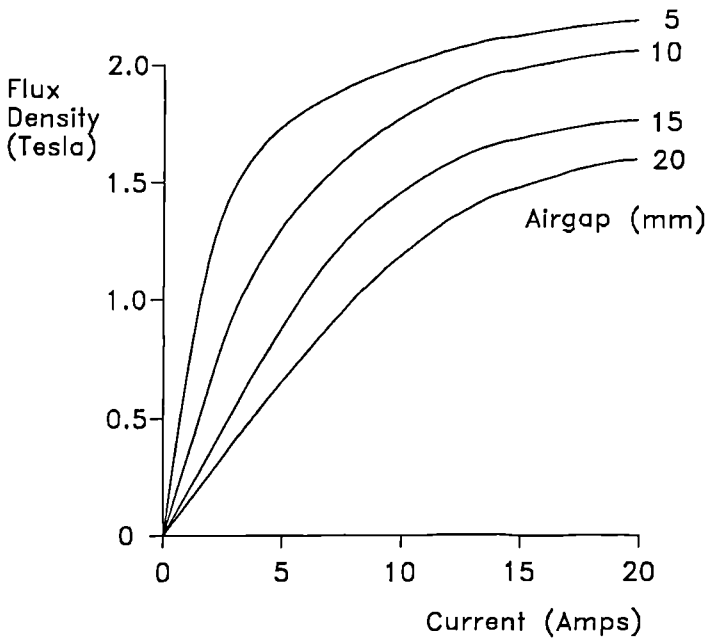

Fig. 1.22 Variation of the airgap flux density with current and pole spacing for a Lewis DMR LMV100 d.c electromagnet.

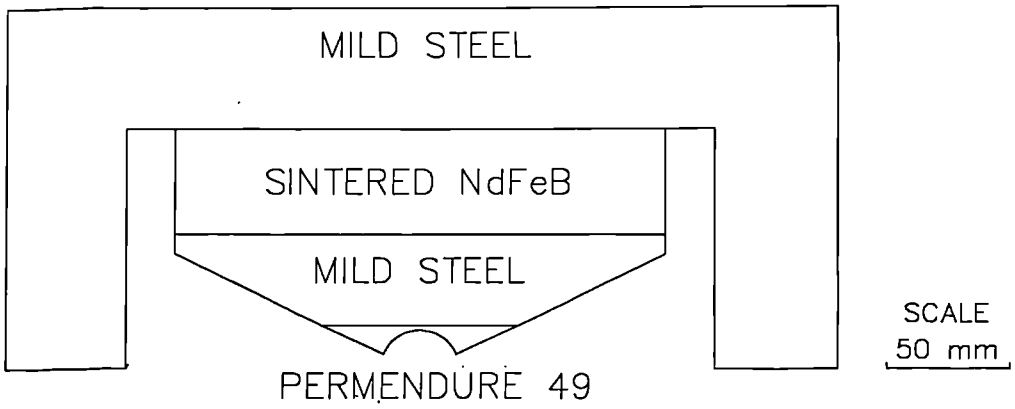

Axial length = 30mm

Fig. 1.23 Two-pole permanent magnet magnetizer for the in-situ magnetization of a fully assembled brushed d.c motor equipped with a bonded ferrite magnet.

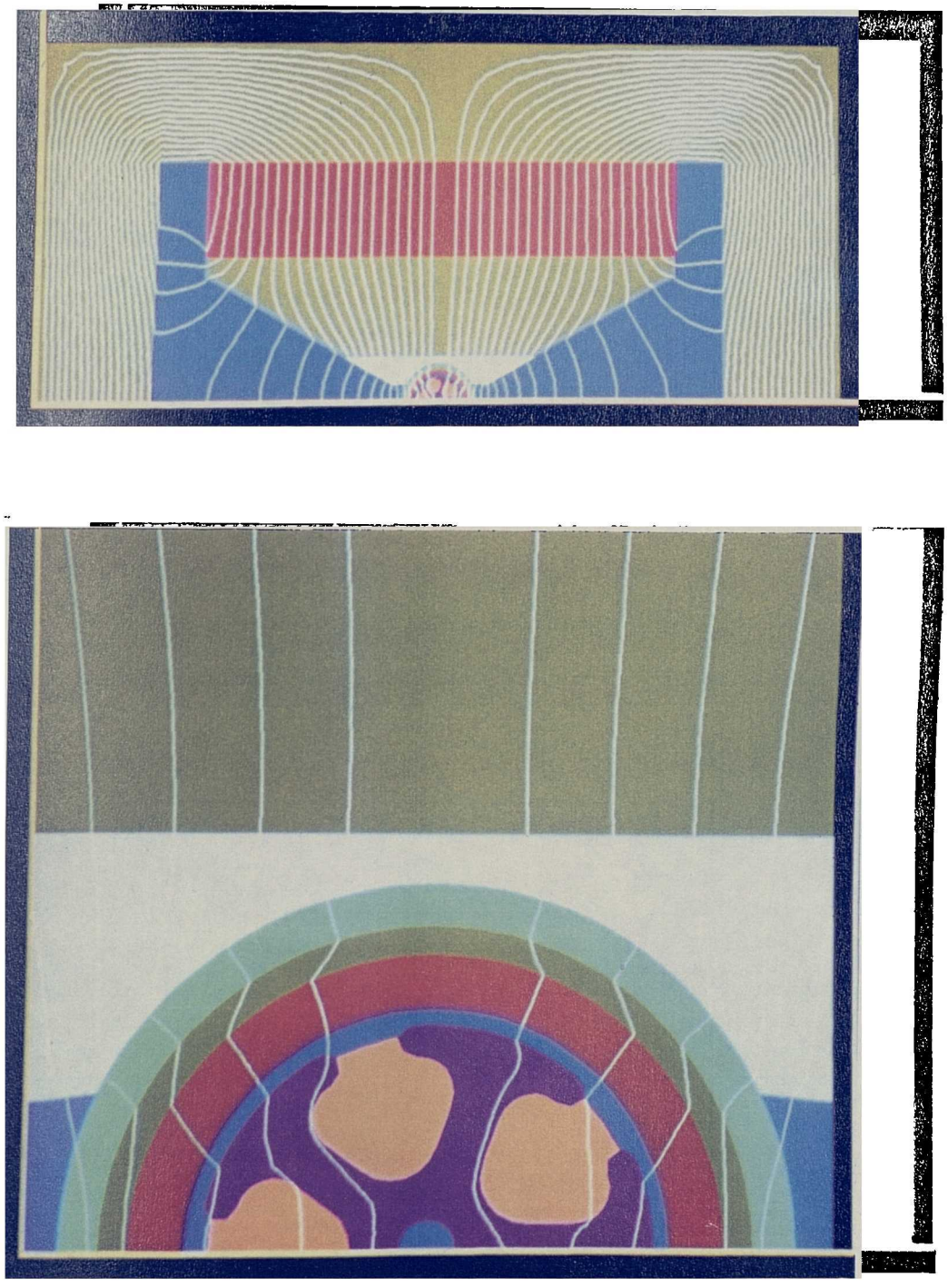

Fig. 1.24 Predicted field distributions for the permanent magnet magnetizer of fig 1.23.

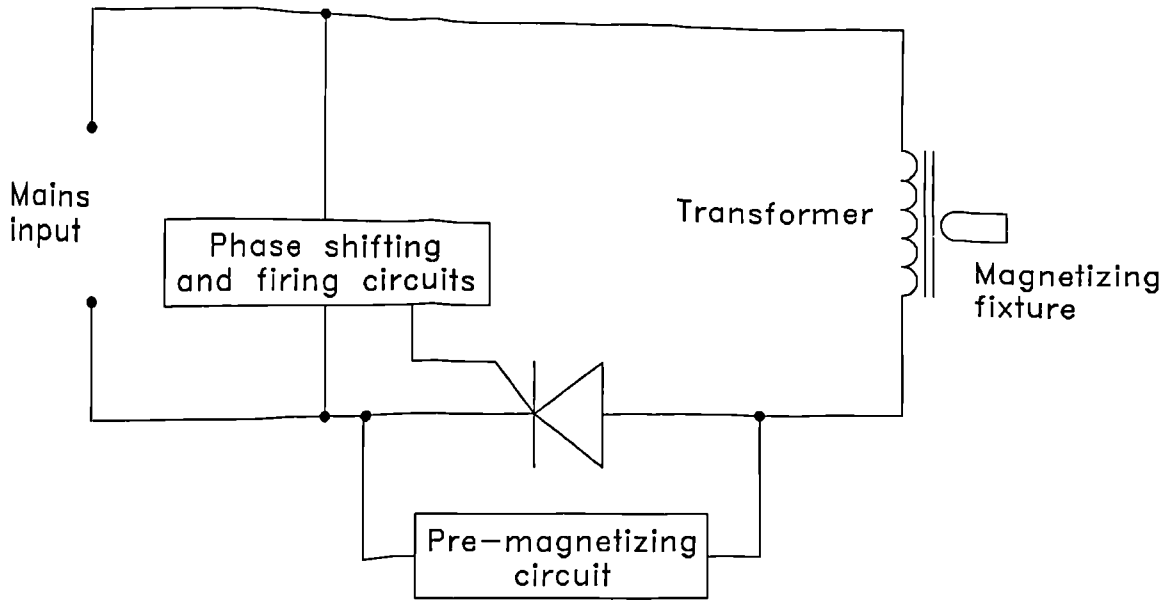

Fig. 1.25 Schematic of a typical half-cycle magnetizer.

Conductor diameter (mm)	Peak current for a 200°C temperature rise (A).
0.5	470
1.0	1880
1.5	4230
2.0	7520

Fig. 1.26 Calculated peak currents for a 200°C temperature rise for a range of conductor diameters used with a 50Hz half-cycle magnetizer

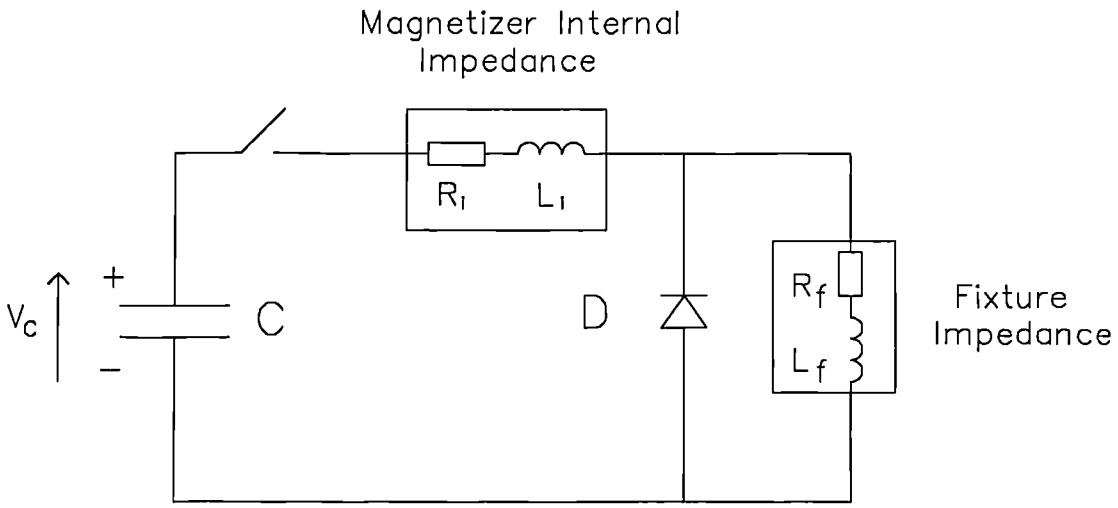

Diode Voltage	R	L
> 0	$R_i + R_f$	$L_i + L_f$
< 0	R_f	L_f

Initial conditions:

$Vc = Vo$

$i = 0$

$$\frac{di}{dt} = \frac{V_o}{L}$$

Fig. 1.27 Linear equivalent electrical circuit for a capacitor discharge magnetizer and fixture.

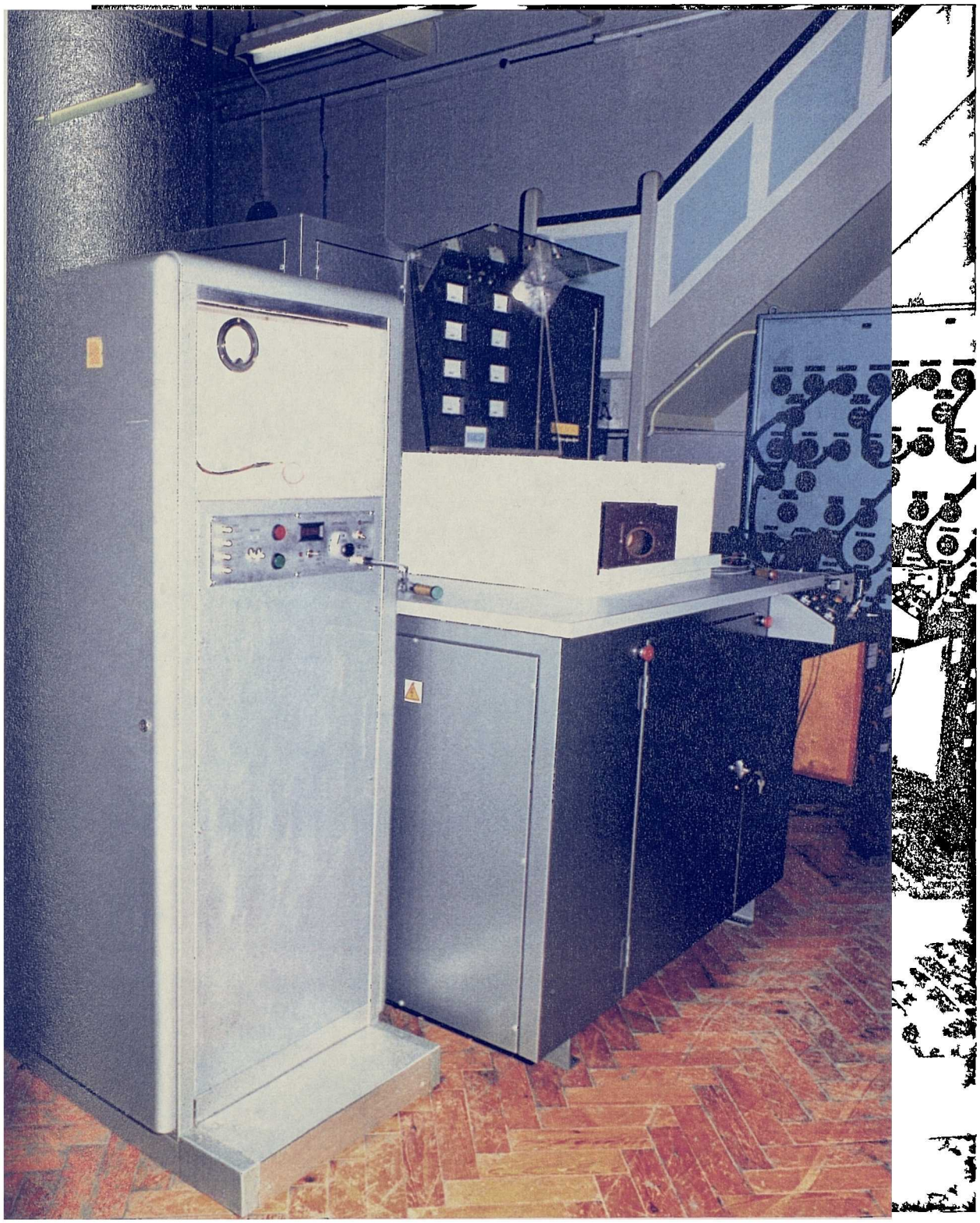

Fig.1.28 Experimental magnetizers used in the case studies of chapters 4,5 and 6.

Left: High voltage, low capacitance 6.6 kJ capacitor discharge magnetizer.
(0 - 530 μF , 0-5000 V)
Right: Low voltage, high capacitance 14.2 kJ capacitor discharge magnetizer.
(0 -42500 μF, 0-800V) .

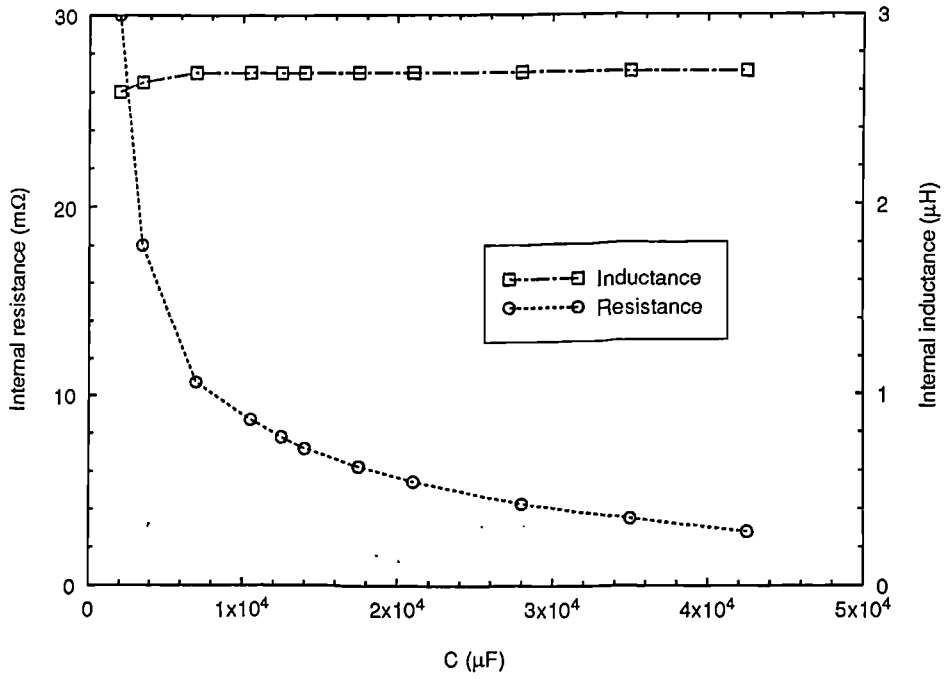

Fig. 1.29 Measured variation of internal impedance with connected capacitance for the low voltage magnetizer (Measured under short-circuit conditions with an initial capacitor voltage of 250V).

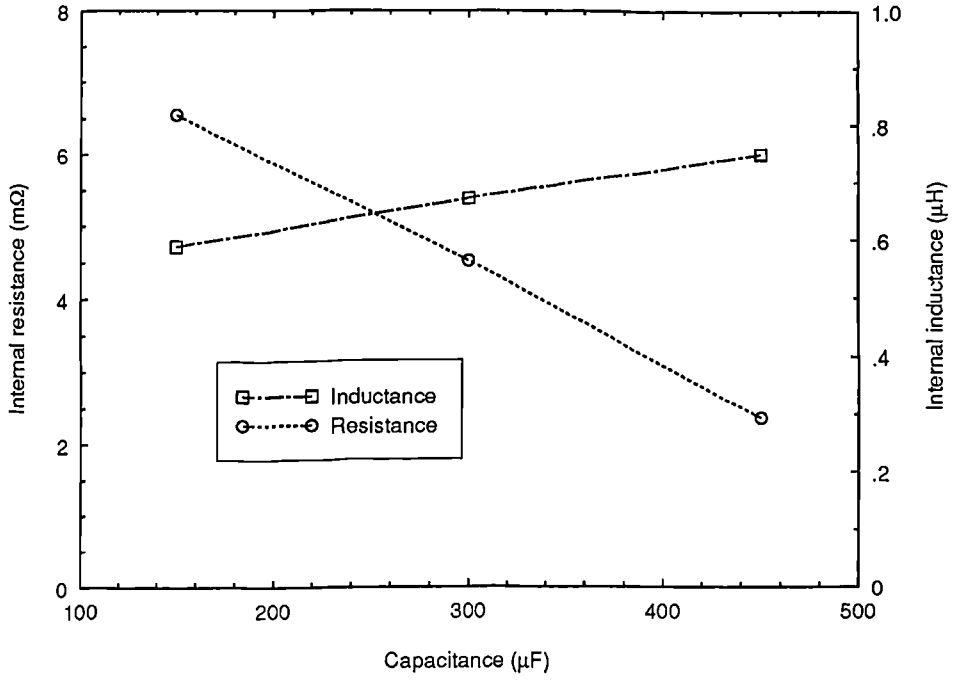

Fig. 1.30 Measured variation of internal impedance with connected capacitance for the high voltage magnetizer (Measured under short-circuit conditions with an initial capacitor voltage of 750V).

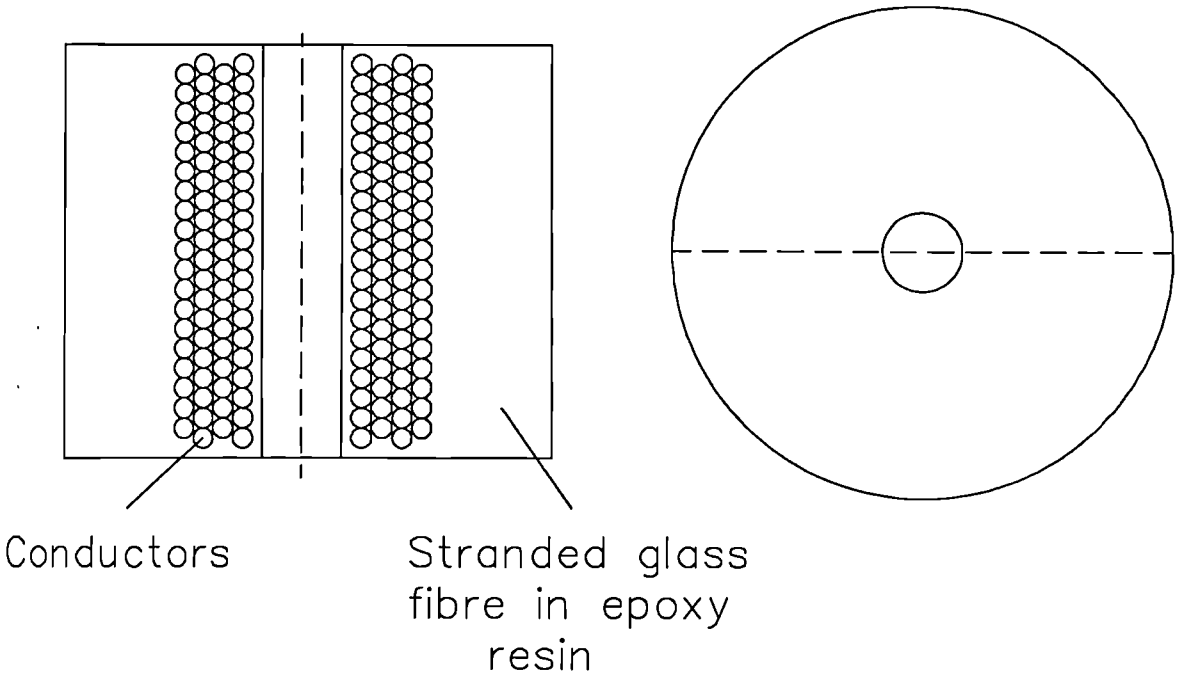

Fig. 1.31 Typical dipole solenoid.

'Serpentine' radial field.

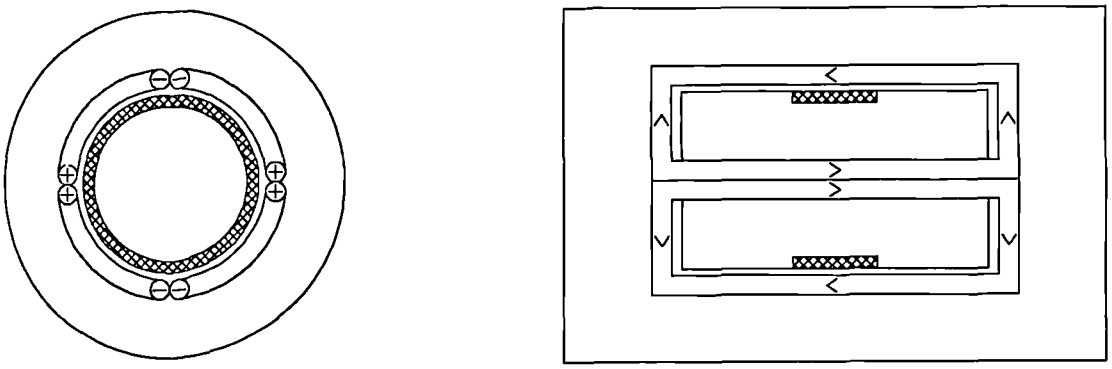

Double sided circular axial field.

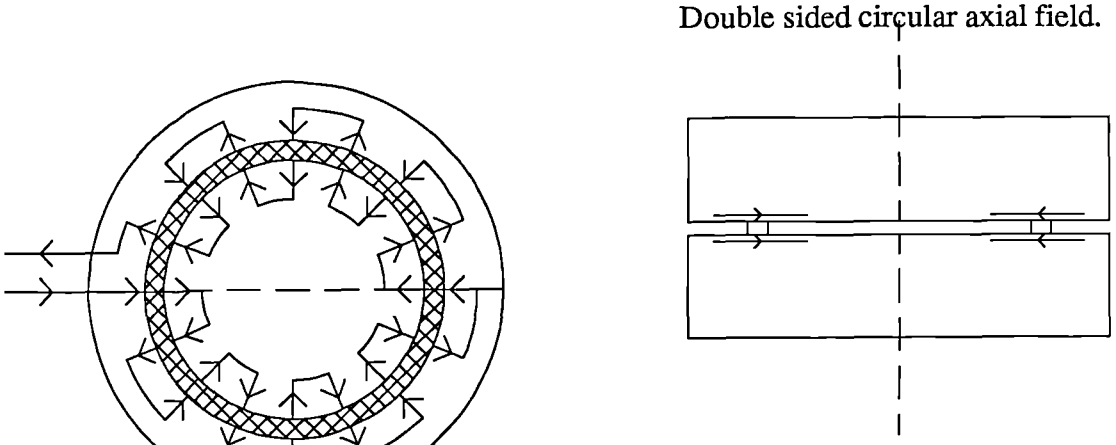

Double-sided planar axial field.

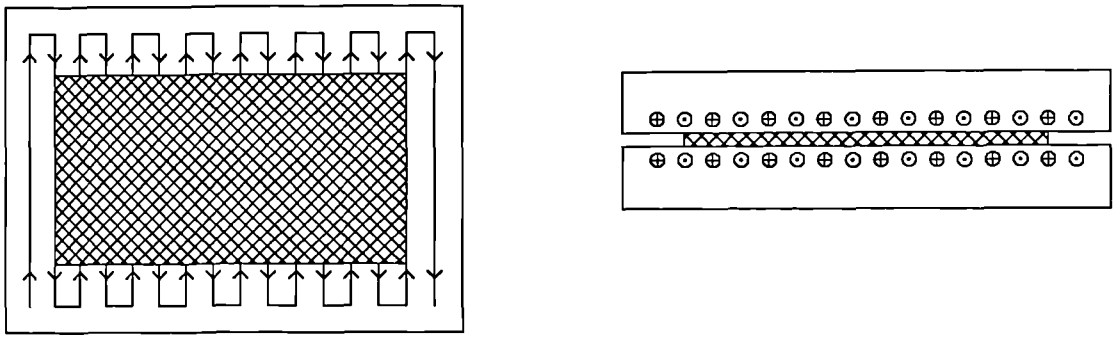

Fig. 1.32 Schematics of circular radial-field, circular axial-field and planar axial field multipole air-cored magnetizing fixtures.(Bulk material retaining the windings is non-conducting and non-magnetic e.g glass fibre loaded epoxy resin).

CHAPTER 2

DESIGN METHODOLOGY

2.1 INTRODUCTION

The large electromagnetic forces which result from the high currents and fields required in pulsed magnetization dictate that a fixture must be constructed as a structurally integrated device before any experimental performance assessment can be undertaken. Since this involves resin encapsulation of the fixture conductors, there is little scope for modification of the fixture once it has been constructed. Accurate design and analysis is, therefore, critical so as to avoid an expensive and time-consuming trial and error approach to design, or a compromise in the performance of the magnetized magnet. The design methodology described in this chapter spans the entire design process from problem specification to the detailed analysis of the performance of the device into which the magnet is subsequently incorporated. Although it is heavily based on finite element techniques, wherever possible attention has been directed towards minimising the computation time so as to improve its viability as a routine design tool.

2.2 EXISTING TECHNIQUES

A number of authors have proposed methods for the design and analysis of capacitor-discharge magnetizing fixtures. For example, a methodology for designing multipole magnetization fixtures has been proposed by Lee and Furlani [2.1][2.2]. For a specified winding arrangement the average flux density in the region to be occupied by the magnet per amp of fixture current is determined from a linear two-dimensional magnetostatic finite element calculation, which is also used to estimate the fixture inductance. For a specified magnet saturating flux density, the peak current required to ensure saturation can then be readily calculated. Given the capacitance of the magnet-

izer and the estimated fixture inductance, the governing electrical circuit equation for the magnetizer/fixture circuit is solved, with due account of the variation in fixture resistance due to heating, for various magnetizer voltages and conductor diameters until the required peak current is achieved. A similar magnetostatic finite element method for calculating the peak current necessary to achieve saturation has been proposed by Astapov and Ovchinnikov [2.3]. In this case, however, the methodology was not extended to include the design of the electrical circuit. Instead the calculated peak current requirement for saturation was used to set the magnetizer parameters for use with an existing single-turn fixture.

However, both the above methods are severely restricted in that the calculation of the current required to achieve saturation is based on a fixed pre-defined winding arrangement, in terms of both the disposition and the number of turns. The tendency in these studies has been to direct the design towards fixtures having low numbers of turns, often as low as a single turn. However, the results presented in this thesis will illustrate that with the exception of a few special cases, single-turn fixtures are often far from optimal in terms of achieving the maximum saturation for a given fixture dissipation. Constraining the design space to such a limited pre-conceived region inevitably reduces the chances of determining optimal fixture parameters. Further, neither of the methods has taken account of induced eddy-currents. However, the results of chapters 5 and 6 will demonstrate that the role of eddy-currents in the enviroments studied by these authors are minimal.

In large permanent magnet machines(>100W), it is common to construct the rotor from a number of discrete magnet blocks or segments. Chang et al [2.4] proposed a system for the in-situ magnetization of such a rotor, albeit by magnetizing one magnet block at a time using an air-cored two-pole solenoid fixture. A series of magnetostatic field calculations were performed to predict the effect of the solenoid winding dimen-

sions on the field distribution. For a fixed magnetizer stored energy, the inductance, resistance and field distribution for a range of solenoid parameters were calculated in order to aid the selection of a preferred design. Again, the static field calculation technique employed inherently neglects the effect of eddy-currents induced in the magnet. However, their existence was recognised by stipulating an essentially arbitrary minimum pulse duration of 20ms. The results presented in this thesis will demonstrate that this overestimates the required pulse duration for this problem by some one to two orders of magnitude. Such an overspecification is extremely uneconomical in terms of the required magnetizer energy, and highlights the need to establish general guidelines as to the likely effect of eddy-currents and to include eddy-current modelling within the design synthesis procedure.

The most detailed study of the magnetization process using the finite element method has been undertaken by Nakata et al [2.5] who proposed a transient non-linear finite element technique for analysing the dynamic field in the fixture with due account of eddy current and material non-linearities. Although sophisticated and computationally intensive, a number of simplifying approximations were made e.g the temperature rise of the fixture windings was neglected, which can cause a significant error in the analysis of optimal multipole fixtures designs. The results presented in this thesis will demonstrate that it is often necessary to have a large temperature rise in order to gain the maximum level of magnet saturation from a given magnetizer stored energy. Nakata applied this method to the analysis of a single fixture but no methodology for the selection of its design parameters was presented.

In conclusion, a number of authors have proposed alternative methods for the design and analysis of capacitor-discharge magnetizing fixtures. However, a number of approximations are implicit in these methods, and enforced constraints severely limit the scope for reliably establishing the optimal fixture and magnetizer parameters. An

integrated computer aided design methodology with specific tools for comparing candidate designs has not been previously realised. In addition, no previous work has been reported on the effects of a partially saturated magnet on the subsequent performance of a complete device. This an important consideration since, as the case studies of chapters 4,5 and 6 will illustrate, ideal multipole magnetization is very rarely achieved.

2.3 OUTLINE OF DESIGN METHODOLOGY

In the design of magnetizing fixtures the performance specification is often stipulated largely in terms of constraints rather than absolute performance e.g maximum temperature rise, maximum peak current etc. This constraint oriented design, when combined with the large number of design parameters which can be varied in magnetizing fixtures, often results in numerous alternative designs which meet the performance specification, although in general there will be an optimal design in terms of some specified criteria. There are 3 broad categories of computer aided design tools available for implementing a design strategy which is based on selecting the optimal design by assessing the merits of a wide range of alternative designs:

1) Analysis tools which are usually, but not exclusively, based on analytical methods in which the response of the system is calculated for a wide range of pre-specified system parameters. This scanning based design approach is usually implemented by incrementing the leading system parameters in uniform increments between pre-set user specified limits. The large number of designs which have to be analysed in such an approach necessitate that the analysis techniques should be computationally efficient, a requirement which is usually achieved by introducing a number of simplifying approximations.

2) Detailed analysis tools which calculate the detailed response of a given system, and include a number of effects which are neglected in the scanning based design approach. The subsequent modification of the system parameters is usually undertaken interactively in the light of the analysis results achieved. The more complex, and hence computationally more demanding analysis techniques which are employed, together with the increased user interaction dictate that this approach is limited to a small number of designs in the vicinity of the likely optimum. Commercial finite element packages are typical of the design tools which would be used.

3) Automated design tools which vary the parameters of the system in response to the calculated performance of a previous best estimate to the optimal design e.g formal optimization techniques [2.6], expert systems [2.7], and inverse field techniques [2.8]. Although the use of such methods for designing electromagnetic devices is an attractive proposition, particularly in terms of minimising the user interaction, they were regarded as being outside the scope of this project.

The computer aided design methodology which has been developed is, therefore, based purely on analysis tools of types 1 and 2 above. Since the duration of the design synthesis stage is an important consideration in the viability of computer aided design, the philosophy has been one of using analysis tools of increasing complexity whilst simultaneously reducing the feasible design space. Thus the more complex and time-consuming analyses are applied only to those fixture designs which are likely to provide the most promising performance, the majority of the combinations of possible system design parameters having been discarded on the basis of simpler analyses. The selection of candidate designs for detailed analysis is a manual procedure in which a number of practical considerations are taken into account. However, post-processing has been added to the early design phases to automatically exclude designs which do not meet

user specified minimum performance criteria, thus greatly reducing the information which must be assessed by the designer.

One important consideration in adopting such a strategy is that during the initial stages of design, which are necessarily based on simplifications, the analysis is sufficently accurate over a wide range of parameters that feasible designs are not inadvertently discarded. This is particularly important in the design of capacitor discharge systems since there are larger variations in field levels, topologies, materials and time constants than in more constrained electromagnetic device design e.g permanent magnet motors. One method of ensuring a reasonable degree of accuracy in the initial stages of design is to adopt some form of feedback in the design strategy, such that the validity of the initial approximations are checked by performing a detailed analysis at a relatively early stage. If necessary the criteria used in the simple analysis for discarding fixture designs can then be modified. A flowchart of the design methodology, which is described in the following sections, is shown in fig 2.1.

2.4 SPECIFICATION OF DESIGN CONSTRAINTS AND FIXED DIMENSIONS.

There are a number of practical considerations which impose constraints on the design space:

1) In order to prevent damage to the fixture insulating materials, there is a maximum tolerable temperature rise during the magnetizing pulse. This is typically of the order of 200^{o}C for enamel coated conductors and standard epoxy resins.

2) For a given conductor diameter there is minimum bending radius below which excessive mechanical stress of the insulation or distortion of the cross-section will occur. The pole pitch and shape of the magnet will, therefore, determine the maximum conductor diameter which can be formed into neat end-windings.

3) The protective layer that separates the fixture conductors from the magnet to be magnetized can be exposed to an onerous mechanical load in certain fixture topologies. However, from the point of view of the electromagnetic performance of the fixture, the thickness of this layer should be minimised. Some appreciation of the minimum tolerable mechanical dimensions are therefore required prior to the electromagnetic design. The method described in Appendix C for the calculation of the force on the fixture conductors can be used to estimate the minimum wall thickness required to prevent mechanical failure of the fixture. This theoretical value of minimum wall thickness must, however, be treated with extreme caution since the practical realisation of the modelled structure will inevitably have imperfections in both the construction and the materials. Therefore, the calculated minimum thickness requires modification by a somewhat arbitrary safety factor to ensure long-term reliability. Hence, the calculation of the minimum wall thickness is of limited utility, but is nevertheless useful in establishing feasible boundaries on the design.

4) If the fixture is for use with an existing capacitor-discharge magnetizer unit, there will be limits on the maximum voltage and capacitance which can be utilised. Indeed, severe constraints may be imposed by the fact that most commercial magnetizers do not have facilities for varying the capacitance. Even given the freedom to specify the magnetizer parameters, due account should be taken of the discrete minimum steps in capacitance which might be available in commercial magnetizers.

5) The ratings of the switching devices in typical magnetizers will limit the peak fixture current to 30kA or so.

2.5 TOPOLOGY SELECTION.

For the majority of applications, there are a number of possible fixture topologies which can be used to realise the desired magnetization, although considerations such as the incorporation of cooling ducts in the fixture or mechanical handling requirements may impose restrictions. The feasible design space can be significantly reduced, and hence the design synthesis duration shortened, if the topology selection is made as early as possible. Usually the choice is between single-sided topologies, in which the conductors are placed near one surface of the magnet and double-sided topologies, in which conductors are placed on either side of the magnet through which the required magnetization is to be oriented. In general double-sided fixtures are the preferred option when there is unimpeded access to both surfaces of the magnet, since they allow the application of approximately twice the magnetizing mmf at the same effective distance from the magnet for the same thermal performance.

2.6 SELECTION OF THE STATIC FIELD CALCULATION TECHNIQUE.

In order to relate the peak current of a magnetizing fixture to a level of saturation achieved in the magnet, a method is required for calculating the local magnetizing field. The most straightforward method for analysing magnetic circuits is the formulation of a set of algebraic equations, an approach which is readily applicable to devices in which the flux paths are well defined e.g d.c electromagnets, permanent magnet motors etc. The parameters obtained from such equations are generally global averages, e.g total flux across an machine airgap, and effects such as saturation and leakage are either neglected or accounted for by use of correction factors [2.9]. In capacitor-discharge multipole magnetizing fixtures, it is common to have either air or very heavily saturated iron forming a large fraction of the magnetic circuit, thus leading to an essentially open-boundary problem. The estimation of the field and even global parameters is then

very difficult using either simple algebraic equations or lumped reluctance methods because of the difficulty in calculating the circuit permeances. In such problems, global parameters such as the total flux produced by the fixture can only be estimated satisfactorily from a detailed field solution, which in any case is required to assess the percentage volume of the magnet which is magnetized to saturation. Thus the estimation of the local magnetizing field produced by a given fixture fixture mmf is based on a series of field calculations at discrete points in space.

At this early stage of the design synthesis the estimation of the mmf required to achieve a given level of saturation in the magnet is based on static field calculations with no account being taken of eddy-current effects. There are essentially two methods for obtaining static field solutions, viz analytical techniques e.g Biot-Savart law, and numerical techniques e.g finite element analysis. One limitation of analytical field calculation techniques is the constraint of linear isotropic material characteristics. Hence they are of limited utility in environments where non-linearity, due to either the permanent magnet or iron components, is a significant factor. Despite this limitation, they offer a number of advantages compared to a numerical method such as finite elements which make them the preferred option when they can be applied with acceptable accuracy:

i) Within the inherent limitations of the model utilised, the analytically calculated values of magnetizing field are exact and are not influenced by spatial discretization errors as in finite element formulations.

ii) The computation time is much shorter than for finite element analysis, since the calculation of the magnetic field at any point is decoupled and non-iterative.

iii) There is no requirement for extensive user generated geometric data as required for a finite element mesh. The position of each conductor of a fixture and the polarity of

its current, which is the only information required for an analytical calculation, can be readily calculated from a few parameters, viz. magnet dimensions, number of poles, conductor diameter, and the number of conductors per pole.

As a result of these advantages, a large number of possible fixture designs can be assessed in a small fraction of the time required to construct and solve the corresponding designs by finite element analysis. A test problem, which is solved by both the analytical and finite element methods, can be used assess the applicability of the analytical method to a given problem. This test problem would be framed to be a worst case in terms of non-linearities. e.g the use of a compact winding arrangment located in close proximity to any non-linear materials, when the non-linear material constitutes a high proportion of the flux path.

An informative and concise representation of the vast quantity of data generated in calculating the field distribution at numerous points for a range of fixture currents is to calculate a percentage saturation versus mmf characteristic for a given winding layout. This is calculated by specifying a level of magnetizing field strength which is regarded as being the threshold of saturation for the particular permanent magnet material. For each value of magnetizing current, the percentage volume of the magnet which is exposed to a field is greater than this specified level is determined from the field calculated at an array of points distributed over the magnet cross-section. In the case of the analytical calculation the saturation is assessed at a regular grid of points whereas for the finite element analysis it is assessed at the centroid of each triangular element. A comparison between the percentage saturation versus mmf characteristic predicted by both methods allows the accuracy of the analytical method for the particular problem to be determined. Although this does not compare the local magnetizing field on a point by point basis, and hence explicitly confirm agreement between the two calculation methods, it nevertheless demonstrates the degree of agreement in

the most useful figure of merit for assesssing alternative fixture designs.

2.7 ANALYTICAL CALCULATION OF THE MAGNETIZING FIELD STRENGTH IN A PERMANENT MAGNET.

The analytical method is based on the assumption that if the dominant reluctance in the magnetic path of the flux produced by a given winding arrangement consists of air, then the presence of the magnet will have a minimal effect on the total flux produced by the winding. Thus the analytically predicted local flux density at any point within the region which is to be occupied by the magnet to be magnetized, will be a good approximation to that which will be produced with the magnet in place in terms of its magnitude, although in practice its direction may be influenced by a preferred orientation in the magnet. The magnitude and direction of the magnetizing field produced by a given multipole serpentine winding in air can be calculated analytically using the Biot-Savart law. However, the following approximations are employed to ease the calculation, their validity being demonstarted in the case studies to be described in chapters 4,5 and 6:

i) All materials in the region have isotropic linear B-H characteristics, and an identical permeability (usually μ_o).

ii) The fixture has infinite axial length, i.e the model is two-dimensional.

iii) The current flow in a conductor of finite cross-section is represented as an idealised line current positioned at the geometrical centre of the conductor.

A cross-section through a typical multipole serpentine winding is shown in fig 2.2. The flux density B_p at the point (x_p,y_p), produced by a circular conductor of diameter d_c, carrying a current I and located at the point (x_c,y_c) is given by equation (2.1), whilst the components of flux density in the radial and circumferential directions

are given by equations (2.2) and (2.3) respectively.

$$B_p = \frac{\mu_o I}{2 \Pi r} \tag{2.1}$$

where

$$r = \sqrt{(x_i - x_c)^2 + (y_i - y_c)^2}$$

$$B_{ri} = B_p \ (\cos\Theta \sin\alpha - \sin\Theta \cos\alpha) \tag{2.2}$$

$$B_{ci} = B_p \ (\cos\alpha \cos\Theta + \sin\Theta \sin\alpha) \tag{2.3}$$

By adopting a consistent convention, the net radial and circumferential components at the point (x_p,y_p) produced by a fixture with p poles and n conductors per pole are given by equations (2.4) and (2.5)

$$B_r = \sum_{i=1}^{i=np} B_{ri} \tag{2.4}$$

$$B_c = \sum_{i=1}^{i=np} B_{ci} \tag{2.5}$$

By varying the radius and angular displacement of the point P, a detailed profile of the applied magnetizing field within the magnet can be obtained, thus allowing investigation of the degree of saturation achieved and the quality of alignment of the magnetizing field with the desired direction of magnetization.

In situations where the absence of significant regions of non-linear materials result in the analytical method predicting the total field distribution to an acceptable accuracy, the non-linearity of the magnet characteristic must nevertheless be considered in calculating the level of saturation achieved in the magnet.

Permanent magnet materials have a first quadrant permeability which is greater than that of air e.g Philips Components RES270 sintered NdFeB has a maximum relative permeability of 19.35, although at the field strength required for saturation the relative permeability is approximately 1.5. Thus, calculation of the flux density at a given point within the magnet assuming it to have a permeability of μ_o does not give the magnetizing field strength which is locally applied to the actual magnet. However, the effect of the increased permeability on the local magnetizing field strength can be accounted for by an approximate correction method which utilises the non-linear material characteristic. The net magnetizing field strength in the magnet material, allowing for its actual permeability, can be calculated by reference to the non-linear initial magnetizing curve as shown in fig 2.3. Although this method of accounting for the non-linear characteristic in a linear field solution is not rigorous, the case studies of chapters 4,5 and 6 will demonstrate that excellent agreement with a full non-linear field solution can be achieved given suitable problem environments.

The calculation of the percentage volume saturation from the magnetizing field level at several hundreds of points within the magnet can be achieved in a very short time (<<1s), even for complex fixtures with numerous turns per pole. Thus this approach can be used in conjuction with an electrical circuit simulation to assess the field levels which are achievable with a wide range of fixture/magnetizer combinations. A similar method to that which has been described for the serpentine winding can be used for other fixture topologies. A description of the calculation for a planar fixture, such as that used for for the magnetization of an axial disk magnet, is given in Appendix A.

2.8 FINITE ELEMENT ANALYSIS

The magnetostatic finite element method is readily applied in environments having a complex geometry and/or non-linear materials. Thus the numerous simplifications which had to be made in the analytical method, which in turn made its applicability problem dependant, are not necessary with the finite element method. Hence, it is much more general, but requires a large increase in computation time.

In the finite element method the problem region is discretized into a large number of discrete elements in each of which simplifying approximations are made with regard to the local variation of the field. By coupling together these elements with suitable interface and boundary conditions a piecewise solution for the field over the problem region is obtained. The finite element formulation adopted in the design methodology is two-dimensional, since although the finite element method can be readily extended to three-dimensions, this is achieved at the expense of a greatly increased user input and computation time. In a two-dimensional planar model the field distribution under static conditions is governed by equation (2.6), which is derived from Maxwells equations of electromagnetics[2.10]. In order to solve equation (2.6) variational theory is utilised to formulate the functional of equation (2.7), the minimisation of which yields the solution of the governing field equation [2.11]. A detailed description of the finite element formulation, which was also used as the basis of the dynamic simulation and the magnet performance assessment stages to be described later, is given in Appendix B.

$$\frac{\partial}{\partial x}\left(\nu_y \frac{\partial A_z}{\partial x}\right) + \frac{\partial}{\partial y}\left(\nu_x \frac{\partial A_z}{\partial y}\right) = -J_o \qquad (2.6)$$

$$F = \int_{\Omega} \nu_y \left(\frac{\partial A_z}{\partial x}\right)^2 + \nu_x \left(\frac{\partial A_z}{\partial y}\right)^2 - 2 J_o A_z \; d\Omega \qquad (2.7)$$

In the analytical method, the static magnetizing field is calculated for each combination of fixture and magnetizer assessed in the electrical design stage. However, due to the greatly increased computation time and the requirement for a specific finite element mesh to model each fixture, this approach is not feasible with the finite element method. The problem of mesh generation could be alleviated to some degree by the development of an application specific mesh generator in which the mesh is generated automatically from a few input dimensions [2.12]. However, even if such a method was employed, the usefulness of such a detailed analysis technique at this early stage of the design procedure is limited, since numerous simplifying approximations are made with regard to the effect of eddy-currents on the penetration of the magnetizing field and the non-linear inductance of the fixture.

A less computationally demanding alternative to modelling each specific conductor arrangement is to represent an array of individual conductors as an equivalent idealised rectangular conductor. By varying the dimensions of this idealised conductor in discrete steps and solving for the field, a three-dimensional surface can be generated which relates the percentage of the magnet volume which is magnetized to saturation to the dimensions and total mmf of the conductor. The level of magnet saturation produced by any given fixture at a specified current can then be calculated by interpolation between discrete points on this surface.

2.9 ELECTRICAL DESIGN.

The objective of the electrical design phase is to determine the parameters of the fixture and magnetizer which produce the highest levels of saturation for a given stored energy, subject to a number of practical constraints. The utility of a given fixture can be decomposed into two separate and often conflicting efficiencies, viz. the electrical efficiency in converting the stored energy of the capacitor bank into fixture mmf, and

the efficiency of this mmf in saturating the magnet. The electrical efficiency improves as the winding volume is increased, whilst the mmf is most effective as the winding volume is reduced. Hence, for fine-pole pitch fixtures in which the efficiency of conversion of mmf to magnet saturation degrades very rapidly with increasing fixture dimensions, the resulting optimal fixture may well be electrically very inefficient. The electrical design phase is based on a scanning method in which the performance of a large number of possible fixtures is assessed by incrementing the leading design parameters between limits. For each fixture the peak current is calculated by an electrical circuit simulation, and the corresponding level of magnet saturation by the method which has previously been found to be most appropriate for the fixture and magnet assembly. The analytical method calculates the field and hence the level of saturation which is achieved for each set of fixture parameters, whilst in the finite element approach the level of saturation is calculated by reference to the percentage volume saturation versus mmf characterisitc which has been deduced for the same overall winding dimensions.

In order to allow a wide range of design parameters to be investigated, the electrical simulation must be computationally very efficient. To this end, the inductance of the fixture is calculated by an analytical technique in which the presence of the magnet assembly is neglected, i.e the fixture is assumed to be air-cored, and is assumed to be constant during the pulse, whereas in practice it is affected by eddy-currents and the non-linearity of the magnet and any iron components in the assembly. These effects cannot be satisfactorily included without recourse to a far more complex and time consuming simulation, an option which is not feasible at this stage given the large number of possible magnetizer/fixture combinations which have to be assessed. The significance of these non-linear phenomena on fixture performance can however be subsequently quantified by the dynamic simulation phase which couples the non-linear transient field solution to the electrical circuit simulation.

The effect of temperature rise on the resistance of the fixture, which can be calculated without excessive computational overhead, is included in the electrical simulation, since the large current density which is required in pulsed magnetization can cause a significant temperature rise of the fixture conductors during the impulse period. The inclusion of this temperature effect requires that the governing electric circuit equations are solved numerically by a time-stepped method. Despite the need to resort to such a method the total simulation time is very short (i.e <<1s), and hence it is suitable for use in a scanning based design strategy. This phase of the design process has been implemented in a sufficiently flexible manner that differing strategies for exploring the design space can be employed. The case studies of chapters 4,5 and 6 illustrate a number of these, viz. designing to a maximum temperature rise, to a minimum pulse duration etc.

Even though a number of the fixture dimensions are fixed during the initial specification the resulting multi-dimensional design space still has six degrees of freedom, viz:

1) Magnetizer capacitance.

2) Magnetizer initial voltage.

3) Number of conductors per pole.

4) Disposition of the conductors at each pole.

5) Conductor cross-section.

6) Axial length of the fixture.

In practice, the variation of all these parameters with small scanning increments can rapidly lead to a combinatorial explosion, which is a phenomena often encountered in such a scanning based design approach. This results in extremely long computation times and generates more data than can be assessed by the designer. A more efficient strategy is to use coarse increments of the principal parameters initially and gradually adapt the scanning intervals as the relative importance of the parameters becomes clear.

Whilst the effect of the axial length of the fixture conductors on the electrical performance can be accurately assessed, the effect on the field distribution is more difficult to quantify. In an idealised fixture the end-windings are at right angles to the axial section, and hence they only produce axial and radial components of magnetizing field, which in the case of a double-serpentine wound fixture cancel at the axial mid-point along the axial length. This axial field produces negligible axial magnetization in a material with a strong anisotropy, implying that the axial length of the fixture can be set equal to that of the magnet with no detrimental effects on the multipole pattern produced. However, constructional limtations necessitate that the fixture is longer than the magnet to be magnetized. The conductor layout of a typical multipole fixture is shown in fig 2.4. Due to limitations in the minimum bending radius and the need to interleave the end-windings as they pass from one pole to the next, the end-windings are curved and produce components of magnetizing field in both the circumferential and radial directions, which in turn distort the net magnetizing field near the ends of the fixture.

To minimise such effects, it is necessary to extend the fixture length beyond the magnet such that the coupling of this distorting field with the magnet is reduced to a negligible level. The problem of end-winding coupling is compounded in the magnetization of isotropic materials since the axial field can produce a significant axial

component of magnetization thus reducing the net component in the radial direction. Since end-winding effects are related to the construction and the complexity of the winding, and do not scale with the dimensions of fixtures they are somewhat unpredictable, even if the analysis techniques were extended to three dimensions. Given this uncertainty in the effect of the end-winding coupling with the magnet, the aim of the design is to maximise the axial length subject to the constraint that is does not lead to an excessive compromise in the fixture performance. Therefore, the axial length of the fixture is a variable parameter within the design synthesis rather than a pre-specified dimension.

2.10 ELECTRICAL CIRCUIT SIMULATION

The equivalent circuit which is used in the electrical simulation is shown in fig 2.5. The fixture current for the two conduction states of the clamping device is governed by the linear circuit equations (2.8) and (2.9), subject to the initial conditions of equations (2.10) and (2.11).

$$(L_{int} + L_{fix})\frac{d^2 i}{dt} + (R_{int} + R_{fix})\frac{di}{dt} + \frac{i}{C} = 0 \qquad (2.8)$$

$$L_{fix}\frac{di}{dt} + i R_{fix} = 0 \qquad (2.9)$$

$$i = 0 \quad at \ t = 0 \qquad (2.10)$$

$$\frac{di}{dt} = \frac{V_o}{L_{int} + L_{fix}} \quad at \ t = 0 \qquad (2.11)$$

The solution of the governing circuit equations is realised by a 4th order Runga-Kutta integration technique. The capacitance of the magnetizer is assumed to remain constant during the pulse and to be independant of the initial capacitor voltage, whilst the magnetizer internal impedance is modelled as a time and current invariant series resistance and inductance which are determined experimentally under a short-circuit condition.

The series switch of the magnetizer can be either a thyristor or an ignitron. A conducting thyristor has an approximately constant voltage drop, typically of the order of 1V, and can be neglected altogether in most cases. A conducting ignitron has an approximately constant 20V drop across the arc and an additional small inductive and resistive impedance. Therefore it can be modelled as a negative offset on the intial capacitor voltage with its impedance lumped in with the other components of the magnetizer impedance. The ignitron can also exhibit certain non-linearties with current level and rise time,temperature etc. However these effects have not been included due to the difficulty in obtaining reliable and consistent parameters and their likely minimal role in determining the peak current. The turn-on process of the switch is assumed to be instantaneous, a valid assumption for most simulations since the turn-on time for both thyristors and ignitrons is generally less than 1μs.

2.11 CALCULATION OF THE INDUCTANCE OF A MULTIPOLAR MAGNETIZING FIXTURE.

An analytical technique has been developed for the calculation of the inductance of an air-cored serpentine winding. A similar calculation for an axial-field topology of fixture, which is significantly simpler due to the increased degree of symmetry in such fixtures, is discussed in Appendix A. The inductance calculation is simplified if the end-windings are assumed to be at right angles to the axial conductors, i.e the pre-

viously discussed curvature effects in the end-windings are neglected. This allows the calculation to be divided into two decoupled 2-dimensional calculations.

Axial section.

A cross section through the axial region of a typical fixture, including the principal geometric parameters is shown in fig. 2.6. The x and y coordinates (x_i,y_i) of a conductor i, referenced to the axes shown, and its polarity u_i can be readily calculated. In the calculation of the x,y coordinates of the individual conductors, an insulation factor k_i, which is defined in fig 2.6, is included to allow for the conductor insulation.

The total inductance of this region is calculated by summing the self inductances of each conductor(which is the same for all conductors), and all the components of mutual inductance between the individual conductors, with due account of the current polarities.

$$L_{ax} = p\,(L_S\, m\, n + \sum_{i=1}^{i=mn} \sum_{j=1}^{j=pmn} (1-\delta_{ij})\, M_{ij}\, U_{ij}\,) \qquad (2.12)$$

where

$\delta_{ij} = 1$ if i=j or $\delta_{ij} = 0$ if $i \neq j$

U_{ij} =1 if conductors i and j carry currents of the same polarity.

or

U_{ij} =-1 if conductors i and j carry currents of opposite polarity.

The components of self and mutual inductance are evaluated by standard formulae for finite length conductors, equations (2.13) and (2.14). Since they are derived from three-dimensional field calculations they inherently include the end-effects associated with finite length conductors [2.13].

$$L_s = 2x10^{-7}\ l_{ax}\left(\log_e\left(\frac{2\,l_{ax}}{d_c}\right) - \frac{3}{4}\right) \tag{2.13}$$

$$M_{ij} = 2x10^{-7}\ l_{ax}\left(\log_e\left(\frac{l_{ax}}{S_{ij}}\right) + \sqrt{1+\frac{l_{ax}^2}{S_{ij}^2}} - \sqrt{1+\frac{S_{ij}^2}{l_{ax}^2}} + \frac{S_{ij}}{l_{ax}}\right) \tag{2.14}$$

where

$$S_{ij} = \sqrt{(x_i - x_j)^2 + (y_i - y_j)^2}$$

End-winding region.

A schematic of one end of a double wound 4-pole serpentine fixture, together with the directions of current flow in each conductor bundle, is shown in fig. 2.7. The calculation of the end-winding inductance is simplified if the curvature of the end-windings is neglected and the simplified end-winding representation considered. For a fixture with any number of poles, a given conductor bundle only has a net mutual inductance with the bundle directly facing it, since the contributions from the other symmetrically arranged bundles cancel each other. Thus, the model for calculating the inductance per pole pair of the end-windings, neglecting curvature, reduces to that of fig 2.8 for any pole number. The inductance of this simplified representation is calculated in the same way as the inductance of the axial section of the fixture. The total fixture inductance is then given by:

$$L_{fix} = L_{ew} + L_{ax} \tag{2.15}$$

For the purpose of comparing results from the finite length analytical model with the two-dimensional finite element model, the inductance of the fixture of fig 2.9 was calculated by both techniques. The fixture has 20 turns per pole of 3.35 mm diameter

wire (arranged as a bundle 5 turns wide and 4 turns deep) and a bore diameter of 50mm. For the purpose of the finite element and analytical models the insulation factor was set at 1.1, which is representative of that achieved in the constructed fixture. The total fixture inductance was measured at 1kHz using a Marconi TF1313 RLC bridge. Although there will a degree of skin effect in such large cross-section conductors at 1kHz, in a fixture with such a high number of turns per pole, the current distribution in each individual conductor will not significantly affect the overall field distribution and hence the inductance.

For the finite element calculation all the materials were assigned a permeability of μ_o, and the axial region inductance was found by scaling the inductance per metre calculated for the infinte model to the actual 72mm axial length. The analytical model is based on a finite length conductor. However for comparison with the finite element model the analytical inductance was also calculated by scaling the inductance per unit the length with the conductor length set to 72m, i.e essentially infinitely long with respect to the actual fixture length. The agreement between the calculated and measured values of total inductance is excellent, as shown in fig 2.10, although it is somewhat fortuitous given the simplified representation of the end-windings, which in reality were a complex interleaving of conductors. There is much better agreement between the measured inductance and that derived from the finite length analytical model than with results deduced from both the two dimensional analytical and finite element models. This highlights the fact that end effects are more significant in air-cored magnetic circuits than in devices such as motors, where the presence of iron in the active axial section tends to dominate the inductance.

2.12 CALCULATION OF RESISTANCE

The resistance of a serpentine winding at a 20°C is given by equation (2.16). No account is taken of the practical difficulties associated with forming the end-windings since any correction would be rather empirical and influenced by the constructional techniques employed. Forming neat end-windings is particularly difficult for windings with a high number of large cross-section conductors because of the complex interleaving of conductors and the large minimum bending radii, and in such cases the end-winding length may increase from that assumed with neatly formed end-windings. However, fixtures with a high number of large cross-section conductors are generally associated with very lightly damped circuits and hence any error in the resistance will have only a small influence on the peak current. In cases where the resistance has a significant bearing on the magnitude of the current, i.e a fixture winding with a low number of small cross-section conductors, the constructional problems are greatly reduced and the widings tend to follow the ideal geometry implicit in equation (2.16) more closely.

$$R_{fix} = \frac{(N\, l_{ax}\, p \;+\; N \Pi\, (\, d_b + \frac{w_d}{2}\,)\, \rho_{Cu}}{A_c} \qquad (2.16)$$

where

N = number of complete winding turns.

d_b = Bore diameter.

w_d = Size of the winding cross section in the radial direction.

A_c = Cross-sectional area of individual conductor

l_{ax} = Fixture axial length

p = Number of poles

ρ_{Cu}= Electrical resistivity of copper at 20°C.

The large current densities which are required in pulsed magnetization can cause significant temperature rises in the fixture conductors during the impulse period. However, the thermal time constant of a bundle of conductors encapsulated in an epoxy resin is typically several orders of magntiude greater than the current pulse duration. Heating of the fixture conductors can, therefore, be regarded as an adiabatic process, i.e no thermal energy leaves the conductors during the pulse. Thus, from a given starting temperature the subsequent tempertature rise during the pulse is given by :

$$\Delta T = \frac{1}{C_h D_{Cu} A_c l_c} \int i^2(t) R(t) dt \qquad (2.17)$$

where

D_{cu}= density of copper (8900 kgm^{-3})

C_h= Specific heat capacity of copper (385 J Kg^{-1} K^{-1})

l_c = Total conductor length

The energy loss and change in resistance during a discrete time step of duration Δt can be approximated by equations (2.18) and (2.19). The integration of the power loss can be simplified with negligible error by dividing the time step into 10 sub-intervals, during each of which a constant resistance is assumed.

$$\Delta E = I_{AVE}^2 R' \Delta t \qquad (2.18)$$

$$\Delta R = \frac{\Delta E R' \alpha}{C_h D_{Cu} A_c l_c} \qquad (2.19)$$

where

I_{AVE} = Average value of current for the sub-interval.

R' = Fixture resistance during the sub-interval.

2.13 CALCULATION OF FORCE ON THE FIXTURE CONDUCTORS

It has been previously been emphasised that ideally the ultimate mechanical strength of a fixture should be estimated from the material properties and a detailed structural model. However, since the practical realisation of the fixture will be limited by inevitable imperfections in construction, the specified maximum mechanical load would need to be subject to a somewhat arbitrary safety factor of say 10 or more. Hence, the variation in the peak force in fixture designs which are predicted to produce similar levels of magnetizing field is likely to be much smaller than the safety factor which would be applied. Thus, in terms of mechanical reliability, there is little point in selecting a particular fixture design on the basis of it having a lower calculated force. Therefore, this is neglected in the electrcial design phase.

2.14 POST-PROCESSING OF RESULTS

Following extensive scanning of the design space the results are post-processed to allow selection of potentially optimal designs. For each valid fixture design, i.e one which does not violate imposed constraints, there are a large number of dimensional and calculated performance parameters. To ease interpretation of such data the parameters are plotted on a series of graphs against the common abscsissa of design number. To further reduce the volume of data to be handled in the post-processing stage, the valid designs are filtered by specifying a minimum percentage volume saturation criteria.

2.15 DYNAMIC SIMULATION

The preceeding design stages are based entirely on static field calculations. However, the transient dynamic nature of the field must be considered, since eddy-currents induced in conducting materials within the fixture or the magnet assembly to be

magnetized may inhibit penetration of the magnetizing field into the magnet. Thus a fixture design which appears to meet the target specification under the initially assumed static conditions may have its performance severely degraded under dynamic conditions, leading to an unacceptable dilution in the subsequent magnetic properties of the magnet.

The assessment of the effect of eddy-currents in likely optimal designs is important since the electrical phase of the design process tends to favour magnetizer and fixture parameters which produce short duration pulses, which in turn are the most likely to be affected by induced eddy-currents. Short duration pulses tend to be favoured since they permit the application of the highest mmf per unit of winding volume for a given maximum temperature constraint, and hence will tend to produce the highest statically predicted volume saturation levels. Therefore, the true optimal fixture when dynamic factors are considered, may well have been passed over in the earlier design phase.

The dynamic simulation, which is based on a coupled time-stepped electric-circuit/finite element technique, is used initially to assess the significance of eddy-current effects in the fixture which appears to be optimal. If these effects are shown to be minimal, as is often the case, particularly in the magnetization of a magnet alone, no further dynamic simulations are necessary. However, if the statically predicted levels of magnet saturation are not realised, the criteria used to select the optimal designs must be modified such that a performance premium is associated with the pulse duration. A fixture design is then selected on the basis of this modified performance criteria and its dynamic performance assessed. This process can be repeated until either a fixture design which produces useful levels of saturation is identified or the feasibility of the magnetization within the imposed constraints is ruled out. In a case where the magnetization is not feasible, the design procedure can be recommenced with a less

ambitious specification, e.g the magnetization of the magnet alone rather than the magnetization of a sub-assembly. The techniques utilised in the dynamic simulation are discussed in detail in chapter 3.

2.16 ASSESSMENT OF MAGNET PERFORMANCE.

Inevitably in multipole magnetization there will be some dilution in the magnetic properties of the magnet compared to those of an idealised magnet, i.e a magnet which is assumed to be fully saturated throughout its entire volume with the required field orientation. The assumption of such an idealised magnet often forms the basis of the design synthesis process of the device into which the magnet is to be incorporated. It is important, therefore, during the design of the magnetizing fixture to assess whether the dilution in properties will cause an unacceptable deteriation in the performance of the device.

To allow such an assessment, a magnetostatic finite element package has been developed which can model a device when its magnet has a distribution of magnetic properties determined according to the results from the dynamic simulation. Following the decay of the magnetizing pulse, each element in the magnet is modelled as if it recoils along a characteristic determined by the level of peak magnetizing field to which it was exposed during the impulse magnetization. This is achieved by scanning the transient field distributions predicted during the dynamic simulation and determining the magnitude and orientation of the maximum magnetizing field strength in each element. These values are subsequently used together with a measured family of demagnetization characterisitcs, such as those of fig 2.11, to model the magnetostatic performance of the impulse magnetized magnet in the device.

In most permanent magnet machines the degree of symmetry in the field distribution is often not as great as in a magnetizing fixture, particularly if rotation of the

permanent magnet rotor is being considered e.g a 4-pole rotor of a brushless dc machine can be fully modelled by a 45^{o} segment of its cross-section in a magnetizing fixture but requires a 90^{o} segment of its cross-section when rotated in a 12-slot 3-phase brushless motor. Therefore, as part of the post-processing of results from a dynamic simulation the operations of repeating and mirroring of the permanent magnet can be undertaken to provide the relevant data.

In the finite element analysis of electrical machines, a single field solution can often provide useful information e.g peak cogging torque, peak flux-linkage etc. However more extensive information is obtained by incrementally rotating the machine and producing a series of magnetostatic solutions, from which, for example, the flux-linkage and the induced emf waveforms can be calculated. To produce such a series of field solutions with minimum user interaction an application specific finite element package has been developed to effect automatic rotation of the rotor.

Numerous methods have been proposed to cater for the relative movement between the rotor and stator regions of a finite element mesh.These include analytical solutions of the airgap field [2.14], the use of special airgap elements [2.15] and the use of overlapping elements [2.16]. They are all entirely general, since the rotor and stator mesh are decoupled, and hence there is no requirement to maintain a fixed continuity of discretization across the airgrap region. They can, therefore, be readily applied to machines having complex rotor geometries, e.g buried magnet brushless machines, induction motors etc. Additionally since no limitation on the angular resolution of the relative motion is imposed the methods are suitable when the rotor is not required to move through a fixed angle between successive field solutions e.g in a coupled drive/motor/mechanical simulation [2.17].

However, a far simpler method for rotating the rotor, albeit in fixed discrete steps

and constrained to have a surface mounted magnet rotor topology, can be effected by constraining the angular discretization in the magnet region to be uniform. Rotation is then simulated by re-allocating the demagnetization characteristics of the elements with due account of any change in polarity as elements pass over the imposed periodic boundaries. The minimum resolution of the motion which can be modelled by this approach is limited to the angle subtended by the finite elements in the magnet. The requirement for uniform mesh discretization limits its applicability to non-salient pole machines, but it can cater for magnet arcs with a pole-arc to pole-pitch ratio which is less than unity. Despite these limitations on the generality of the technique it was utilised for the analysis package since it required no modification of the exisiting finite element formulation, and can cater for the vast majority of permanent magnet machines whose rotors are magnetized as a multipole entity. Fig 2.12 shows two possible mesh discretizations for a 90^{o} cross-section of a 4 pole brushless d.c machine in which the magnetization of 45^{o} section of the magnet has been modelled in a dynamic simulation. To aid clarity, the density of the discretization has been reduced considerably from that which would normally be required in order to achieve a high degree of accuracy in the field solution.

When the multipole magnet is symmetrically oriented with respect to the stator, the field calculation should produce a symmetrical field distribution. However, this cannot be achieved with mesh (b) because of the inherent asymmetry of the discretization errors introduced by the mesh. This problem can be particularly troublesome in the calculation of torque by energy methods, since the change in co-energy between two rotor positions is susceptible to numerical cancellation errors. Thus, mesh (a) is the preferred discretization. However, the simulation of rotation by the method of reallocating demagnetization characteristics is then not possible. This problem has been overcome by combining pairs of triangular elements into a quadrilaterals which are then assigned the average demagnetization characteristic of the two elements. This

allows the magnetization distribution to be rotated readily The finite element formulation for the magnetostatic field including permanent magnets sources is based on the solution of the governing field equation (2.20), and the implementation described in Appendix B.

$$\frac{\partial}{\partial x}\left(\nu_y \frac{\partial A_z}{\partial x}\right) + \frac{\partial}{\partial y}\left(\nu_x \frac{\partial A_z}{\partial y}\right) = -Jo + \frac{\partial M_y}{\partial x} - \frac{\partial M_x}{\partial y} \qquad (2.20)$$

This in-situ analysis of magnet performance represents the concluding step in the fixture design process. However, it can provide feedback within the overall iterative design process for the motor or device in which the magnet is a component. Failure to produce a magnetizing fixture which enables the full device performance specification to be realised may require a revision of the overall motor design, with due account of any limitations on magnet performance dictated by the multipole magnetization stage of production.

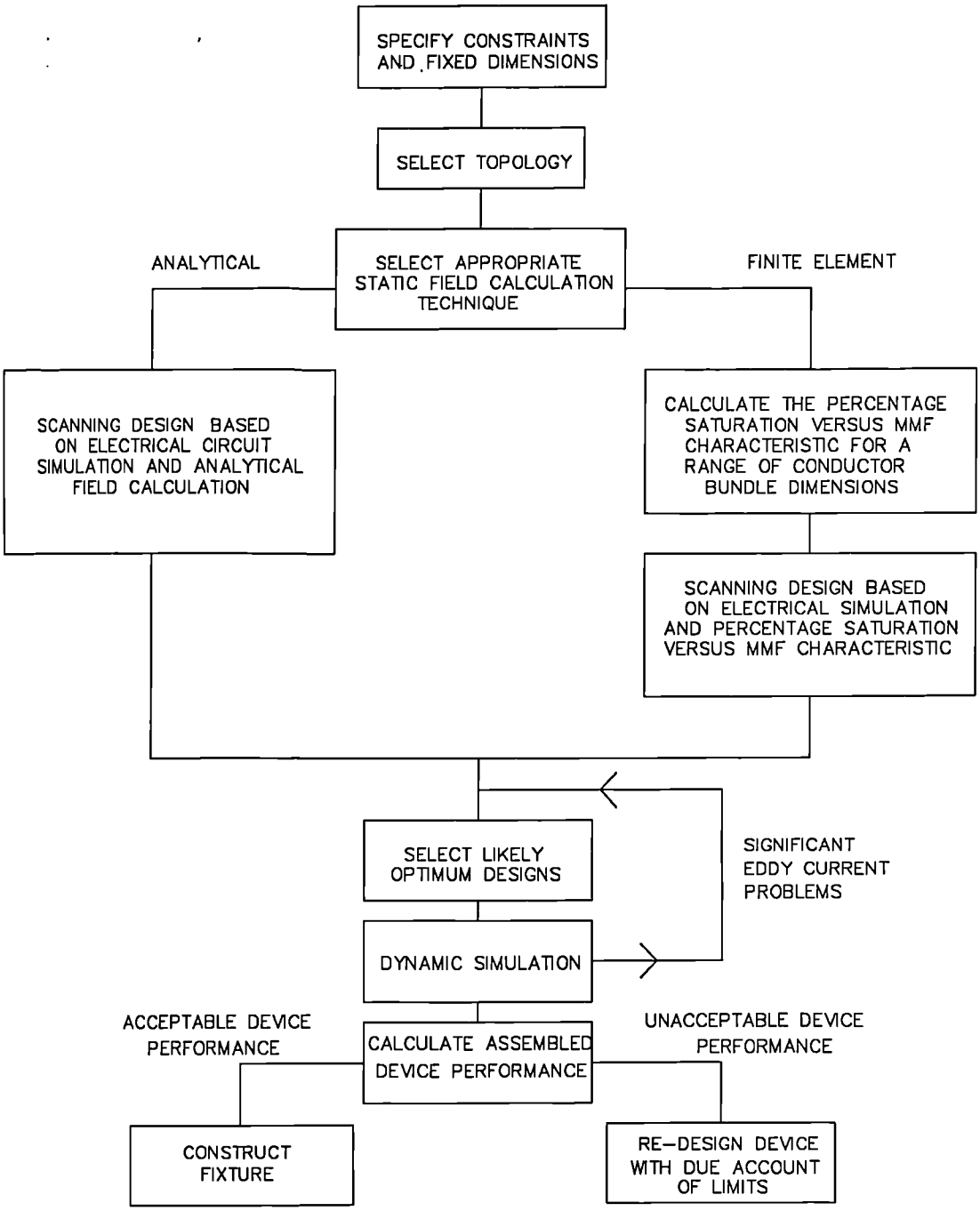

Fig. 2.1 Flowchart of the design methodology.

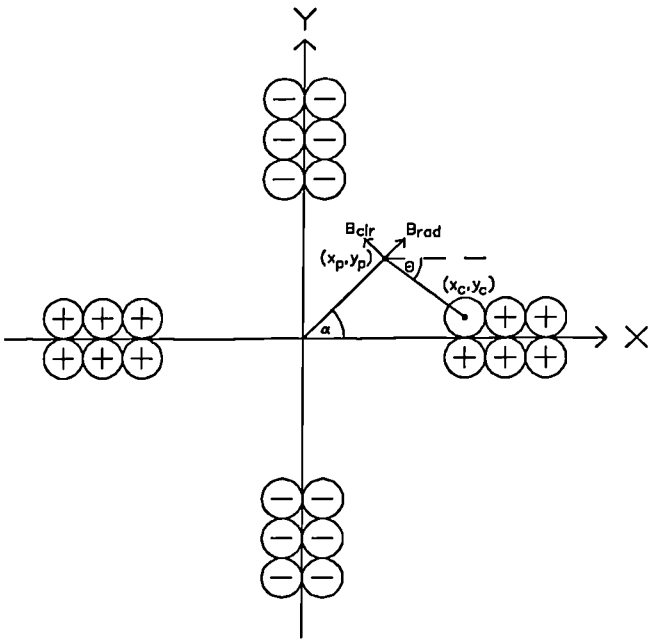

Fig. 2.2 Two-dimensional model of a multipole serpentine fixture for the analytical calculation of the magnetizing field.

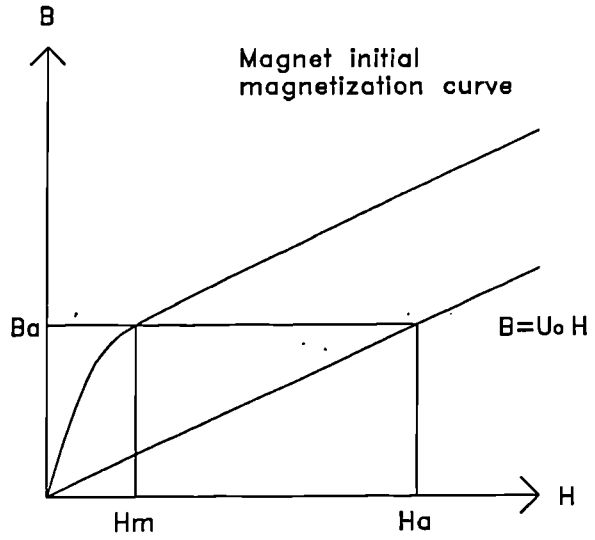

Ha = Analytically calculated H at a point within the region occupied by the magnet.
Ba = Analytically calculated flux density
Hm = Actual local magnetizing field strength in the magnet.

Fig 2.3. Approximate method for the correction of the analytically calculated magnetizing field to take account of the presence of the permanent magnet.

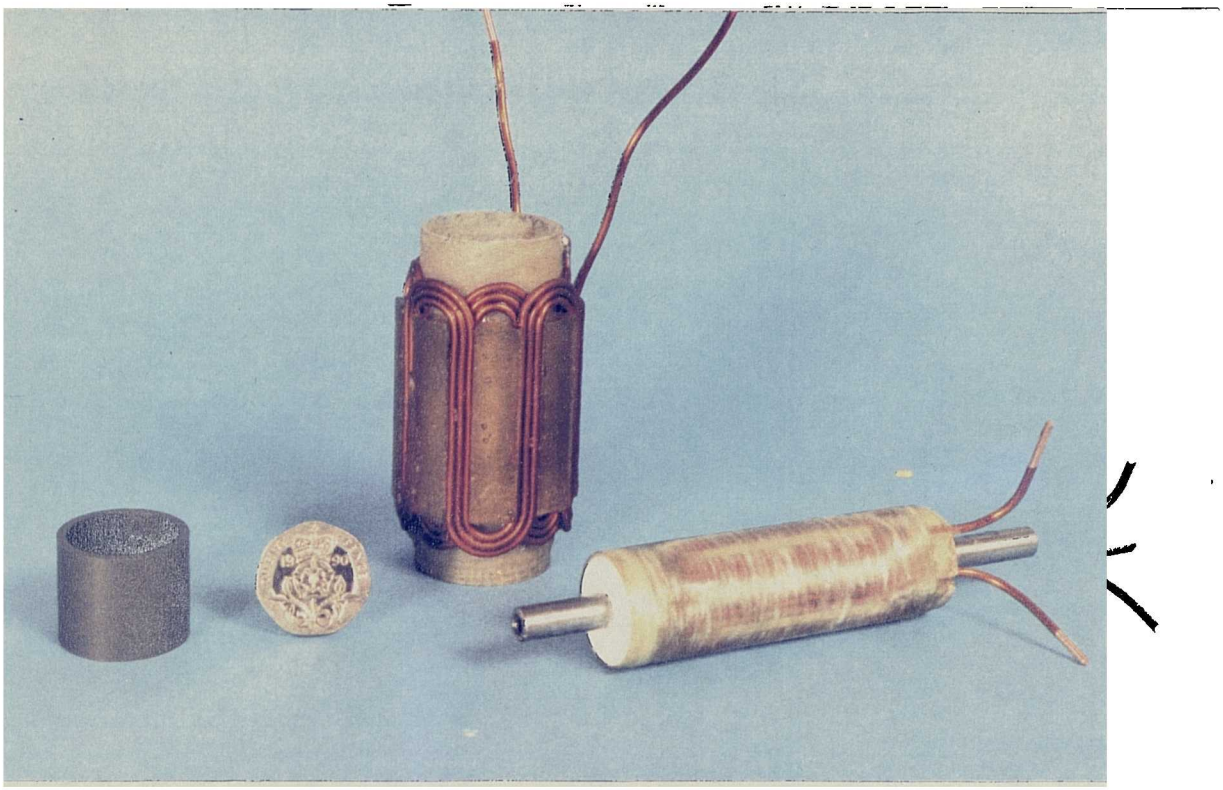

Fig. 2.4 Multipole serpentine magnetizing fixture prior to resin encapsulation.

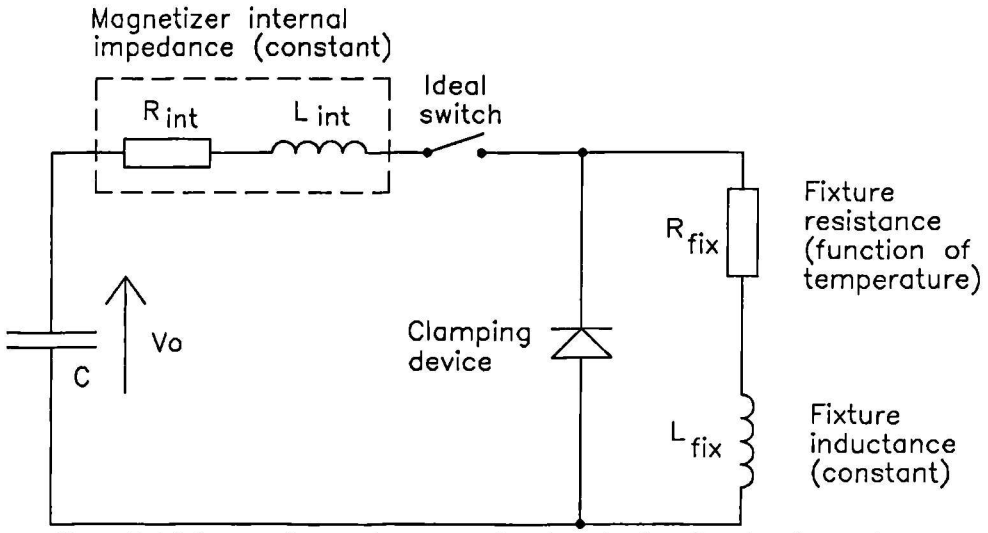

V o = Initial capacitor voltage - switching device fixed voltage drop

Fig. 2.5 Equivalent circuit of a capacitor discharge magnetizer used in the linear electrical simulation.

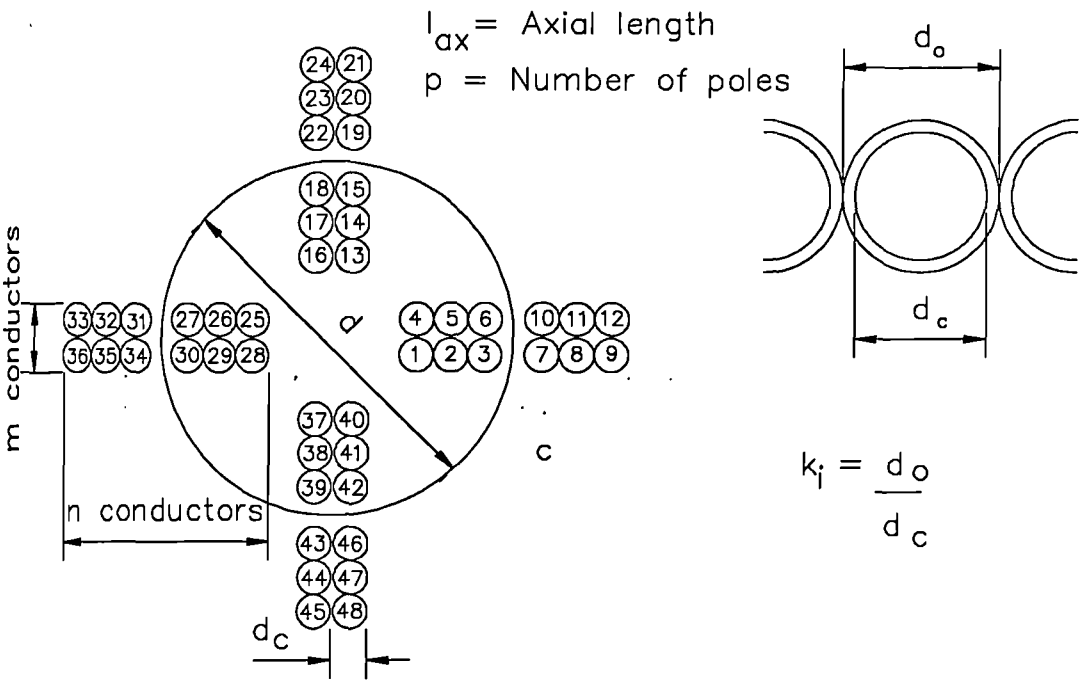

Fig. 2.6 Two-dimensional model for the calculation of the axial component of inductance of a double-sided serpentine fixture.

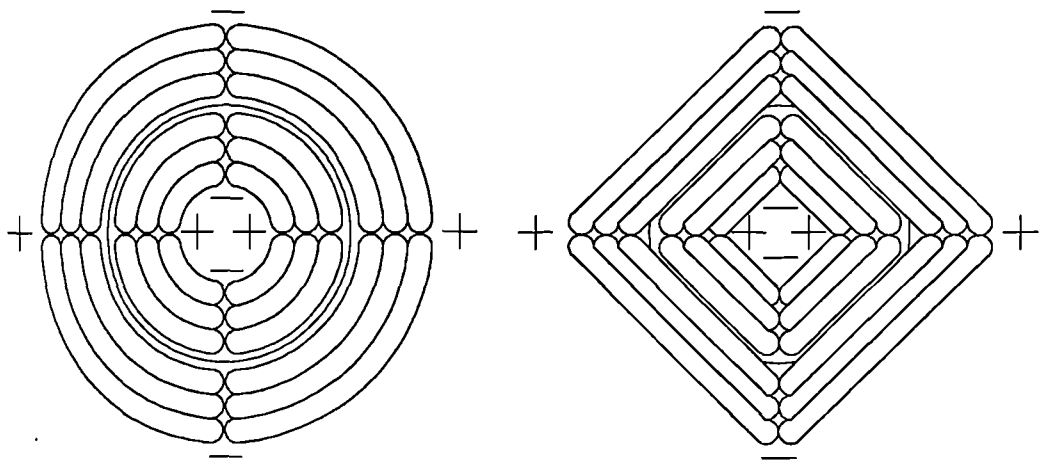

Schematic of end-winding

Simplified end-winding representation (Length of conductor located at a radius r is $\frac{2\Pi r}{p}$)

Fig. 2.7 Schematics of the end-windings.

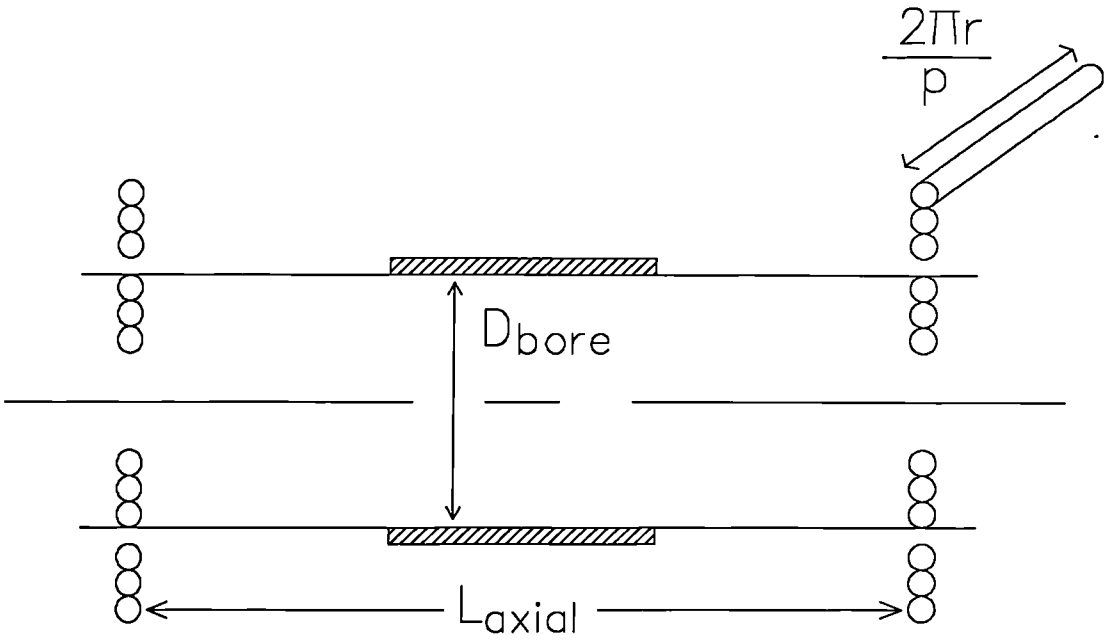

Fig. 2.8 Simplified model for one pole pair.

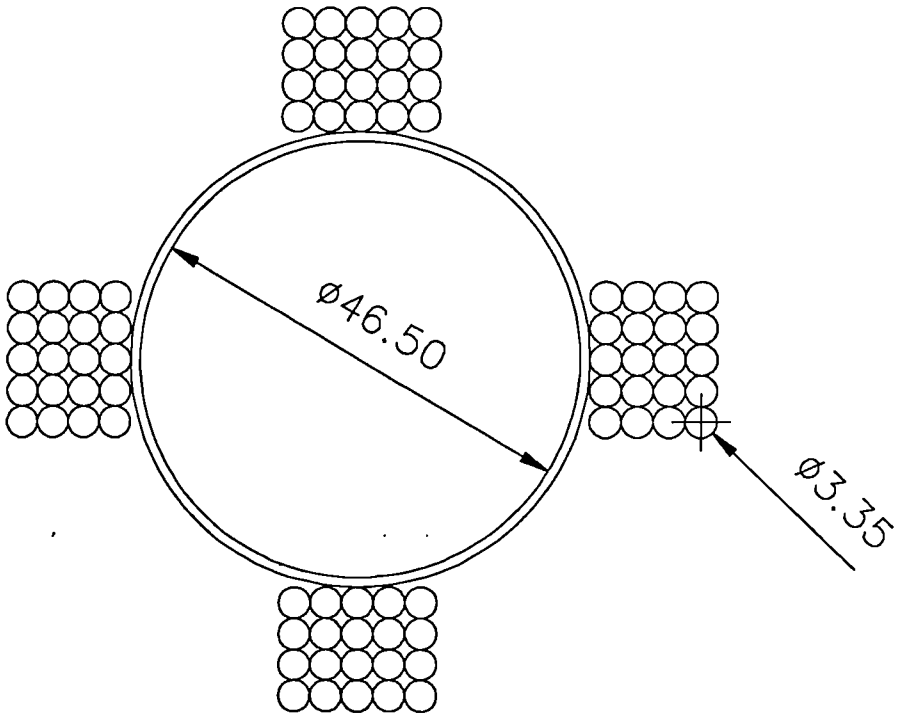

Fig. 2.9 Test fixture for the validation of the analytical inductance calculation.

Calculation method	Component	Inductance (μH)
Two-dimensional finite element	Axial	33.51
Two-dimensional analytical	Axial	34.17
Finite length analytical	Axial	28.28
Finite length analytical	End-winding	8.80
Finite length analytical	Total	37.08
Measured (@1KHz)	Total	37.80

Fig. 2.10 Comparison of alternative techniques for the calculation of fixture inductance.

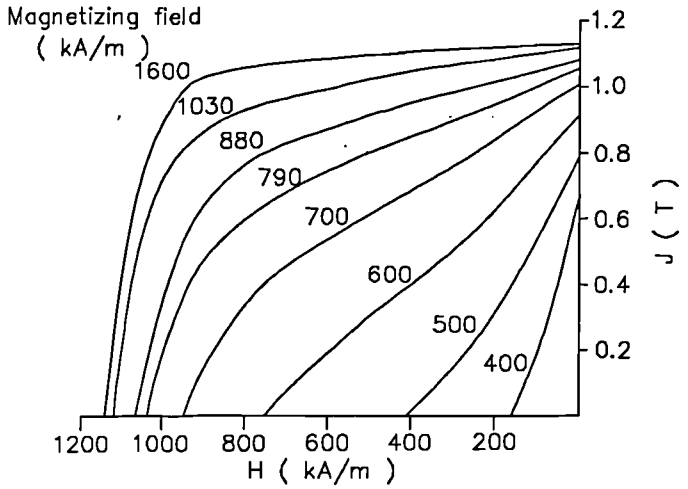

Parallel to the preferred orientation

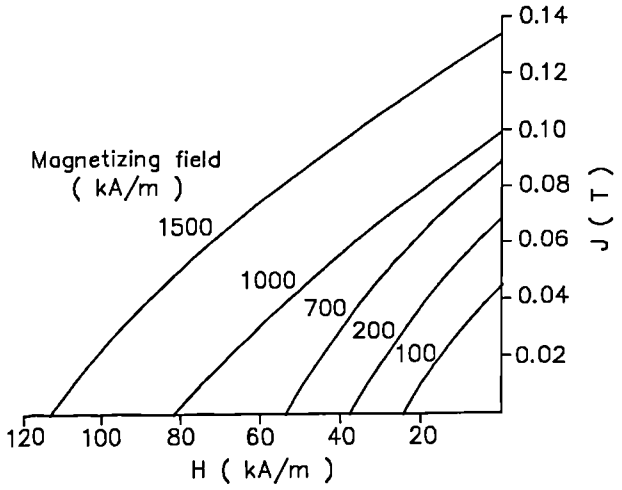

Perpendicular to the preferred orientation

Fig. 2.11 Dependance of the demagnetization curves of sintered NdFeB (Philips Components RES270, 20 °C) on the magnitude of the initial magnetizing field.

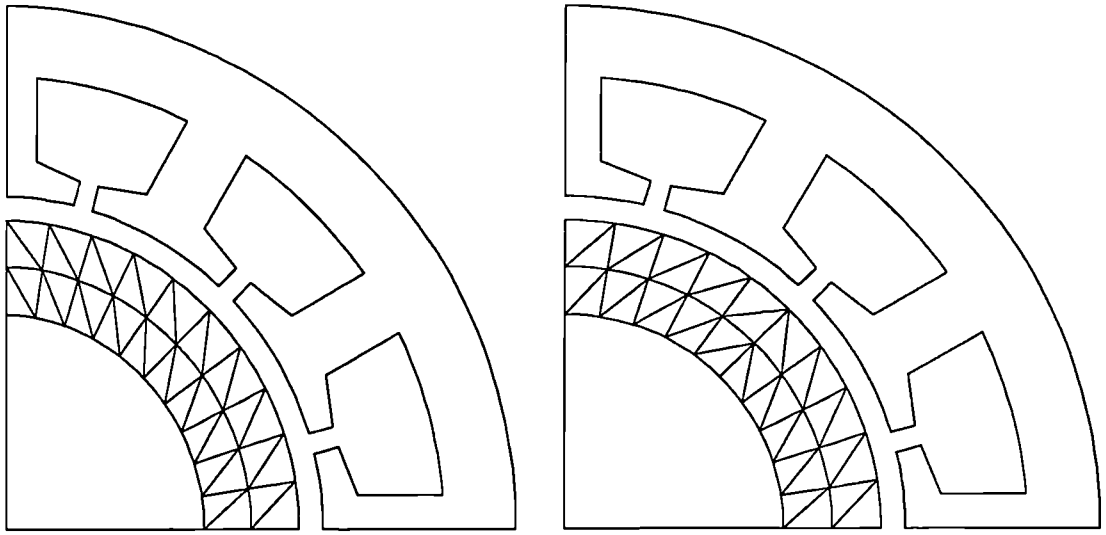

Fig. 2.12 Alternative discretizations for the magnets in a 4-pole motor

CHAPTER 3

DYNAMIC SIMULATION

3.1 INTRODUCTION

The dynamic simulation of candidate magnetizing fixture designs is by far the most detailed and time-consuming phase of the design synthesis/analysis process, and is thus restricted to a few selected designs in the vicinity of the likely optimum. It models the effects of eddy currents and saturation on the field distribution and the fixture inductance, as well as the effect of heating on the fixture resistance. The simulation is based on a time-stepped solution of a coupled electric circuit/non-linear finite element model of the transient magnetization process. Comprehensive post-processing facilities have also been developed which display the variation of electrical circuit parameters during the impulse period, magnetic flux distributions at selected instants of time and the spatial variation of flux density. The provision of such comprehensive facilites allows the iterative process of design refinement to be minimised since detailed insight can be gained into the role of various parameters on the degree of magnet saturation which is achieved. However, prior to the incorporation of such a complex tool in the design methodology it is imperative to establish its accuracy and limitations over a range of saturation levels and pulse durations. To this end, a thorough experimental validation, based on an existing magnetizing fixture and a purpose built instrumented mild steel core was performed.

3.2 ELECTRIC CIRCUIT COUPLING OF DYNAMIC FIELD CALCULATIONS.

Non-linearities due to saturation and eddy currents induced in the materials of the fixture and/or the permanent magnet assembly will result in a variation of the fixture inductance during the current pulse, this variation being a function of both the magni-

tude and rate of change of fixture current. Thus in problems which exhibit a significant degree of these non-linear phenomena there is a need to couple the calculation of the transient field distribution to the analysis of the electrical circuit if large errors in the predicted current and hence magnetizing field level are to be avoided. The importance of this coupling is problem dependant, ranging from being critical in the magnetization of a solid mild steel cored permanent magnet machine rotor in an iron-cored fixture, to being of negligible significance in the magnetization of a small bonded permanent magnet in a large air-cored fixture. In a dynamic simulation with a time step of Δt, in which the field distribution at a time t_o is known, there are two possible methods for calculating the current and the field distribtuion at a time $t_o+\Delta t$:

1) Forward approximation method - Calculate the inductance of the fixture and its rate of change from the field solution at t_o. Use these values to calculate the circuit current at to+Δt. This value of current then remains fixed while the field distribution at to+dt is iteratively solved by the finite element method.

2) Backward approximation method - Solve simultaneously by an iterative technique the field distribution and the electrical circuit equation at $t_o+\Delta t$, modifying the magnitude and rate of change of the inductance in the electrical circuit and magnitude of the current density in the finite element model at each iteration. This method uses the inductance calculated at $t_o+\Delta t$ as the value for the discrete time step.

In selecting one of the above methods for initial evaluation, the following factors were taken into consideration:

1) Since in practice the fixture inductance is changing during the course of a discrete time step, neither method is a true representation of the behaviour of the inductance during the time step. The interpolation between the two extreme values at t_o and $t_o+\Delta t$ necessary to obtain a single value which best represents the average overall state

of the non-linear system will vary according to the relative magnitudes of the eddy-current and saturation non-linearities. Since the best representation of the inductance is, therefore, problem dependant, in general, neither method is inherently more accurate than the other. The influence of saturation and eddy-currents on the inductance tend to counteract each other, and the resulting variation of inductance is usually much smoother than the variation in either the permeability of the non-linear materials or the rate of change of the applied field. A large number of time steps is employed in the simulation in order to accurately represent the source and permeability variations. Hence, the change in inductance between succesive time steps will be small. Thus, whereas the overall variation in the inductance throughout the impulse period may warrant its inclusion in the simulation model, the variation between succesive time steps is likely to be sufficiently small as to make minimal difference between the two methods. Hence, the selection of the preferred method of coupling can be made with respect to practical considerations rather than any inherent accuracy differences.

2) The backward approximation method involves additional iterations of the field solution since the current density in the finite element model is an additional field dependant unknown. Hence, this method is more computationally demanding due to its inherently slower convergence.

3) The forward prediction method offers a useful degree of de-coupling, in that the calculation of the circuit current is not within an iterative loop as is the case for the backward approximation method. Thus the addition of other factors which are not necessarily dependant on the field solution but nevertheless govern the circuit current, e.g the increase in the fixture resistance due to the power dissipation during the impulse period, can readily be incorporated into the simulation without affecting the convergence of the field solution. The addition of such electrical circuit effects in the backward prediction method results in an additional simultaneous equation needing to be solved

with the field, with the resultant deliterious effect on the convergence and computation time.

Since the forward prediction offers advantages in terms of convergence it was selected as the preferred method for the initial investigation. An outline flow chart for a simulation which utilises the forward approximation coupling technique is shown in fig 3.1.

3.3 CALCULATION OF THE CIRCUIT CURRENT.

The method for calculating the circuit current is similar to that used used in the linear electrical simulation, described earlier in chapter 2, except that the fixture inductance now varies with the magnitude and rate of change of current. The equivalent circuit for the magnetizer and the fixture is shown in fig 3.2. The fixture impedance is divided into two components which represent the active axial section, which is modelled by finite elements, and the end-winding regions. The governing circuit equations for this modified equivalent circuit representation of the fixture impedance are:

For $V_D > 0$

$$(L_{ew} + L_{int})\frac{d^2i}{dt^2} + \frac{d^2}{dt^2}(L_{fe}\, i) + R_{int}\frac{di}{dt} + \frac{d}{dt}(R_{ew} + R_{fe}) + \frac{i}{C} = 0 \qquad (3.1)$$

For $V_D < 0$

$$L_{ew}\frac{di}{dt} + \frac{d}{dt}(L_{fe}\, i) + (R_{ew} + R_{fe})\, i = 0 \qquad (3.2)$$

subject to the initial conditions:

$$i = 0 \quad \text{at} \quad t=0 \qquad (3.3)$$

$$\frac{di}{dt} = \frac{V_o}{L_{@t=0+}} \qquad \text{at} \quad t = 0+ \tag{3.4}$$

The electrical circuit initial conditions of (3.3) and (3.4) are critical in determining the magnitude of the peak current. The inductance in equation (3.4) is the value at t=0+, and includes the effects of eddy-current screening. Hence, in general, it is less than the unsaturated d.c value which represents the system prior to the initiation of the pulse. A reliable method for calculating the inductance at t=0+ is necessary since the error in the peak magnitude of the current is directly proportional to any error in the initial inductance. To this end, the iterative procedure shown in fig 3.3 has been implemented.

The unsaturated d.c inductance is calculated from a magnetostatic finite element calculation in which the current in the fixture winding is set arbitrarily at 1A. This initial value of inductance is used to estimate the initial electrical circuit conditions for the first dynamic field calculation. The rate of change of flux-linkage at the first time step is obtained from the dynamic field calculation and is used is to re-estimate the inductance at t=0+ by a linear backward extrapolation. This new estimate of the inductance at t=0+ then forms the initial condition for the next dynamic simulation, and the procedure is repeated until subsequent estimates of the inductance at t=0+ converge within a specified tolerance.

3.4 TRANSIENT FIELD CALCULATION

The calculation of the transient electromagnetic field in the dynamic simulation is by a two-dimensional finite element analysis, and implicitly neglects end-effects in the fixture, the validity of which is problem dependant. A more general and refined

approach would be to use a three-dimensional finite element method. However, the computation time would be some two orders of magnitude greater than for the equivalent two-dimensional implementation, since there are an increased number of unknown potentials at each node, and a requirement for an increased number of nodes to represent the geometry with the same level of discretization. Additional time overheads compared to a two-dimensional implementation would also be associated with the mesh generation and the post-processing of the results. The greatly increased computation time can be reduced to a degree by using hybrid methods in which the field in non-current carrying regions is calculated from a scalar magnetic potential function. However, although the three-dimensional implementation gives a more comprehensive and accurate description of the field distribution, the additional computational overhead was judged to be excessive for inclusion as a design tool within an iterative CAD system.

The two-dimensional finite element method which has been implemented has a number of features which are common to the magnetostatic formulation which was used earlier in the design synthesis procedure and discussed in Appendix B. However, there a number of additional factors which must be considered in relation to the time-stepped nature of the dynamic field calculation, and these are addressed in the following sections.

3.5 FINITE ELEMENT MODEL FORMULATION.

For the two-dimensional model utilised in the simulation the field distribution under dynamic conditions is governed by equation (3.5) which is the vector potential form of the transient diffusion equation derived from Maxwells equations

$$\frac{\partial}{\partial x}\left(\nu_y \frac{\partial A_z}{\partial x}\right) + \frac{\partial}{\partial y}\left(\nu_x \frac{\partial A_z}{\partial y}\right) = -J_z + \sigma \frac{\partial A_z}{\partial t} + \sigma \frac{\partial \varphi}{\partial z} \qquad (3.5)$$

The physical significance of the electrical scalar potential term has been extensively studied by Nakata and Takahashi[3.1] . For problem domains in which the axis of symmetry between current carrying conductors can be represented by a Dirichlet boundary condition the variation of the scalar electrical potential can be set to zero thus reducing the governing vector potential field equation to that of equation (3.6). In a series connected multipole magnetizing fixture, a Dirichlet boundary condition can also be enforced at a pole axis in order to exploit the symmetry in the fixture, thus satisfying the conditions necessary for the elimination of the electrical scalar potential term.

$$\frac{\partial}{\partial x}\left(\nu_y \frac{\partial A_z}{\partial x}\right) + \frac{\partial}{\partial y}\left(\nu_x \frac{\partial A_z}{\partial y}\right) = -J_z + \sigma \frac{\partial A_z}{\partial t} \qquad (3.6)$$

In order to solve equation (3.6) a variational theory technique was utilised to formulate a functional, the minimisation of which yields the solution of the governing field equation [3.2]. The functional which corresponds to equation (3.6) is given in equation (3.7), and represents the total energy stored in the system. The procedure for the minimisation of this functional by the non-linear Newton-Raphson technique is given in Appendix B.

$$F = \int_{\Omega} \nu_y \left(\frac{\partial A}{\partial x}\right)^2 + \nu_x \left(\frac{\partial A}{\partial y}\right)^2 - 2J_z A_z + 2\sigma \frac{\partial A}{\partial t}\, d\Omega \qquad (3.7)$$

The time dependant term in the finite element formulation i.e $\frac{\partial A}{\partial t}$, can be approximated by a number of methods. The Θ method represents the time derivative by the general equation (3.8) in which the parameter Θ can be set to a value between 0 and 1 e.g $\Theta = \frac{1}{2}$ -forward difference, $\Theta = \frac{2}{3}$ - Galerkin, $\Theta = 1$- backward difference.

$$\frac{\partial A_{t1}}{\partial t} = \frac{A\Theta - A_{t0}}{\Theta \Delta t} \qquad (3.8)$$

where:

$\frac{\partial A_{t1}}{\partial t}$ = Derivative at time step of interest.

A_{to} = Node potential at previous time step

A_{Θ}= Node potential the intermediate instant determined by the value of Θ.

A detailed analysis of the application of the Θ method to transient magnetic field problems has been undertaken by Nakata et al.[3.3] who concluded that under under non-linear conditions involving saturation, the most consistent and physically reasonable results, particularly with respect to preventing oscillations in the solution, are obtained by the backward difference approximation i.e $\Theta = 1$. Thus, this approximation for the time derivative term was adopted in the initial simulation.

3.6 CONDUCTOR CURRENT DISTRIBUTION

The non-uniform current distribution in a conductor, which results from variations in flux-linkage across the conductor cross-section and induced eddy-currents in the conductor itself, was not included in the finite element model, since in order to gain any benefit from its inclusion a fine mesh discretization would be necessary in each individual conductor. Since the fixtures which have been analysed often contain a number of conductors per pole, such a fine discretization, which would also need to be reflected in the discretization of the regions surrounding the fixture winding, is not practical without causing an excessive increase in the computation. The modelling of a non-uniform current distribution would also result in non-uniform heating of the conductor, and hence further complicate the calculation of the impedance.

The neglect of the above effects results in a simplified problem formulation in which the externally driven current is distributed uniformly over the cross-section. This inherently results in better convergence of the iterative solution due to the fewer degrees of freedom in the problem domain. The minimal role of skin and proximity effects in the electrical circuit, and hence the validity of the uniform current density assumed in the conductors, was confirmed by the results of the case studies for which no significant differences between the measured and predicted currents were observed even for very short duration pulses i.e current rise times of the order of 20μs.

3.7 BOUNDARY CONDITIONS

Whereas the finite element method has a number of advantages over analytical methods it suffers from the disadvantage that the problem region, which is often of infinite extent, must be discretized into a finite number of elements. In the analysis of electrical machines the problem region can usually be made finite by imposing a boundary condition on the outer radius of the motor back-iron which forces the radial component of flux density to be zero, a valid approximation if the degree of saturation in the motor is not unduly high. In modelling pulsed magnetizing fixtures however, the problem region often contains large regions of air or heavily saturated iron, and the field domain is effectively infinite with the only applicable boundary condition being that the field decays to zero at infinity.

The method used in the simulation to represent this boundary condition is that of truncation [3.4] , which is shown schematically in fig 3.4. An additional implied source is introduced by applying a Dirichlet boundary condition at a finite distance from the centre of the mesh. For a vector potential formulation, the added source is of equal magnitude, polarity and distance from the boundary as the true source in the finite element discretized region. The field that this additonal source introduces at the point

P of fig 3.4, which is effectively a truncation error, is $\frac{1}{4}R^2$ that of the field produced by the true source. Thus extension of the problem domain to 10 times that of the region of interest, i.e 10 times the overall dimensions of the fixture, introduces an error of approximately 1 part in 400, which is well within the errors involved in the discrete nature of the solution within the fixture region, the tolerance between the geometry modelled and that which can be realised in practice, and the accuracy of the material characteristics.

This method has the advantage that it requires no modifications to the finite element formulation since it is entirely consistent with the mesh generated for the fixture. However, it suffers the drawback that additional elements are required to model the exterior region up to the imposed boundary. However, the discretization of this exterior region can be graded to be increasingly coarse as the boundary is approached.

3.8 SOLUTION CONVERGENCE

The Newton-Raphson iterative process results in rapid convergence for the non-linear system of equations. The convergance is based on the potential at the nodes meeting the criteria of equation (3.9)

$$\frac{A_i - A_{i-1}}{A_i} \leq \varepsilon \qquad (3.9)$$

where

A_i = Vector potential at iteration i

A_{i-1} = Vector potential at iteration i-1

ε = Tolerance (set to 0.001 for the dynamic simulation).

The screening effects of eddy currents are such that the field variation within a solid conducting region under dynamic conditions is far more pronounced than under

static conditions, since the magnetizing flux is largely confined to a surface layer during the initial stages of the transient. Therefore, there is a much larger variation in the magnitude of the vector potential between nodes near the surface and those which are deeper within the conducting material than is the case under static conditions. As a consequence, the application of the convergence criteria of equation (3.9) alone leads to problems, since the potential at nodes deep within the conducting region have been calculated as being as much as 8 orders of magnitude lower than the potential at nodes near the surface. Such small values of potential are very susceptible to cancellation and rounding errors in the inversion process, and hence the convergence of these nodes to the correct potential value is very problematic. These potentials are, however negligible in terms of their effect on the global field solution and the eddy current flow. Therefore, the additional convergence criteria of equation (3.10) has been applied to each node, a failure to meet this criteria resulting in the convergence criteria (3.9) being neglected for the node.

$$A_m \geq A_{ave}\ \gamma \tag{3.10}$$

where

A_m = Vector potential of node m

$A_{ave} = \sum_{i=1}^{i=n} \frac{Ai}{n}$ where n is the total number of nodes.

γ = negligble tolerance (set to 10^{-4} in the dyanmic simulation)

3.9 MAXIMUM DISCRETE PRINCIPLE

Previous workers on transient time-stepped finite element methods, in both thermodynamics and electromagnetics [3.5][3.6], have observed that during the initial stage of the transient physically unreasonable phenomena can be predicted, e.g the reaction field produced by eddy currents exceeding the applied field. This occurs when the so called maximum discrete principle is contravened.

This principle states that for any given spatial mesh discretization, there is a lower limit on the time step which can be used without introducing significant errors. If the time step necessary to accurately represent the source variation is shorter than that allowed by the maximum discrete principle, the problem can be alleviated by increasing the mesh density. However, since there is a practical limit to the degree of mesh discretization, in terms of solution time and convenience of post-processing, the element size cannot reduced indefinitely. Thus, cases may arise where the time step required to give a reasonable representation of the source variation is too short for the maximum practical level of mesh discretization.

A method for overcoming this problem is so called mass or inertia lumping. In mass lumping the shape functions of the elements, which are discussed in Appendix B, are modified to be constants rather than continous functions. The effect of using either a lumped or consistent matrix on the predicted transient field distribution in a test problem is discussed in the validation of the simulation technique.

3.10 MATERIAL CHARACTERISTICS.

There are a number of mathematical methods for the representation of non-linear initial magnetization curves, based on either piecewise polynomial curve fits [3.7] or continuous analytical functions [3.8]. The initial magnetization curve of a soft magnetic material is composed of three distinct regions [3.9], viz. the reversible, irreversible linear and saturated regions, fig 3.5. The reversible region is characterised by a much higher reluctivity than the linear region of the irreversible magnetization characteristic. Fig 3.6 shows the reluctivity versus magnetizing field strength characteristic derived from the measured initial magnetization curve of a sample of EN1A free cutting mild steel.

In magnetostatic finite element analyses, the presence of the reversible region can, in certain circumstances, be neglected, such as in a magnetic circuit constructed from a material having a narrow hysteresis loop and in which the airgap is the dominant reluctance, when the small error in the mmf absorbed by the iron may not be too critical to the calculation of global parameters, such as flux linkage, torque etc. Neglecting the reversible region, i.e modifying the characteristic to eliminate the sharp 'knee' results in a much smoother derivative at lower values of magnetizing field strength, which is advantageous from a convergence point of view. Techniques such as this are employed in a number of commercial magnetostatic finite element packages [3.10]. However, in time-stepped finite element solution techniques the time history is important, and the greatly reduced permeability of the reversible region can have a significant effect on the predicted field distribution.

Although a number of analytical representations have been proposed for the representation of initial magnetization curves [3.11][3.12], they are unable to model the irreversible region. However, the representation of the initial magnetization curve by a series of piecewise cubic polynomials allows the reversible region of the initial magnetization curve to be modelled. The general form of such a cubic spline curve fit is shown in fig 3.7. From convergence and stability points of view, it is crucial to eliminate any oscillations in the fitted material curve. Such oscillation free curves can be obtained by ensuring that each individual cubic curve is monotonic, i.e the maxima and minima of each cubic are outside the interval in which the curve is utilised.

The initial magnetization curves which are used in the simulation are fitted by smooth cubic splines which have the advantage of having continuous smooth derivatives. However, since monotonic curves are not guaranteed by a smooth fit, a check on the position of each local minima and maxima is undertaken. If any of these fall within

the interval in which the individual curves are utilised, the locations of sampled data points on the magnetization curve are modified. By a judicious choice of the sampling points on measured or published material characterisitcs, smooth monotonic curve fits can be obtained.

When the field locally applied to a region of a non-linear material decays the working point of this region does not follow the initial magnetization curve back to the completely demagnetized state. However, hysteresis was not included in the simulation for the following reasons:

1) Neglecting the hysteresis simplifies the simulation method.

2) The aim of the dynamic simulation is to establish the peak level of magnetizing field to which each finite element of the magnet is exposed under dynamic conditions. The behaviour of a particular region following the peak is rather less important, unless the phase shift within the material is so large that it has a significant effect on the level of peak magnetizing field to which an adjacent region is exposed.

3) At field levels typical of those encountered in the pulsed magnetization of rare-earth materials, viz 3-4T, a significant proportion of the recoil follows a curve which shows only minimal departure from the initial magnetization characteristic. It is only when the field falls below about 1.8T or so for soft magnetic materials and 1.2T for rare-earth magnets, that hysteresis causes any significant departure from the initial magnetization curve. Further, the behaviour of materials during the very final stages of recoil is of no practical importance in the design of magnetizing fixtures.

4) The inclusion of hysteresis would greatly increase the material characterisation necessary, since the recoil locus of a material is a function of the level of magnetizing field to which it was exposed.

3.11 MESH GENERATION.

There are two approaches to finite element discretization which can be utilised in field calculations, viz fixed and adaptive. In a fixed mesh, the number, position and interconnection of the nodes does not change during the calculation. However, in such a fixed geometry mesh the accuracy of the field solution depends on the skill of the user. In adaptive meshing, the mesh is continually refined according to estimated local errors in the field, and is a well etablished method for magnetostatic problems [3.13] [3.14]. It is inherently more accurate and produces more reliable results than for a fixed mesh since the generated mesh is near optimal and not subject to the preconceptions of the user. For a given accuracy, adaptive formulations usually result in meshes with a greatly reduced number of nodes, since the densely discretized regions are concentrated only in areas of high field variation, which is unlikely to be the case in a fixed mesh.

Despite these advantages, however, the increased complexity of such methods in relation to transient eddy-current problems was regarded as being outside the scope of this work and the far simpler fixed mesh method was adopted. The mesh for the simulations were generated using the MESHGEN automatic mesh generator [3.2] developed at the University of Sheffield. The level of discretization of any region within a fixed finite element mesh was selected with reference to the following factors:

1) The accuracy of static and dynamic field solutions, which are piecewise linear solutions, improves as the number of nodes is increased. Therefore, the density of the discretization should be highest in areas having the greatest field gradients.

2) The region should be sufficiently finely discretized so as to adequately represent the geometry of each region. The first order triangular elements utilised in the formulation have straight sides, and curved boundaries are hence represented by a piecewise linear

approximation. Therefore, a region containing circular holes or individually meshed circular conductors, at least 16 elements are required around the periphery of each circle so as to obtain a reasonable representation of the geometry.

3) The region should be discretized to provide the required spatial resolution of information at the post-processing stage. In the analysis of multipole radial magnetization of rotors a circumferential resolution of 1^{o} is often required, particularly in the vicinity of the pole transitions where the magnetization varies from a fully saturated value to zero over a few angular degrees. Defining such an angular discretization over a region as large as a rotor magnet determines to an extent the discretization over the remainder of the machine because of the need to avoid rapid changes in spatial discretization levels.

4) The calculation time for each iteration of the solution usually increases in direct proportion to the square of the number of nodes. The total number of iterations required for convergence can also increase with the number of nodes due to the additional degrees of non-linear freedom which have to satisfy the convergence criteria.

3.12 CALCULATION OF THE FINITE ELEMENT REGION INDUCTANCE

The use of two-dimensional finite element analysis to model the three-dimensional geometry of magnetizing fixtures, necessitates the division of a fixture into a region in which the finite element model is used to calculate the time varying fixture flux linkage, and a region in which an analytical method is used for the calculation of a time-invariant inductance. The constant inductance regions consist of the fixture end-windings and the axial section of the fixture which extends beyond the magnet assembly. The division of the axial section into a finite element region and a constant inductance region requires consideration of the limitations of two-dimensional modell-

ing. The results presented in chapter 2 for the air-cored inductance of a radial field magnetizing fixture, demonstrate the error which can be introduced in the calculation of the inductance of a region by simply multiplying the two dimensional finite element inductance by the axial length. This simple scaling usually overestimates the inductance, particularly for regions of short axial lengths in which the end effects are significant.

The effective axial length of the finite element region must, therefore, be modified from the actual dimension, such that the finite element calculated inductance component contributes the appropriate proportion of the total fixture inductance. The analytical method for calculating fixture inductance, which is based on a full three-dimensional representation and hence accounts for end-effects, has been shown to give excellent agreement with measurements on constructed fixtures. Thus by regarding the analytically calculated inductance, L_{an}, as the true total inductance of the fixture in the absence of any magnetic materials, the modified axial length of the finite element region can be calculated:

$$z'_{fe} = \frac{L_{fe}}{l_{fe}} \tag{3.12}$$

where

z_{fe}' = modified axial length of the finite element region.

l_{fe} = air-cored finite element region inductance per unit axial length calculated from a two-dimensional linear magnetostatic field solution.

L_{fe} = analytically calculated inductance for the axial section of the fixture.

Therefore, the constant component of fixture inductance in the equivalent circuit, Lew, is given by:

$$L_{ew} = L_{an} - z'_{fe}\, l_{fe} \tag{3.13}$$

Having established the modified axial length, the rate of change of flux linkage in the fixture section modelled by the finite element model can be calculated at each time step of the simulation. It will be noted that the calculation of the flux-linkage of a conductor in the fixture winding takes account of any variation in field over its cross-section, although this variation is not used to redistribute the conductor current, as was discussed above.

If the winding is constructed from a large number of turns then the dimensions of each individual conductor can be regarded as being insignificant with respect to the gradient of the field, i.e the field is assumed to be constant over its cross-section. In this case the flux-linkage of a conductor can be calculated simply from the value of flux at its centre. However, often in multipole fixtures each individual conductor can extend over a significant fraction of the pole pitch, i.e a distance over which the field varies from a maximum to a minimum. In such cases a weighted average flux-linkage over the conductor cross-section is necessary in order to obtain an accurate estimate of the effective flux-linkage. In a finite element model of a multipole fixture in which the boundary between two poles is defined with a Dirichlet boundary which is imposed by specifying zero vector potential, the average potential of the current carrying elements in an individual fixture conductor, A_{AVE}, is given by:

$$A_{AVE} = \sum_{e=1}^{e=n_e} \frac{a_e}{a_c} A_e \qquad (3.14)$$

where

n_e = Number of elements in the conductor cross-section

a_c = Cross-sectional area of the conductor

a_e = Cross-sectional area of element e

A_e = Average potential of the three nodes which form element e

Hence, the total inductance of the finite element region of a fixture with p poles and n conductors is given by:

$$L_{fe} = \frac{z'_{fe} \sum_{i=1}^{i=np} A_{AVE}}{I} \qquad (3.15)$$

where:

I = Fixture current.

3.13 VALIDATION BASED ON THE 'FELIX' CYLINDER BENCHMARK.

In the development of finite element software, and indeed any other software, it is essential that thorough validation is undertaken prior to its integration into a design methodology. Therefore, even though the finite element formulation is based largely on existing and well proven theory, the complexity of the program neccesitates a validation process to ensure that it contains no errors in the coding. Although the analysis of trivial problems, involving meshes with only a few nodes, are useful during the development of the program so as to check various modules, ultimately a simulation using a typical problem environment is required.

The problem of validating eddy-current calculations has been addressed by a number of published benchmark problems which include numerical results submitted by numerous establishments using a range of solution techniques. The FELIX cylinder benchmark was used as problem 1 of the International Eddy Current Workshop [3.15], experimental results being measured at Argonne National Laboratory under the FELIX program (Fusion ELectromagnetic Induction EXperiment) [3.16]. The benchmark is based on the hollow aluminium cylinder shown in fig 3.8 which was initially placed in a constant uniform field of 0.1T applied in the direction shown. The applied field

was then forced to decay as shown in fig 3.9, and the flux density component By at the centre of the cylinder was measured. The induced field at the centre, i.e the difference between the measured field and the applied field, was calculated from data measured at the discrete time instants of 10,20 and 40 ms after initiation of the field decay. These values of induced field were then used as the basis for comparison with those predicted by the various formulations submitted.

Although the cylinder is a three-dimensional structure a number of submissions to the Workshop solved the problem two-dimensionally using a variety of analytical and numerical techniques. For finite element formulations, the mesh of fig 3.10 which comprises 186 triangular elements was recommended. For the vector potential formulation the time-varying applied field is imposed by setting the appropriate time-varying vector potentials on the boundary AB.

The applied, net and induced flux density waveforms at the centre of the cylinder, calculated with a 1ms time step are shown in fig 3.11. The calculated induced flux density at the centre of the cylinder for a range of time steps is shown in fig 3.12 from which it will be seen that the calculated values are largely insensitive to the time step. Increasing the mesh density by doubling the number of divisions along the sides of each region to give a mesh having 760 elements, also has minimal effect on the calculated induced field, fig 3.13. Comparison with published results shown in fig 3.14, confirms good agreement with predictions obtained by two-dimensional first-order triangular elements (Diserns using the PE2D finite element package from Vector Fields Ltd.). The spread of results in fig 3.14 reflects the wide range of numerical, analytical and equivalent circuit techniques, formulated in both 2 and 3 dimensions. It also is worth noting that the errors between the measured flux-densities and those predicted by the dynamic simulation although somewhat large are well within the bounds of the errors produced by the other methods.

3.14 EXPERIMENTAL VALIDATION.

Whereas the standard FELIX benchmark is useful in verifying the implementation of a given finite element formulation, it is based on linear materials. The presence of non-linear materials in a region introduces a number of additional considerations, particularly for pulsed magnetization since often extreme saturation occurs during fast transients. For such cases, there is a significant skin-effect in solid soft magnetic materials, which results in finite elements near the surface being driven rapidly into saturation, and the dynamic nature of the permeability becomes critical in determining the penetration of the field into the bulk steel. In addition to the non-linearities, the range of time constants encountered in pulsed magnetization is significantly different from those of the FELIX problem which is based on an applied field rather than an externally driven current. Hence, verification of the simulation method by a standard linear benchmark, although useful, is not sufficiently comprehensive.

Since no suitable published benchmark problem was available for a full validation of the circuit coupled simulation, an experimental investigation was undertaken. In developing a test problem for the absolute validation of a given simulation, it is usual to experimentally establish an environment which is ideally suited to the solution technique, i.e the test problem is dimensioned such that the field distribution is a very good approximation to being two-dimensional. However, the aim of the test problem in this case was not to develop such a environment, but rather to verify the performance of the simulation method against measurements in a typical application environment, in order to allow investigation of issues such as the validity of using a two-dimensional finite element methods in fixtures which are essentially three dimensional due to their comparitively short axial length.

In order to verify the simulation, a test problem was devised based on an existing 4-pole magnetizing fixture which is shown in fig 3.15. The fixture was used previously

for magnetizing the 4-pole sintered ferrite rotor of a brushless d.c machine. However, the mild steel core shown in fig 3.16 was used rather than a NdFeB permanent magnet or a composite structure comprising a mild steel core and a surface mounted NdFeB permanent magnet ring for the following reasons:

1) Eddy current effects are much more pronounced in solid steel than in sintered permanent magnets due to its higher maximum relative permeability, typically being of the order of several thousand compared to 20 or so, and its higher electrical conductivity, mild steel being 11 times more conductive than sintered NdFeB.

2) The magnetic assembly which is exposed to the pulsed field must be structurally robust and hence a composite structure consisting of a mild steel hub and a permanent magnet would need to have either a tight mechanical fit and/or adhesive bonding between the materials. Prior to each measurement the magnet requires demagnetizing by heating to 320^{o}C for five minutes or so. However, a composite assembly with mild steel within the magnet ring could not be heated to 320^{o}C since the larger coefficent of thermal expansion of the mild steel results in excess stress of the magnet ring with resultant cracking of the ring. Therefore, in order to demagnetize the magnet a complete dissassembly would be required, which would have been an extremely cumbersome and time-consuming process.

It will be seen from fig.3.16 that numerous holes were drilled in the mild steel core so that search coils could be accomodated to measure the flux-linkage between various pairs of holes. These are sufficiently large to necessitate their inclusion in the corresponding finite element model of the problem. Search coils rather than Hall-effect probes were used since the high levels of predicted field viz. up to 5T, are well beyond their limit of linearity, which is typically 1.5T. The search coil voltages were integrated by an analogue integrator and captured on a digital storage oscilloscope, with sub-

sequent downloading to a computer for comparison with the simulation results.

. The axial length of the steel core was limited by difficulties in accurately drilling the holes, since there was a tendency for the drill bit to wander from the desired path when the axial length was increased beyond 30mm. However, the aspect ratio of the constructed core, i.e diameter to axial length, is typical of the motors which form the case studies described in chapter 4. Nevertheless, the feasibility of constructing the core from a number of 10mm long sections was also investigated since this would allow a much longer core to be produced. However, in this case the contact resistance between the individual sections was problematic, and for such a stacked core construction the repeatability of the results was influenced by the clamping force applied. This construction, was, therefore discarded on the basis of the uncertainty regarding the effect of the laminar structure on the flow of eddy-currents. However, the construction of a single piece core prevents the axial variation of flux from being measured other than along the surface.

The initial d.c magnetization curve of the isotropic mild steel, fig 3.17, was measured using a suitably dimensioned toroidal ring (i.d 100mm, o.d 110mm, height 10mm). The d.c electrical conductivity was measured as 7.82×10^6 Sm^{-1} on a 1.2m long bar having a cross-sectional of $60mm^2$. Prior to each pulsed field measurement the mild steel core was demagnetized by placing it between the poles of an electromagnet supplied from a manually controlled biploar d.c supply and exposing it to a slowly deacying alternating field (<< 1Hz). In order to ensure complete demagnetization was achieved the gap between the poles of the electromagnet was gradually increased for low values of the alternating field until the measured alternating flux density at the surface of the steel core was less than ± 2mT. The finite element mesh utilised in the simulation, whose discretization was determined primarily by the need to model the geometry of the individual holes, is shown in fig 3.18.

3.15 COMPARISON OF EXPERIMENTAL AND PREDICTED RESULTS

Long Duration Pulse

Initially the fixture was connected to a magnetizer capacitance of 7000μF in order to produce a time to peak of the fixture current pulse of approximately 0.5ms. To produce the most pronounced eddy-current effects for this time constant, the capacitor voltage was set at 200V, for which the predicted level of the resultant field indicated that there is little saturation in the mild steel during the pulse. A reduction below 200V was not feasible, since the electrical simulation than becomes progressively more difficult as the ignitron turn-on departs from the assumed ideal turn-on. Operation predominantly in the linear region of the material characteristic, although not necessarily representative of the field level required in the magnetization of rare-earth magnets, is a demanding test in terms of material characteristic modelling and the accuracy of the material characterisitic measurement.

The predicted and measured fixture currents, fig 3.19, are in good agreement, both in terms of magnitude and time to peak. The predicted variation of the electrical circuit parameters is shown in fig 3.20, from which it will be noted that the total fixture inductance is only minimally affected by eddy-currents and saturation, partly due to the fact that only a small proportion of the fixture axial length is actually occupied by the mild steel core.

The flux per pole entering the steel was measured using the 5 turn search coil shown fig 3.21 which is wound on the surface of the core. The search coil flux-linkage was predicted at the surface of the core and 0.25mm above the surface in order to account for the measured search coil thickness of approximately 0.25mm. The measured and predicted variation in flux-linkage are in good agreement, as will be seen

in fig 3.22. The flux-linkage predicted from a simulation in which the mild steel was modelled as being non-conducting, is also shown, and clearly illustrates the modifying effect of eddy-currents on the flux penetrating the core, both in terms of its magnitude and the phase shift from the peak of the current waveform.

The measured and predicted flux-linkage for a 5 turn search coil wound between holes E and F, fig 3.23, show reasonable agreement but also certain discrepancies. As discussed previously with regard to the maximum discrete principle, the consistent inertia matrix solution tends to predict non realistic physical phenomena during the intial stages of the pulse. In this case the flux-linkage of the coil predicted at the first time step is of opposite polarity to the applied field, albeit 4 orders of magnitude less than the subsequently calculated positive flux-linkage. This indicates the calculation of a larger reaction field than the applied field. The lumped inertia matrix produces physically reasonable results during the initial transient and contributes negligible additional damping for the remainder of the pulse.

Simulations using both lumped and consistent inertia matrices predict a larger eddy-current screening effect than that measured, as indicated by the slower rise and decay of the flux-linkage and the greater screening during the initial 75μs. During the initial 75μs the simulation predicts negligible penetration of the magnetizing flux to a depth where it links the search coil whilst experimentally a flux-linkage is measured from the moment the pulse is initiated. The distinct change in the measured and predicted slope of the flux-linkage waveforms, which occurs at approximately 65-75μs in both cases, is due to eddy-current shielding as clearly demonstrated in the series of predicted field distributions, fig 3.24.

During the initial 75μs of the transient, the magnetizing flux is confined largely to the surface layer of the core with no significant penetration to the search coil. The

agreement between the measured and predicted instant at which there is a significant change in the flux-linkage of the coil, viz 75μs and 65μs, is within the discrete time step length thus indicating that the simulation is accurately predicting the delay between initiation of the pulse and significant penetration of the field to the search coil. The over-estimation of eddy current screening of the search coil is primarily due to the two-dimensional nature of the finite element model. The eddy-currents in the finite element formulation consist only of an axial component, whereas in practice the eddy current flow is three-dimensional, as shown schematically in fig 3.25. The three-dimensional nature of the eddy current flow results in less shielding near the ends of the core, and hence a measurable search coil flux-linkage due to end-effects during the period when the central region of the coil is almost completely screened.

A further limitation of the two-dimensional model is its inability to model fringing flux-linkage with the search coil produced by regions of the fixture winding situated beyond the axial length of the core, fig 3.26. There is strong tendency for this fringing to occur because the permeability of the bulk of the core is high at the predicted levels of flux density, although eddy currents induced in the core will to an extent inhibit fringing.

Decreasing the number of time steps to model the same period has only a small effect on the predicted flux-linkage of the coil EF, fig 3.27. This relative insensitivity to the time step is an indication that the maximum discrete principle is not being violated. The number of total non-linear iterations required to obtain the field solutions does not increase linearly with the number of time steps, fig 3.28, since a reduced time step length gives a better starting approximation for the following time step. The lack of any significant saturation and hence non-linearities results in fairly rapid convergence for this case. The apparent agreement between the simulation with 10 time steps and the measured waveform during the initial 100μs period is due to the resolution of

the simulation time steps being insufficient to model the initial stages of the transient.

There is a large discrepancy between the measured and predicted flux-linkage of a search coil located between holes F and G. The comparison of fig 3.29, in which the two waveforms are plotted to different vertical scales due to their widely differing magnitudes, shows little correlation in terms of either magnitude or form. The measured flux-linkage waveform does not exhibit a sudden change in slope, as occurs for the flux-linkage waveform for coil EF, and has only a small phase shift from the fixture current. This implies either that there is only a small eddy-current screening effect, a phenomena not consistent with its position within the steel core and the observed behaviour of the flux-linkage with coil EF, or that the search coil is completely screened and the measured flux-linkage is due entirely to end-effects, which is consistent with the simulation results and the lack of a pronounced change in slope of the measured flux-linkage. The axially directed contribution to the flux-linkage of the various search coils was estimated by measuring the flux-linkage with the search coil which is shown in fig 3.30 which measures the axial flux entering a pole at one end of the core through the area bounded by holes EAIJ.

The calculation of the proportion of the measured total axial flux on the end surface of the core which links any of the test search coils requires its subsequent distribution within the core to be known. In practice, the distribution of the fringing magnetizing flux is complex and involves a consideration of the full three-dimensional eddy current flow and the effects of localized saturation. The measured flux-linkage with the end search coils which is shown in fig 3.31, can therefore only be regarded as being indicative of the magnitude of the end effects rather than providing an absolute correction to any of the search coil flux-linkages presented previously .

Increasing the initial capacitor voltage to 800V, whilst maintaining a constant

capacitance and hence time constant, results in a higher level of saturation in the steel core and improved agreement between the predicted and measured current and flux-linkage waveform with search coil EF, fig 3.32 and fig 3.33 respectively. This improvement can be attributed to the higher degree of saturation in the steel reducing the tendency for the magnetizing flux produced by the conductor regions outside the axial length of the core to fringe into the core, thus resulting in a more two-dimensional field system. Compared to the unsaturated case of fig 3.23, there is a reduction in the delay between initiation of the magnetizing pulse and the distinct change observed in both the measured and predicted flux-linkage waveforms of coil EF, which is indicative that flux now penetrates the previously screened search coil. This is due to the extreme saturation of the surface layer of the core in which the magnetizing flux is intially confined, forcing the field to penetrate more rapidly into the bulk of the steel than in the unsaturated case.

The predicted rapid saturation of selected elements near the surface of the core is shown in the post-processor output of fig 3.34, which also shows the large spread in peak flux densities achieved in the core. The good agreement between measured and predicted results is particularly encouraging given that these levels of saturation are more typical of those encountered in the pulsed magnetization of rare-earth permanent magnets. However, a consequence of the higher saturation is larger number of iterations which are required to solve the field distributions compared to the 200V case, fig 3.35.

Effect of Hysteresis

The measured major d.c hysterisis loop of the mild steel, fig 3.36, has a coercivity of 1560 A/m which is comparatively large for a soft magnetic material. Thus, the application of a magnetizing pulse to the steel will result in some residual magnetism following the decay of the pulse, and hence during the application of subsequent pulses

the working points of the material will not follow the initial magnetization curve as is assumed in the simulation. To prevent this form happening, the steel was demagnetized for each measurement.

However, in order to assess the effect of hysteresis on the penetration of the magnetizing field, the core was magnetized by exposing it to a series of uniform pulses. After a number of pulses the steady state behaviour is achieved and the excursion of the working points within the steel follow the same locii for all subsequent pulses and a repeatable flux-linkage waveform from the search coils is obtained.

The measured flux-linkage from coil EF for an initial capacitor voltage of 800V is significantly different for the magnetized and demagnetized samples, fig 3.37. However, even in the residually magnetized state, negligible external field was measured with a Hall probe positioned at the surface of the core. Therefore, if the steel is represented by a single working point this would suggest that the working point is at or very near to the coercivity. However, the measured magnetization curve traversed from an initial starting point at the coercivity, fig 3.38, is not sufficiently different from the initial magnetization curve to account for the large measured difference in flux-linkage observed in fig 3.37. However, the difference can be attributed to localised variations in residual magnetization within the core, which are not measurable externally. Indeed, the much better correlation between the measured and simulated waveforms than between the two measured waveforms for different initial conditions of remanent magnetism shows the importance of modelling the dynamic nature of the permeability in the simulation.

Short duration pulse

Reducing the capacitance to 150μF produces a time to peak for the current waveform of approximately 85μs. Two levels of initial capacitor voltage were selected

to produce the same magnitudes of current pulses as for the 0.5ms rise time pulses described above, viz 780V for 2000A and 3200V for 8000A. The measured flux per pole entering the central 10mm axial section of the core for an initial capacitor voltage of 780V, fig 3.39, has a considerable phase shift from the current waveform, and its peak magntiude is reduced considerably from that measured for the 0.5ms rise time current pulse of the same magnitude, viz 0.564mWb and 0.842mWb respectively. The measured and predicted waveforms of the flux per pole for the central 10mm of the core, show close correlation during the time period up to the peak of the fixture current. Despite the large eddy current effects, as evidenced by the large phase shift and attenuation of the search coil flux-linkage, the simulation is accurately predicting the flux which enters the mild steel core and hence its effect on the inductance of the fixture.

Less satisfactory correlation exists between the simulated and measured waveforms as the field decays. This can largely be attributed to the fact that the dynamic behaviour of the mild steel is based on an initial magnetization curve only, and eddy current phenomena during the reduction of the magnetizing field within the mild steel are strongly influenced by the permeability. The relatively large coercivity of the steel dictates that the recoil permeability is considerably different from that deduced from the initial magnetization curve for the corresponding value of magnetizing field strength. However, this is only critical for field levels around or below saturation, when the recoil permeabilities are significantly different from the permeability of the inital magnetization characteristic.

The measured and predicted flux-linkage of search coil EF is shown in fig 3.40. There is a significant difference between the waveforms, although the instants at which there is a marked change in slope of the waveforms are coincident within one discrete time step. Thus, the screening of the bulk of the search coil is being accurately

modelled, the measured flux-linkage during the screening interval being predominantly a result of end-effects. The measured and predicted peak flux-linkage are also in good agreement, viz 0.564mWb and 0.542mWb respectively, although there is a significant difference in the instant at which this peak occurs, viz 220μs and 275μs respectively. This is due to the end-effect contribution in the measurements, which has a reduced phase shift from the current waveform. During the period after the field has penetrated to the search coil location, there is a significant error between the measured and predicted flux-linkage, e.g there is an error of 24% at 100μs, which corresponds to 0.11 mWb.

In this case the flux-linkage over the central section of the core is reduced by eddy-current effects to an extent where the end-effects become a significant fraction of the total flux-linkage of coil EF. The simulation of a short duration pulse requires slightly more iterations per time step than the corresponding simulation for the 0.5ms pulse, as shown in fig 3.41. This additional iteration of the field solution, which is indicative of an increase in the overall non-linearity, is due to the higher predicted flux densities and hence saturation resulting from the increased skin effect.

Increasing the capacitor voltage to 3200V produces a current pulse with a measured peak of 8080A. The measured and predicted flux-linkage waveforms of a search coil EF are shown in fig 3.42. As is the case with the longer duration pulse, there is an improved correlation between the measured and predicted waveforms compared to the 2000A current pulse. The error during the decay of the field is greatly reduced, since the recoil permeability of the initial magnetization curve and the saturated hysteresis loop are in good agreement above to 2T or so.

3.16 VALIDATION CONCLUSIONS

From the experimental validation, the results of which are summarised in fig 3.43, the following conclusions can be drawn:

1) There is good agreement between the measured and predicted total flux per pole which enters the core and its distribution within the core over a wide range of time constants and applied field levels.

2) The correlation between the measured and predicted results improves as the degree of saturation within the mild steel increases.

3) The simulation overestimates the effect of eddy currents due to it being based on a two-dimensional model in which the non-linear material characteristic is represented as a single initial magnetizing curve, even under recoil conditons.

4) The magnetic history of the mild steel has a significant bearing on its performance during transients which induce significant eddy-currents.

5) The spatial discretization of the mesh was sufficiently fine to allow time steps as short as 3.4μs to be used with no apparent contravention of the maximum discrete principle, since the results were largely insensitive to the time step and the lumping of the inertia matrix.

6) The use of a Newton-Raphson method raises the question of stability since the Newton-Raphson method, in common with a number of other solution methods, is based on derivitives of the functions, and is susceptible to instability when the derivitives approach zero. In a large mesh with non-linear materials, which may contain a number of inflections in the derivative quantities of their B-H characteristics, the number of degrees of freedom and the non-linearity make any formal mathematical

statement of a stability criteria for each nodal derivative unfeasible. However, the results of this validation have demonstrated that the simulation converges for a wide range of saturation levels, time steps and number of time steps per solution with no hint of instability. Thus on the basis of this validation the simulation appears to be robust, however, due to its problem depenant nature, the unconditional stability of the method cannot be guaranteed.

7) The role of end-effects has been clearly demonstrated by the measurement of the axial fringing flux. The correlation between the actual and the predicted field over the central region of the core is, therefore, likely to be better than was the case with the measured and predicted results discussed previously.

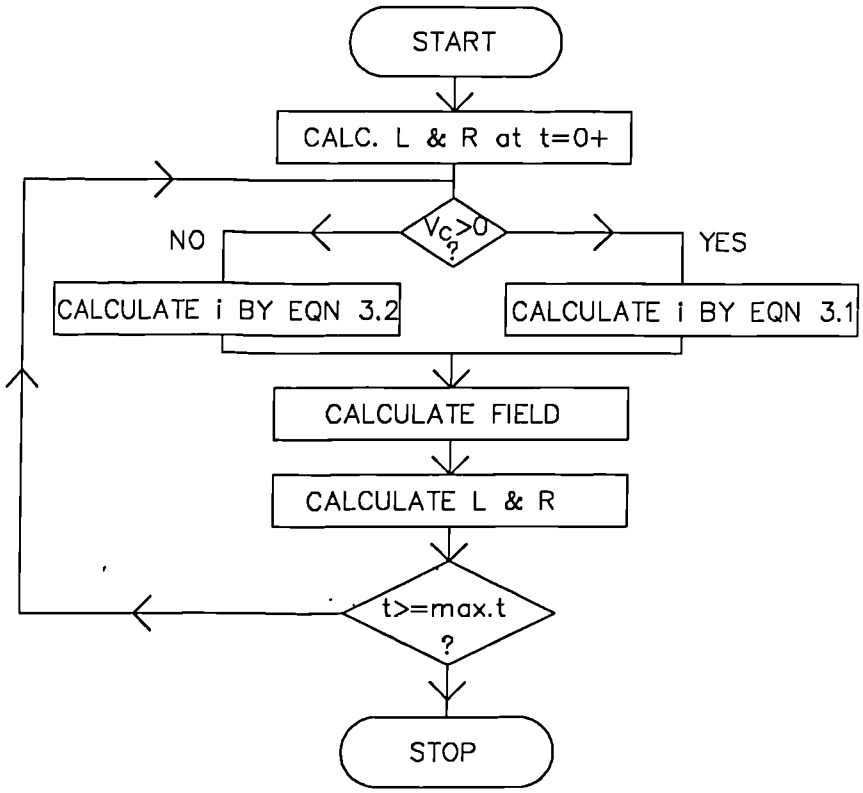

Fig. 3.1 Flowchart of the simulation method.

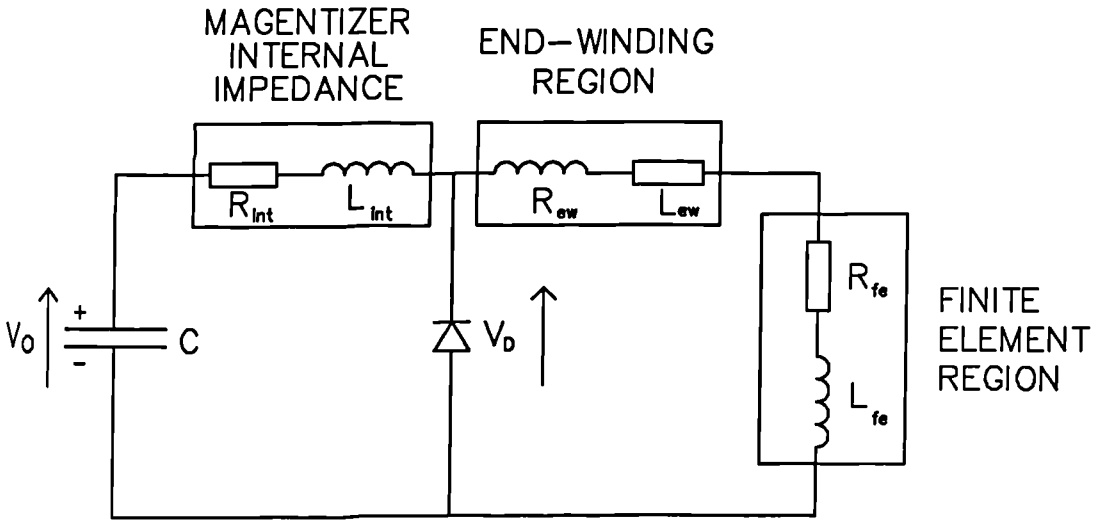

Fig. 3.2 Magnetizer / fixture equivalent circuit.

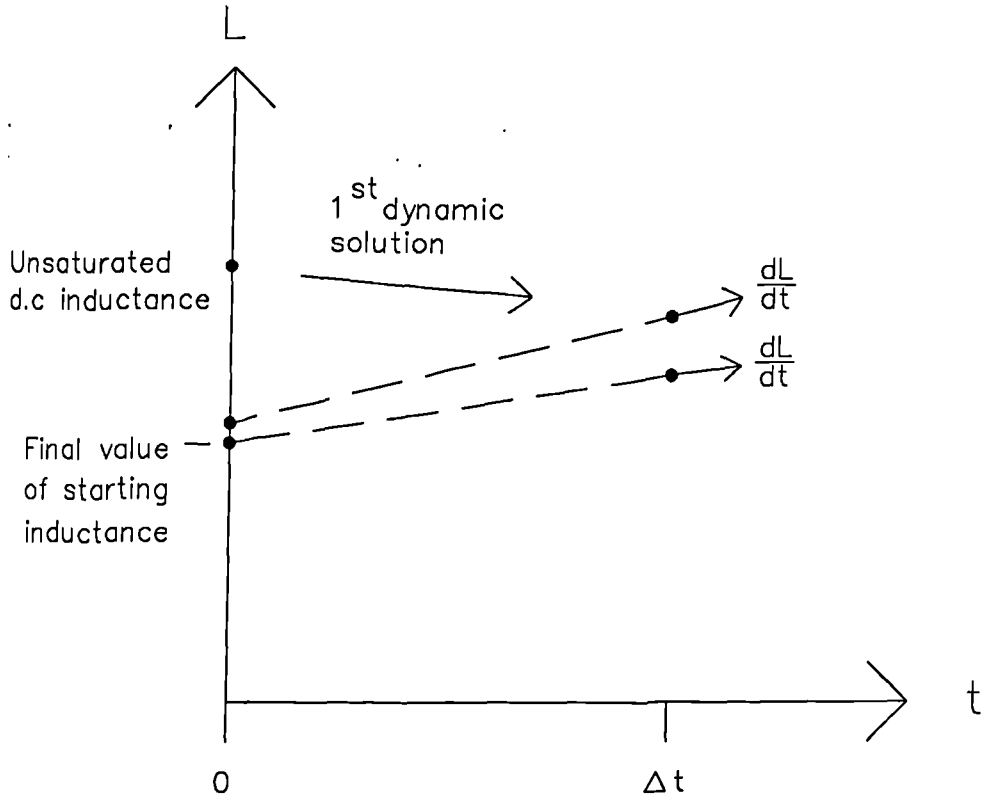

Fig. 3.3 Iterative scheme for the calculation of the fixture inductance at t= 0+.

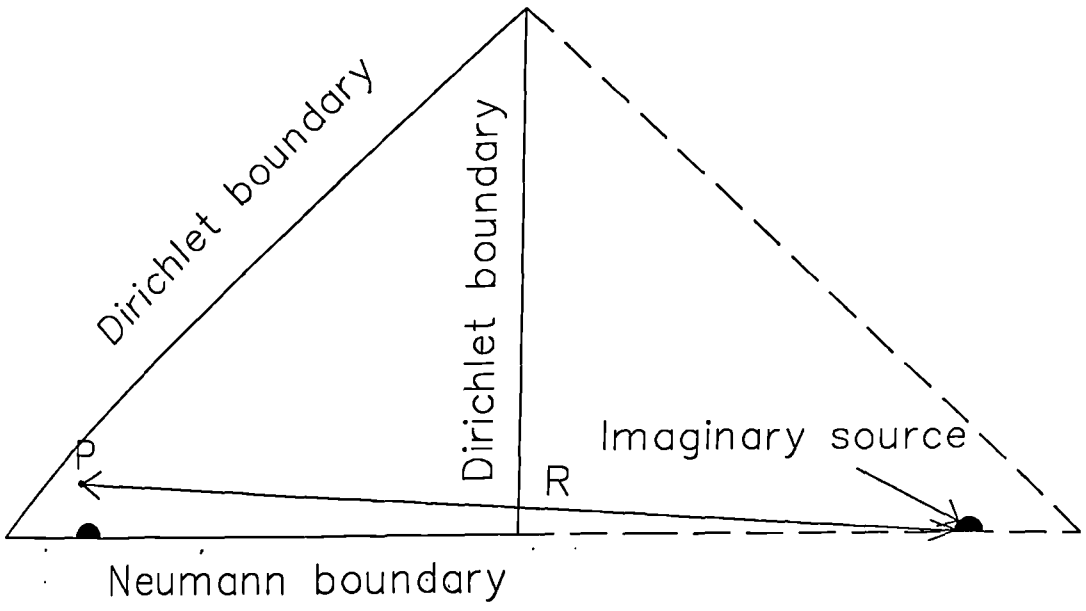

Fig. 3.4 Representation of an open boundary by imposition of a Dirichlet boundary condition at a finite distance from the region of interest in a 4-pole fixture.

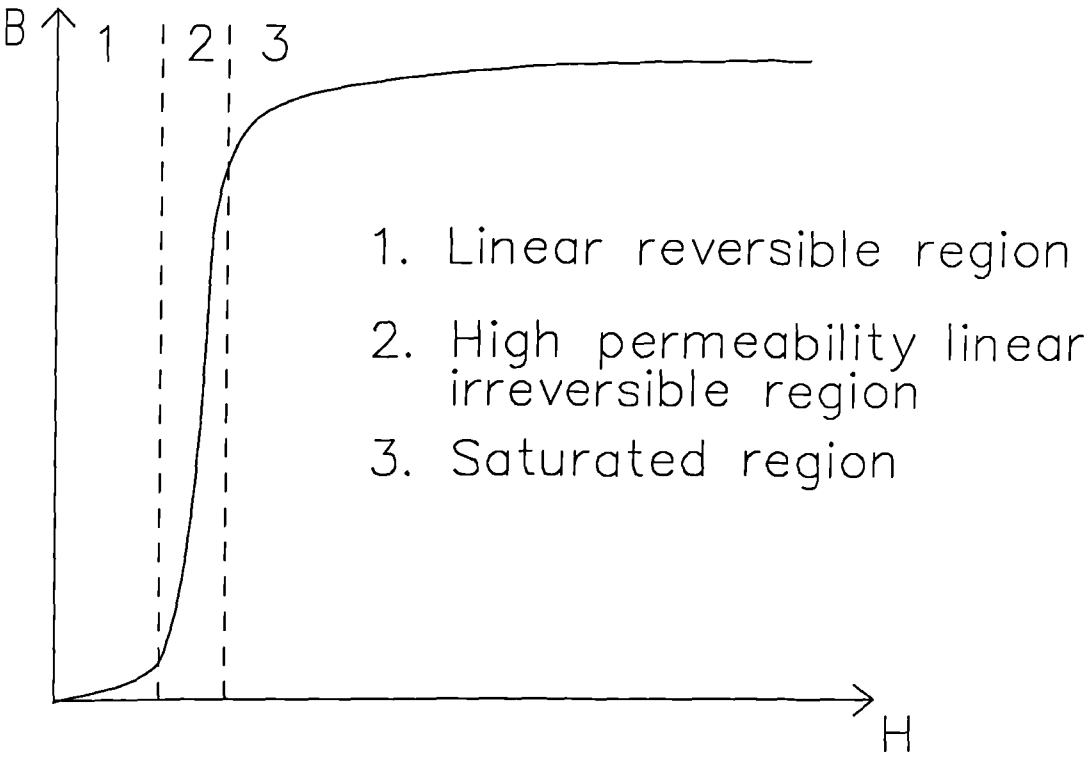

Fig. 3.5 Typical initial magnetization curve of a soft magnetic material. (The irreversible region has been extended to aid clarity).

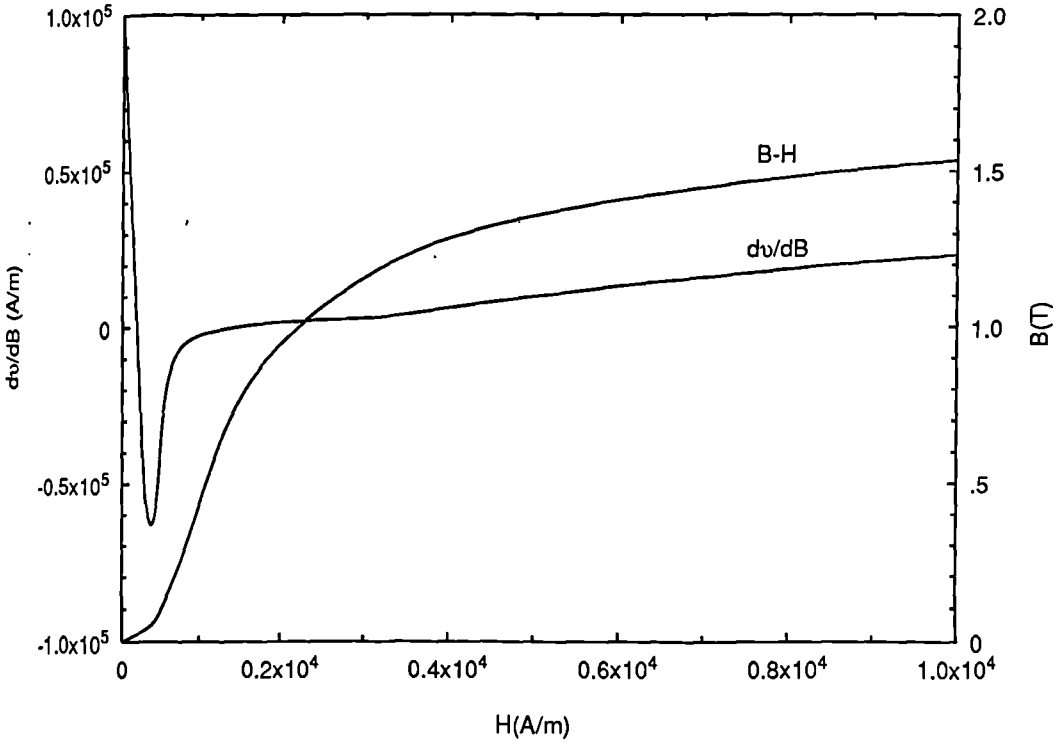

Fig. 3.6 Measured initial magnetization curve and derived variation of the differential

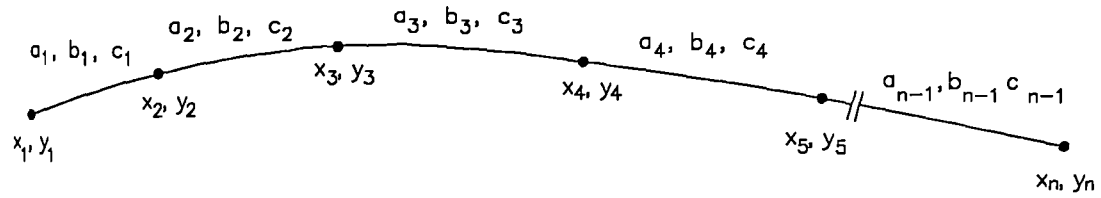

for $x_n < x < x_{n+1}$

$$y = a_n (x-x_n)^3 + b_n(x-x_n)^2 + c_n (x-x_n) + y_n$$

Fig. 3.7 General form of a smooth cubic-spline curve fit.

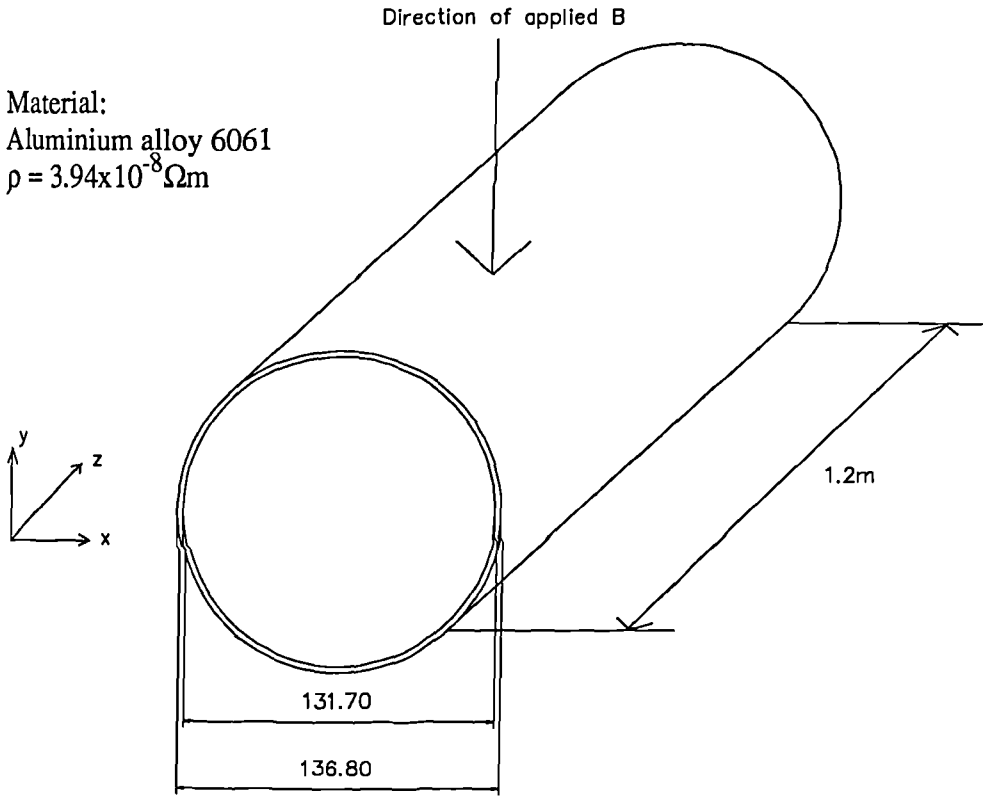

Fig. 3.8 The "FELIX" cylinder (axial length not to scale).

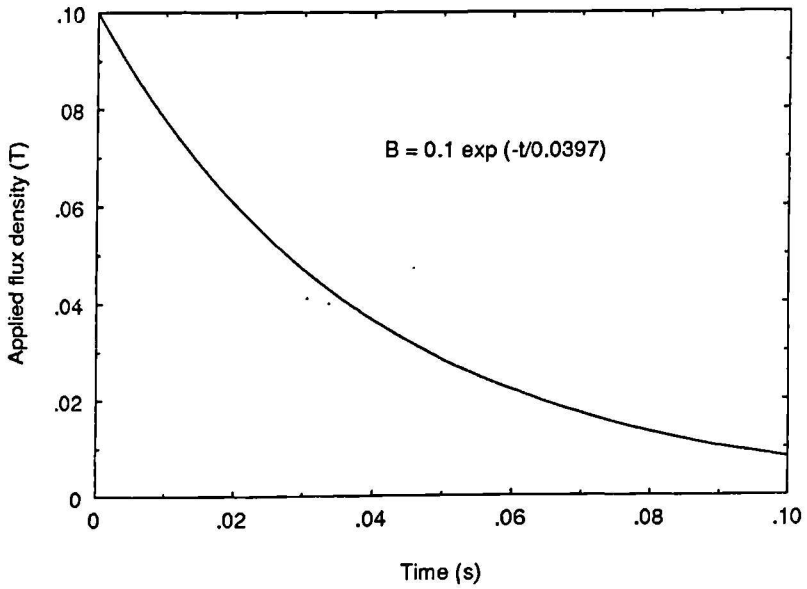

Fig. 3.9 Variation of the applied flux-density in the FELIX benchmark problem.

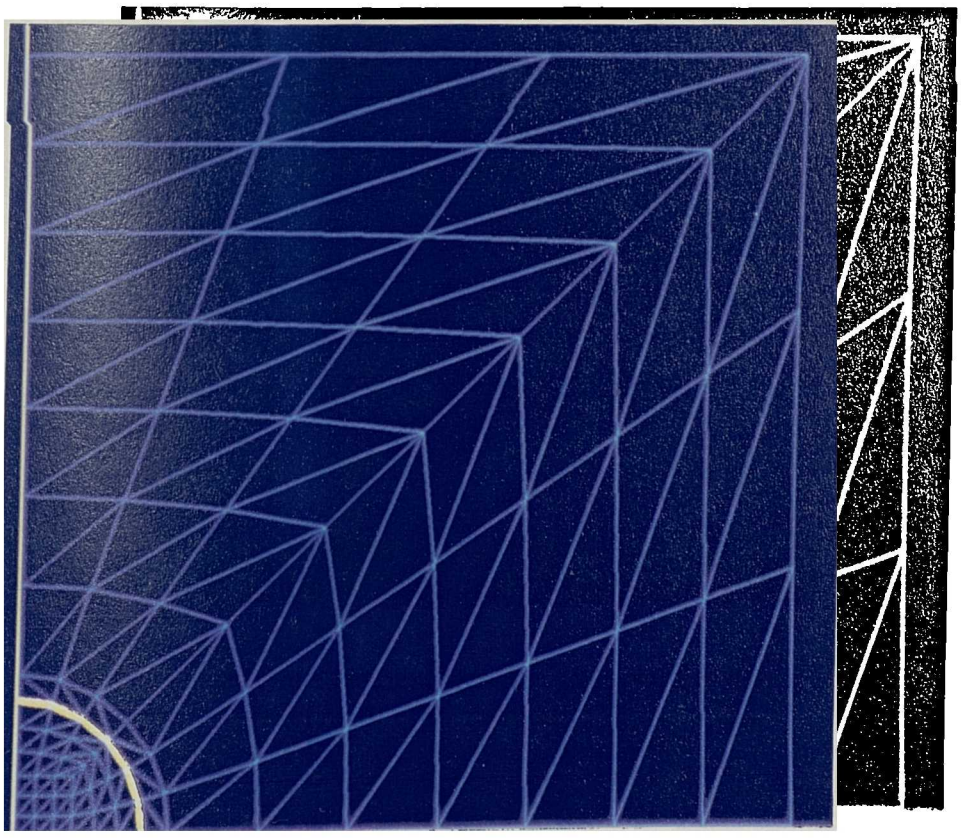

Fig. 3.10 Recommended finite element mesh for the solution of the FELIX benchmark (186 elements).

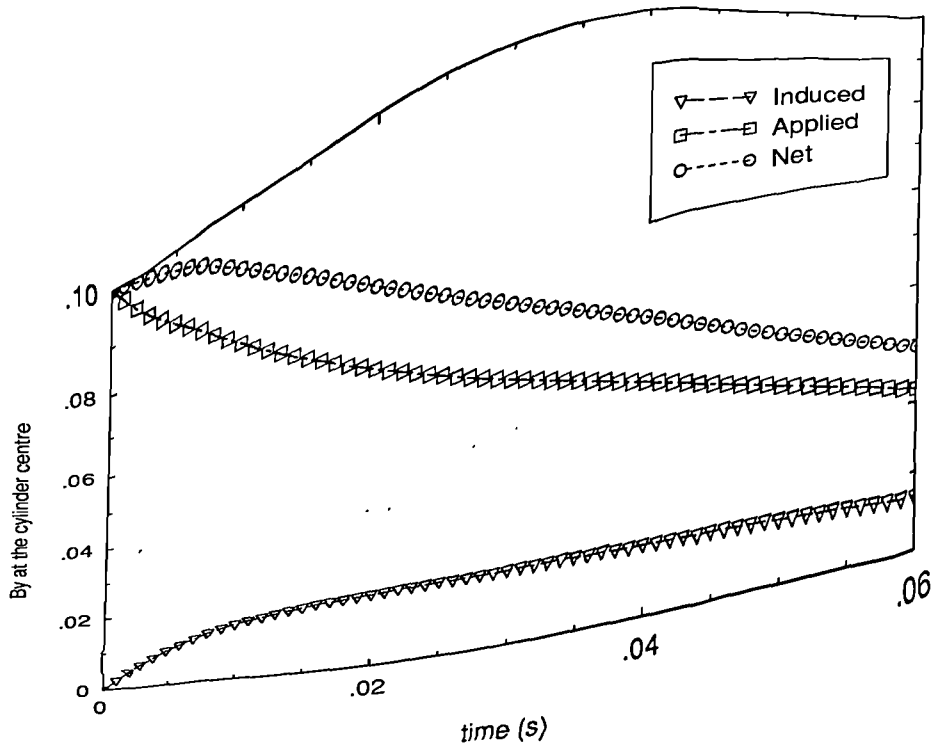

Fig. 3.11 Predicted applied, net and induced flux-density waveforms at the cylinder centre for a 1ms time step.

Time step /ms	t = 10ms	t = 20 ms	t = 40 ms
0.50	0.0133	0.0149	0.0108
1.00	0.0131	0.0148	0.0108
1.667	0.0128	0.0147	0.0109
2.00	0.0127	0.0147	0.0109
2.50	0.0126	0.0146	0.0109
5.00	0.0118	0.0142	0.0111

Fig. 3.12 Variation of the induced flux-density component By at the centre of the cylinder for a range of time steps and the original recommended mesh.

Mesh	t = 10ms	t = 20ms	t = 40ms
Original	0.0131	0.0148	0.0108
Refined	0.0134	0.0154	0.0115

Fig. 3.13 Variation of the induced flux-density component By at the centre of the cylinder for the original and refined mesh with a time step of 1ms.

Method	t = 10ms	t = 20ms	t = 40 ms
Dynamic Simulation	0.0133	0.0149	0.108
PE2D two-dimensional finite element (Diserns [3.15])	0.0133	0.0148	0.107
Measured [3.15]	0.0114	0.0128	0.0098
Range of submitted results	0.0113-0.0146	0.0128-0.0166	0.0098-0.0123

Fig. 3.14 Comparison of calculated results with published data.

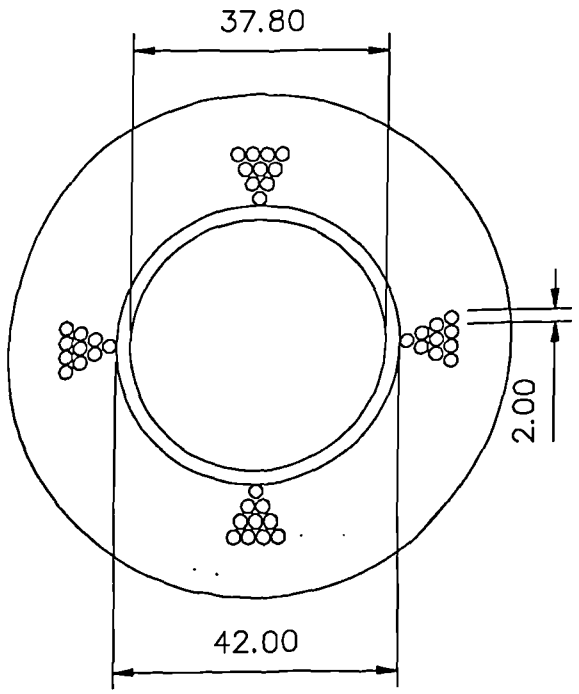

Fig. 3.15 4-pole magnetizing fixture used for the experimental validation.

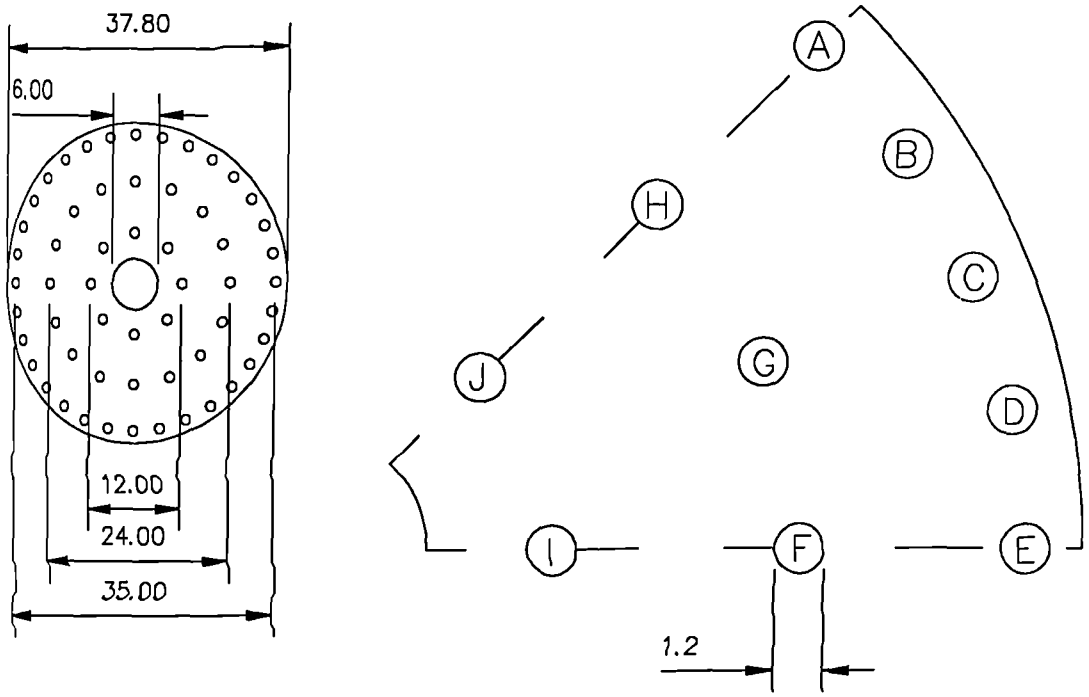

Material: EN1A mild steel
Axial length = 30mm

Fig. 3.16 Cross-section through the test core.

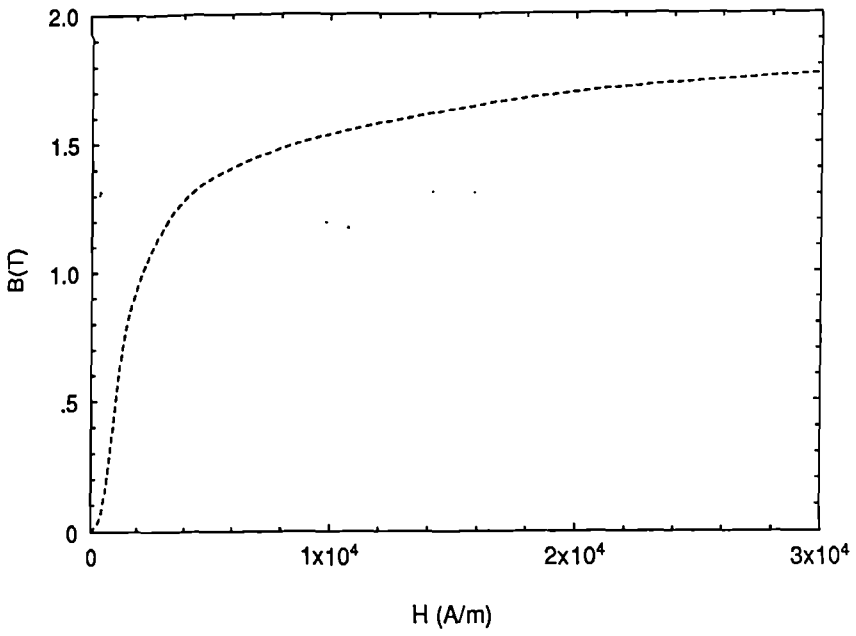

Fig. 3.17 Measured initial magnetization curve of EN1A mild steel.

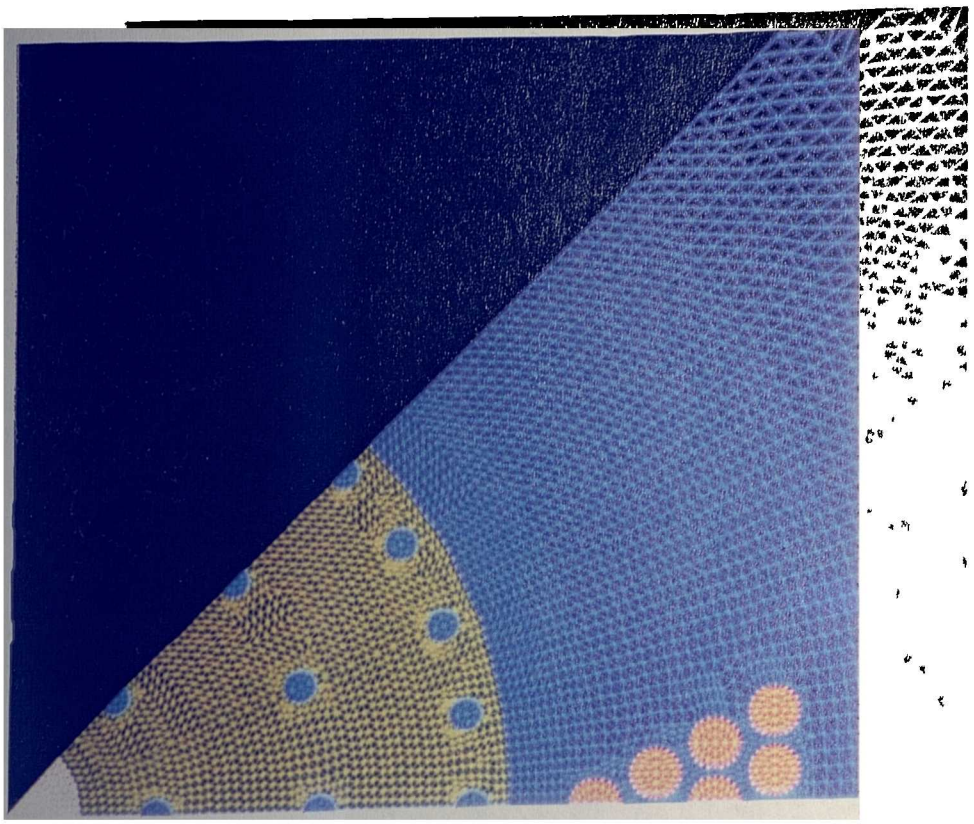

Fig. 3.18 Close-up of the core region in the finite element mesh used for the dynamic simulations. (Total elements = 7876, total nodes = 4077).

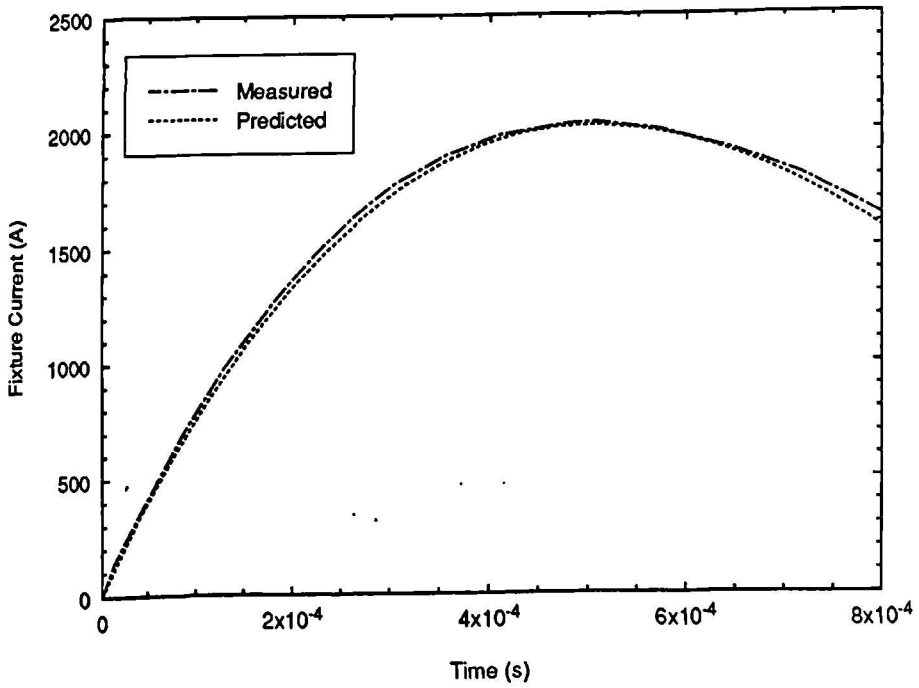

Fig. 3.19 Comparison of the measured and predicted fixture current (C = 7000μF , V = 200 V).

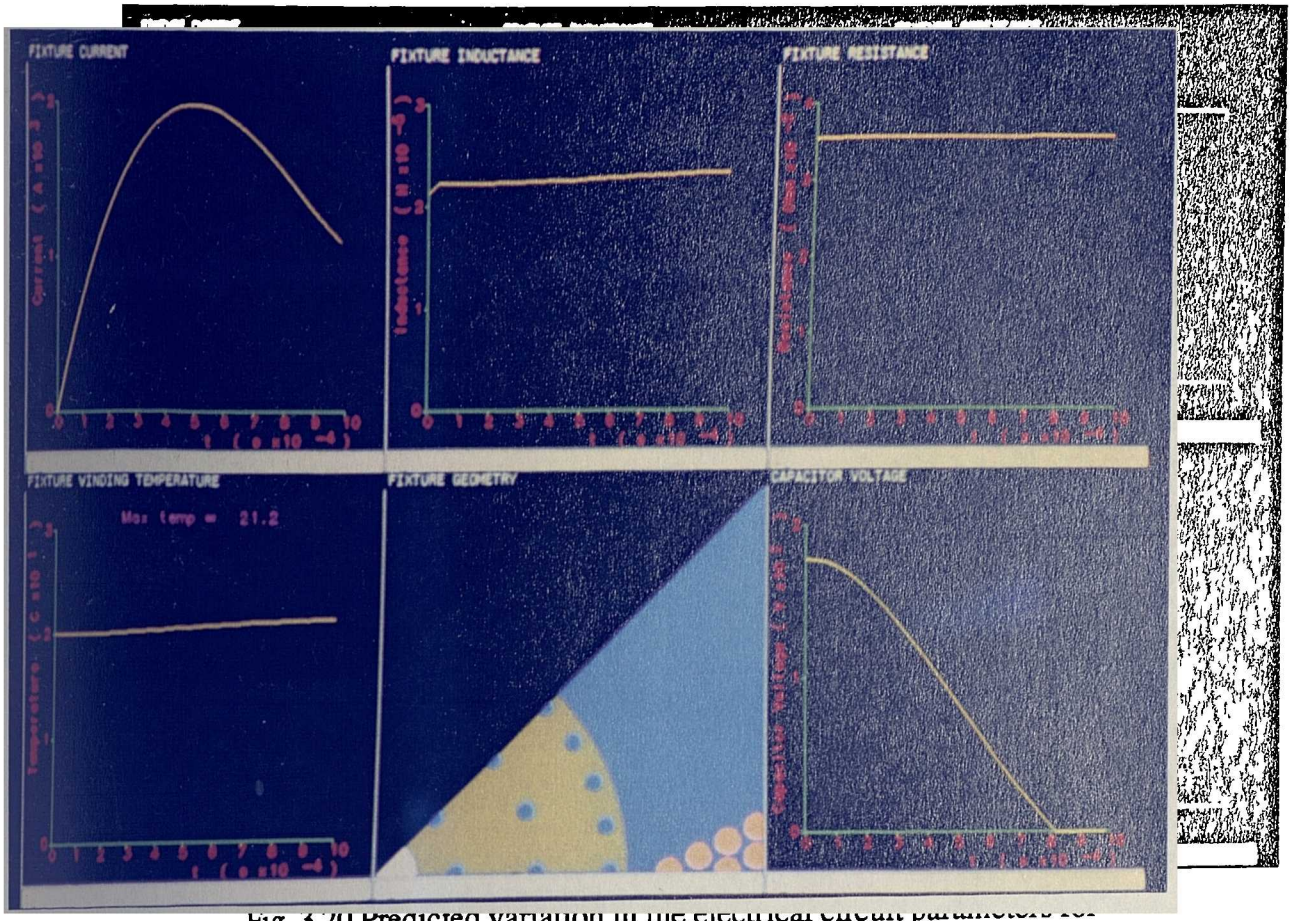

Fig. 3.20 Predicted variation in the electrical circuit parameters for C=7000uF, V= 200V

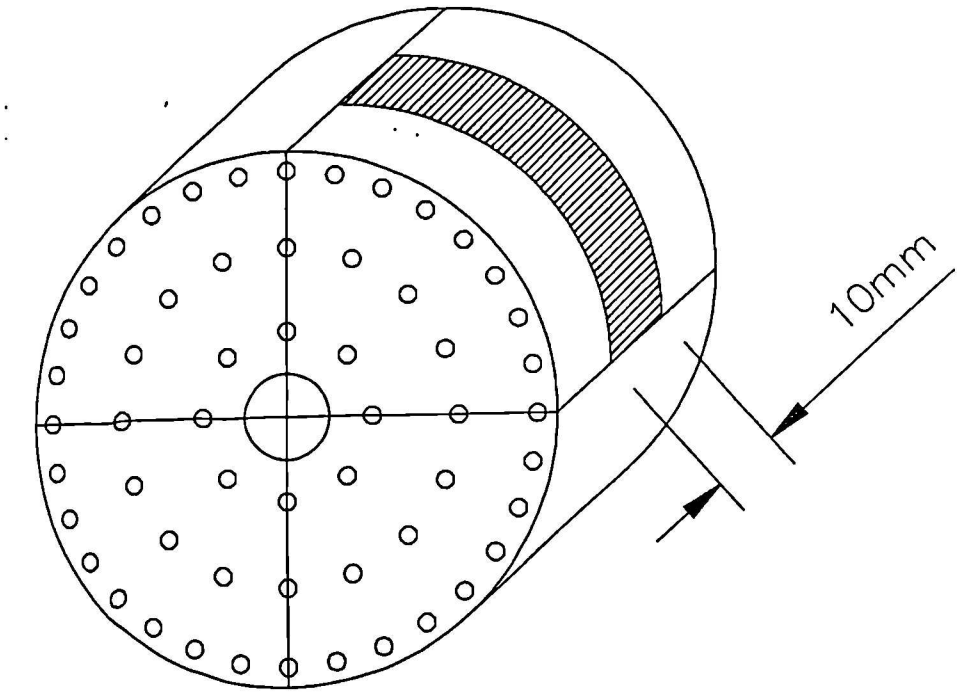

Fig. 3.21 Search coil for measuring the flux per pole entering the central region of the core.

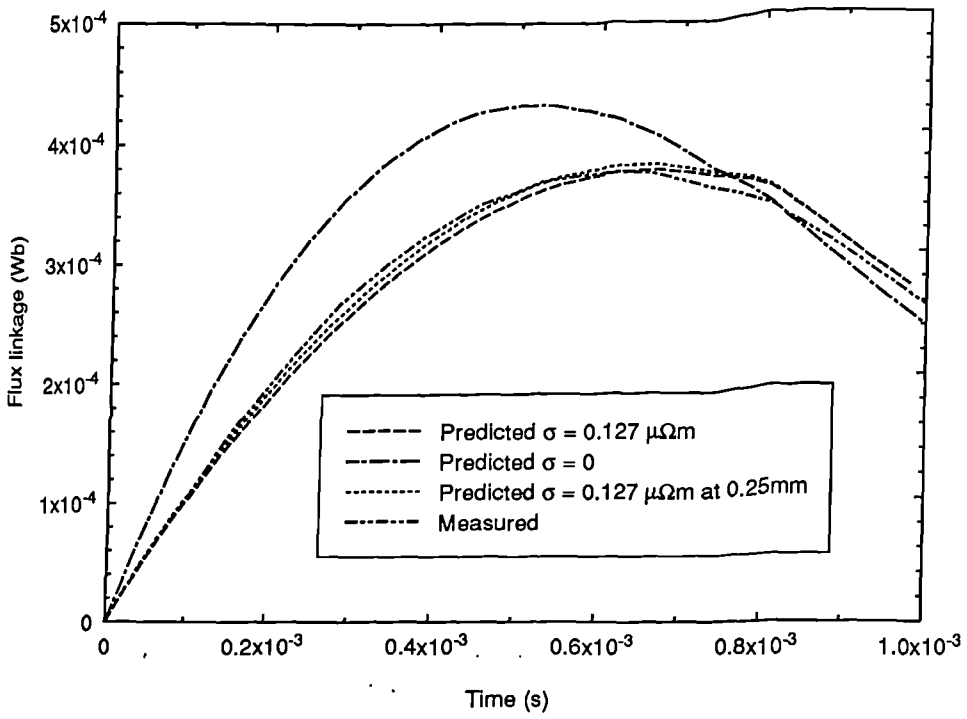

Fig. 3.22 Comparison of the measured and predicted flux-linkage of the search coil of fig 3.21. (C = 7000 μF, V= 200V).

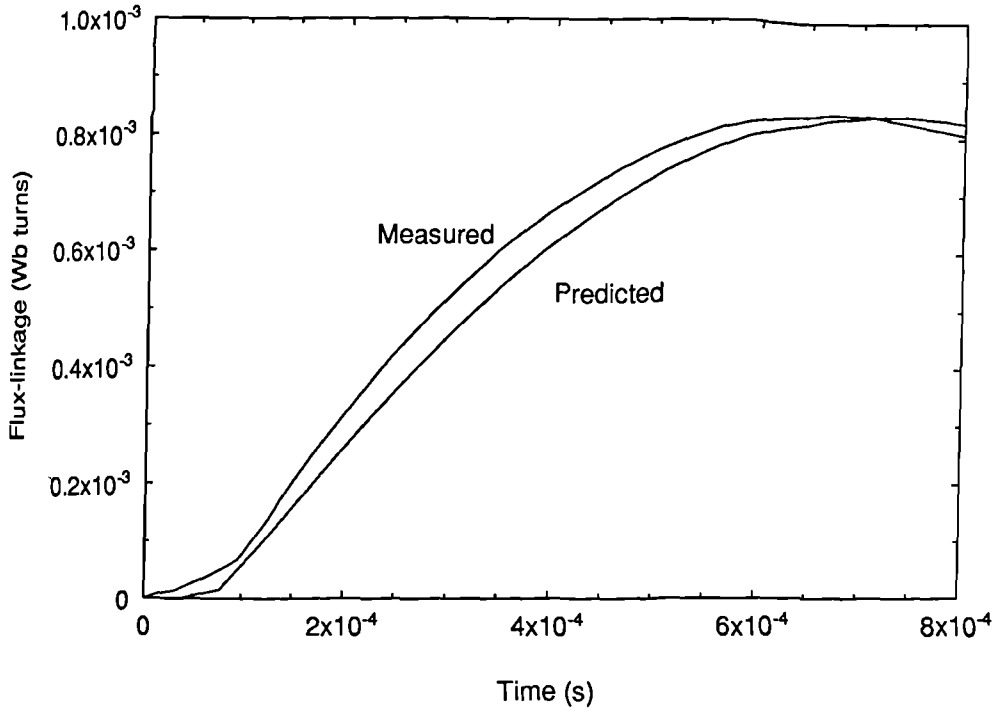

Fig. 3.23 Comparison of the predicted and measured flux-linkage of a 5 turn search coil wound between holes E and F in the steel core. (C = 7000 μF, V= 200V).

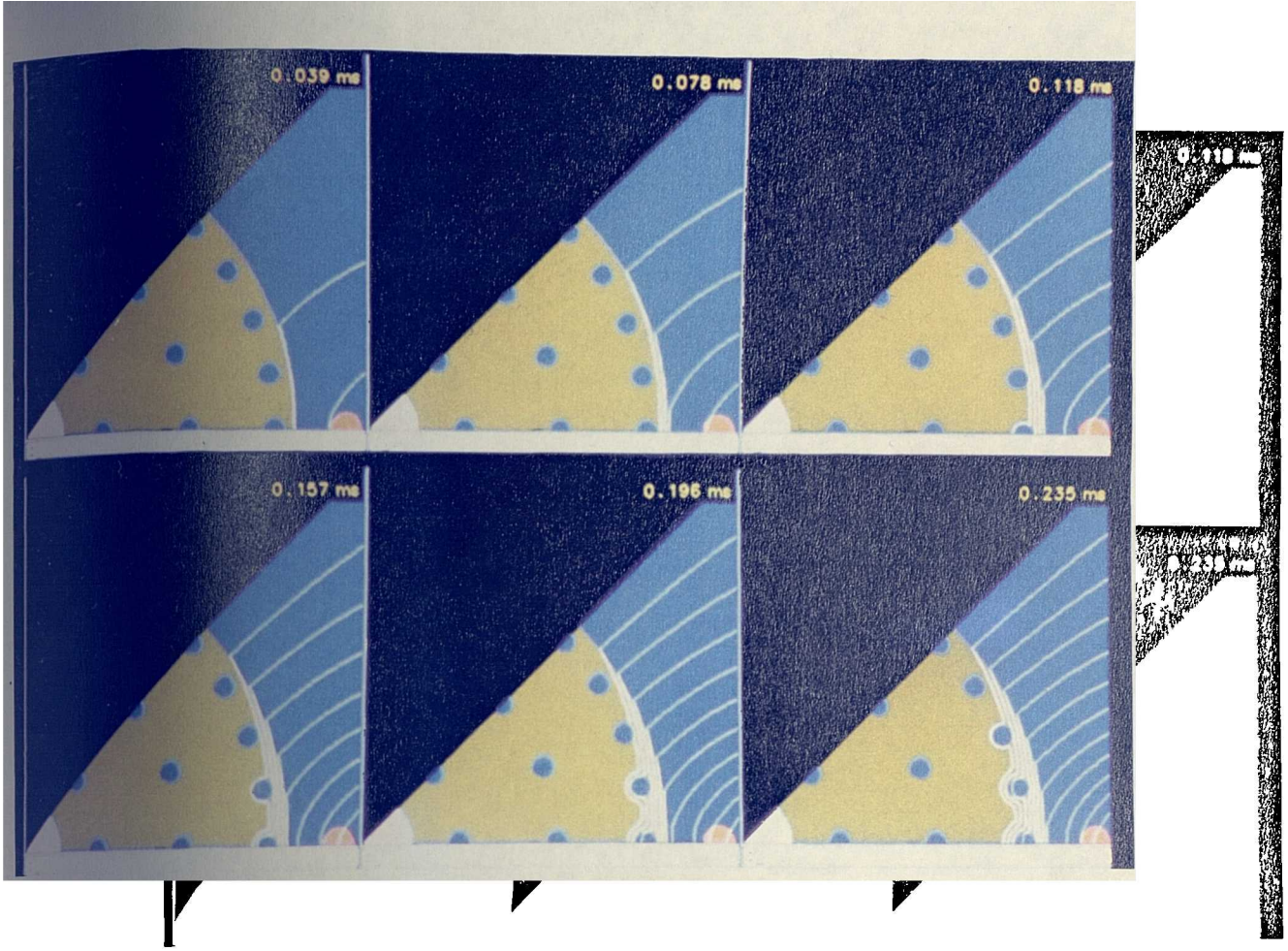

Fig. 3.24 Predicted field distributions during the impulse period.
(C = 7000 μF, V= 200V).

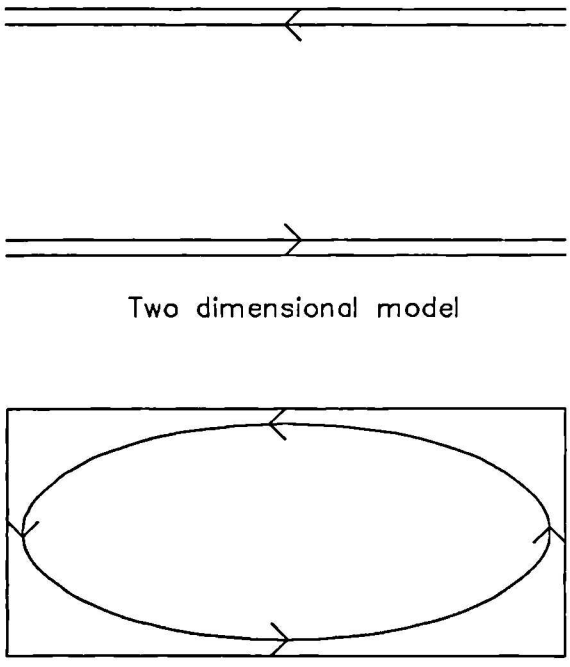

Fig. 3.25 Schematics of eddy-current flow in one pole of the steel core.

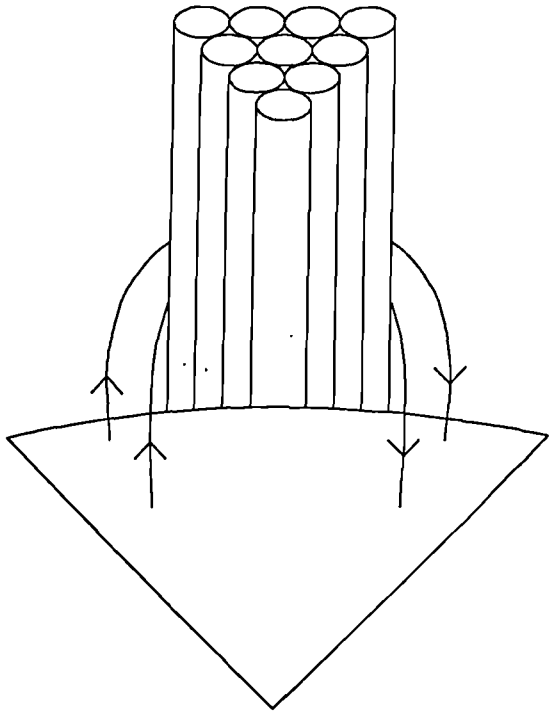

Fig. 3.26 Schematic of axial fringing flux into the steel core from the overhanging fixture conductors.

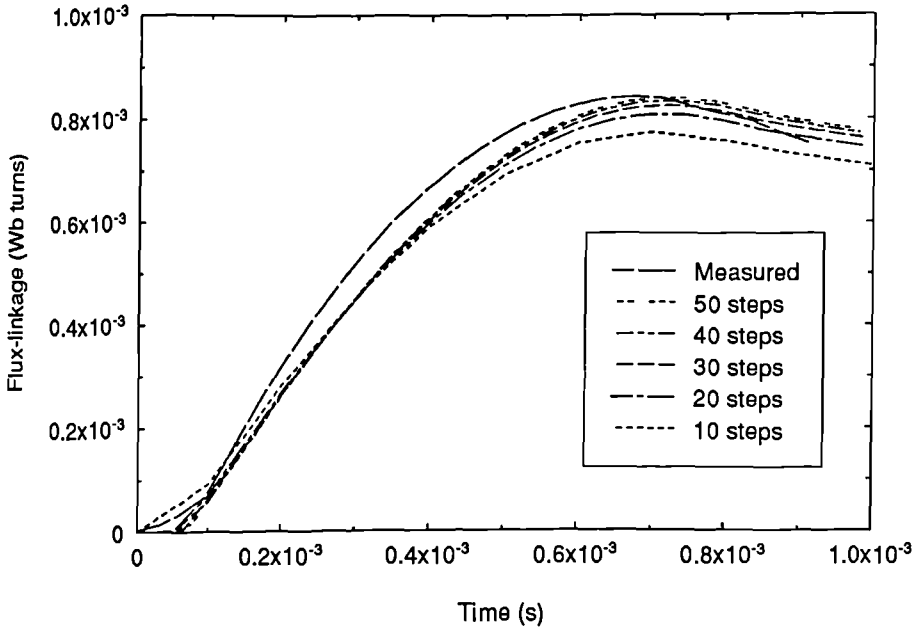

Fig. 3.27 Effect of the time step duration on the predicted flux-linkage of a 5 turn search coil wound between holes E and F of the steel core. (C = 7000μF, V= 200V). (Total Simulation duration =1ms)

Number of time steps	Time step length (ms)	Total Iterations	Iterations per time step
10	0.1	74	7.40
20	0.0495	125	6.25
30	0.0328	172	5.73
40	0.0245	210	5.25
50	0.0196	259	5.18

Fig. 3.28 Comparison of total field solution iterations required for a simulation period of 1ms (C= 7000μF, V = 200V).

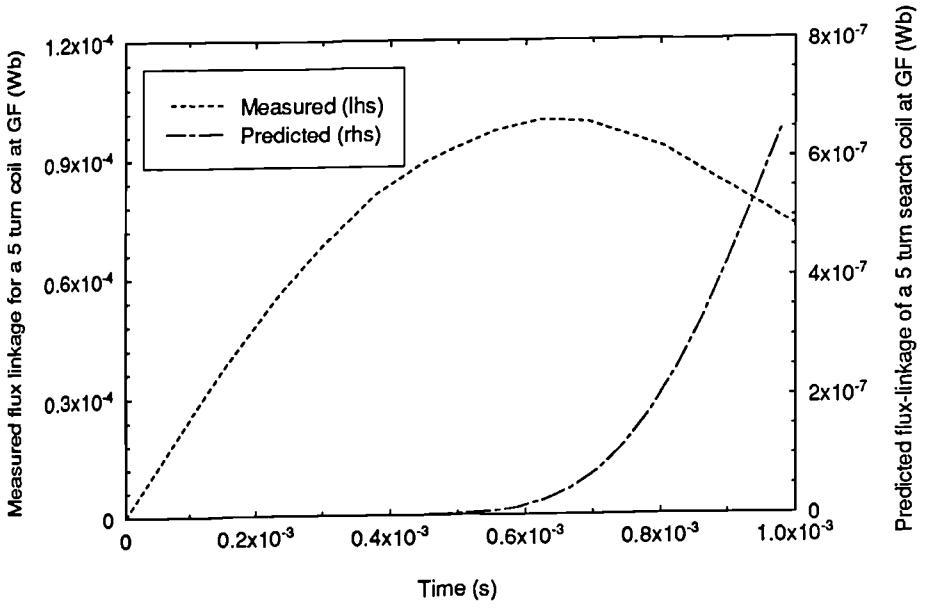

Fig. 3.29 Measured and predicted flux-linkage of a 5 turn search coil wound between holes F and G.

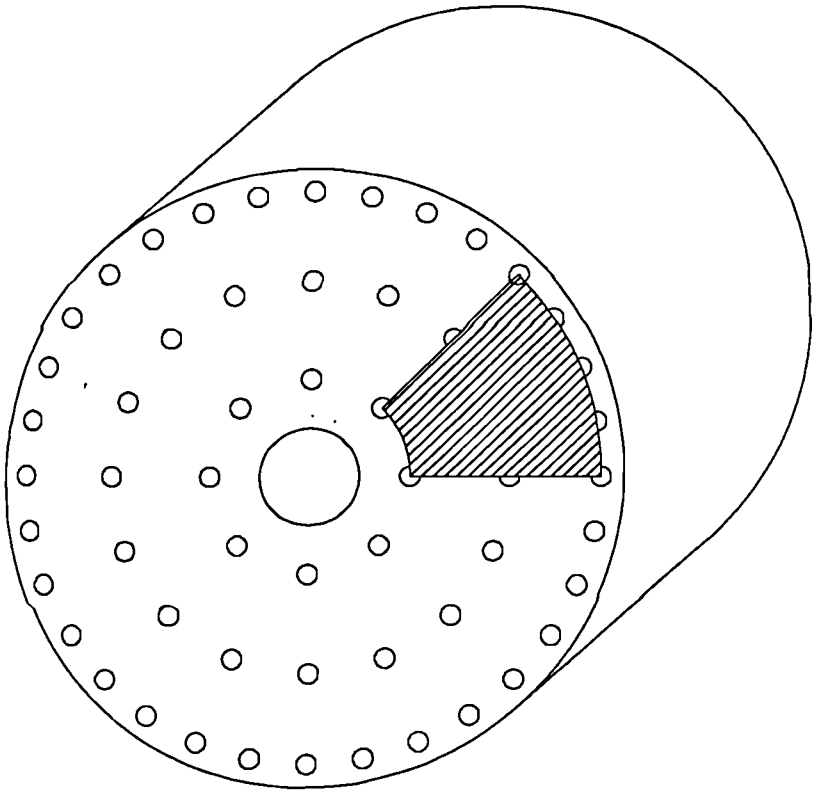

Fig. 3.30 Search coil arrangement for the measurement of axial fringing flux.

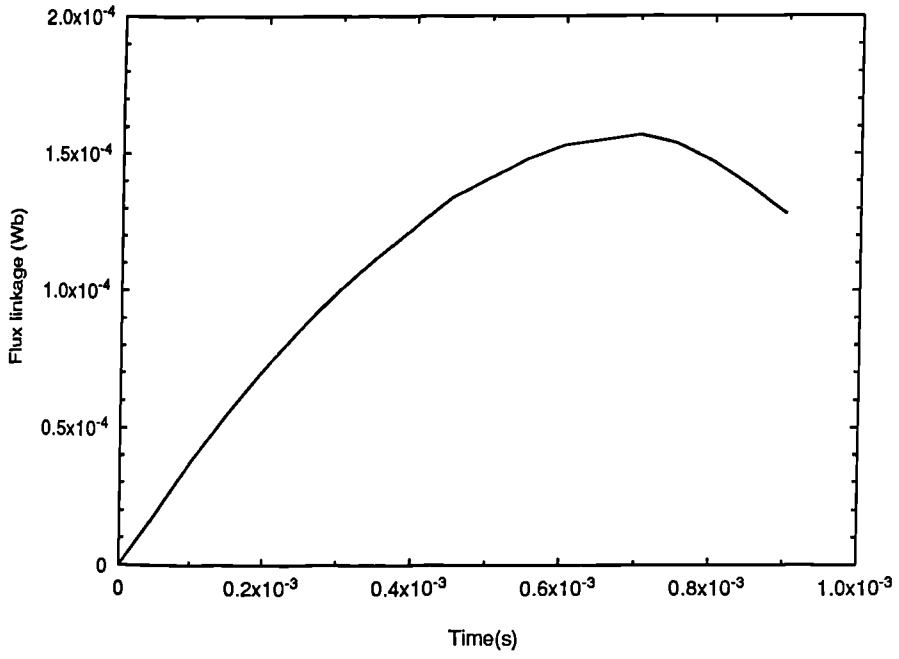

Fig. 3.31 Sum of the measured flux-linkage for two coils such as in fig 3.30 on either end of the core .

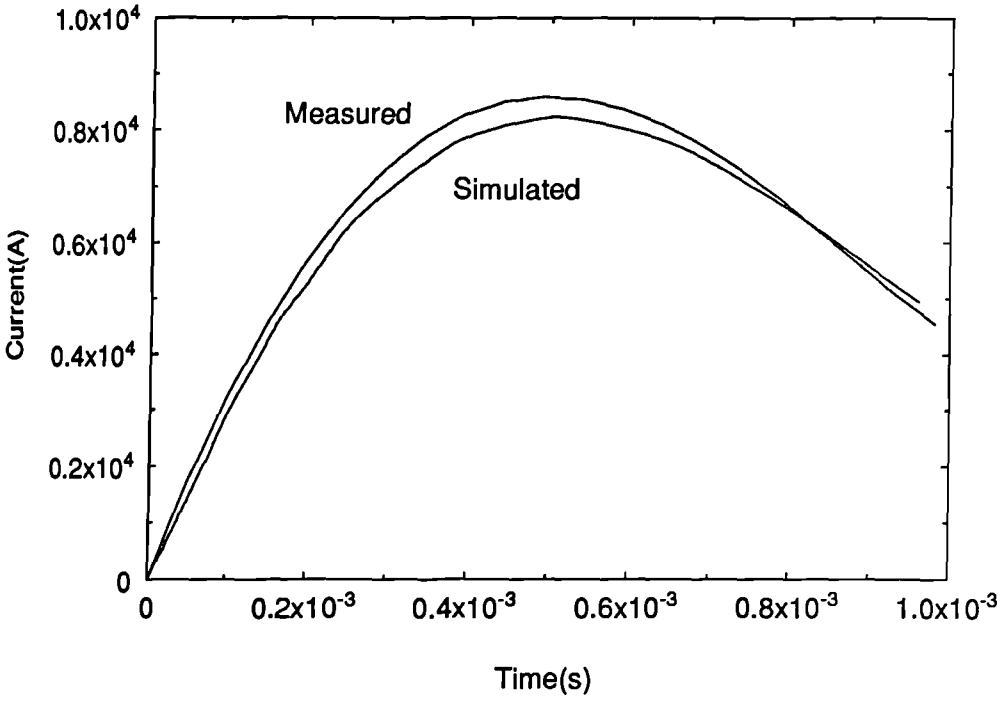

Fig. 3.32 Measured and predicted fixture current (C = 7000 μF , V = 800V).

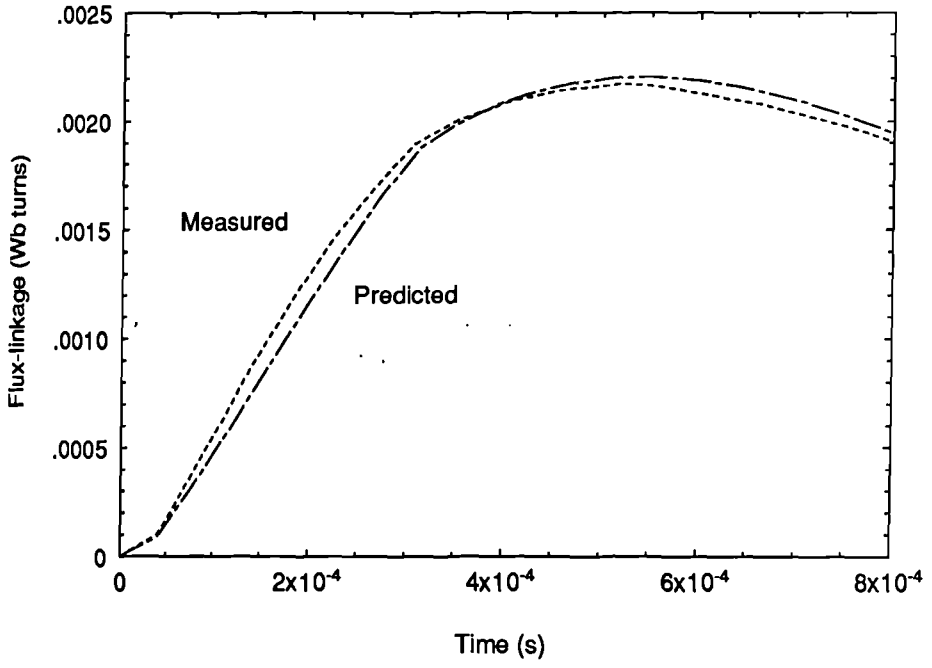

Fig. 3.33 Predicted and measured flux-linkage for a 5 turn search coil wound between holes E and F in the steel core. (C = 7000 μF , V = 800V).

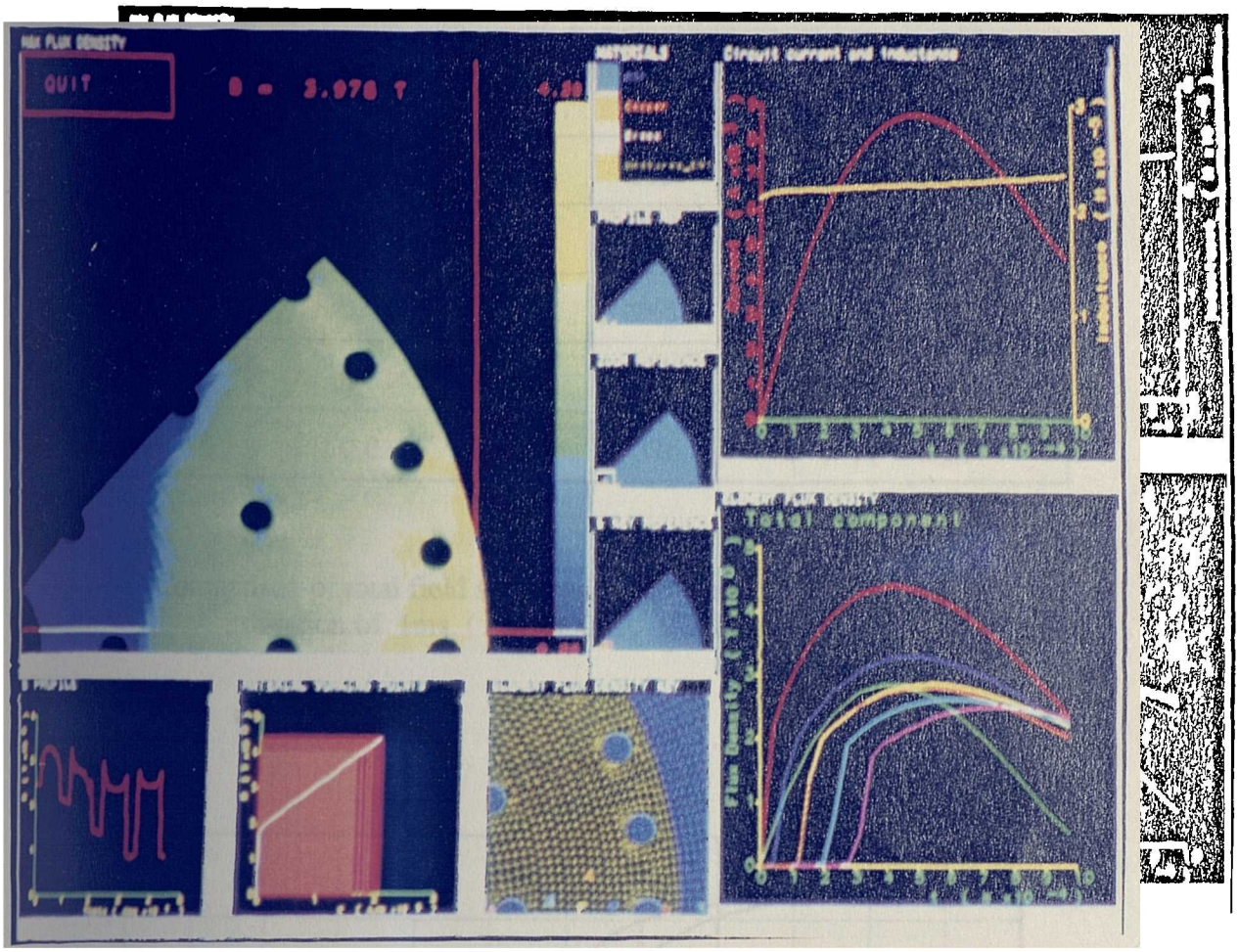

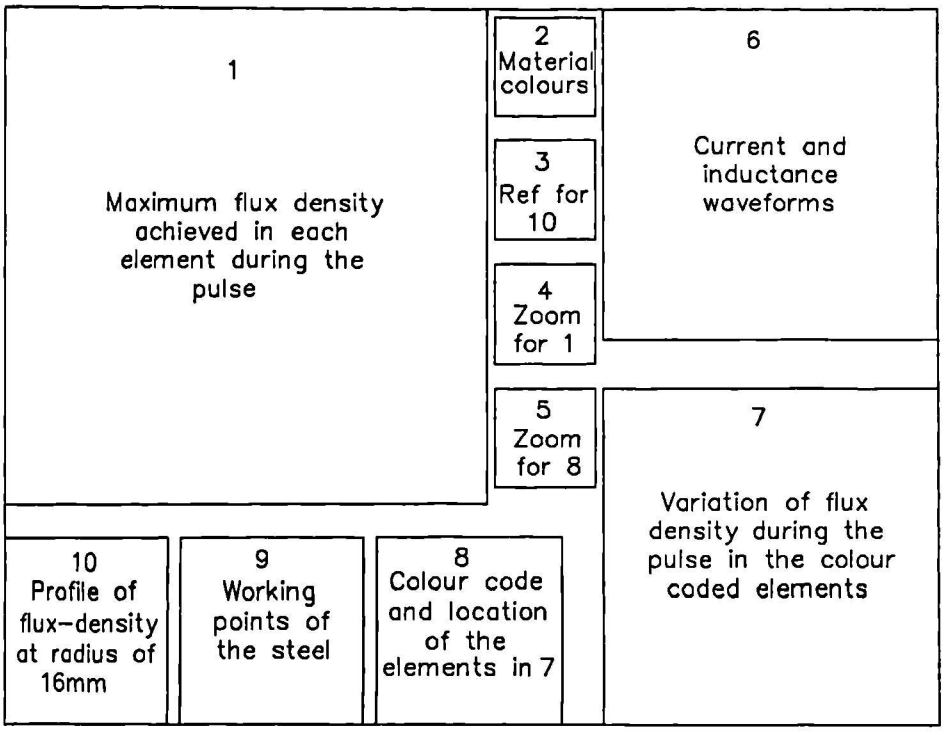

Fig. 3.34 Post-processor output. (C = 7000 μF, V = 800V).

Time steps	Time step length(ms)	Total Iterations	Iterations per time step
10	0.1	115	11.50
20	0.0495	197	9.85
30	0.0328	268	8.93
40	0.0245	323	8.07
50	0.0196	376	7.52

Fig. 3.35 Comparison of total field solution iterations required for a simulation duration of 1ms. (C= 7000μF, V = 800V).

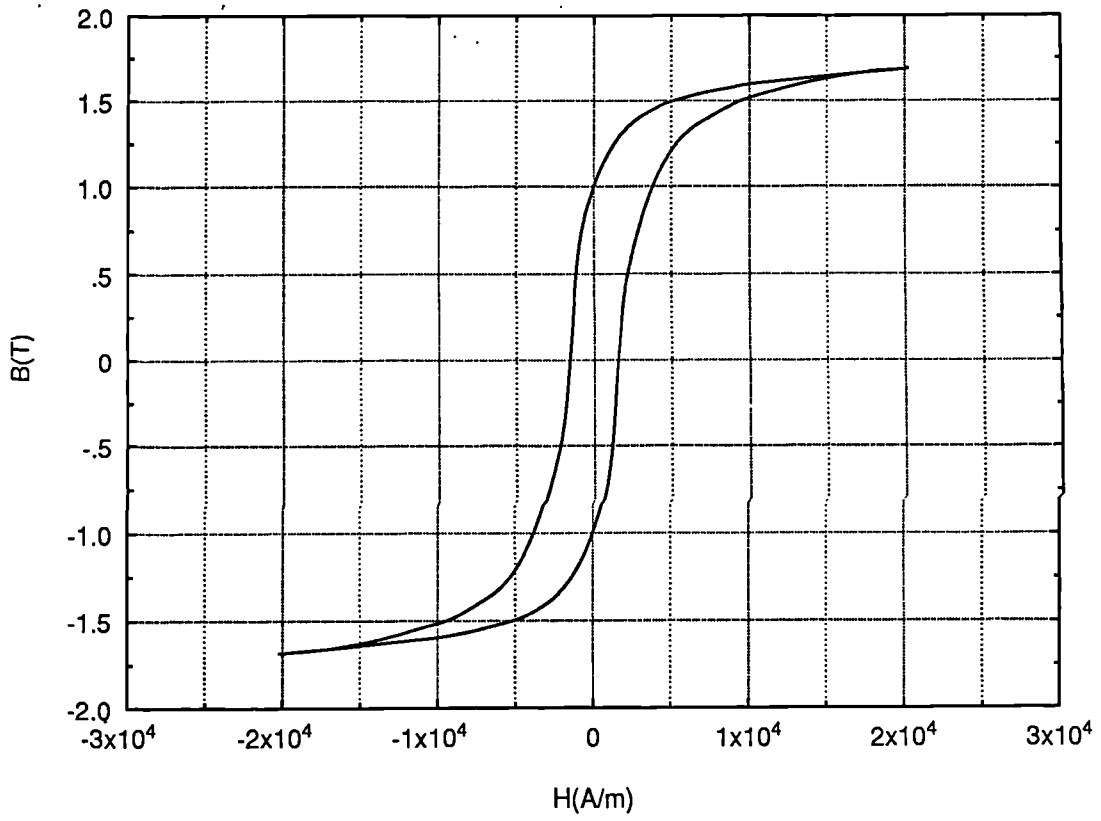

Fig. 3.36 Measured major d.c hysterisis loop for EN1A mild steel.

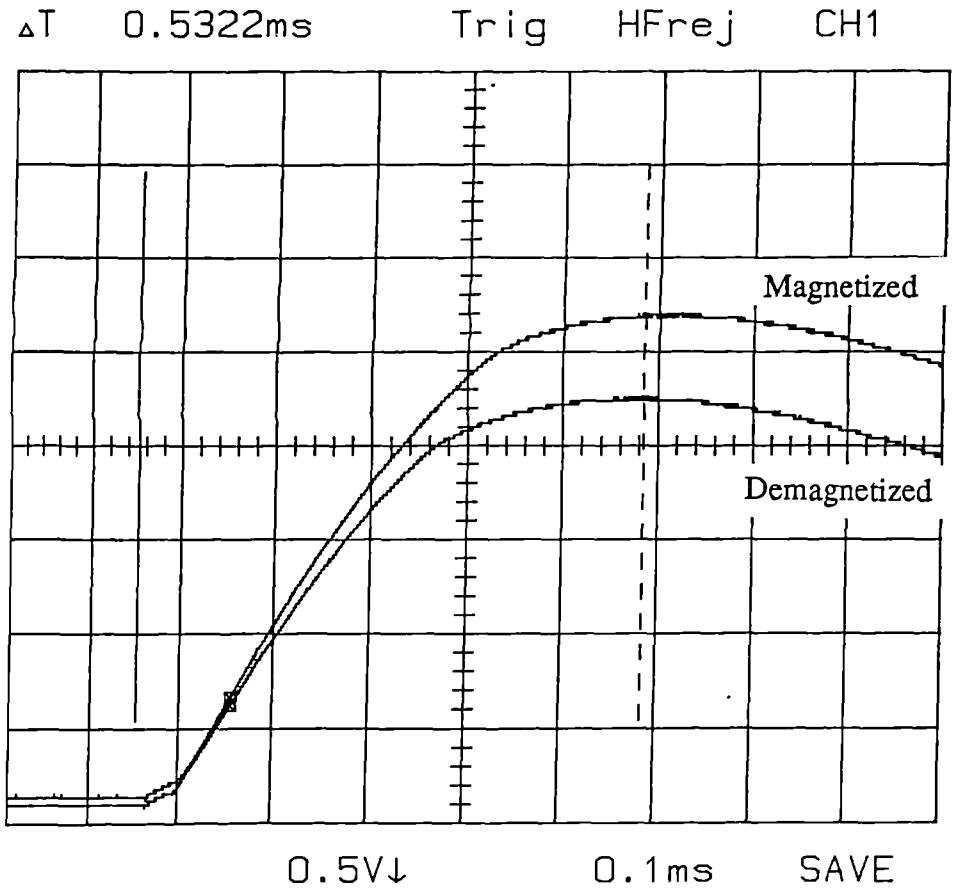

Fig. 3.37 Effect of the initial conditions of the steel on the measured flux-linkage of a search coil wound between holes E and F. (C = 7000μF , V = 800V).

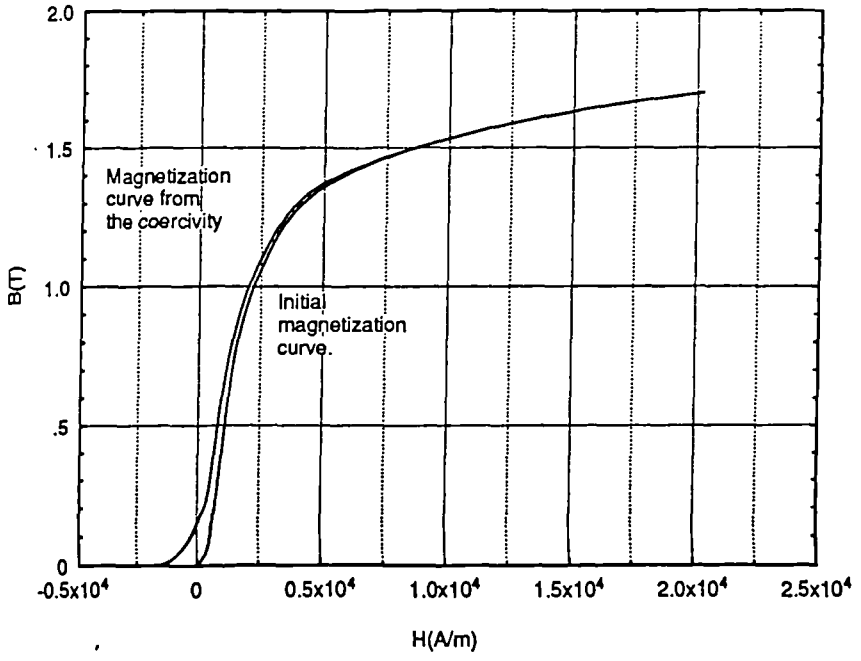

Fig. 3.38 Measured initial magnetization curve and the magnetization curve traversed form an inital starting point at the coercivity.

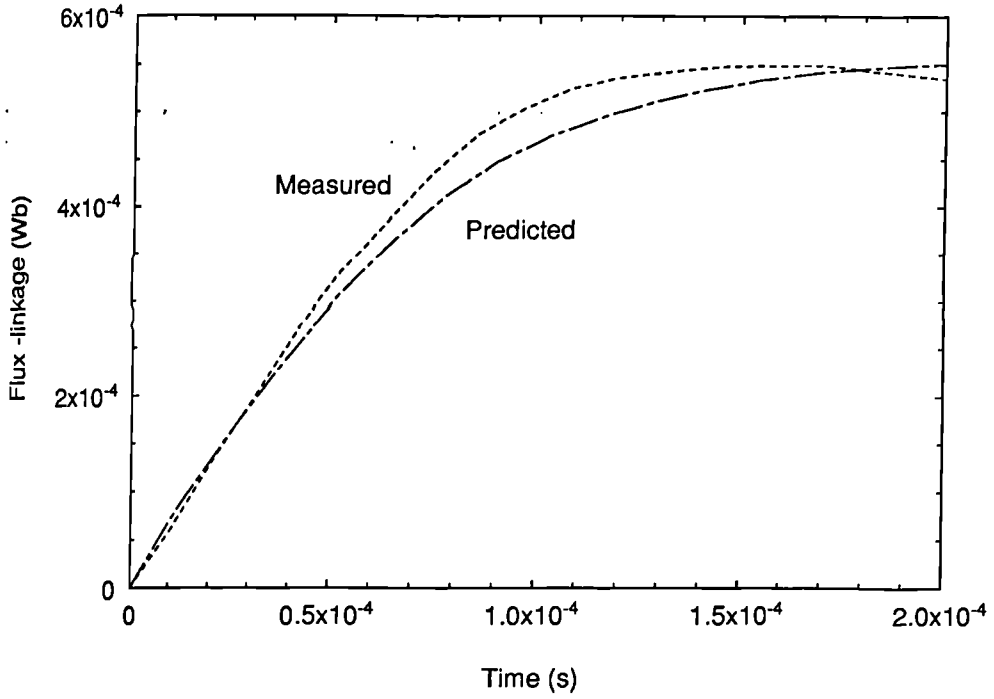

Fig. 3.39 Measured and predicted flux per pole entering the central 10mm axial section of the core.

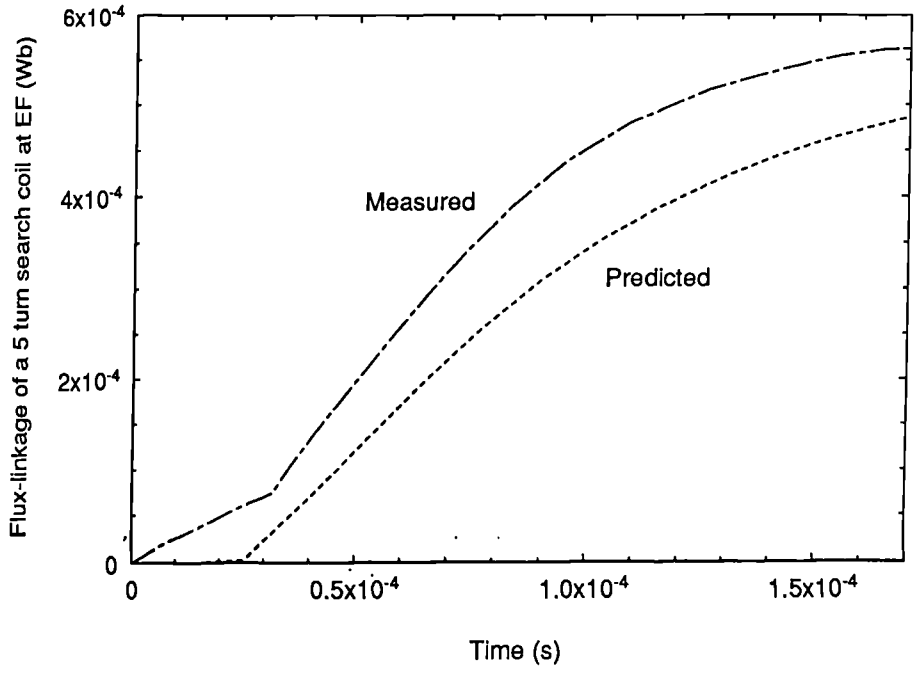

Fig. 3.40 Comparison of predicted and measured flux-linkage of a 5 turn search coil wound between holes E and F of the steel core (C = 150 μF , V = 780V).

C (μF)	V_o(V)	Current rise time (ms)	Total Iterations	Average number of iterations per time step
150	780	0.084	285	5.70
700	200	0.50	259	5.18

Fig. 3.41 Comparison of the convergance of simulations for long and short duration unsaturated cases with 50 time steps covering the period of twice the time to peak of the current waveform.

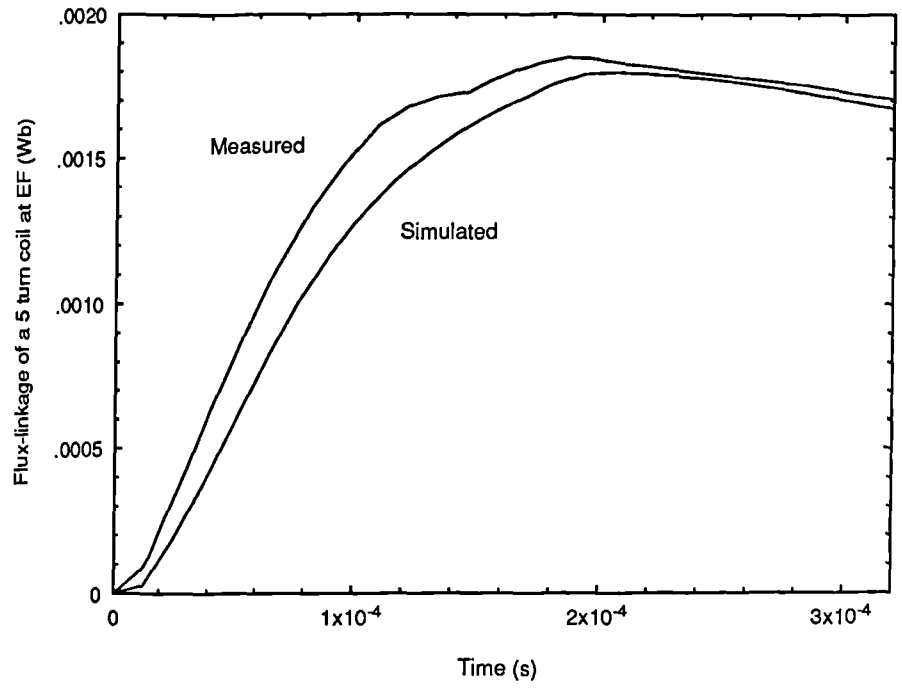

Fig. 3.42 Comparison of predicted and measured flux-linkage of a 5 turn search coil wound between holes E and F (C= 150 μF, V = 3200V).

	$C = 7000\ \mu F$ $V_0 = 200V$		$C = 150\ \mu F$ $V_0 = 780V.$	
	Measured	Predicted	Measured	Predicted
Peak Current (A)	2040	2020	1980	2000
Current rise time (μs)	502	490	84	83
Peak EF flux-linkage (mWb)	0.84	0.84	0.56	0.54
EF flux-linkage rise time (μs)	706	744	220	275

Low saturation levels.

	$C = 7000\ \mu F$ Vo = 800V		$C = 150\ \mu F$ Vo = 3200V	
	Measured	Predicted	Measured	Predicted
Peak Current (A)	8340	8580	8110	8250
Current rise time (μs)	498	492	85	83
Peak EF flux-linkage (mWb)	2.17	2.20	1.85	1.80
EF flux-linkage rise time (μs)	528	543	190	200

High saturation levels.

Fig. 3.43 Summary of results of the experimental validation.

CHAPTER 4

MAGNETIZATION OF AN EXTERNAL ROTOR BRUSHLESS DC MACHINE EQUIPPED WITH RADIALLY ANISOTROPIC NdFeB MAGNETS

4.1 INTRODUCTION

During the manufacture of permanent magnet devices the magnetization can generally be carried out at any one of a number of stages. However, the preferred option is for post-assembly or in-situ magnetization since it eliminates the handling of pre-magnetized magnets, with all the attendant problems which this creates. In the construction of permanent magnet machines in particular the main problems associated with handling pre-magnetized sub-assemblies are the large attractive forces between the rotor and stator during final assembly, and the possibility of ferrous debris being attracted to the magnet surface. The case studies presented in this chapter investigate the relative difficulties in multipole magnetizing at the component, sub-assembly and post-assembly stages in the construction of a small brushless dc machine.

4.2 EXTERNAL ROTOR BRUSHLESS MOTOR

The 3-phase, 4-pole external rotor brushless d.c machine which forms the basis of the case studies is shown in fig 4.1. The external rotor topology, which inherently has a higher rotor inertia than the equivalent internal rotor motor, has numerous applications in systems which require low speed ripple e.g. in-hub hard disc drives and tape drives etc. The peformance specification and the principle dimensions of the motor are given in figs 4.2 and 4.3. The stator is formed from 60 Transil 335 photo-etched laminations, each of 0.35mm nominal thickness. The magnetically active axial length of the stator is therefore 21.0 mm, compared to a mechanical axial length of 23.7mm, i.e a lamination stacking factor of 88.5%. This active length of 21.0mm was used for

scaling the values of motor performance predicted by two-dimensional finite element analysis.

The rotor of the machine consists of a 24mm long stack of radially anisotrpic sintered NdFeB magnet rings(Philips Components RES270) mounted inside a solid mild steel cylinder. Complete rings with a radial preferred direction of magnetization are an attractive configuration for small radial-field machine rotors since they are mechanically more robust and easier to assemble than a rotor constructed with a series of discrete arc segments which must be individually bonded to the rotor core. However, three principal factors lead to the manufacture of radially anisotropic rings being comparatively expensive, viz:

1) Differential cooling rates at various points in the ring introduce mechanical strains during the final cooling stage of the sintering process. These strains can be sufficient to cause severe cracking of the ring, particularly in thin walled rings. To prevent such structural damage to the finished magnet, the rings have to be sintered to be significantly thicker than the finished magnet dimensions. For example, the finished rings utilised in the motor of fig 4.1 have a radial thickness of 1.5mm after grinding, whereas they were sintered to a thickness of 4mm. This introduces a significant ratio of scrap material to finished magnet, with a subsequent cost penalty. It will be noted that the strains introduced during the cooling of sintered ferrite rings exceed the maximum sustainable by the material, with the result that it is not possible to sinter complete radially anisotropic ferrite ring magnets.

2) The radial aligning field which is applied during the pressing of the magnet is produced by connecting the upper and lower field coils of an electromagnetic punch in series opposition. Although this produces a radial field at the mid-point between the two coils, the orientation of the field departs from the radial direction with increasing

distance from the mid-point. Thus, for a given inner diameter there is a maximum axial length in which the field can be aligned within a given tolerance of the required radial direction. The rings used in the motor of fig 4.1 have an axial length of 4mm, which necessitates that the rotor is constructed from 6 separate rings, thus reducing some of the production and mechanical strength advantages compared to arc segments.

3) The tolerance and concentricity of the inner and outer surfaces of the magnet ring are critical, since they must either form one airgap surface or must have a close fit with the rotor core. Grinding of the internal bore surface of a ring to a high tolerance is a considerably more expensive operation than grinding the other surfaces, and can add significantly to the cost of small volume magnet pieces. In contrast, the inner bore of axially anisotropic ring magnets is often not a critical dimension and can often be left as sintered.

4.3 MAGNETIZATION SPECIFICATION FOR THE MOTOR.

The initial magnetization curve for RES270 NdFeB measured in a d.c permeameter, is shown in fig 4.4, whilst the corresponding relative permeability versus magnetizing field strength characteristic, derived from the initial magnetizing curve, is shown in fig 4.5. The maximum relative permeability is 19.35, although at field strengths required for saturation, viz 1000-1600 kA/m, the relative permeability is approximately 1.5. The curves of figs 4.4 and 4.5 were measured using rectangular blocks of magnet of nominally the same grade as the radially anisotropic rings. However, because of the difficulties in producing the rings there is considerable potential for a dilution in the properties from those measured on blocks. However, since the properties of the radially anisotropic rings could not be satisfactorily measured, the curves of figs 4.4 and 4.5 had to be assumed representative of the properties of the rings.

The measured dependance of the intrinsic demagnetization curves on the magnitude of the applied magnetizing field for RES270 is shown in fig 4.6. Clearly, the specification of a single valued saturating magnetizing field strength from the characteristics of fig 4.6 is somewhat arbitrary, and should be made with due account of the intended application of the magnet. The three main issues which were considered in the case of this particular brushless motor are:

1) At room temperature, with the magnet in a low reluctance circuit and not subjected to a strong demagnetizing field, the flux produced will not be very sensitive to the level of the applied magnetizing field, provided it is above 1000 kA/m. Thus, the normal steady-state operation of the motor, which is designed to operate at a high magnet working point, may not be too adversely affected by a failure to expose the entire magnet volume to a magnetizing field of 1600 kA/m.

2) The specification of permanent magnet motors normally stipulates a demagnetization withstand factor to enable them to operate under a short term overload condition without irreversible demagnetization. However, the demagnetization withstand capability is normally assessed by assuming full saturation of the magnets throughout their entire volume. Failure to fully saturate, and thereby achieve the required linearity of the normal demagnetization characteristic over the subsequent excursion of the magnet working point, can lead to localised irreversible demagnetization. However, often, particularly in the case of small machines employing rare-earth magnets, the magnet length required to provide the withstand capability is less than the minimum magnet length determined by mechanical and/or material production considerations. Indeed, the motor of fig 4.1 requires a magnet thickness of 0.4mm for a 5 times overload withstand capability, whereas, due to limitations in the processing, the actual magnets had a radial thickness of 1.5mm. This additional magnet thickness provides a degree

of additional protection against irreversible demagnetization, and hence reduces the requirement for the intrinsic demagnetization characteristic to have its full squareness.

3) Failure to fully saturate a magnet can lead to a degradation of its properties at elevated temperature. In order to maintain the linearity of the normal second-quadrant demagnetization characteristic at elevated temperatures, the full squareness of the intrinsic characteristic must be developed by ensuring full saturation. However, since the motor of fig 4.1 is designed for a maximum steady-state temperature of only 50°C, the full elevated temperature linearity is not critical to its performance under normal operating conditions.

In summary, for this particular motor, the magnitude of the saturating field, providing it is above 1000-1200 kA/m, is not likely to be critical to the subsequent performance of the motor. However, effects due to localised factors, such as the sharpness of the pole transition regions, may influence the percentage volume of the magnet which must be to fully magnetized. As a starting point however, the initial target was to design a magnetizing fixture which would be capable of producing a magnetizing field of at least 1600 kA/m throughout the entire magnet volume.

4.4 DESIGN CONSTRAINTS

The fixture conductors are to be separated from the magnet by a glass fibre reinforced epoxy resin layer which provides mechanical strength and an additional degree of electrical insulation between the conductors and the magnet surface or motor frame. The selection of the thickness of this layer is a compromise between achieving improved mechanical strength from a thick structure and realising electromagnetic benefits from locating the conductors close to the magnet surface, viz reduced mmf for a given level of magnetizing field and an improved radial orientation of the magnetizing field in the magnet .

The radial anisotropy of the magnet ring ensures that the resulting remanent magnetism will be essentially radial irrespective of the degree of radial alignment of the magnetizing field, although the mmf required to ensure the radial saturation will increase for a reduced radial alignment of the applied magnetizing field. Thus, the radial clearance between the fixture conductors and the magnet is far less critical to the orientation of the remanent magnetism for anisotropic materials than would be the case for isotropic materials. Therefore, a separation of 1mm was selected for the fixture design, c.f the 0.5mm clearance used for the isotropic bonded magnet fixture of chapter 5. The additional thickness and hence rigidity of the retaining layer between the fixture winding and the magnet ring compared to that used for the bonded ring in chapter 5 is also useful since sintered magnets are more brittle than polymer bonded magnets, and hence more susceptible to damage as a result of small deformations in the fixture during the application of the magnetizing pulse.

4.5 MULTIPOLE COMPONENT LEVEL MAGNETIZATION.

The single component ring magnet precludes magnetization of each pole individually, and hence the multipole magnetization of the ring magnet prior to assembly of the rotor is the most basic and least demanding of three possibilities for magnetization. It allows a greater freedom in the selection of the fixture topology since the magnet is directly accessible at both the inner and outer surfaces, although production enginnering considerations such as a requirement for an robotic "pick and place" system may preclude the use of a double sided fixture. For comparison with the other magnetization procedures which follow, the fixture design was aimed towards magnetizing the entire 24mm magnet stack length in one operation. The three possible fixture topologies, viz, single sided internal, single sided external and double sided, show little difference in their respective volume saturation versus mmf characterisitcs, fig 4.7. However, since a double sided fixture produces a given mmf at half the current density of the others it

was selected as the preferred topology.

Selection of the field calculation method

The absence of iron in the component to be magnetized implies that the problem region is essentially linear, and hence ideally suited to the analytical method for calculating the magnetizing field strength in the magnet for a given fixture mmf. However, the applicability of the analytical method for estimating the mmf required for saturation of the magnet was assessed by comparing the percentage volume saturation versus mmf characteristic for a double sided, air-cored fixture having a single turn per pole of diameter 1mm located 1mm from the magnet surface on both sides of the magnet, with the corresponding characteristic deduced from finite element analyses.

The variation in the percentage of the magnet volume exposed to a saturating field strength in excess of 1600 kA/m in the radial direction for an increasing mmf, calculated using both the analytical and non-linear finite element methods, are shown in fig 4.8. There is good agreement between results from the two methods since the NdFeB material only forms a small fraction of the magnetic circuit, and hence its effect on the flux-density per ampere is minimal. The agreement between the two methods confirms that the use of an analytical linear field calculation coupled to the non-linear initial magnetization curve of the magnet material is adequate to subsequently analyse the effectiveness of a range of alternative fixture parameters.

The maximum achievable saturated percentage volume from fig 4.8 is close to 100%, the apparent limit of 97% being due to the discretization at the pole transition regions, where the flux density in both the analytical and finite element models must be defined as being normal to the boundary in order to maintain continuity of flux.

Electrical design

The electrical design was directed initially towards a low capacitance/high voltage magnetizer, since a given mmf can be obtained for a lower temperature rise and stored energy compared to a high capacitance/low-voltage magnetizer. Further, since there is only a small volume of conducting magnet within the fixture, the short duration pulses produced by a low capacitance magnetizer are likely to be adequate to ensure full penetration of the magnetizing field. For the maximum magnetizer voltage of 3000V and capacitances of 450, 300 and 150μF, the following fixture parameters were scanned:

1) The fixture axial length was varied from 30 mm to 50mm in 10mm increments.

2) The conductor diameter was varied from 0.5mm to 3.0mm in 0.5mm increments.

3) The number of conductors in the circumferential direction was incremented from 1 to 5

4) The number of conductors in radial direction was incremented from 1 to 10

In order to produce the highest degree of radial alignment of the magnetizing field, a symmetrical distribution of conductors on either side of the magnet is desirable. Thus initally, a symmetrical distribution of conductors was enforced. Fixture arrangements for which there was insufficient space within the magnet bore to accomodate the winding were discounted rather than modifying them to have an unsymmetrical conductor distribution. The maximum permissible peak current and final temperature from 20°C were set at 30 kA and 200°C respectively.

The total number of designs which were analysed was 2700, although a large proportion of these were eliminated on the basis of there being insufficent space for

the winding within the magnet bore.. A minimum volume saturation criteria of 90% was enforced so as to reduce the number of valid designs. Of the 2700 fixtures which were analysed, 85 produced predicted saturation levels in excess of 90%, comprising 40, 29 and 17 valid designs for the fixture axial lengths of 30, 40 and 50mm respectively. As a consequence of the large number of valid designs for an axial length of 50mm and the fact that they produced levels of saturation comparable with the best 30mm and 40mm axial length fixtures, an axial length of 50mm was selected because of its inherent advantages in reducing the field distortion due to end-windings.

The parameters of the 17 valid designs for an axial length of 50mm are shown in fig 4.9. They are all are associated with a 3kV, 450μF magnetizer. The rather ill-defined nature of the optimum is clearly demonstrated by the fact that all the fixture designs produce percentage volume saturation levels in the range 90% - 93.5%. This is a direct result of the incremental slope of the percentage saturation versus mmf curve being small above a saturation level of 90%, and hence a wide range of fixture efficencies and maximum mmfs produce only small variations in the predicted saturation level. However, the fixture selected for further analysis was design 7 since it produces the highest level of volume saturation with no significant penalties in other aspects of performance compared to the other fixture designs. The principle dimensions and conductor layout for the selected fixture are shown in fig 4.10. The analytically calculated inductance and room temperature resistance of the fixture are 5.70 μH and 23.7 $m\Omega$ respectively.

Dynamic simulation.

The relatively low electrical conductivity and small volume of magnet, and the absence of any solid soft magnetic materials, suggests that eddy-currents will have a minimal effect on the field distribution. Hence the analytically predicted levels of static

saturation are likely to be realised under dynamic conditions. Nevertheless, a dynamic simulation of fixture design 7 was performed both to confirm the minimal modifying effects of eddy-currents, and to obtain the distribution of demagnetization characteristics within the magnet volume in order to assess its subsequent performance in the assembled motor. In the normal course of design synthesis, this numerically intensive stage could be omitted, and in such instances, the distribution of demagnetization characteristics would be obtained from a single magnetostatic field calculation, in which the fixture current is set to the peak magnetizing current calculated in the electrical design phase.

The axial length of the finite element model was modified for the dynamic simulation using the method described in chapter 3, from 24 mm to 21.8mm in order to correctly weight the effect of its variation on the total fixture inductance. The finite element mesh, is shown in fig 4.11, and consisted of 2823 nodes and 5442 elements with uniform angular and radial discretizations in the permanent magnet of 1^{o} and 0.25mm respectively.

The predicted variation in the electrical circuit parameters during the impulse period are shown in fig 4.12. There is a discernable change in the fixture inductance during the pulse due to eddy-current screening during the initial 25-30μs of the impulse period. Following the initial 30μs however, the inductance is relatively constant, indicating that as the peak of the current is reached, the modifying effect of eddy-currents on the field distribution is small. The reduction in the initial inductance results in an increased current compared to that predicted by the linear electrical simulation, viz 23.1kA cf 20.8kA.

However, the change in inductance and the resulting increase in peak current are somewhat suprising given the low electrical conductivity and small volume of the

magnet. The mechanism by which the eddy-currents, although relatively small affect the inductance to such a degree is clearly demonstrated by fig 4.13, which shows a series of instantaneous field distributions during the initial stages of the pulse, which highlight the almost complete absence of mutual coupling between the inner and outer windings during the initial stages of the pulse. This dramatic decrease in mutual coupling dictates that double sided fixtures are inherently more susceptible to variations in inductance due to eddy-currents than an equivalent single sided fixture.

The predicted field distributions at selected instants during the the impulse period, fig 4.14, demonstrate the minimal modifying effects of eddy-currents on the field distribution at 77μs, which corresponds to the peak of the current pulse. Fig 4.14 also illustrates the relatively high degree of radial alignment of the magnetizing field over a large volume of the magnet, viz 93.5%. The alignment in the remaining 6.5% of the magnet volume near the pole transitions which is not saturated, is very poor, indicating that the realisation of an idealised fully saturated magnet cannot be achieved without an impractical increase in magnetizing mmf.

The predicted distribution of demagnetization characteristics throughout the magnet volume are shown in fig 4.15. The only regions of the magnet which are not fully saturated, i.e exposed to a magnetizing field in excess of 1600 kA/m, are located near the pole transitions. The predicted volume saturation of the magnet under dynamic conditions of 93.5% is identical to the static value of 93.5% predicted by the linear electrical simulation and the analytical field calculation, despite the slightly higher peak current which is predicted under dynamic conditions.

The predicted demagnetization curves of fig 4.15 were utilised in a series of magnetostatic finite element calculations to model the subsequent performance of the open-circuit assembled motor. The predicted phase flux-linkage versus rotor position

and the normalised induced emf waveforms are shown in figs 4.16 and 4.17, together with those predicted for an idealised fully saturated magnet. They demonstrate that the multipole magnetized ring magnet results in little reduction in motor performance from that which would be obtained with pre-magnetized fully saturated magnet segments, which can essentially be regarded as idealised magnets.

4.6 MAGNETIZATION OF THE ASSEMBLED ROTOR.

The assembled rotor of fig 4.1 consists of 6 radially anisotropic NdFeB magnet rings, each of axial length 4mm, and a 5.75mm thick solid EN1A grade mild steel back-iron ring. The axial length of the mild steel ring is 52mm, the additional axial length compared to the 24mm long magnet stack being required since it forms the outer casing of the motor, and must include sufficient space for the machine end-windings, phase terminations and the Hall-effect rotor position sensors.

For the magnetization of the magnet ring prior to assembly of the rotor, a double sided fixture was selected as the preferred topology. However, in a double sided fixture for magnetizing the assembled rotor, the conductors external to the rotor are forced to be more remote from the magnet, and their effectiveness in producing both a high level of magnetizing field for a given current, and a high degree of radial alignment is therefore diminished. The percentage volume saturation versus mmf per pole characterisitics predicted by non-linear finite element analysis for both a double sided fixture and an internal single sided fixture are shown in fig 4.18. In this case the single sided topology is best suited in terms of its efficiency in producing a given level of saturation for a given mmf, despite the drawback of limited space for the fixture winding. The initial design was, therefore, focussed on single sided fixtures in which the conductors are located only within the assembled rotor.

In order to assess the applicability of the analytical field calculation method to

the magnetization of the assembled rotor, the volume saturation versus mmf characteristic was calculated for a single sided internal fixture with a single 1mm diameter conductor located 1mm from the magnet surface. The percentage volume saturation versus mmf characterisitics as predicted by both the analytical and finite element methods are shown in fig 4.19. In this case the analytical model, in which the permeability of the mild steel was set to μo, is not representative of the actual problem environment, since the mild steel forms a large fraction of the magnetic circuit and significantly reduces the total reluctance even though it is heavily saturated. Therefore the subsequent design must be based on a finite element field calculations.

Having established that the finite element method is the most appropriate for the problem environment, the dependance of the required saturating mmf on the disposition of the conductors of the fixture winding was investigated. This dependancy was calculated for a 1mm deep conductor bundle having a width varying between 1 and 5mm , fig 4.20 , and a 1mm wide conductor bundle with a radial depth varying between 1 and 5mm, fig 4.21. The finite element mesh which was used for the estimation of the required magnetizing mmf and its dependance on the radial distribution of the fixture winding is shown in fig 4.22. The mesh discretization is determined predominantly by the requirement for a high degree of spatial resolution of information in the magnet, particularly at the pole transitions, and the requirement for a uniform tangential discretization to allow analysis of the subsequent performance of the magnet as the rotor is rotated in the motor.

The predicted variation in percentage volume saturation shown in figs 4.20 and 4.21, demonstrate that the dominant variation in the required magnetizing mmf is with the radial depth of the conductor bundle. The calculation of the characteristics of figs 4.20 and 4.21, which have an mmf resolution of 10 kA, required a total of 200 field solutions with an average of 4.5 non-linear iterations per solution. Clearly, the extension

of these calculations to all possible combinations of conductor bundle widths and depths would lead to a large overhead in computing time, even in such a geometrically constrained fixture topology. The estimation of the required magnetizing mmf is only the initial stage of design and incorporates a number of simplifying assumptions, particularly with regard to the time dependancy of the field. Hence, a detailed magnetostatic calculation of the positional dependancy of the required magnetizing mmf is not an efficient utilisation of design time. In order to avoid this a modified strategy was employed which calculates the mmf required to achieve a target percentage saturation.

By specifying a target level of percentage saturation, the mmf required to achieve this can be calculated for all the possible conductor bundle dimensions with a dramatically reduced number of field calculations compared to obtaining a complete set of percentage volume saturation versus mmf characterisitcs. The starting estimate of the required mmf to achieve the target saturation for a given conductor bundle distribution is based on the mmf required for the nearest previously calculated winding distribution, and is incremented in predetermined steps until the saturation specification is achieved.

The form of the predicted volume saturation/mmf characteristics suggest that a level of volume saturation of 90% is possible, albeit with no consideration of the electrical circuit implications of achieving this saturation. For a target saturation level of 90%, a spatial resolution in the winding distribution of 1mm, and an mmf increment of 10 kA the calculation of the mmf required for a given winding distribution was usually achieved within 3 field calculations. However, a number of winding distributions near the maximum allowable dimensions required a larger number of steps since the alignment between the applied field and the magnet preferred radial orientation becomes so poor that the required increase in mmf becomes progressively greater. The various mmfs required for conductor bundle dimensions covering the available winding

space within the magnet bore are shown in fig 4.23. Such a characterisitc can be incorporated into the electrical design stage to indicate whether a given fixture/magnetizer combination achieves the target level of saturation. For this purpose it is useful to define a factor α :

$$\alpha = \frac{\textit{Maximum mmf produced by the fixture / magnetizer combination}}{\textit{The required mmf} \text{ for } \textit{the fixture conductor disposition}} \quad (4.1)$$

For values of α other than 1 the actual value of the percentage volume saturation cannot be evaluated directly since it depends on the disposition of the conductors. This problem is the major drawback of the method of performing field calculations only around the mmf which produces the specified volume saturation. This does not arise with the analytical or finite element methods in which a percentage volume saturation versus mmf characteristic is calculated for all possible conductor bundle geometries, since the actual percentage saturation can be predicted accurately even when it is below a specified level. However, by considering the likely sensitivity of the percentage volume saturation to values of α less than 1 the relative merits of alternative fixtures can be compared.

For a given fixture there is a portion of the magnet volume in which there is a reasonable degree of alignment between its preferred direction of magnetization and the applied magnetizing field. This portion can be readily saturated compared to the rest of the magnet which has poor field alignment, as demonstrated by the levelling off of the percentage saturation versus mmf characteristics such as those of figs 4.20 and 4.21. The incremental increase in saturation beyond this levelling off point is achieved at the expense of a greatly increased mmf requirement. For fixtures in which the well aligned portion of the volume is greater than 90 % i.e fixtures having a low number of small cross-sectional area conductors, a value of α slighlty less than 1 could result in a significant reduction in the percentage volume which is saturated. In contrast, fixtures

with a high number of turns which inherently have worse alignment, tend to reach a saturation of 90% well beyond the levelling off point of the percentage volume versus mmf characteristic, and hence the volume saturation is not as sensitive to values of alpha which are slightly below 1. Thus for two fixtures with similar values of alpha less than 1 the best performance in terms of the volume saturation which is likely to be achieved will be with the fixture having the most distributed winding.

Electrical design

For the maximum rating of the high voltage magnetizer, viz a capacitance of 450μF at 3000V, the electrical performance of a range of possible fixture designs were analysed using the linear electrical simulation, subject to the constraints of a maximum peak current of 30kA and a maximum final temperature of 200°C from a 20°C ambient. The resultant values of α for each of the fixtures was determined by reference to fig 4.23. The following leading parameters were scanned in the design process:

1) The fixture axial length was varied between 30 mm and 50mm in 10mm increments.

2) The conductor diameter was varied between 0.5mm and 2.5mm in 0.5mm increments.

3) All possible rectangular array combinations of conductor layouts for each conductor diameter were analysed, up to maximum bundle dimensions dictated by space constraints imposed by the magnet bore diameter.

The performance of the 50 fixtures which resulted in values of α greater than 0.6 whilst remaining within the electrical circuit constraints, are shown in fig 4.24. The maximum predicted value of α is 0.90 produced by design 5, which is based on a 3x3 arrangement of 1.5mm diameter conductors per pole and an axial length of 30mm. The corresponding fixtures with axial lengths of 40mm and 50mm, i.e designs 25 and 42,

also produce the highest values of α for their respective axial lengths.

The failure to achieve α values in excess of 1 indicates that the specified target saturation of 90% was somewhat optimistic. However, such an over specification cannot be identified prior to undertaking the electrical design stage. The target specification could be modified in response to the results of the electrical design stage, but such an iterative specification of a viable target saturation reduces the benefit of specifying a target level compared to calculating a complete volume saturation versus mmf characteristic. In spite of the inability to achieve α values in excess of 1.0 for a target saturation of 90%, fig 4.24 provides a useful guide to the merits of the alternative fixture designs, and is sufficient to select the likely optimum fixtures.

Dynamic simulation

The predicted fixture performances of fig 4.24 are based on static field calculations. However, the short rise times necessitate that consideration must be given to the dynamic nature of the magnetizing field. The effect of eddy currents on the performance of fixture design number 42, which produces the longest pulse length of the 3 optimal fixtures, was therefore assessed by a dynamic simulation. A close-up of the rotor region of the finite element mesh which was utilised in the dynamic simualtion is shown in fig 4.25. The entire mesh, in which a Dirichlet boundary condition was imposed at a distance of 180mm from the centre of the fixture, consisted of 3298 nodes and 6347 elements, with the same rotor discretization as was used for the static field calculations. The axial length of the finite element region was modified by the method presented in chapter 3, from 50mm to 48.4mm in order to weight the contribution of its two-dimensional inductance to the total fixture inductance.

The predicted variation of the electrical circuit parameters is shown in fig 4.26, whilst predicted field distributions at selected instants during the pulse are shown in

fig 4.27. The eddy-currents flow predominantly in the mild steel and have two effects on the level magnetizing field to which the magnet is exposed. Firstly, the eddy currents inhibit the penetration of the magnetizing field into the mild steel, as is clearly demonstrated in the predicted field distributions of fig 4.27. Secondly, the inductance of the fixture is decreased by the screening action of the eddy currents which to a certain extent compensate for the reaction field produced by the eddy currents, resulting in a larger peak current than that predicted in the analytical electrical design phase, viz 21.8KA and 18.6kA respectively .

The large eddy-currents which flow in the mild steel rotor can be observed in the dynamic post-processor output of fig 4.28. There is an increase in phase shift in the flux density waveforms with increasing depth into the mild steel, and the failure of the field to penetrate to the centre of the pole is demonstrated by the large variation in maximum flux density throughout the mild steel. For further comparison with the dynamic simulation the percentage volume saturation was calculated from a magnetostatic finite element calculation using the predicted peak current of 18.6kA from the analytical electrical design stage.

The large modifying effect of eddy currents is illustrated by the predicted static and dynamic field distributions at the peak of the current pulse, fig 4.29. The dynamic and static calculations predict volume saturations of 31.5% and 83.2% respectively. This level of dynamic volume saturation is achieved at 120 μs, which is significantly later than the peak of the predicted current pulse which occurs at 82μs. This large phase shift between the instants of peak current and peak saturation is indicative of large eddy-current effects.

Thus, the approximations made in the electrical design stage, viz. the level of saturation achieved by the pulsed magnetizing field can be calculated from a series of

magnetostatic finite element calculations and the effective inductance is given by the air-cored inductance, are not valid for this particular case. The static field calculation also serves to show the degree of insensitivity of the level of percentage volume saturation to a value of α significantly less than 1, 83.2% being achieved for an α of 0.78 in this case.

The predicted distributions of the subsequent second quadrant demagnetization characteristics in the preferred and non-preferred orientations are shown in fig 4.30. Although 68.5% of the magnet volume has not been exposed to a field in excess of 1600kA/m in the preferred direction, 85.6% of the volume is exposed to a magnetizing field in excess of 1000kA/m. This 85.6% of the magnet volume, which is shaded in white in fig 4.30b, has properites which lie in the interval between characteristics which is shaded white in fig 4.30a.

Calculation of motor performance

The predicted distribution of demagnetization characteristics in fig 4.30 was used in a series of magnetostatic finite element calculations to predict the performance of the magnetized rotor in the assembled motor. The series of predicted static field distributions as the rotor is rotated is shown in fig 4.31. The flux-linkage versus rotor position and induced emf per phase waveforms derived from the field solutions are shown in figs 4.32 and 4.33, together with those predicted assuming an idealised fully saturated magnet. Despite the failure to achieve a magnetizing field strength of 1600 kA/m over a large volume of the magnet, the resulting open-circuit performance of the motor, at least at room temperature, shows only a small difference from that which would be achieved with an idealised magnet.

Experimental

Since the aim of this case study was to validate and demonstrate the utility of the design methodology as well as to produce a fixture to magnetize the rotor, the predicted failure of the fixture to achieve near static preformance under the actual dynamic impulse conditions was investigated further. Fixture design number 42 was constructed to provide experimental confirmation of the predicted eddy-current effects. In the normal course of the design process this fixture would possibly be eliminated from the likely designs selected for construction on the basis of its dynamic simulation results, despite the fact that the relatively good predicted performance of the assembled motor at room temperature and under open-circuit conditions may be sufficient to meet the specification.

The constructed fixture, in which a continuous stranded glass fibre filament encapsulated in epoxy resin was used to restrain the windings, is shown in fig 4.34. The measured resistance and inductance of the fixture in the abscence of the rotor are in good agreement with those predicted at the linear electrical design phase, as shown in fig 4.35.

The effect of eddy-currents on the field distribution during magnetization was measured using the search coil of fig 4.36, which measures the flux per pole which completely penetrates the mild steel ring over the central 10mm axial length of the fixture. The mild steel rotor was de-magnetized prior to the pulse, using the same method used in the experimental validation of chapter 3. The current and search coil flux-linkage waveforms measured during the impulse period are shown in fig 4.37. The measured peak current magnitude of 21.2kA is in good agreement with the peak of 21.8KA predicted by the dynamic simulation. The agreement between the predicted and measured peak currents during the magnetization of the rotor, and their large

difference from the peak of 18.6kA predicted for the air-cored fixture alone, illustrate the importance of the circuit coupled approach adopted in the simulation. The measured search coil flux-linkage shows a delay of 75μs from the initiation of the pulse to the instant at which any significant magnetizing flux links the search coil. A comparison with the flux-linkage of the search coil predicted from the dynamic simulation, fig 4.38, shows good agreement.

The measured induced emf and flux-linkage per phase waveforms of the assembled motor are shown in fig 4.39. They were measured by driving the motor at a constant speed of 800rpm with a cogging free brushed motor connected to a large flywheel having a moment of inertia of 1.43 kgm^2 (c.f the rotor moment of inertia of 0.0040 kgm^2). The large inertia of the system used for measuring the induced emf and the flux-linkage results in the cogging torque fluctuations causing negligible speed ripple, and hence the measured waveforms can be regarded as being accurate representations of the variation as functions of position as well as time. This is a necessary condition to directly compare the measured results with those predicted by finite element analysis.

The measured peak to peak magnitude of the phase flux-linkage is in good agreement with the predicted value, viz 43.4mWb and 42.4 mWb respectively. The form of the predicted emf waveform, although affected to some extent by the discrete angular increments of the field solutions, shows a reasonable correlation with the major features of the measured waveform. The agreement between the measured and predicted waveforms confirm the predicted insensitivity of the open-circuit flux-linkage and induced emf to the failure to expose a large volume of the magnet to a radial magnetizing field strength in excess of 1600kA/m.

The simulation and experimental results illustrate that although a low capacitance,

high voltage magnetizer allows a higher current density for a given temperature rise, which is usually beneficial in obtaining high levels of saturation for a low stored energy, the eddy-currents in this particular problem dictate that such a magnetizer is not suitable for achieving the full properties of the magnet. Nevertheless, the relative assembled motor performance shows little reduction from that which would be achieved with an idealised magnet.

Designs based on a high capacitance / low voltage magnetizer.

A low voltage (0-800V), high capacitance (0-42,500μF) magnetizer can be used to produce longer pulses, so that greater penetration of the mild steel by the magnetizing field can be achieved, with a subsequent improved agreement with statically predicted saturation levels for a given mmf. The longer pulse length does, however, introduce a drawback in that for a given conductor cross-section the maximum current for a given temperature rise is reduced. Therefore, the designs which are suitable for a slower pulse tend towards a large number of turns of large cross-section area which are electrically efficient but tend to be inefficient in the attainable level of saturation for a given level of mmf. Applying the same constraints on the peak current and temperature rise as for the high voltage magnetizer, a scanning based design was undertaken with the same parameter increments and ranges.

For capacitances below 7000μF, the maximum level of α predicted under static conditions for a fixture with an axial length of 50mm was 0.32. For capacitances of 7000μF and 10500μF the highest values of α for fixtures which do not violate the electrical and thermal constraints are obtained with a 3x3 bundle of 1.5mm diameter conductors as shown in fig 4.40. This winding arranagement was also the optimal layout for a capacitance of 450 μF, although the peak currents attainable within the thermal limits are higher for 450μF. The reason for this arrangement being the optimum

arrangement over such a wide capacitance range can be deduced from fig 4.23, in which the values of mmf required to achieve the target volume saturation of 90% begin to increase rapidly for conductor bundles having circumferential dimensions of 5mm or greater.

The time to peak of the pulse for the 50mm axial length fixture connected to a capacitance of 10,500μF is 384μs, which is significantly longer than the 87μs time to peak of the pulse produced by connection of the same fixture to a capacitance of 450μF. The effect of this increased time constant on the eddy-currents and the proportion of the percentage volume saturation which can achieved under dynamic conditions was assessed by a dynamic simulation. However, the results of fig 4.41 show that even for this increased pulse duration, eddy-currents inhibit the field penetration to an extent where useful levels of saturation cannot be achieved under dynamic conditions. Increasing the capacitance to 14000μF and higher tends to severely restrict the scope for feasible designs, since for the resulting long duration pulses, the achievable current densities are limited by the thermal constraints to such an extent that the total mmf which can be accomodated within the bore of the rotor is insufficient to produce useful levels of saturation.

The performance predictions and measurements described above demonstrate that a single sided topology, although more efficient from a saturation per unit mmf point of view than a double sided fixture is not suitable for achieving high levels of saturation at the specified level of 1600kA/m. This is due to the fact that the time constants required to achieve penetration of the solid mild steel, and the mmfs required to achieve useful levels of saturation are incompatible with the limited space available within the magnet bore to accomodate the fixture winding, due to the imposed thermal constraint. However, despite their relatively poor performance in terms of producing the rather arbitrary saturation level of 1600 kA/m, a useful level of motor performance

at room temperature can still be realised.

Double sided fixture topology

The problem of excessive temperature rise with long pulse durations can be alleviated by using a double sided fixture since the volume of the winding in a double sided fixture is not so severely constrained, and therefore larger cross-section conductors can be utilised, with a subsequent reduction in the temperature rise for a given fixture current. This increase in winding volume is, however, gained at the expense of a rapid decrease in the volume saturation per unit of fixture mmf. To assess the applicability of the analytical field calculation, the volume saturation versus mmf characteristic for the double sided test fixture of fig 4.42 was calculated by both analytical and finite element techniques. The volume saturation versus mmf characteristic predicted by both methods is shown in fig 4.43.

It will be seen that there is improved agreement between the two methods compared to the agreement for the single sided fixture. In the double sided topology the presence of the conductors within the rotor bore tends to enhance the radial alignment of the magnetizing field, with a resultant increase in the average total path length of the magnetizing flux. As a result of this increased radial alignment, the path length within the rotor mild steel is reduced compared to a field orientation having a significant circumferential component. Therefore the problem becomes more linear than that of the single sided fixture, since there is a decrease in the proportion of the circuit reluctance which is affected by the addtional permeability of the rotor iron and to a lesser extent the permanent magnet. Hence, for the double sided fixture, although the degree of agreement is not as good as for the magnetization of the magnet rings alone, it is adequate to use the analytical method, particularly as its accuracy will tend to improve as the winding dimensions increase.

Electrical design for a double sided fixture.

For a fixture axial length of 50mm and a fixed magnetizer voltage of 780 V the following parameters were varied in the scanning design :

1) Magnetizer capacitances of 21000, 28000, 35000 and 42500 μF were considered.

2) The conductor diameter was varied from 0.5 to 5 mm in 0.5 mm increments.

3) The number of conductors in the circumferential direction was varied from 1 to 5 (subject to the space constraints within the rotor bore).

4) The total number of conductors in the radial direction was varied from 1 to 10. i.e (up to 5 on either side of the magnet subject to the space constraints within the rotor bore).

The addtional 500μF in the maximum capacitance rating is due to the fact that it is achieved by the connection of 5 standard 7000μF trays, one half tray and two nominally quarter trays of capacitors, as opposed to the other capacitances which can be realised by using only the appropriate number of standard 7000μF trays. In order to produce a balanced capacitor arrangement , a nominally quarter bank is in fact 2000μF rather than 1750μF, hence accounting for the additonal 500μF in the maximum capcitance rating of the magnetizer.

Rather than allow the restricted volume within the rotor bore to limit the number of fixture conductors outside the rotor, a symmetrical winding arrangement was only imposed up to the point at which the internal space limit was reached. Beyond this limit the number of fixture conductors was further increased by adding conductors only external to the rotor.

As well as the maximum temperature and current constraints applied to the design of the single sided-fixture, the number of valid designs for assessment was reduced by applying the performance criteria of a volume saturation greater than 70%, and a minimum pulse rise time of 1ms. Although the latter criteria is somewhat arbitrary given the abscence of any dynamic simulation results for a fixture with a rise time of the order of 1ms, it is a reasonable first estimate given that the dynamic simulation for the single sided fixture above shows a considerable modification from the statically predicted volume saturation for a rise time of 384μs. However, the validity of this minimum pulse duration criteria can be assessed subsequently by the dynamic simulation of likely optimal designs, with a re-assessment if the eddy-currents still prevent useful levels of saturation from being achieved.

A total of 2000 designs were analysed, of which 69 valid designs produced volume saturations in excess of 70% with 10 in excess of 75%. The highest level of saturation was 79.1% for a magnetizer capacitance of 42500μF and a fixture with 9 2.5mm conductors on each side of the rotor arranged in 3x3 bundles. The number of designs producing saturation levels in excess of 70% increases for an increasing capacitance, with 7,25 and 37 designs for magnetizer capacitances of 28,000μF, 35000 μF and 42500μF, respectively and no valid designs for a capacitance of 21000μF. The performance of the best fixtures connected to 28,000μF show only a small reduction from the performance of fixtures connected to the larger values of capacitance. This reduction in performance was judged to be acceptable, given that the energy dissipated in the fixture is reduced from a maximum of 14.2kJ for 42500μF to 9.4KJ for 28,000μF, with the subsequent benefits in terms of the attainable cycle time.

The parameters of the 7 fixture designs which produce saturation levels in excess of 70% when connected to a capacitance of 28,000μF are shown in fig 4.44. Fixture

design number 7, whose principal dimensions are shown in fig 4.45 was selected for further analysis, since despite producing 3% less saturation than the maximum in fig 4.44, it produces the longest pulse duration, and hence is the most likely design to realise its statically predicted volume saturation under dynamic conditions. The predicted fixture resistance and inductance in the abscence of the rotor are 32.9$m\Omega$ and 32.3μH.

Dynamic simulation

A dynamic simulation, using the finite element mesh of fig 4.46, was performed for using both 30 and 60 time steps to model a period corresponding to twice the current rise time, resulting in time steps of 7.0μs and 14μs. As for the previous cases, the peak current and saturation level showed minimal differences between the two simulations, thus largely confirming the elimination of significant errors due to the time discretization of the impulse period. The predicted variation in the electrical circuit parameters during the impulse period is shown in fig 4.47. The double sided topology and the presence of a significant region of solid mild steel make this fixture potentially the most sensitive of those which have been analysed in this chapter to variations in inductance due to eddy-currents. Despite the long pulse duration there is a significant variation in inductance, a variation which clearly merits the use the circuit coupled approach adopted in the simulation.

The predicted transient field distributions of fig 4.49 demonstrate that the mutual coupling between the inner and outer fixture windings is dramatically reduced during the initial stages of the transient due the large eddy-currents which circulate in the solid mild steel rotor. The predicted peak current of 12.2 kA under dynamic conditions is however only slightly higher than the 12.0 kA predicted by the linear electrical simulation. Although the variation in inductance is more extreme than for the short

pulse duration fixture used for magnetization the ring magnet alone, the increase in the predicted peak current under dynamic conditions compared that predicted by the linear electrical simulation is much smaller than for the magnetization of the ring magnet alone, viz. 1.6% and 6% respectively. This is due to the fact that the inductance used in the linear electrical simulation neglects the effect of the mild steel, and hence underestimates the static inductance. The additional permeability in the non-linear solution tends to increase the inductance, and hence reduce the magnitude of the current pulse compared to the linear electrical simulation, whereas eddy currents tend to reduce the inductance.

The relative magnitude of the effects of an increased permeability and the eddy current screening depend on the pulse duration and the degree of saturation of the iron. For the rise time of 1.2ms produced by the double sided fixture of fig 4.45, the effects cancel each other to an extent where the analytically calculated inductance is a reasonable approximation, even though it neglects both of these non-linear effects, which are each significant in this case. For the magnetization of the magnet ring on the other hand, the short duration pulse and the low permeability of the magnet dictate that the eddy-currents dominate, with a resultant decrease in the fixture inductance in the dynamic simulation compared to the value utilised in the linear electrical simulation. In the three cases studied for the magnetization of the magnet ring and the assembled rotor the peak current increased in the dynamic simulation to a greater or lesser degree. However, for a pulse of sufficient duration, the presence of any permeable electrically conducting components in the problem domain will reduce the peak current from that predicted in the linear electrical simulation.

Predicted transient field distributions at selected instants during the pulse are shown in fig 4.49, and indicate that near full penetration of the rotor is achieved. As a result the volume saturation of 71.3% predicted by the dynamic simulation is in good

agreement with the 70.4% predicted by the static analytical field calculation utilised in the electrical design stage. The peak saturation level is achieved at 1.30ms, which although later than the peak of the current at 1.20ms, demonstrates the relatively small modifying effect of eddy currents on the field distibution in the vicinity of the current peak. Further, the agreement between the volume saturations predicted by the dynamic simulation and linear analytical field calculation demonstrate the applicability and accuracy of the analytical calculation in this particular problem environment.

Calculation of motor performance

The predicted distribution of the preferred and non-preferred orientation demagnetization characteristics within the magnet volume are shown in fig 4.50. These were again used in a series of magnetostatic field solutions to predict the subsequent performance of the magnetized rotor in the assembled motor. The series of predicted static field distributions as the rotor is rotated are shown in fig 4.51, whilst the predicted motor flux-linkage and phase emf are shown in figs 4.52 and 4.53. For the double sided fixture, although 71.3% is exposed to a magnetizing field in excess of 1600 kA/m, only 80.0% of the magnet volume is exposed to a field in excess of 1000 kA/m, compared to 85.6% achieved with the single sided fixture. Hence despite the fact that the volume which is exposed to a magnetizing field in excess of 1600 kA/m is significantly higher than for the short pulse duration single sided fixture, 71.3% and 31.5% respectively, the peak motor flux-linkage is slightly lower than for the single sided fixture, 21.6mWb and 21.7mWb respectively.

4.7 POST-ASSEMBLY MAGNETIZATION.

The post-assembly magnetization of the complete motor is the preferred production route, but is the most onerous in terms of both fixture design and magnetizer energy requirements. This difficulty is principally due to the presence of the mild steel of the

rotor which separates the magnet from the external fixture winding. The solid rotor iron which is particularly thick in this case, since the motor has low pole number and a high magnetic loading, has three principle detrimental effects with regard to the magnetization:

i) The conductors are forced to be remote from the magnet, and therefore the radial alignment of the magnetizing field produced by the fixture is inherently much worse than that which can be achieved with a fixture placed close to the magnet surface.

ii) The mild steel rotor core acts as a short-circuit to the magnetizing flux produced by the fixture winding. At field levels required for saturation of the magnet, typically 3.2T, the mild steel relative permeability of 2.56 is sufficient to promote circumferential leakage of flux, resulting in the magnet being exposed to a decreased and less radially aligned magnetizing field.

iii) The eddy-current shielding of the magnet is worse in this case than for the magnetization of the assembled rotor alone. In the case of a single sided fixture located within the bore of the assembled rotor, the eddy-currents in the rotor steel reduced the net field to which the magnet was exposed. Nevertheless, the magnet was still exposed to a significant magnetizing field even though it did not fully penetrate the rotor steel. However, for the case of post-assemby magnetization, the magnetizing field must first fully penetrate the steel in order to expose the magnet to any significant magnetizing field.

Selection of the field calculation method

For the 12-slot stator and 4-pole magnetizing fixture, there are two relative alignments for which the symmetry of the problem region can be exploited to reduce the finite element model to a 45^{o} segement, viz. a slot opening or a tooth axis directly

opposite the interpolar axis of the fixture. The presence of the stator lamination material at a given point on the airgap periphery will promote the flow of radial magnetizing flux at that point, since even at the field levels required for saturation of the magnet, the stator lamination it is typically 2.5 to 3 times more permeable than air. The region near the pole transitions has been previously shown to be the most difficult to saturate, and hence the preferred stator/fixture alignment is with centre of a tooth directly opposite the interpolar axis of the fixture.

The test fixture of fig 4.54, in which a single 2mm diameter conductor per pole is located 1mm from the outer surface of the rotor, was used to assess the applicability of the analytical field calculation. A close-up of the finite element mesh used is shown in fig 4.55. The entire mesh consists of 4750 nodes and 9209 elements with a discretization in the magnet which is identical to that used in the corresponding stage of the design for the magnetization of the assembled rotor, viz one division per 1^{o} tangential and one division per 0.25mm radial.

The percentage volume saturation versus mmf characteristics predicted by both the non-linear finite element and analytical methods for the test fixture are shown in fig 4.56. The non-linear finite element method predicts a higher saturated volume at a given value of mmf than the analytical method. Although the mild steel acts a short-circuit to a proportion of the magnetizing flux, its additional permeability compared to air together with that of the stator laminations ensures that the radial magnetizing field in the magnet is greater than that which would exist in their absence. In view of the effect of the material non-linearities on the predictions, the subsequent phases of the design were based on the finite element technique.

The predicted field distribution for a static applied mmf of 240 kA/m for the test fixture is shown in fig 4.57. It demonstrates that the remoteness of the fixture winding

results in a relatively poor alignment between the magnetizing field and the preferred radial orientation of the magnet over a large proportion of the magnet, with particularly poor alignment near the pole transition regions. This accounts for the relatively low value of volume saturation, at which the incremental slope of the volume saturation / mmf characteristic levels off in fig 4.56. The remaining volume is then only saturated by the application of a greatly disproportionate increase in mmf. Thus, the achievable levels of magnet saturation with practically realisable mmfs are likely to be lower than for the magnetization of either the magnet alone or of the assembled rotor.

The difficulty in achieving the required radial alignment is also highlighted in fig 4.58 which shows the variation of the radial component of flux density with angular displacement from the pole transition. For the applied magnetizing mmf of 240 KA per pole, the magnitude of the flux density is well above that required for complete saturation of the magnet, but the poor radial alignment is such that the pole transition region of the magnet is exposed to a radial field component which is insufficient to ensure saturation.

The effect of the stator slotting is shown by the small undulations in the profile of the radial magnetizing field. However, providing the minimum value of these undulations is above the saturating field strength, the stator slotting will not cause non-uniformity in the resulting remanent magnetism. The onerous requirements of post-assembly magnetization are demonstrated in fig 4.59, which compares the predicted volume saturation/mmf characteristic for the post-assembly test fixture, with the equivalent concentrated winding fixture for the magnetization of the assembled rotor alone.

As for the magnetization of the assembled rotor, the calculation of an extensive series of complete saturation/mmf characteristic is prohibitive, particularly as the

fixture winding is dimensionally far less constrained than the internal winding used for the magnetization of the assembled rotor. The approach of calculating the mmf required to achieve a target level of saturation was therefore adopted again. Since the results of fig 4.59 indicate that post-assembly magnetization is a far more onerous task than magnetizing the rotor alone, the volume saturation target was reduced to 70%.

The predicted magnetizing mmf per pole required to achieve this volume saturation for a wide range of bundle dimensions is shown in fig 4.60. Even for the reduced target saturation, the field levels required are higher than with the corresponding bundle dimensions for the magnetization of the assembled rotor. Nevertheless, the remoteness of the fixture conductors from the magnet does make the mmf required to achieve the target saturation less strongly dependant on the disposition of the fixture conductors than was the case for the magnetization of the assembled rotor. This implies that there is greater scope to use a high number of large cross-section conductors, a useful feature given that a long duration pulse is likely to be necessary to ensure that near static field conditions are established.

Electrical Design Phase

The dynamic simulation results and the experimental measurements for the magnetization of the assembled rotor demonstrated that the high voltage/low capacitance magnetizer is not suited to this particular environment. Therefore, since the problems of eddy-currents are likely to be aggravated in post-assembly magnetization as outlined above, the electrical design was based on the low voltage / high capacitance magnetizer. For the maximum magnetizer voltage of 800V and capacitances of 42500, 35000 and 28000μF, the following fixture parameters were scanned:

1) The conductor diameter was varied from 0.5 to 5 mm in 0.5 mm increments.

2) The number of conductors in the circumferential direction was incremented from 1 to 5.

3) The number of conductors in the radial direction was incremented from 1 to 10.

4) The fixture axial length was varied from 30mm to 50mm in 10 mm increments.

With these scanning increments; a total of 4500 designs were analysed. However, a large number of these failed to meet the maximum temperature and peak current constraints of 200°C and 30 kA respectively. The number of valid designs was reduced further by imposing the minimum performance criteria of α being at least 1.0, and a current pulse time to peak of at least 1ms.

A total of 81 fixtures met these performance criteria, with 39, 27 and 15 valid designs being obtained for fixture axial lengths of 30,40 and 50mm respectively. Of these valid designs, 56 were with a capacitance of 42500μF, and 25 with 35000μF whilst a capacitance of 28000μF failed to yield any valid designs. The highest value of α of all the valid designs was 1.23 for a fixture having an axial length of 30mm, and 20 3.0mm diameter conductors per pole arranged in a 4 wide by 5 deep array. Of the 81 valid designs, 35 produced α values in excess of 1 1, with 22, 10 and 5 valid designs for fixture axial lengths of 30, 40 and 50mm respectively.

Since the values of α which are achievable with the 50mm axial length fixtures are comparable to the best 30mm and 40mm axial length fixtures, the axial length for the final design was set to 50mm, because of the inherent advantage in terms of end-winding field distortion. This also allows a more direct comparison with the 50mm fixtures which were designed for magnetizing both the magnet ring and assembled rotor. The parameters of the 15 valid designs with axial lengths of 50mm are shown in fig 4.61. The highest predicted value of α is 1.11, which is achieved by design 9.

However, it suffers from the drawback of using 4mm diameter conductors, which are very difficult to form into accurate compact windings in such a small fixture. The value of α for design 7, which is based on 3mm diameter conductors, is only some 3% lower than than that of design 9. Despite its slightly lower predicted value of α than that for design 9, the increasing difficulty in forming neat end-windings for the larger cross-section conductor, and hence achieving the predicted fixture impedance, will inevitably reduce the difference in saturation which can be realised in practice. Hence, since no valid designs were achieved with smaller cross-section conductors, design number 7 was selected for further investigation. The parameters of fixture design 7 are identical to those of design 13. However, the lower capacitance in design 13 reduces the predicted value of alpha to 1.00. The principle dimensions of design No. 7 are shown in 4.62.

Dynamic simulation.

The 1.22 ms current rise time of design no.7 is very similar to the 1.20ms of the double sided fixture for the assembled rotor in which the statically predicted level of saturation was realised under dynamic conditions. Nevertheless, the inherently larger shielding of the magnet associated with a fixture toplogy in which a conducting and permeable material separates the magnet from the magnetizing winding, dictated that a dynamic simulation should be undertaken in order to establish the extent of the modifying effects of eddy-currents in design no.7. The finite element mesh of fig 4.63 used in the simulation, consisted of 5208 nodes and 10,094 elements with the same discretization within the motor as was used for the finite element estimation of the static mmf requirement.

The lamination material has a bulk electrical conductivity of 2.04×10^6 Sm^{-1}. However, the laminated structure of the stator ensures that the eddy-currents which

flow in the stator during the impulse period are substantially reduced from those which would flow in an solid stator of the same material. Since a two-dimensional model cannot account for the laminated structure of the stator, and the magnitude of the eddy-currents cannot be established without recourse to a full three-dimensional field calculation, for the purpose of the dynamic simulation, the conductivity of the laminations was assumed to be zero. Neglecting the eddy-currents in the lamination material is unlikely to significantly affect the magnetizing field in the permanent magnet, since the dominant eddy currents are induced in the mild steel of the rotor back-iron which as well as being solid, has an electrical conductivity of 7.62×10^6 Sm^{-1}, i.e 3.8 times that of the lamination material.

The predicted variation in electrical circuit parameters is shown in fig 4.64. The inductance variation is relatively smooth compared to the previously analysed fixtures for magnetizing the assembled rotor, resulting in a peak current of 23.1kA as compared to the 22.8kA predicted by the linear electrical simulation. A series of predicted field distributions at selected instants during the impulse period is shown in fig 4.65, in which the modifying effect of eddy-currents on the field distribution during the initial stages of the magnetizing pulse are clearly visible. However, a predicted volume saturation of 68.0% is achieved, which compares favourably with the 71.3% predicted by a static field calculation using the peak current of 22.8kA predicted in the linear electrical simulation. However, the instant at which the peak percentage saturation occurs during the pulse shows a marked shift from the peak of the fixture current, as shown in fig 4.66. This shift is indicative of eddy-current effects, and accounts for the slight reduction in volume saturation compared to that predicted for static conditions.

The distribution of the demagnetization characteristics in the magnet following the decay of the magnetizing pulse is shown in fig 4.67. The predicted distributions of magnet properties were subsequently utilised in a series of magnetostatic field calcu-

lations in order to predict the open-circuit performance of the motor as the rotor is rotated in 3^{o}(mech), fig 4.68. The resulting flux-linkage and induced emf waveforms predicted for the post-assembly magnetized motor are shown in figs 4.68 and 4.69. The rounding off of the peak of the flux-linkage waveform is more pronounced than was the case for the magnetization of the magnet ring and the assembled rotor.

Experimental Results.

The measured and predicted fixture inductances are 20.4μH (at 1kHz) and 17.9μH respectively, whilst the measured and predicted fixture resistance are 15.2$m\Omega$ and 13.5$m\Omega$ respectively. The error between the measured and predicted parameters can be attributed largely to the practical problems in constructing the fixture, since the large cross-section of the conductors make the forming of neat end-windings difficult, and hence there is inevitably an increase in the impedance of the constructed fixture as compared to the predicted value. The error between the measured and predicted parameters highlights the fact that in selecting likely optimum fixture designs with very similar performance, preference should be given to those having the smallest usable cross-section conductors. In this case the minimum suitable conductor diameter for which a fixture design met the performance specification was the selected value of 3.0mm.

The motor shaft, which is connected to the stator in the external rotor motor, was attached to a graduated angular scale in order to reliably establish the appropriate fixture/stator alignment. The angular reference position was established by removing the rotor and rotating the stator until the voltage induced in a designated phase winding during a pulse was a minimum. Rotation of the motor through one pole pitch produced no discernable inconsistency in the position of the maxima and minima of the induced

voltage, thus establishing an acceptable symmetry in the field produced by the fixture.

The worst case of induced voltage in one phase of the motor windings occurs when the interpolar axes of the motor phase winding and the fixture winding are aligned, a case which cannot be modelled with the 45^{o} mesh segment of fig 4.63. The measured magnetizing current and worst case induced voltage waveforms are shown in fig 4.71. The measured peak current of 22.7 kA is in good agreement with the 23.1 kA predicted by the dynamic simulation. The effect of eddy currents in the rotor steel can be observed by the delay between the peak rate of change of current, which occurs at the initiation of the pulse, and the peak of the voltage induced in the motor windings.

The eddy-currents induced in the rotor are beneficial in greatly reducing the transient voltage induced in the fixture winding. The peak of this transient is well within the voltage rating of the insulation and the slot liner, but is of a sufficiently high magnitude which could preclude the magnetization of the motor when connected to its associated drive electronics. Despite the high rate of change of field experienced by the rotor position sensing Hall-effect devices, they remained fully functional after the impulse magnetization.

The motor phase flux-linkage and emf waveforms of fig 4.72 were measured by driving the motor at a constant speed of 800 rpm using the slotless motor/inertia disc arrangement described earlier. The flux-linkage shows a marked rounding of the waveform, a feature which is indicative of weakly magnetized pole transition regions. The measured peak-peak magnitude of 41.2 mWb for the flux-linkage is in good agreement with the predicted value of 42.6 mWb, bearing in mind that the oscilloscope resolution is equivalent to 0.4 mWb. The predicted and measured emf waveforms also show reasonable agreement, although there are minor differences in harmonic content.

Post-assembly magnetization utilising the motor windings

In addition to post-assembly magnetization of the motor with an external fixture the feasibility of using the actual motor windings to produce the magnetizing field was also investigated. Each phase winding of the motor consists of 60 turns of 0.4mm diameter wire. The static volume saturation versus mmf characteristic predicted by finite element analysis for excitation of both one and two phases is shown in fig 4.73. They demonstrate that in this case excitation of a single phase winding is the most effective. The mmf required to achieve the 70% volume saturation corresponds to a current in each conductor of 4,180A. For a final temperature limit of 200^{o}C, the maximum acceptable pulse duration was estimated to be 34μs by approximating the pulse to a transient half-sine wave.

The scope for achieving a maximum pulse duration of 34μs is severely restricted by the fixed inductance and resistance of the motor windings, which in are 0.24 mH and 0.78 Ω per phase respectively. To simultaneously achieve both a peak current of 4,180A and a rise time of 34μs with such a large motor time constant is clearly unfeasible since it would require a magnetizer capacitance of 1.72μF and voltage of 52 kV. Thus, post-assembly of this motor by passing current through the existing motor windings was not pursued.

Post-Assembly Magnetization of Internal Rotor Machine

An internal rotor machine designed to the same performance specification as the external rotor machine of fig 4.1 is shown in fig 4.74. The post-assembly magnetization of the internal rotor machine is considerably more onerous than the external rotor machine due to the greatly increased remoteness of the fixture winding from the

magnet, particularly since an outer aluminium casing is necessary to attatch the motor end-plates. The volume saturation versus mmf characteristic for a fixture with a single 2mm diameter conductor located 1mm from the motor case, predicted by finite element analysis, is shown in fig 4.75, together with the corresponding characteristic for the external rotor machine. The low value of volume saturation at which the characteristic levels off, indicates that an acceptable volume can only be saturated with a very high mmf. Clearly, the post-assembly magnetization of the internal rotor machine is by far the most onerous case, to the extent that the magnetization of a useful volume of the magnet was considered to be unfeasible.

4.8 CONCLUSIONS

The results of the case studies are summarised in fig 4.76. The width of the flat top of the nominally trapezoidal emf waveform shown in fig 4.76 is the width, in electrical degrees, over which the emf is greater than 90% of the value at the mid-point of the flat-top which would be obtained with an idealised magnet. For all the possible magnetization strategies employed, useful, although not maximum, magnet performance can be realised. In each case the magnitude of the emf flat top shows only a small reduction from that which would be achieved with a fully saturated magnet, whilst the predicted narrowing of the flat-top for each case does not reduce it to less than the minimum stipulated value of 120^{o} electrical. Hence, the magnetization of the external rotor can be satisfactorily undertaken at any stage during manufacture of the device, although the required magnetizer stored energy, and hence fixture energy loss, increases significantly for the more convenient sub-assembly and post-assembly magnetization.

The magnetization of the ring magnet alone can be easily achieved and the design of an appropriate fixture is straightforward, by virtue of it being based on analytical methods and the minimal effect of eddy-currents under dynamic conditions. The

inclusion of the mild steel rotor back-iron for the magnetization of the assembled rotor and post-assembly magnetization adds significant complexity to the fixture design process, although in the case of the double sided fixture for the assembled rotor, the analytical method can still be applied with an acceptable accuracy. However, this case study clearly demonstrates the utility of a dynamic simulation facility in the design of fixtures for assemblies which contain significant regions of solid conducting soft magnetic materials.

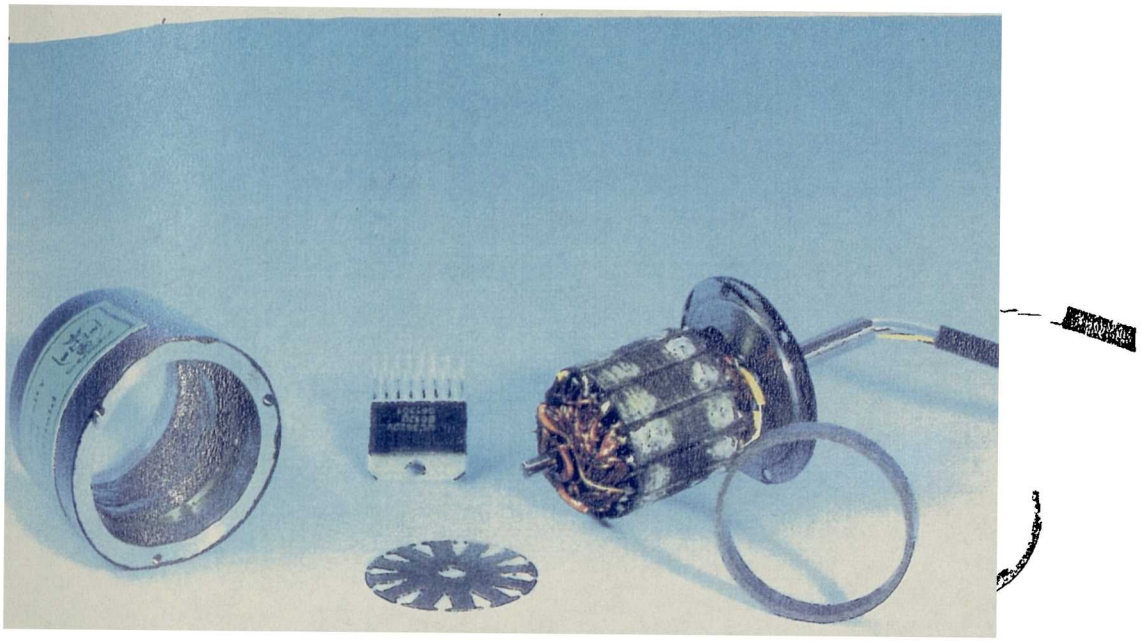

Fig 4.1 External rotor 3 phase brushless d.c machine with associated drive electronics.

Rated voltage	35V
Rated output power	52.3 W
Rated torque	0.1 Nm
Rated speed	5000 rpm
Rated operating temperature	50°C (for a 20°C ambient)
Starting torque	1.25 Nm
Magnetic loading	0.68T
Electric loading	6A/mm
Poles	4
Slots	12

Stator o.d	31 mm
Rotor o.d	46.5 mm
Airgap	0.5mm
Magnet thickness	1.5 mm
Active length	22.7 mm
Phase resistance	0.78 mΩ
Phase inductance	0.24 mH
Wire diameter	0.4mm
Winding Packing factor	0.25

Fig. 4.2 Performance specification and parameters of the motor of fig 4.1.

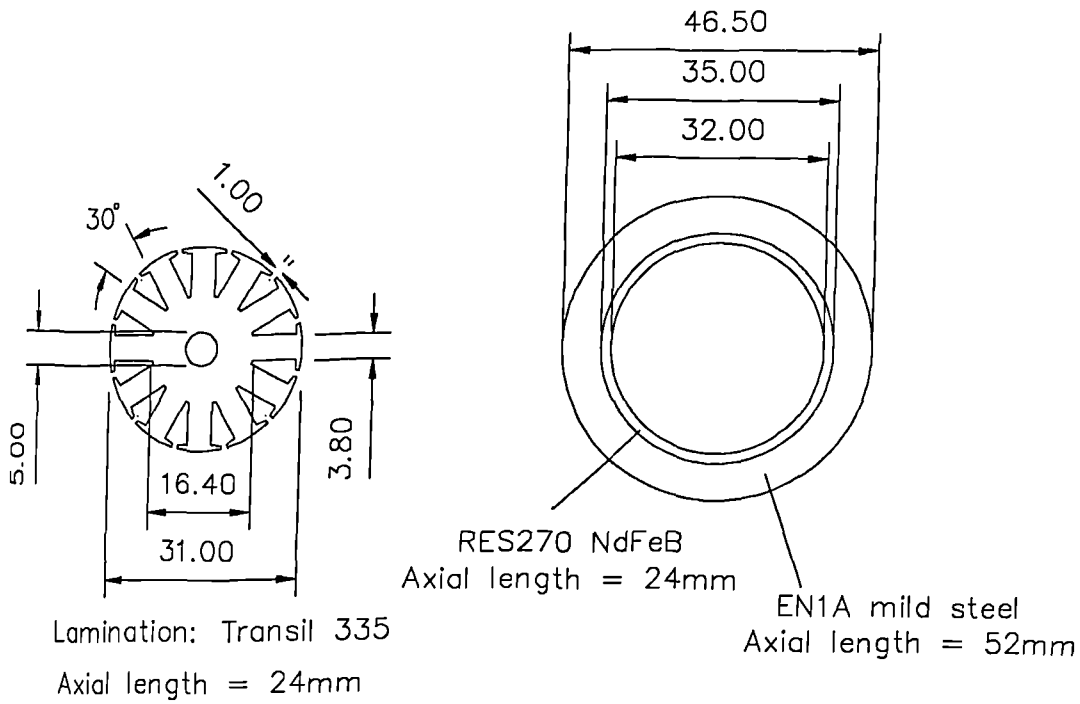

Fig. 4.3 Leading dimensions of the motor of fig 4.1

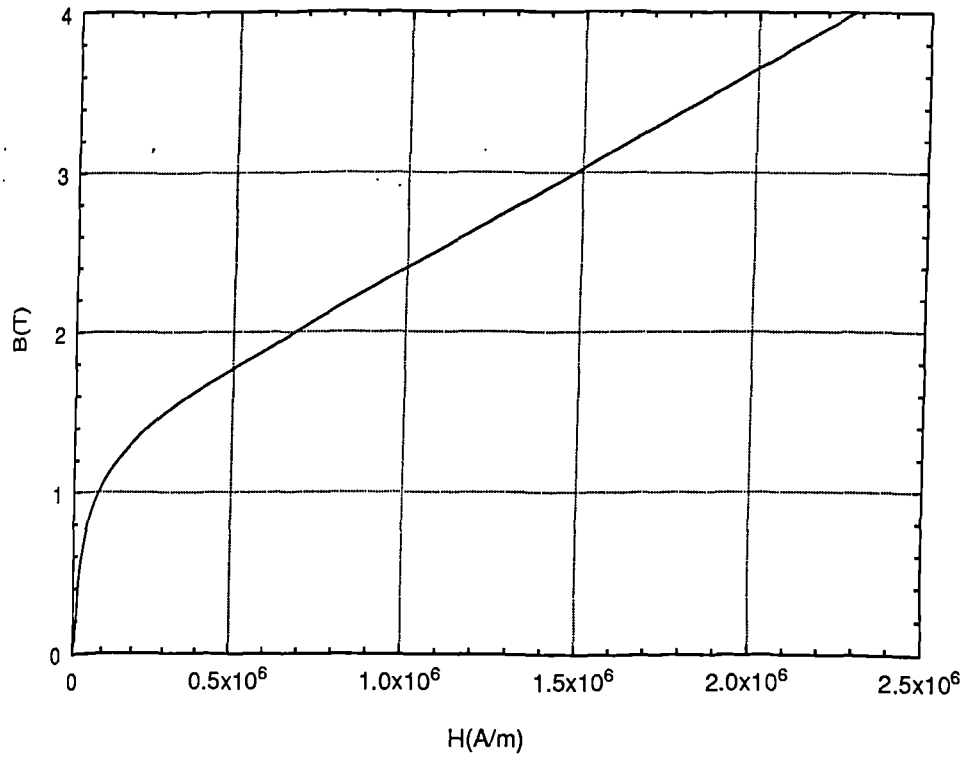

Fig. 4.4 Measured initial magnetization curve for Philips Components RES270 sintered NdFeB.

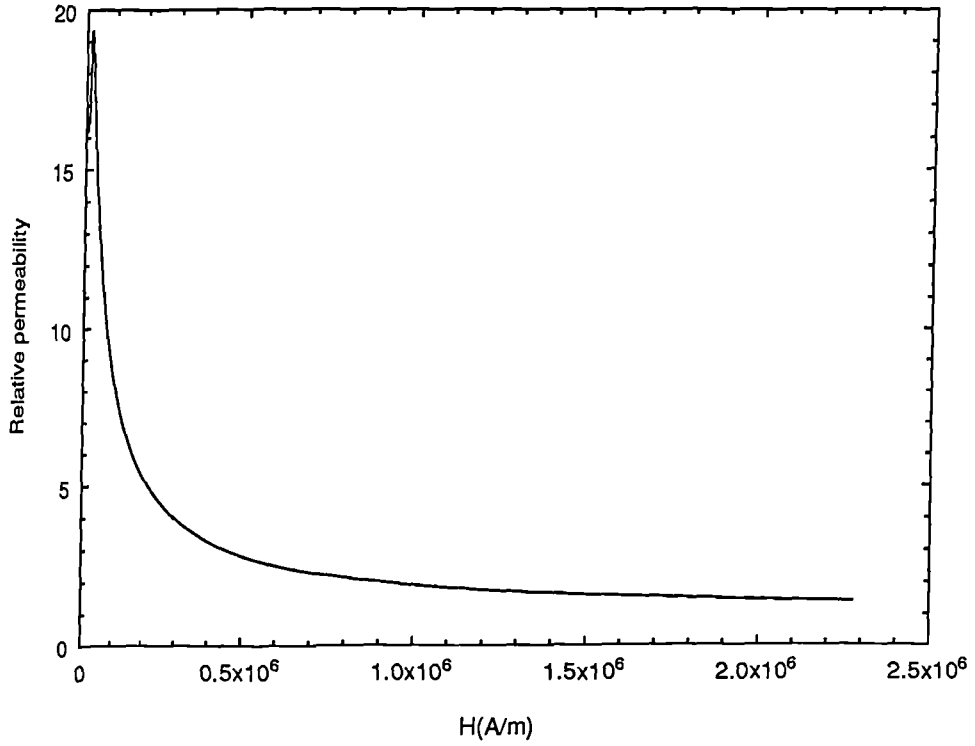

Fig. 4.5. Variation of the relative permeability of the initial magnetization curve of Philips Components RES270 sintered NdFeB with the applied magnetizing field.

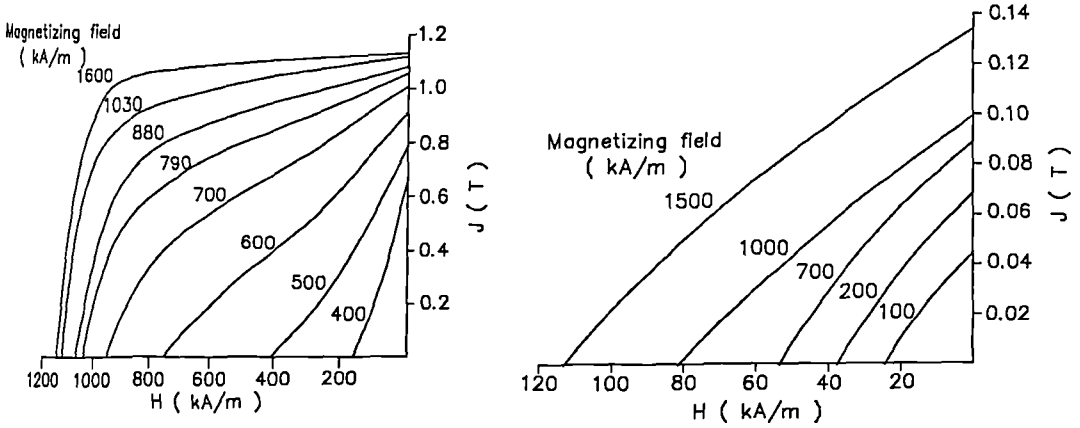

Parallel to the preferred direction

Perpendicular to the preferred direction

Fig. 4.6 Measured dependance of the room temperature demagnetization curves of Philips Components RES270 sintered NdFeB on the magnitude of the initial magnetizing field.

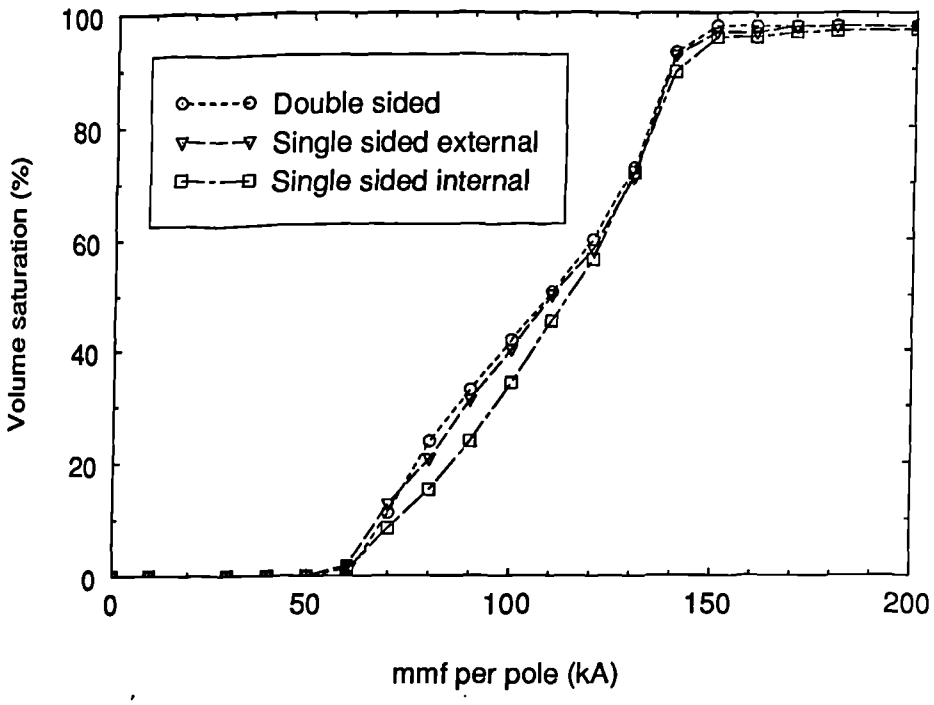

Fig. 4.7 Predicted static volume saturation versus mmf characteristics for equivalent single sided internal, single sided external and double sided fixture topologies.

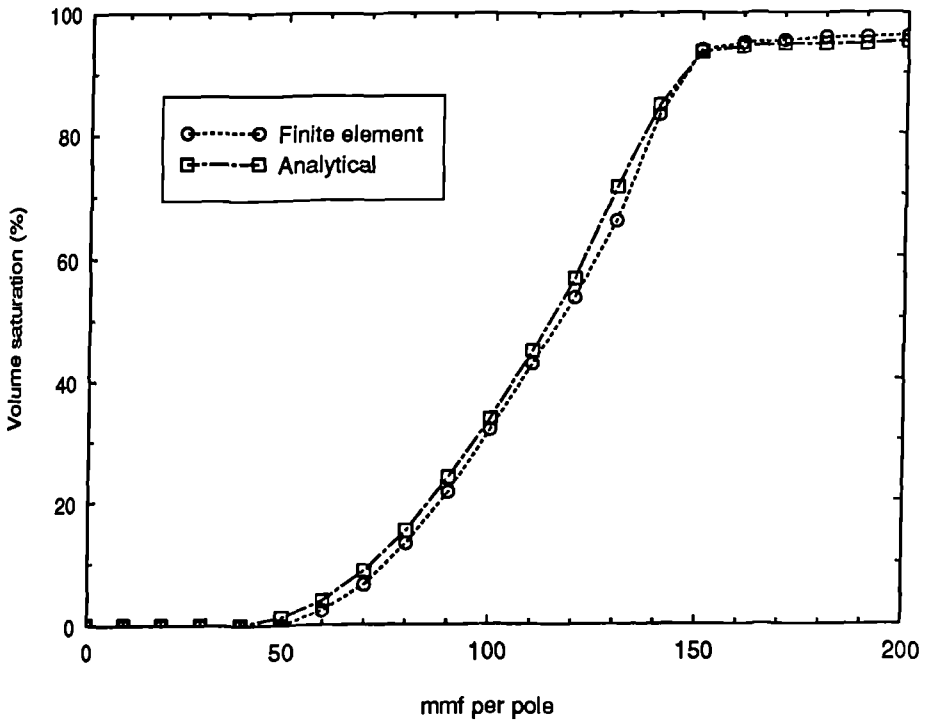

Fig. 4.8. Percentage volume saturation versus mmf characteristics predicted by the analytical and finite element techniques for the magnetization of the magnet alone (Double sided fixture with a single 1mm diameter conductor on either sides of the permanent magnet).

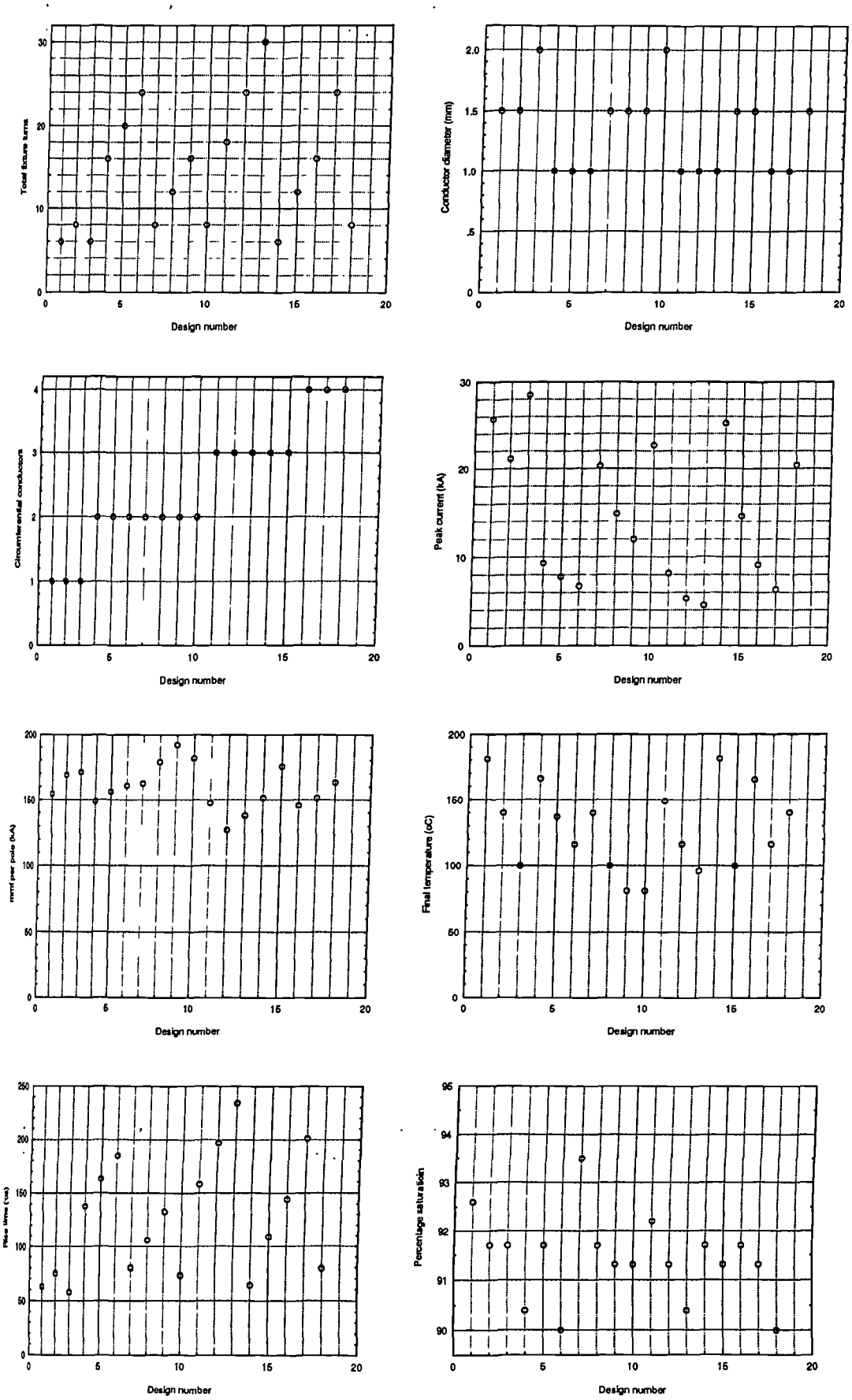

Fig. 4.9 Valid designs of double sided air-cored fixtures with axial lengths of 50mm. (C=450 μF , V = 3000V).

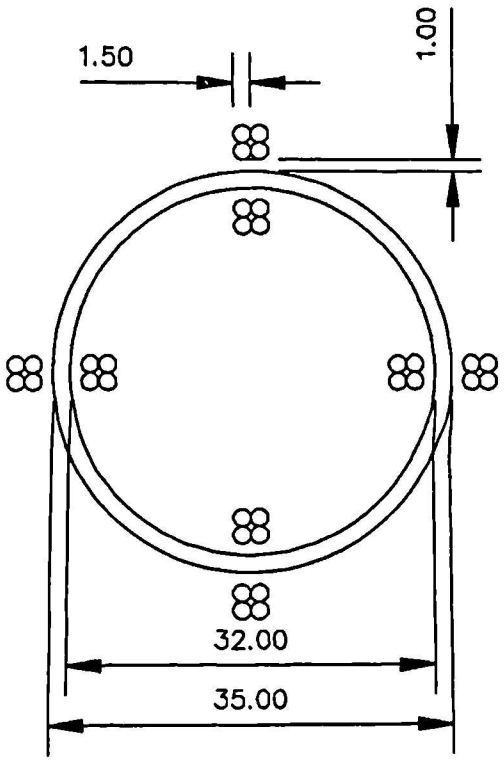

Fig.4.10 Principal dimensions of design No.7 selected for further analysis.

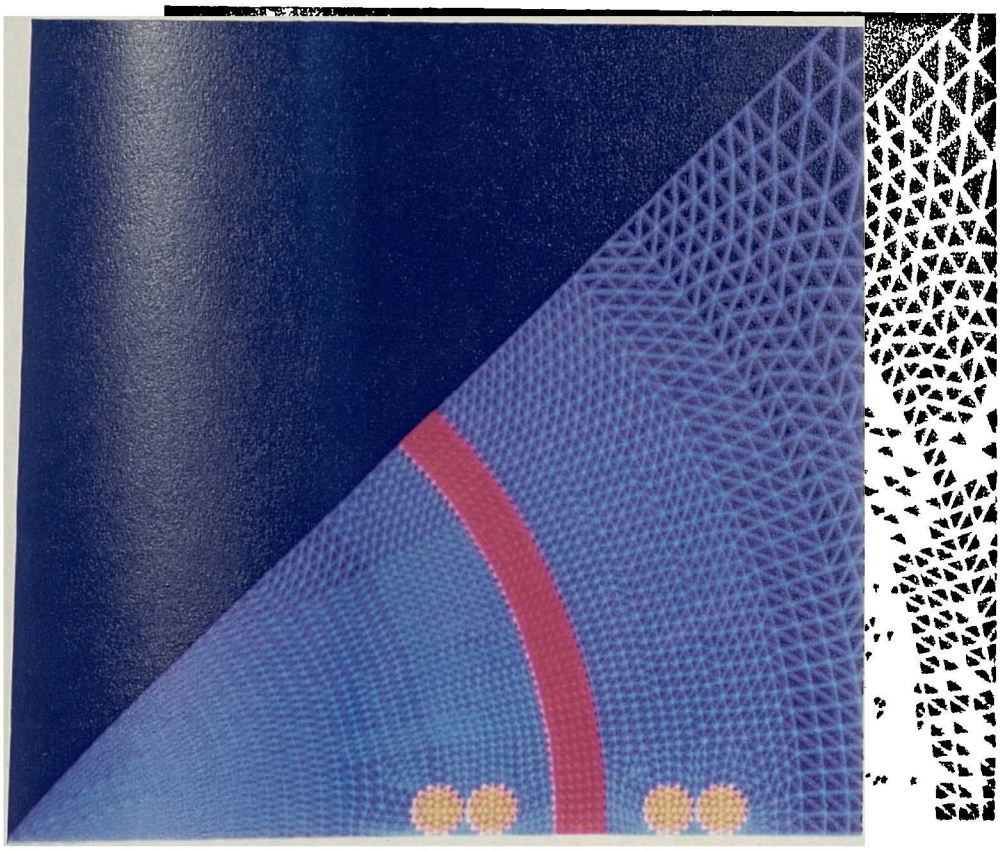

Fig. 4.11 Close-up of the magnet and fixture region of the finite element mesh used in the dynamic simulation of the magnetization of the magnet ring alone. (Total number of nodes and elements in the mesh 2823 and 5442 respectively).

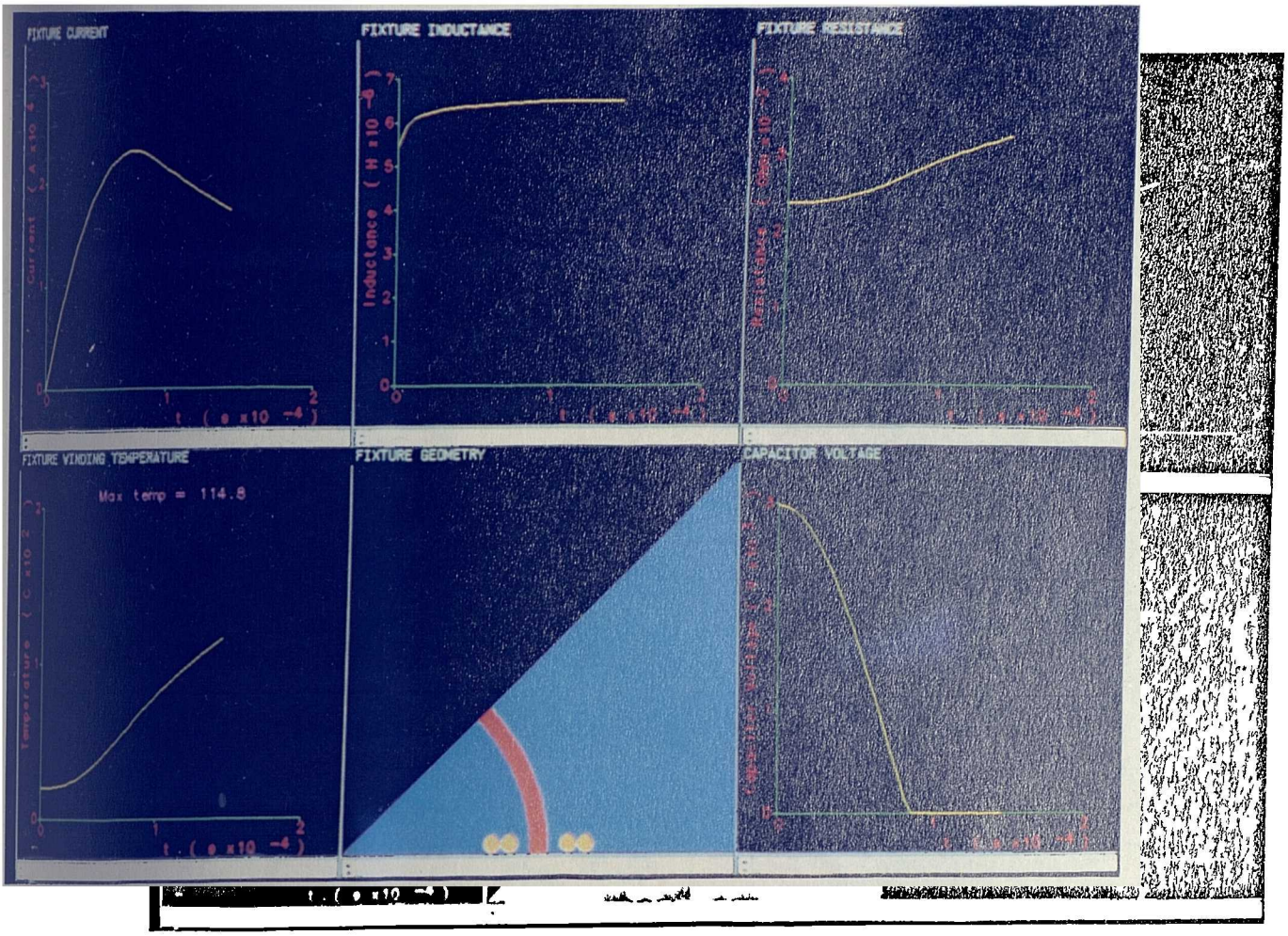

Fig. 4.12 Predicted variation in the electrical circuit parameters during the

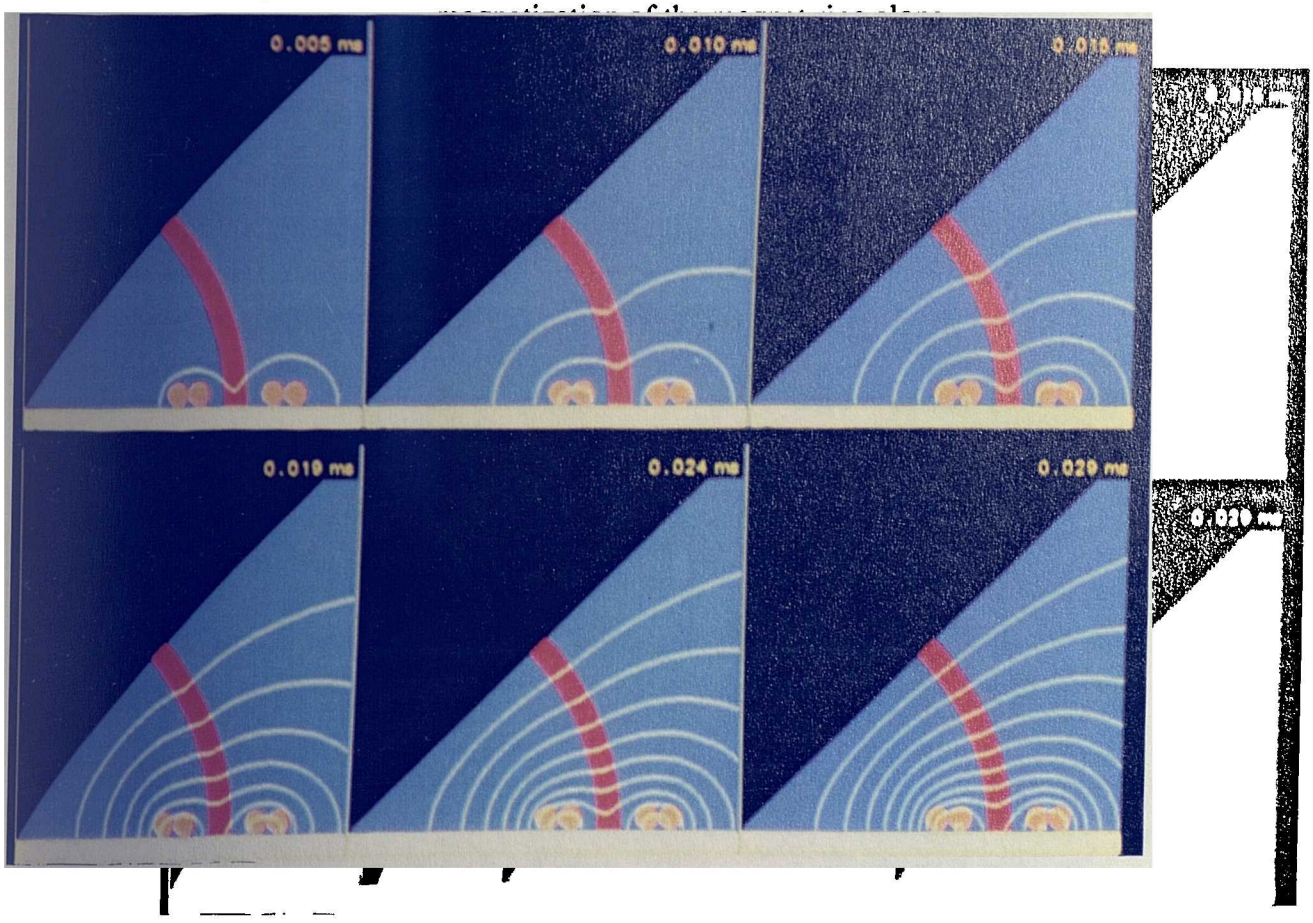

Fig. 4.13 Predicted field distributions at selected instants during the initial stages of the pulse, demonstrating the screening effect of eddy-currents.

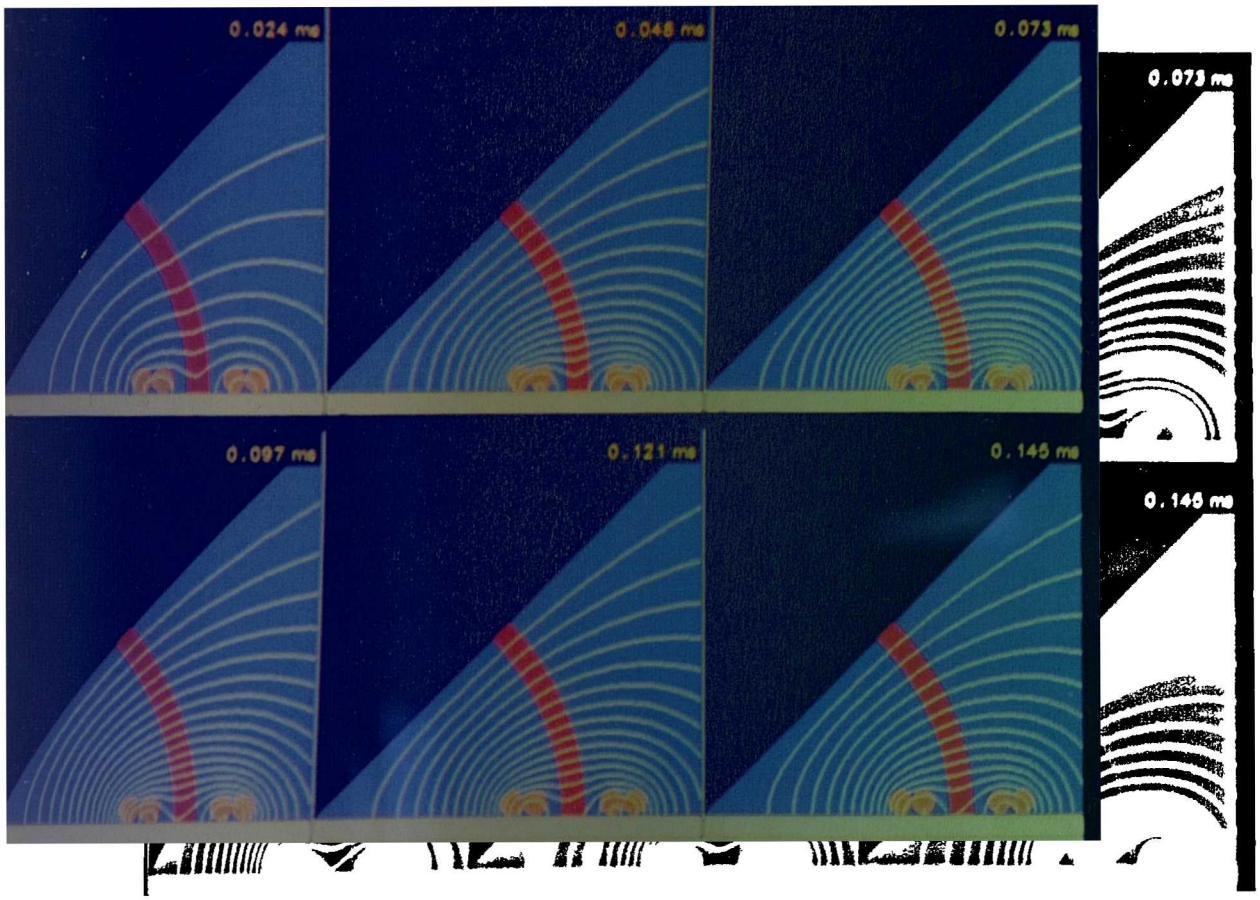

Fig. 4.14 Predicted field distributions at selected instants during the magnetization of the magnet ring alone.

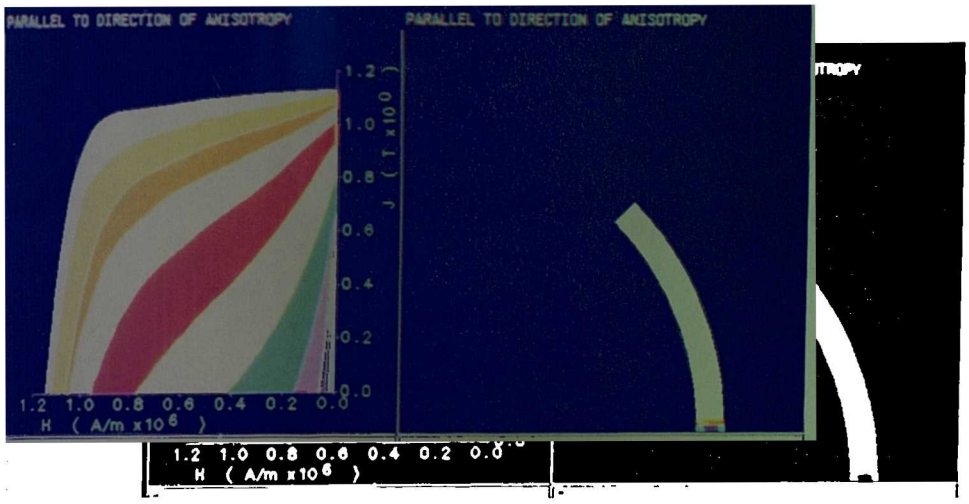

Fig. 4.15 Predicted distribution of demagnetization characteristics in the preferred radial direction following the decay of the magnetizing pulse.

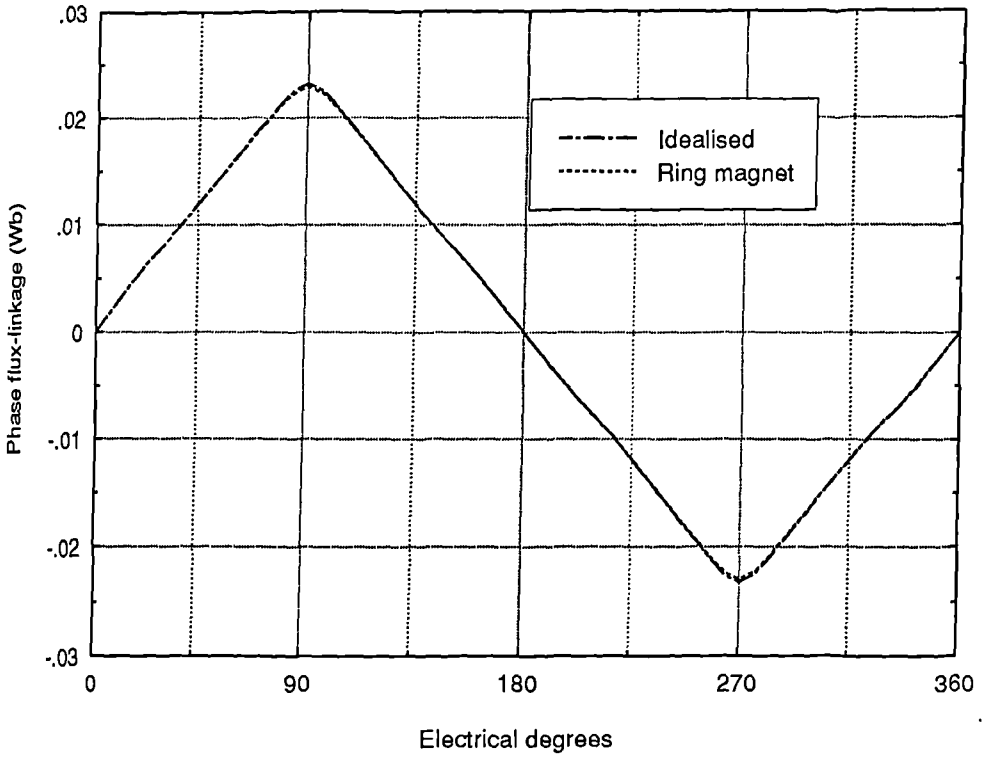

4.16 Predicted phase flux-linkage waveforms for the simulated magnet and an idealised fully saturated magnet.

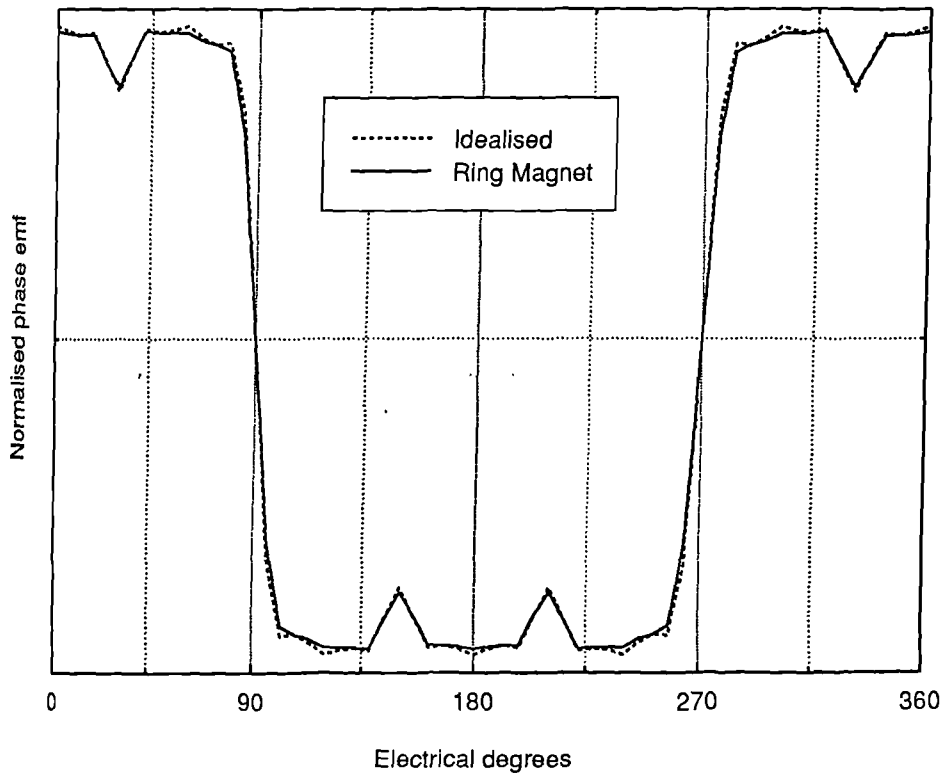

4.17 Predicted normalised phase induced emf waveforms for the simulated magnet and an idealised fully saturated magnet.

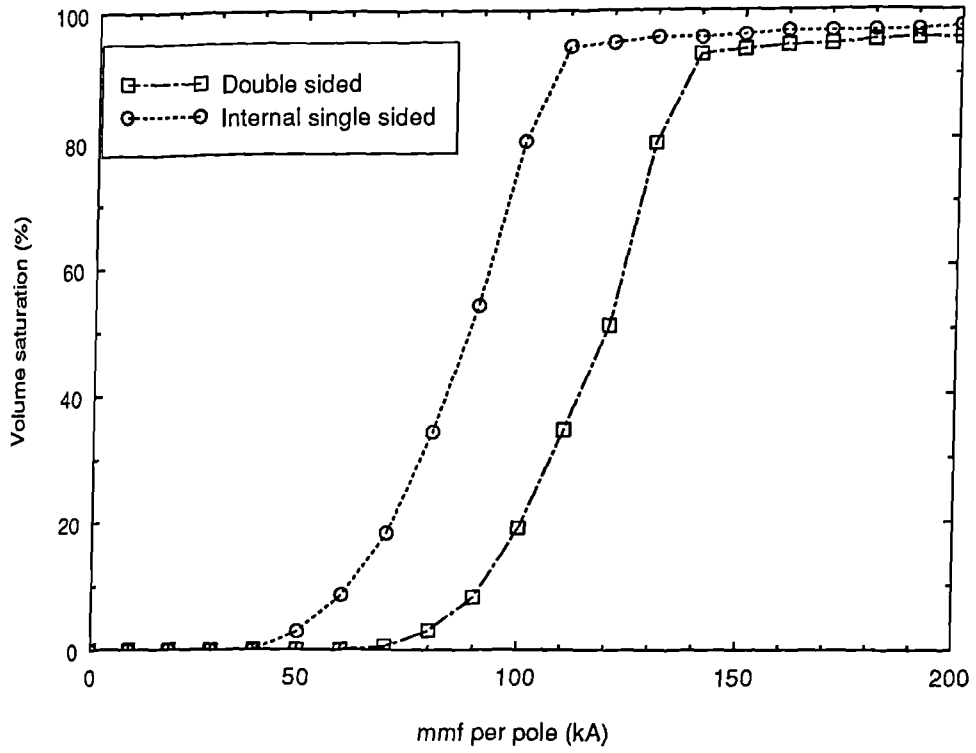

Fig. 4.18 Volume saturation versus mmf characteristics predicted by the non-linear finite element method for equivalent internal single sided and double sided fixtures.

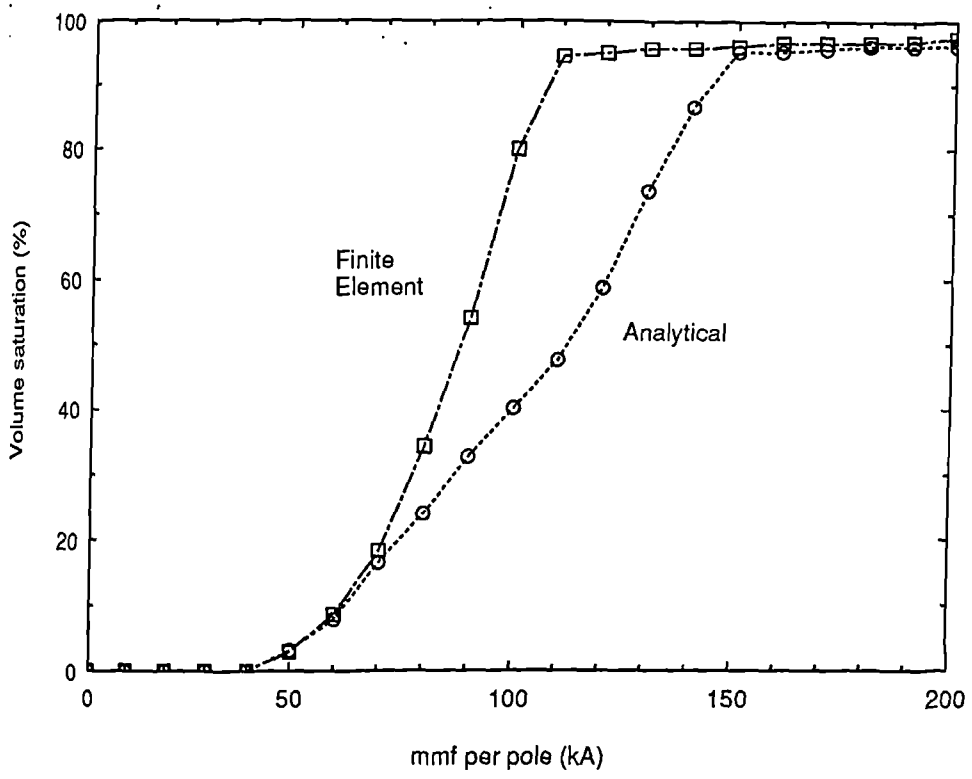

Fig. 4.19 Volume saturation versus mmf characteristics predicted by both the analytical and non-linear finite element methods for an internal single sided fixture

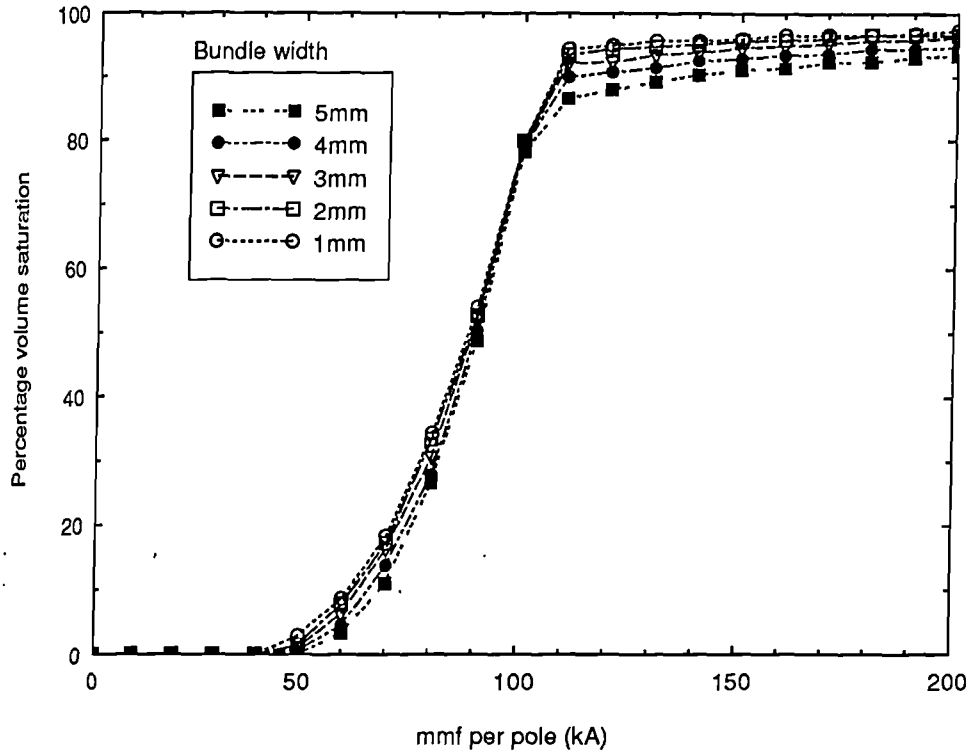

Fig. 4.20 Finite element predicted volume saturation versus mmf characteristics for internal single sided fixtures with conductor bundles 1mm deep and widths between 1 and 5mm.

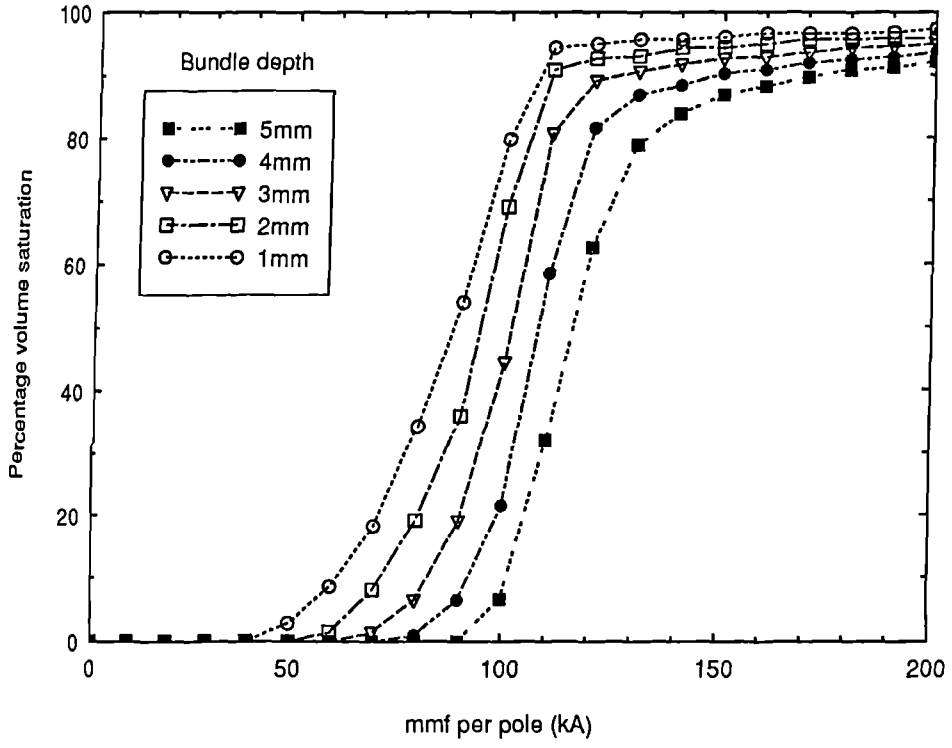

Fig. 4.21 Finite element predicted volume saturation versus mmf characteristics for internal single sided fixtures with conductor bundles 1mm wide and depths between 1 and 5mm.

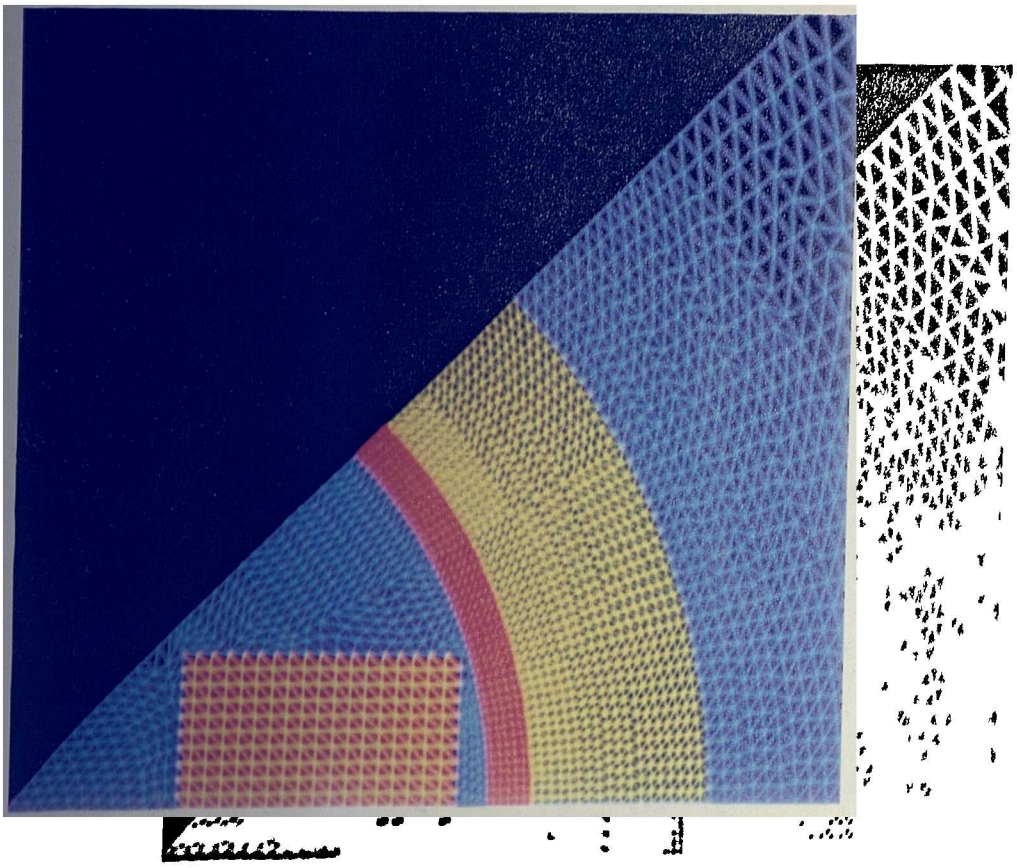

Fig. 4.22 Close-up of the rotor and fixture regions of the finite element mesh used for the calculation of static volume saturation versus mmf characteristics. (Total number of nodes and elements are 2757 and 5306 respectively).

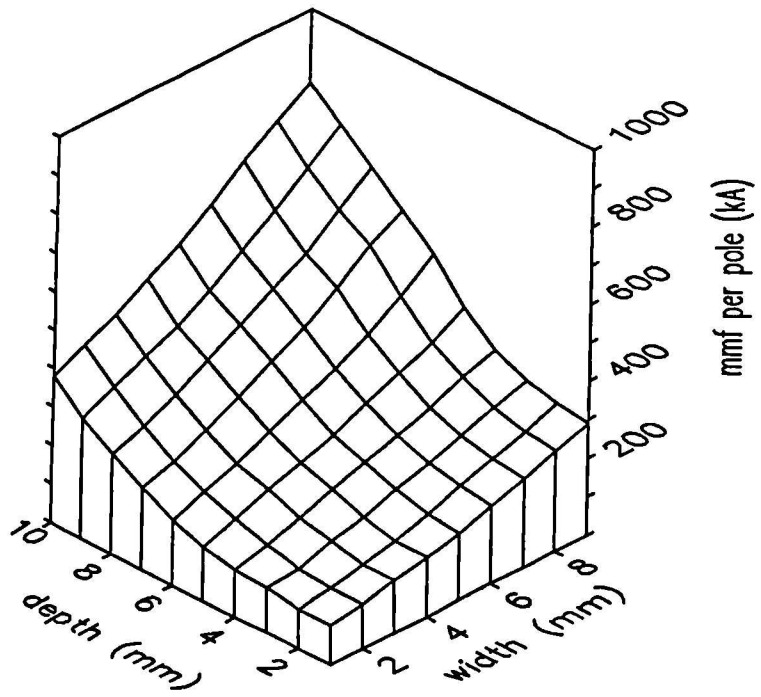

Fig. 4.23 Predicted static mmf required to achieve 90% volume saturation for a range of conductor bundle dimensions.

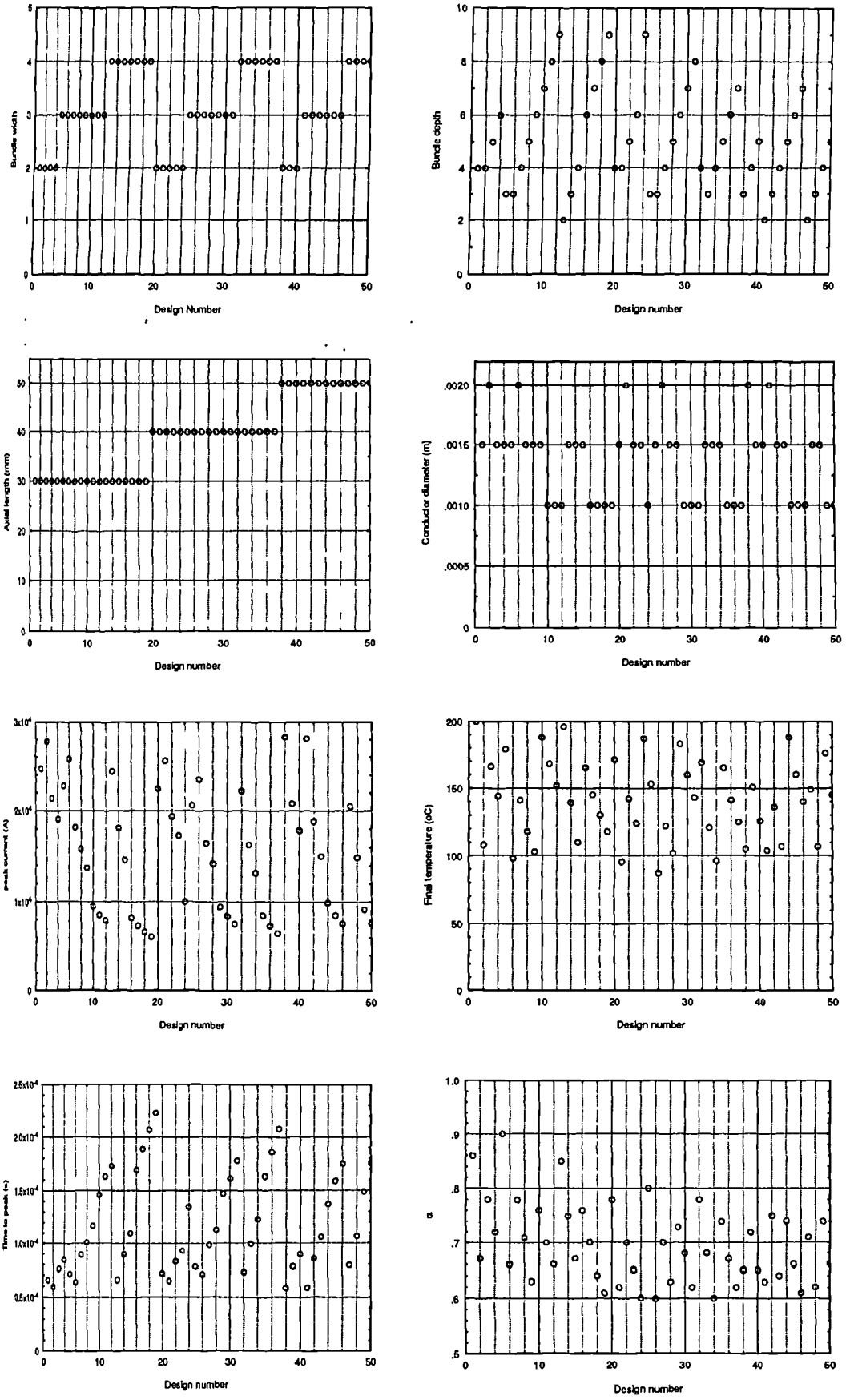

Fig. 4.24 Valid designs of single sided fixtures with axial lengths of 50mm. (C=450 μF , V = 3000V).

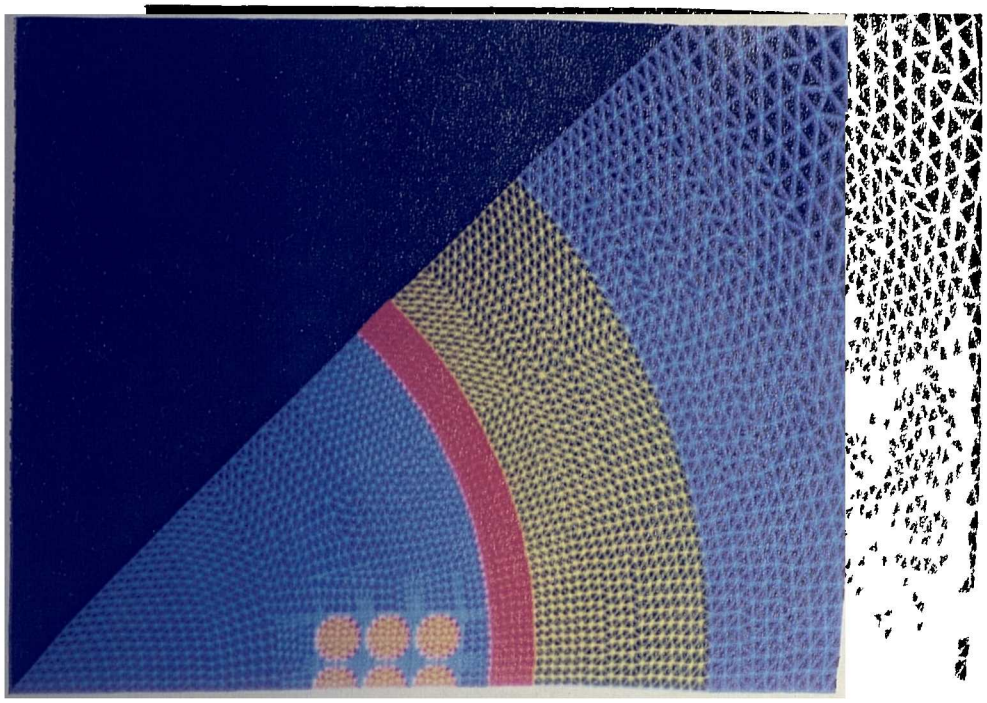

Fig. 4.25 Close-up of the rotor and fixture regions of the finite element mesh used in the dynamic simulation of fixture design No.42 for the magnetization of the assembled rotor (Total number of nodes and elements, 3298 and 6347 respectively).

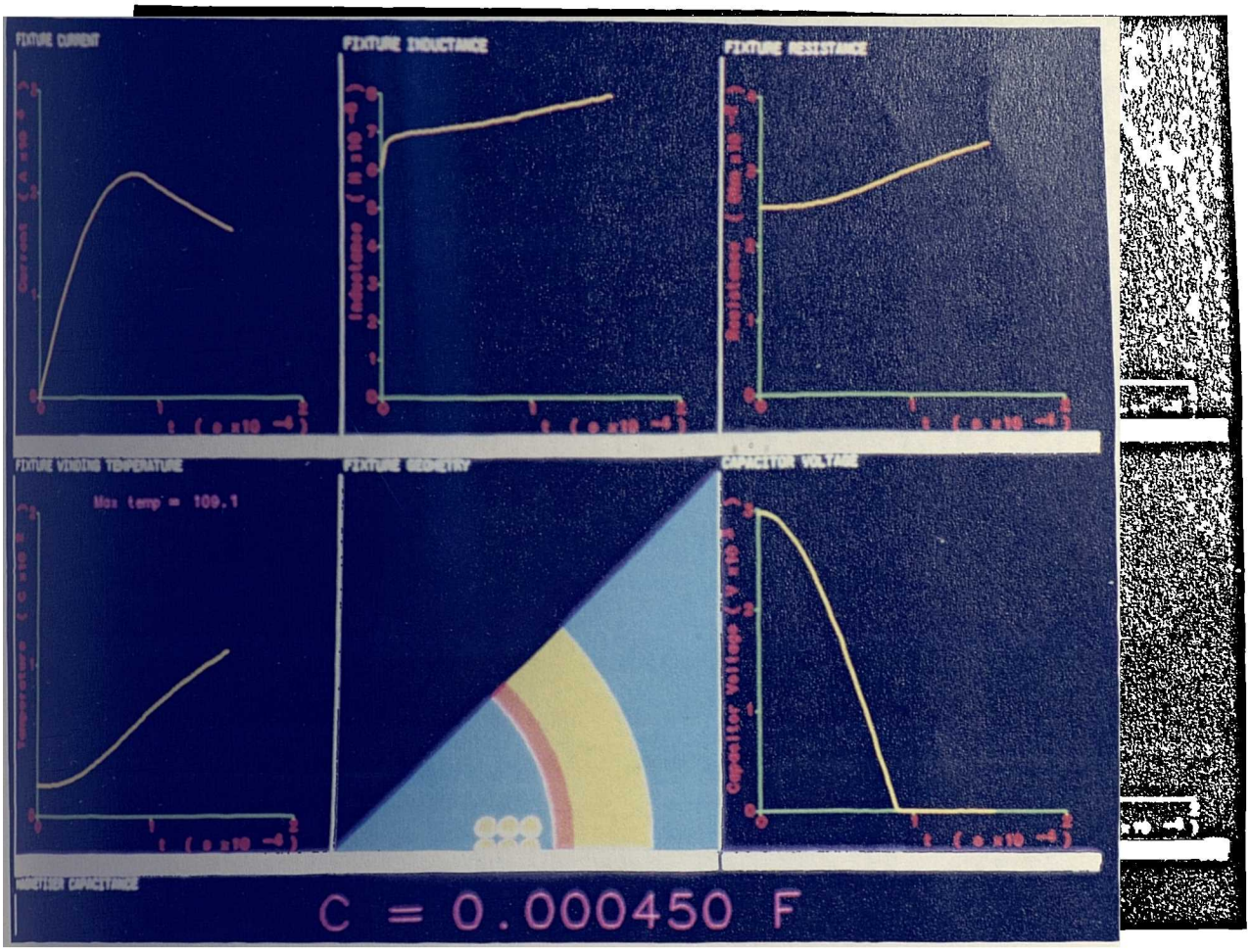

Fig 4.26 Predicted variation in the electrical circuit parameters during the magnetization of the assembled rotor with an internal single sided fixture.

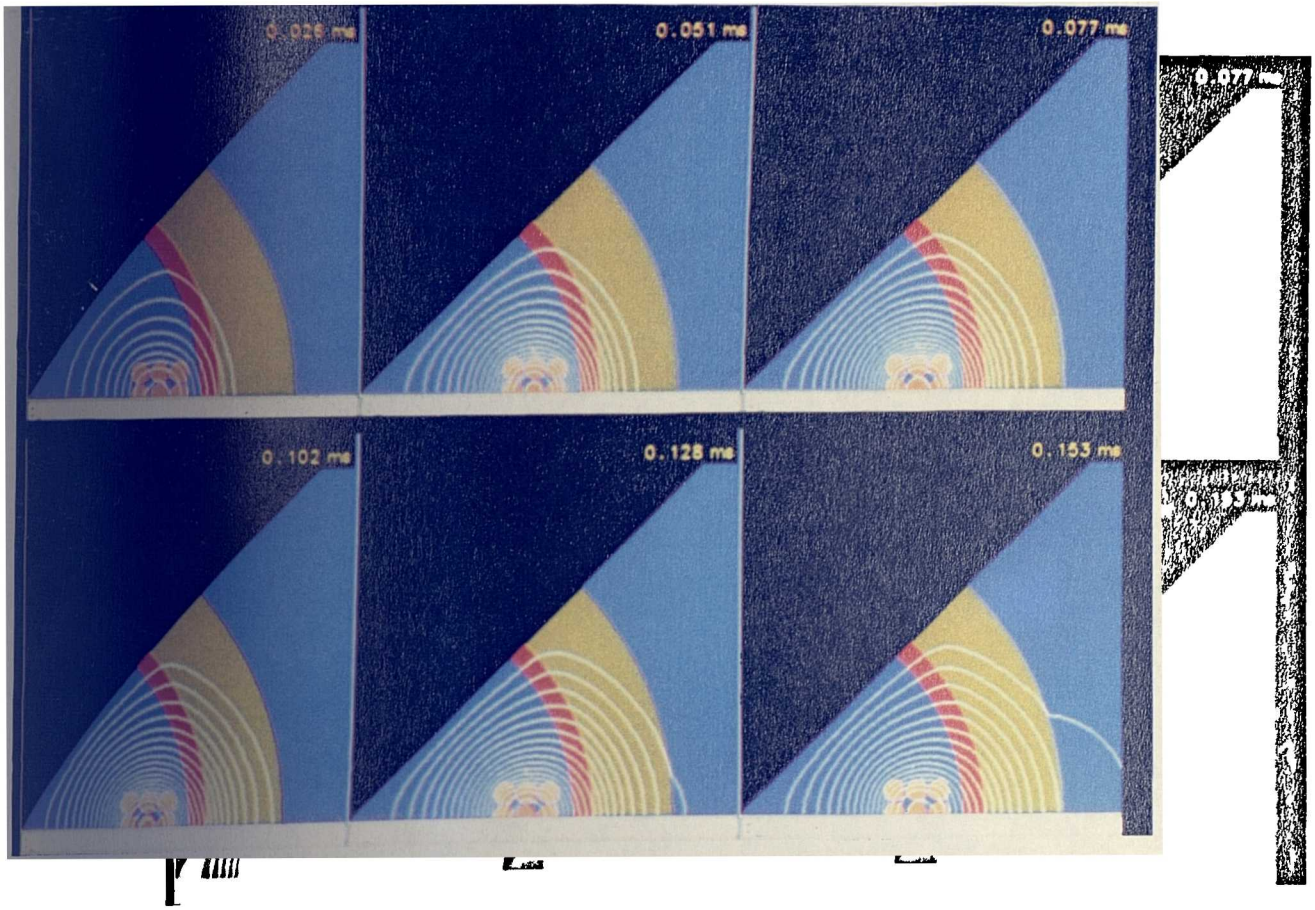

Fig. 4.27 Predicted field distributions at selected instants during the magnetization of the assembled rotor with an internal single sided-fixture. (C=450μF, V = 3000V).

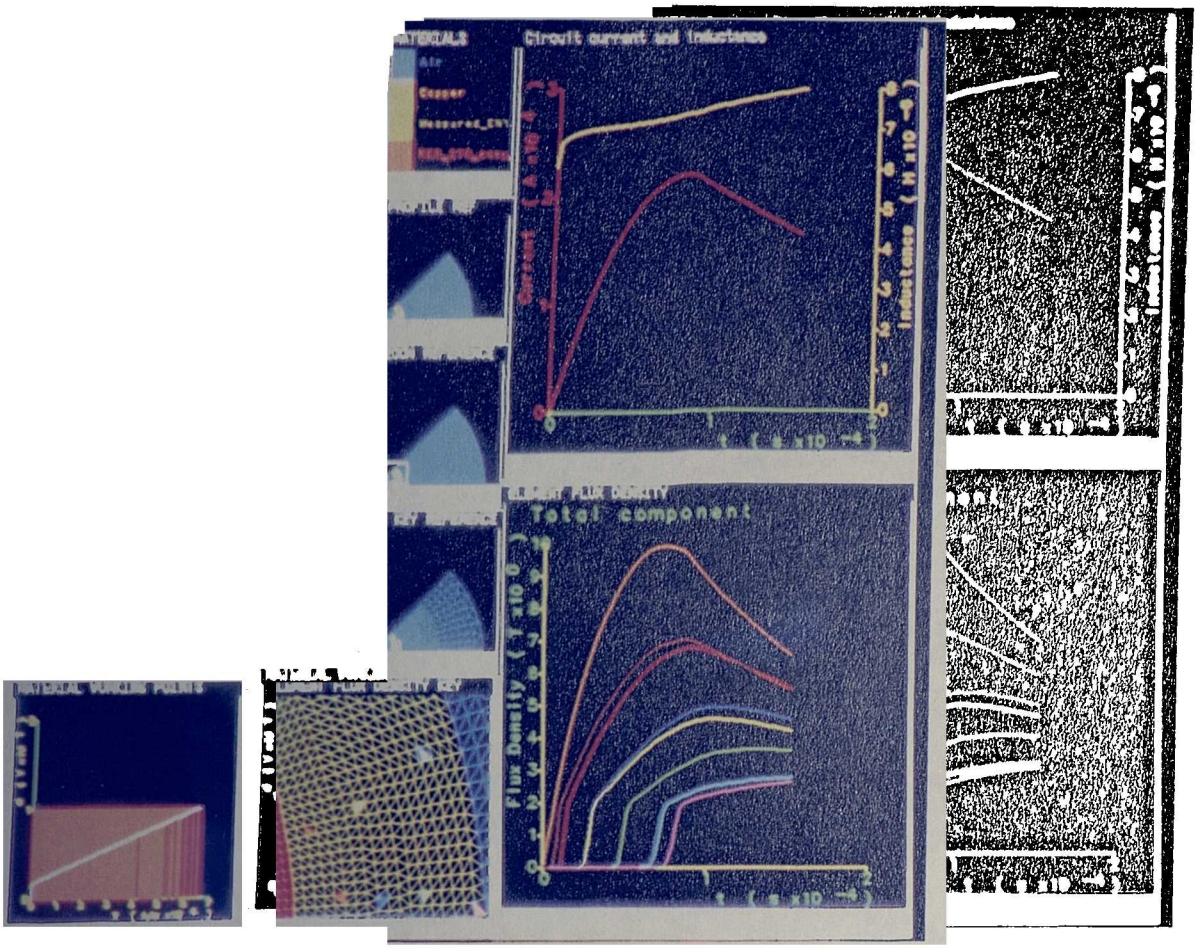

1

2 Material colours

6

Current and inductance waveforms

3 Ref for 10

4 Zoom for 1

5 Zoom for 8

7

Variation of flux density during the pulse in the colour coded elements

mum flux density chieved in each ent during the pulse

9 Working points of the steel

8 Colour code and location of the elements in 7

essor output for the magnetization of the assembled rotor with an ternal single sided-fixture. (C=450μF, V = 3000V).

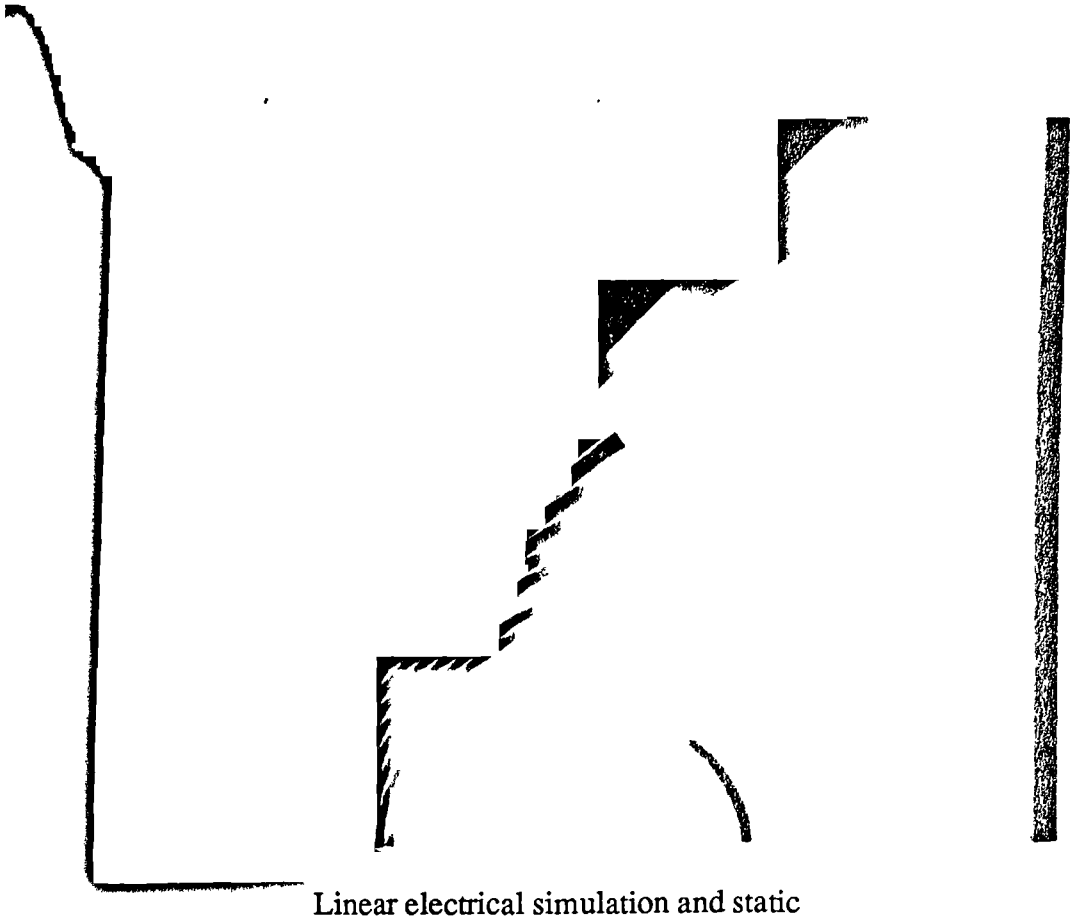

Linear electrical simulation and static field calculation , I_{peak} = 18.6kA.

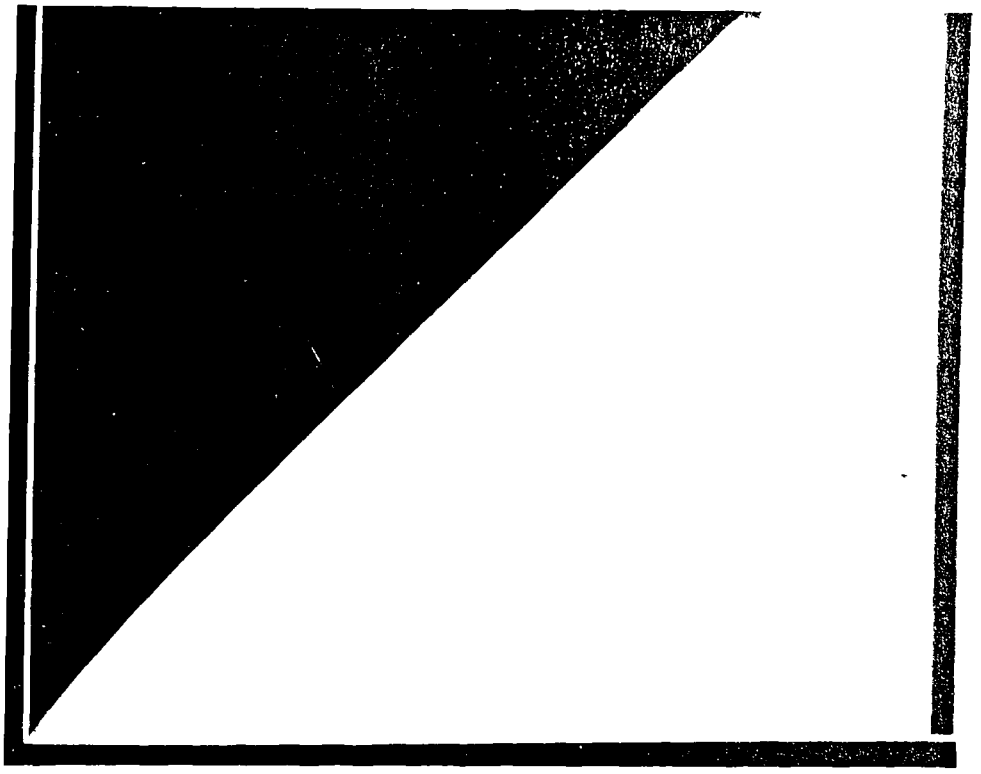

Dynamic simulation, I_{peak} = 21.8kA.

FIg. 4.29 Predicted static and dynamic field distributions at the peaks of the respective current waveforms. (Equipotential contour increments = 2.5×10^{-3} Wb/m for both field distributions)

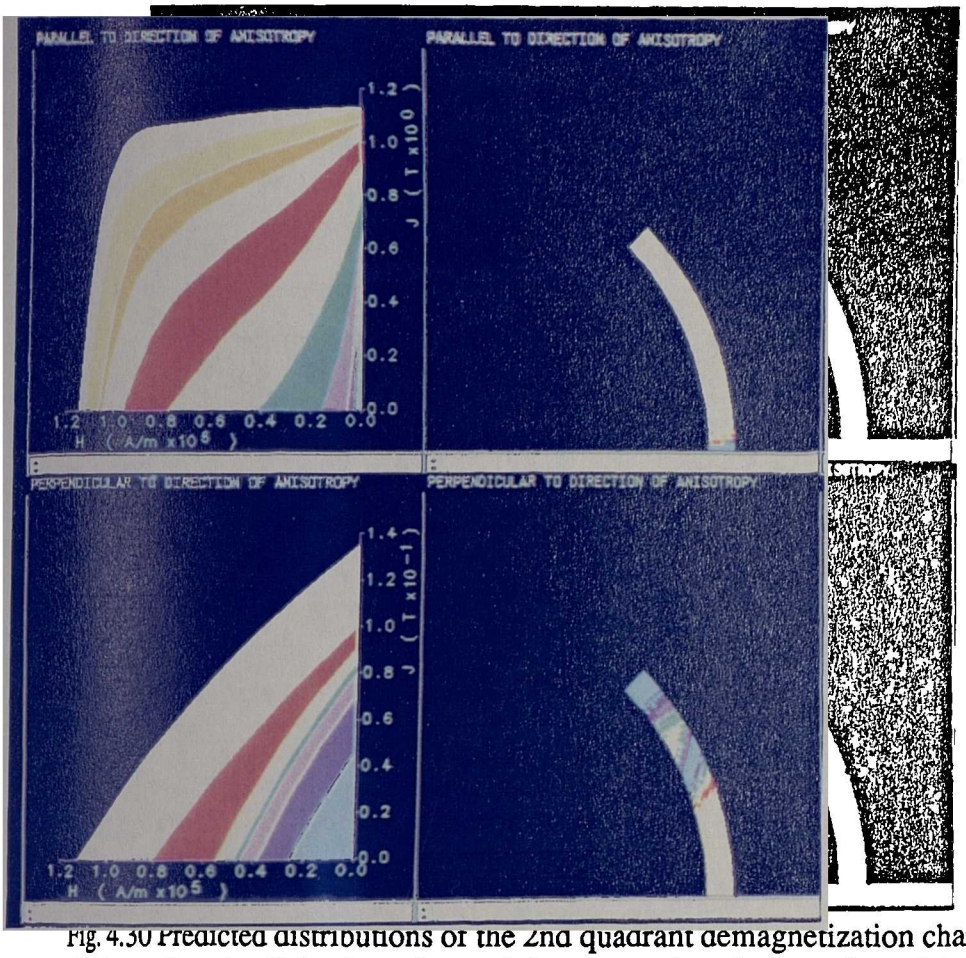

Fig. 4.30 Predicted distributions of the 2nd quadrant demagnetization characteristics in the preferred radial orientation and the non-preferred circumferential orientation following the decay of the magnetizing pulse.

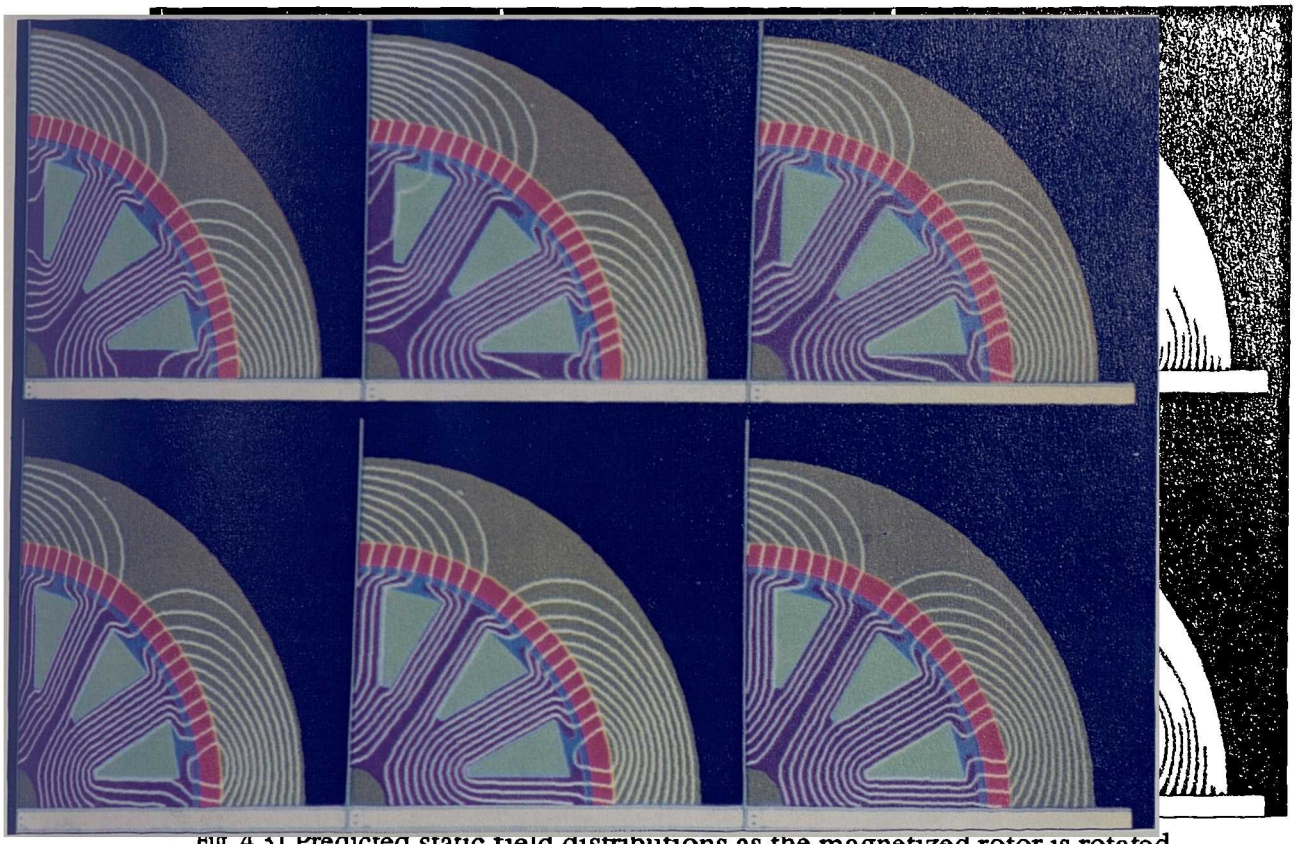

Fig. 4.31 Predicted static field distributions as the magnetized rotor is rotated in an assembled motor.

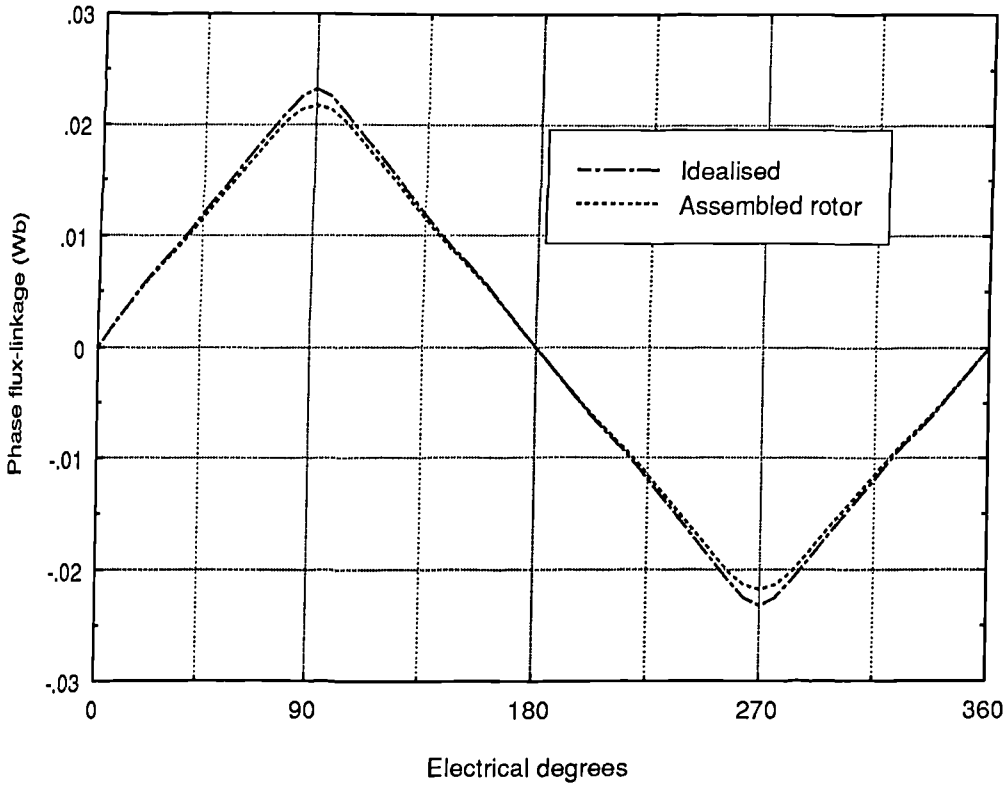

4.32 Predicted phase flux-linkage waveforms for the magnetized rotor and an idealised fully saturated magnet.

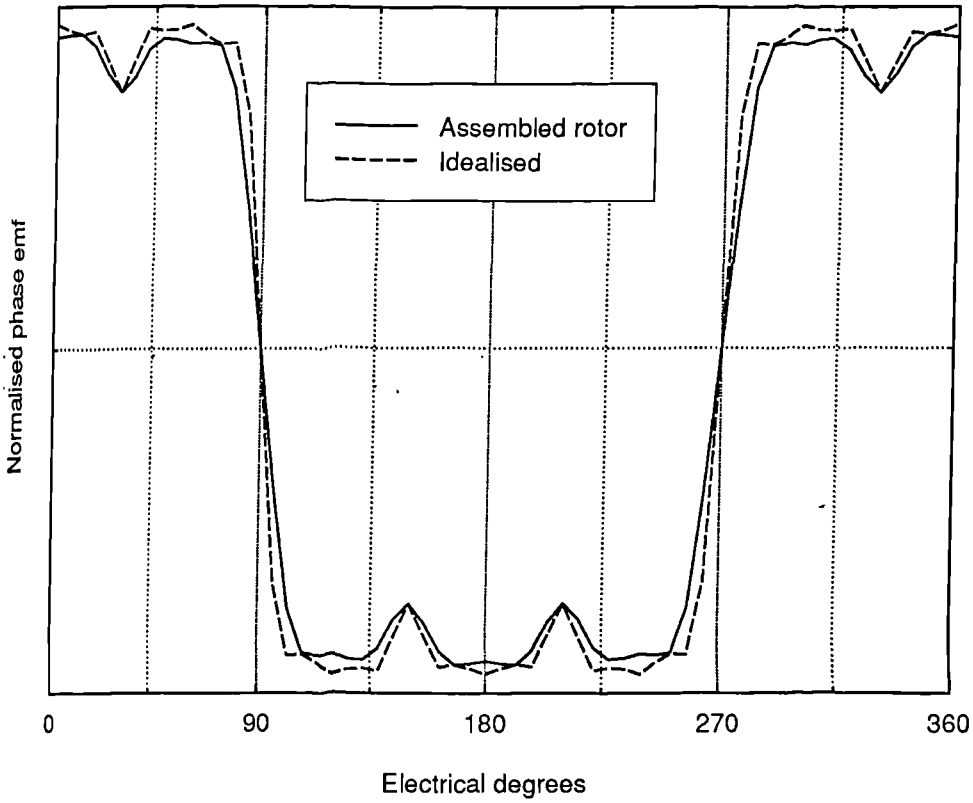

4.33 Predicted normalised phase induced emf waveforms for the magnetized rotor and an idealised fully saturated magnet.

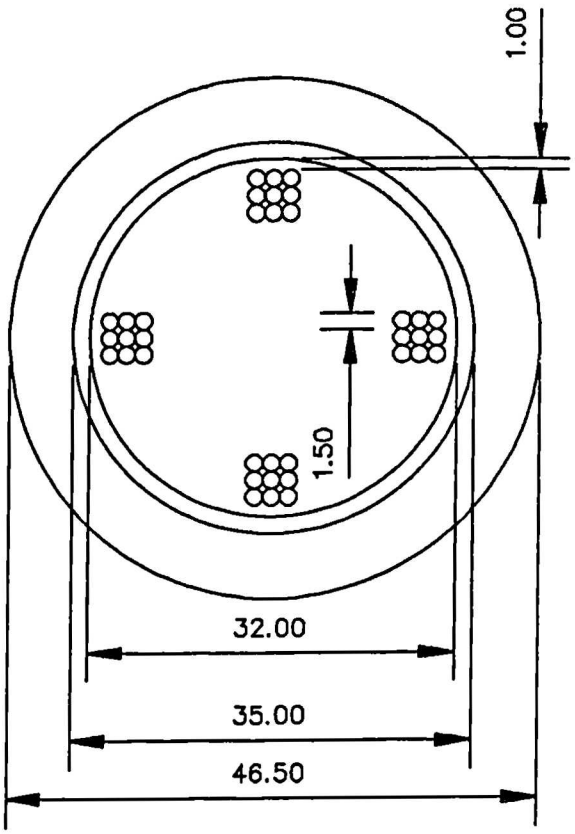

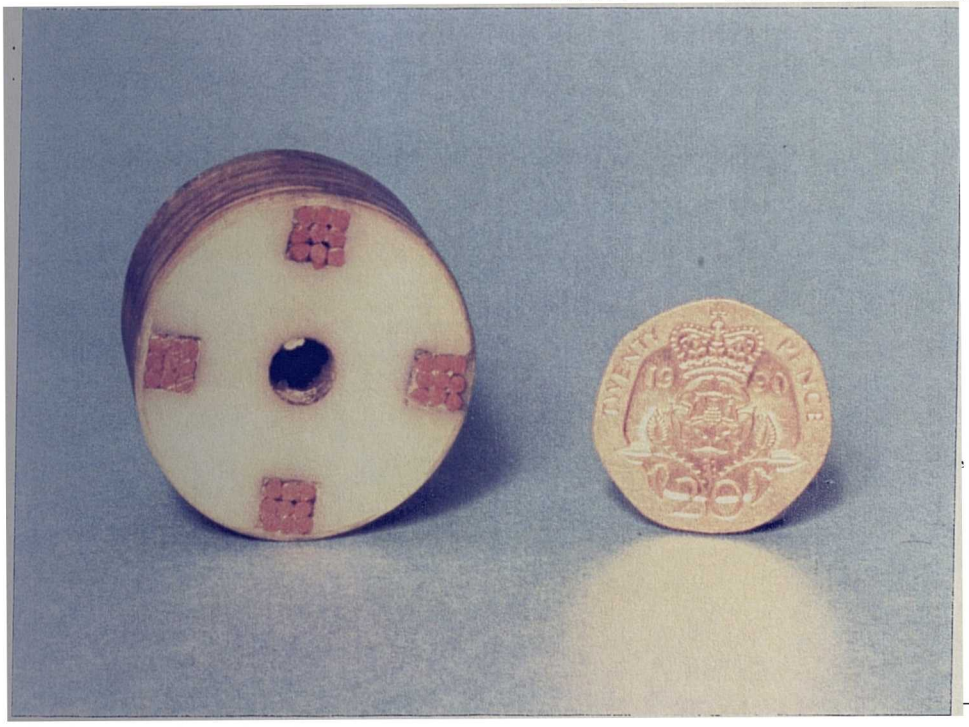

Fig. 4.34 Principal dimensions and a cross-section through the constructed fixture.

	Measured	Predicted
Inductance	7.34 μH (at 1 kHz)	7.29 μH
Resistance	26.2 $m\Omega$	25.1$m\Omega$

Fig. 4.35 Comparison of the predited and measured fixture parameters.

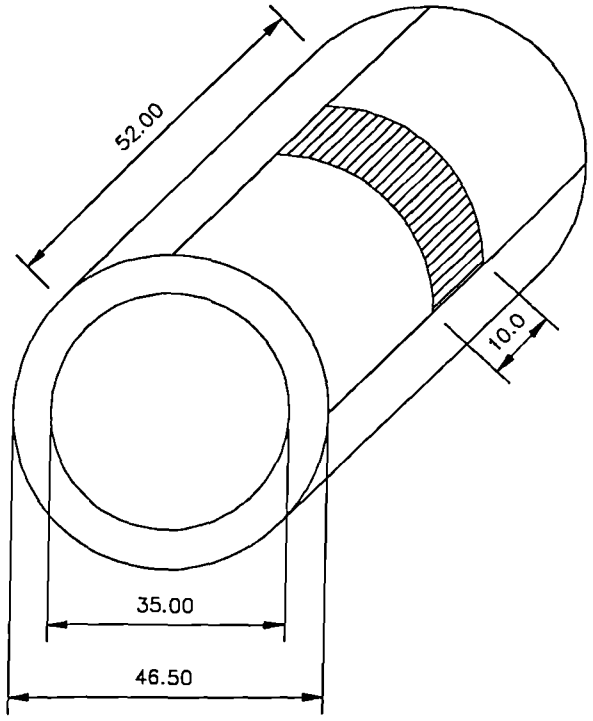

Fig. 4.36 Search coil arrangement for the measurement of the magnetizing flux per pole which penetrates the rotor core.

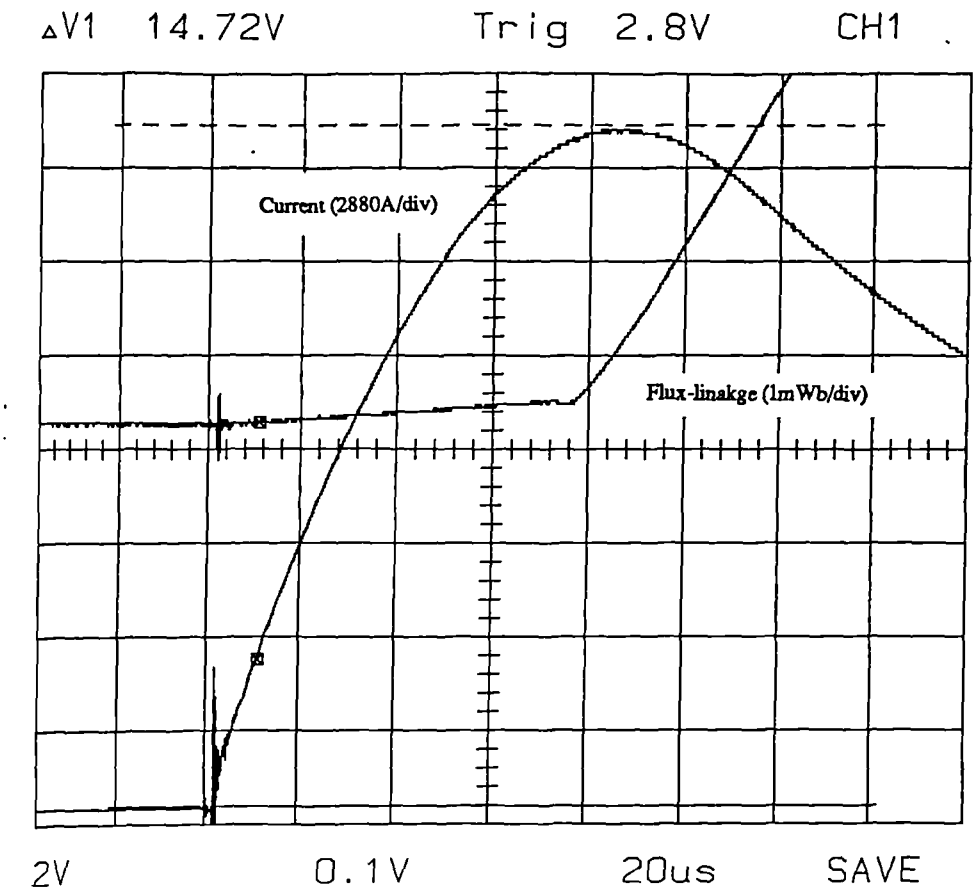

Fig. 4.37 Measured current and search coil flux-linkage waveforms.

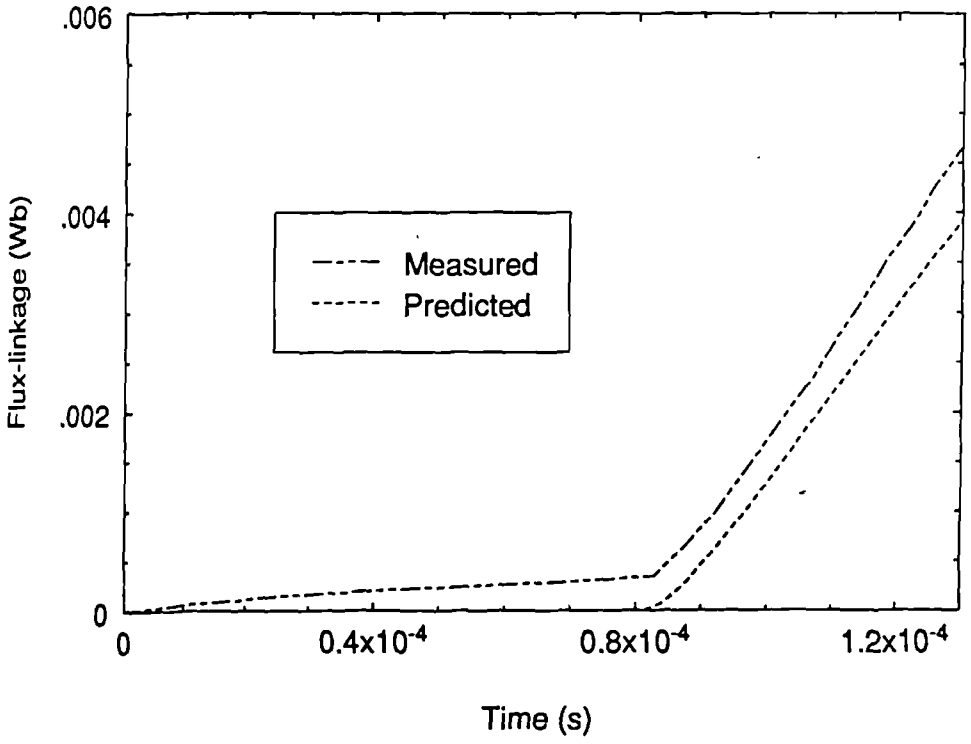

Fig. 4.38 Predicted and measured search coil flux-linkage waveforms.

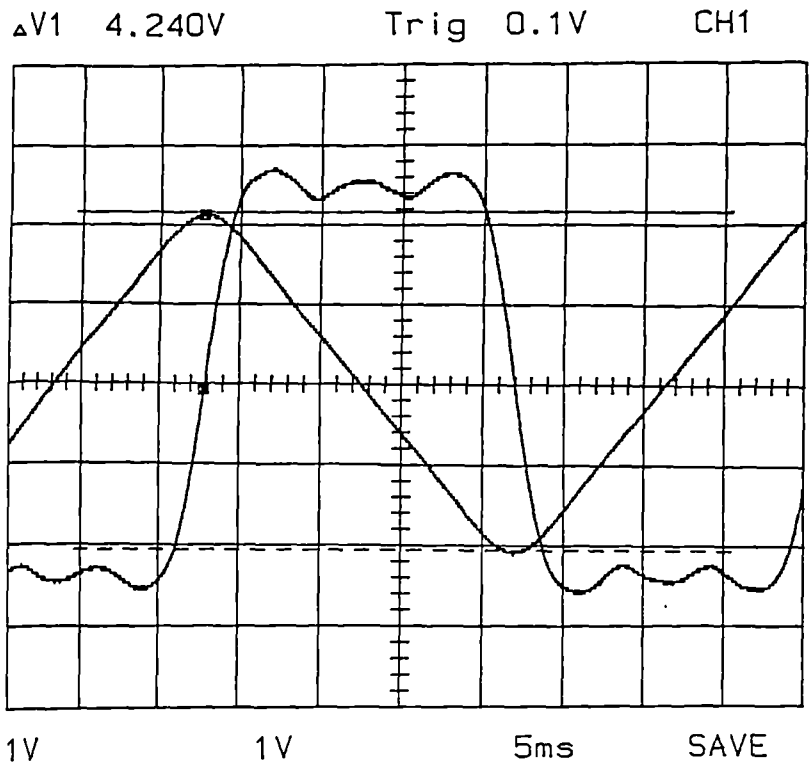

Fig. 4.39 Measured motor induced emf and flux-linkage per phase waveforms.

Design number	C (μF)	Conductors (dxw)	Diameter (mm)	Peak current (kA)	α	Rise time (μs)
1	7000	3x3	1.5	13.8	0.58	287
2	7000	3x3	1.5	12.6	0.53	306
3	7000	3x3	1.5	11.6	0.48	323
4	10500	5x3	1.5	11.5	0.57	450
5	10500	4x3	1.5	11.9	0.51	434

Fig. 4.40 Optimal fixture designs for the low voltage magnetizer (V_0 = 800V in all cases).

Fixture.	Peak Current (kA)		Volume Saturation (>1600 kA/m)	
	Linear electrical design stage	Dynamic Simulation	Static non-linear finite element field solution	Dynamic Simulation
Design No. 6 C = 10,500 μF V_0 =800V	13.2	13.6	55.6% (@13.2 kA)	6.2%

Fig. 4.41 Predicted static and dynamic performance of fixture design 6 of fig 4.40.

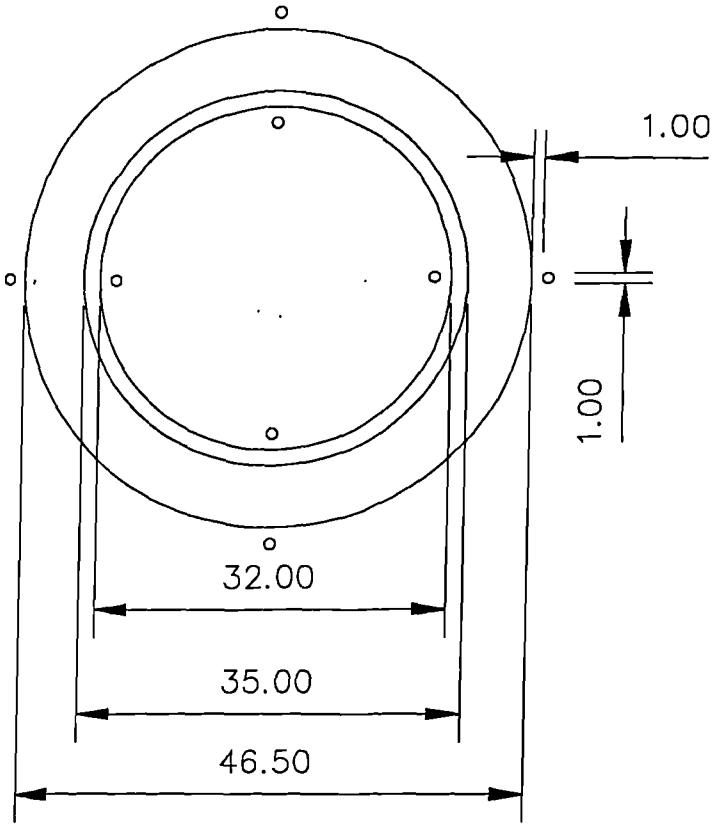

Fig. 4.42 Double sided test fixture for the assessment of the accuracy of the analytical field calculation method.

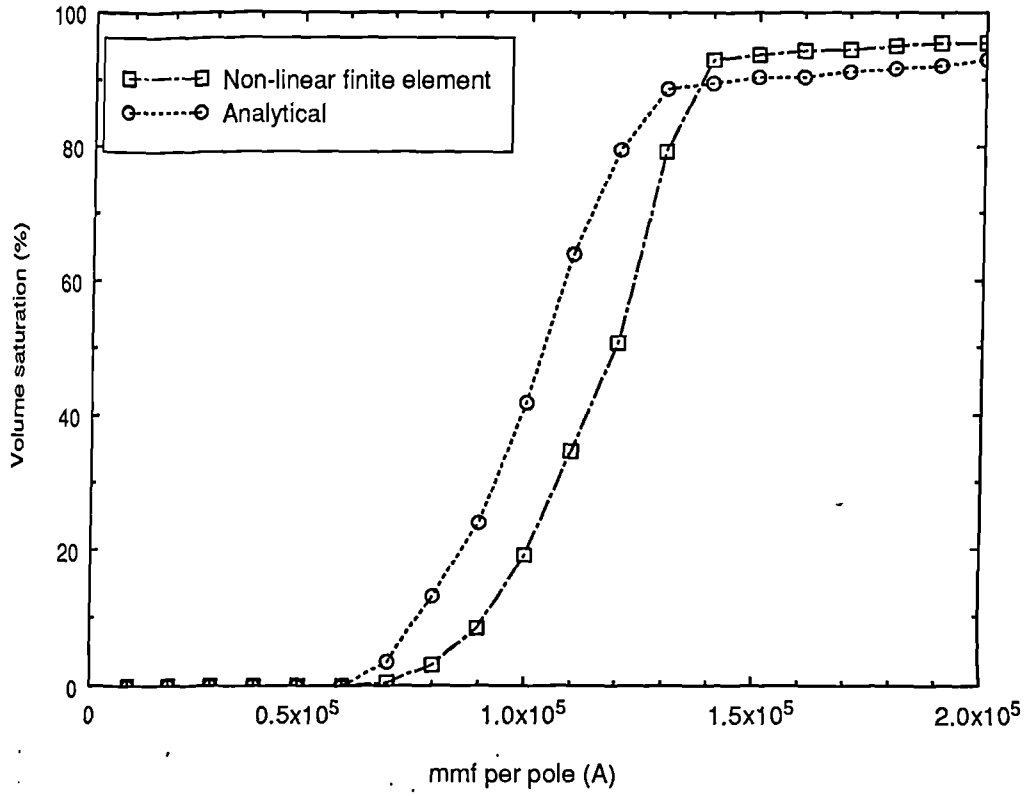

Fig. 4.43 Volume saturation versus mmf characteristics predicted by both the analytical and non-linear finite element methods for the fixture of fig 4.42

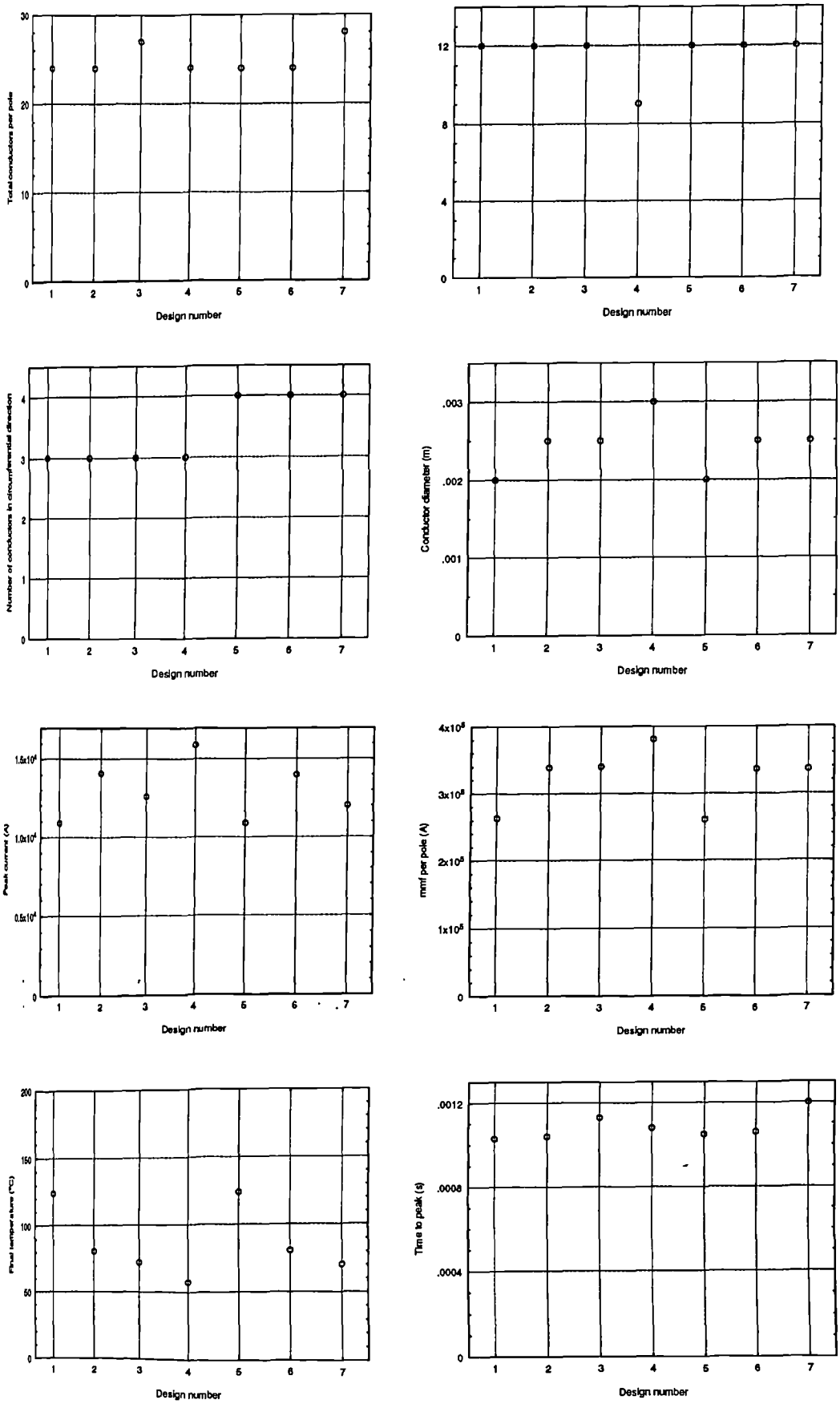

Fig. 4.44 Valid designs of double sided fixtures with axial lengths of 50mm for the magnetization of an assembled rotor (C= 28000 μF , V = 800V).

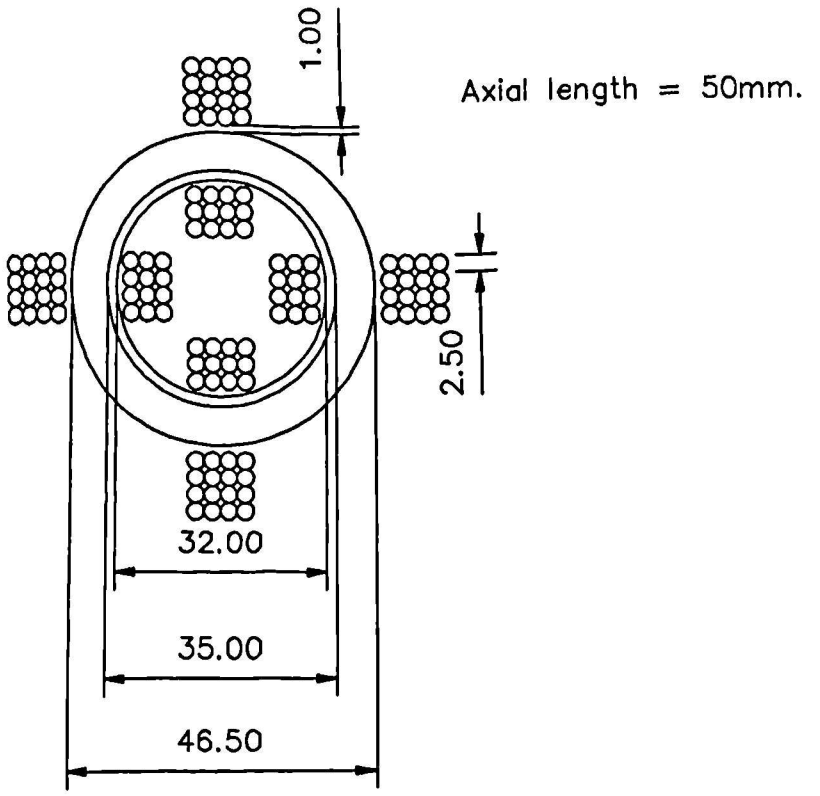

Fig. 4.45 Dimensions of fixture design No. 7 for the magnetization of the assembled rotor.

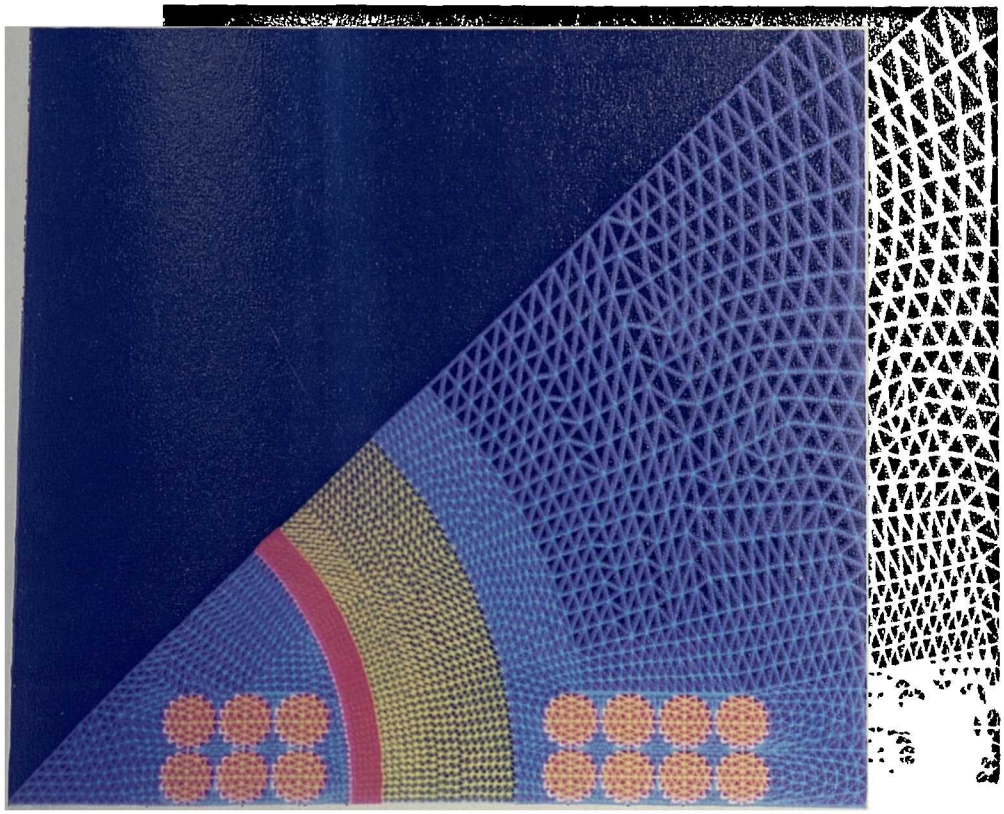

Fig. 4.46 Close up of the rotor and fixture regions of the finite element mesh utilised in the dynamic simulation of fixture design No.7. (Total number of nodes and elements are 3298 and 6347 respectively).

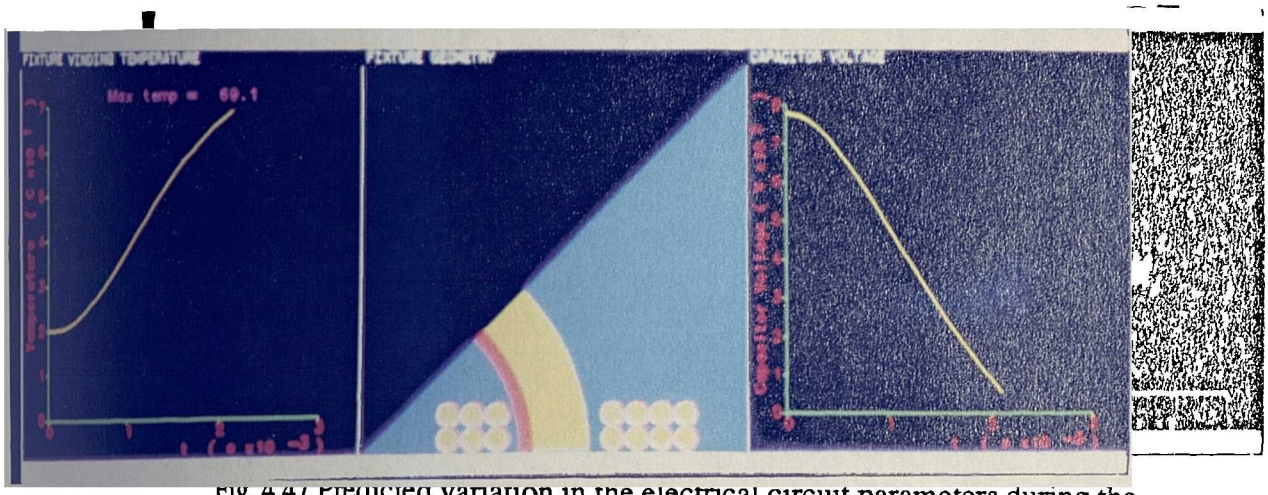

Fig. 4.47 Predicted variation in the electrical circuit parameters during the magnetization of the assembled rotor.

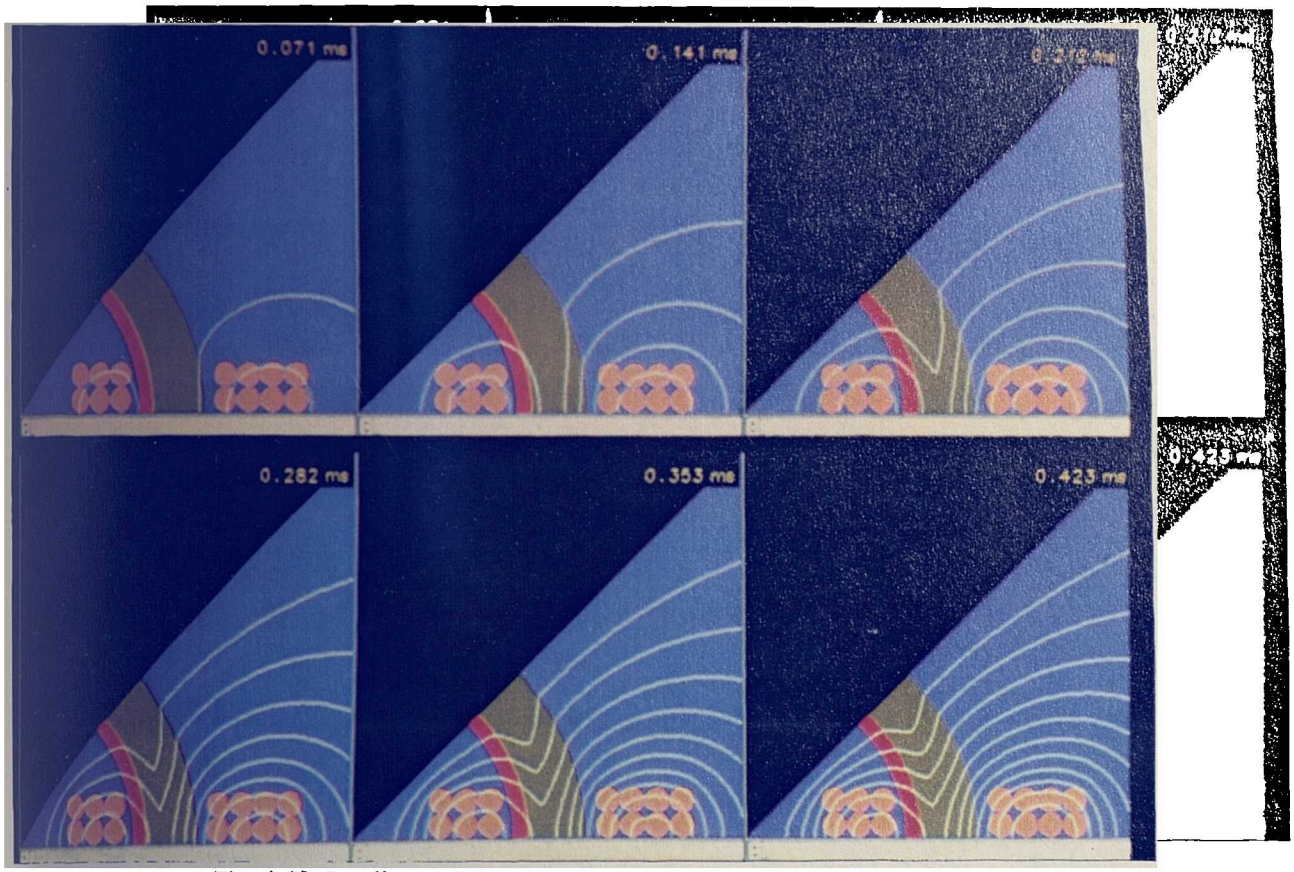

Fig. 4.48 Predicted field distributions at selected instants during the initial stages of the pulse, demonstrating the screening effect of eddy-currents.

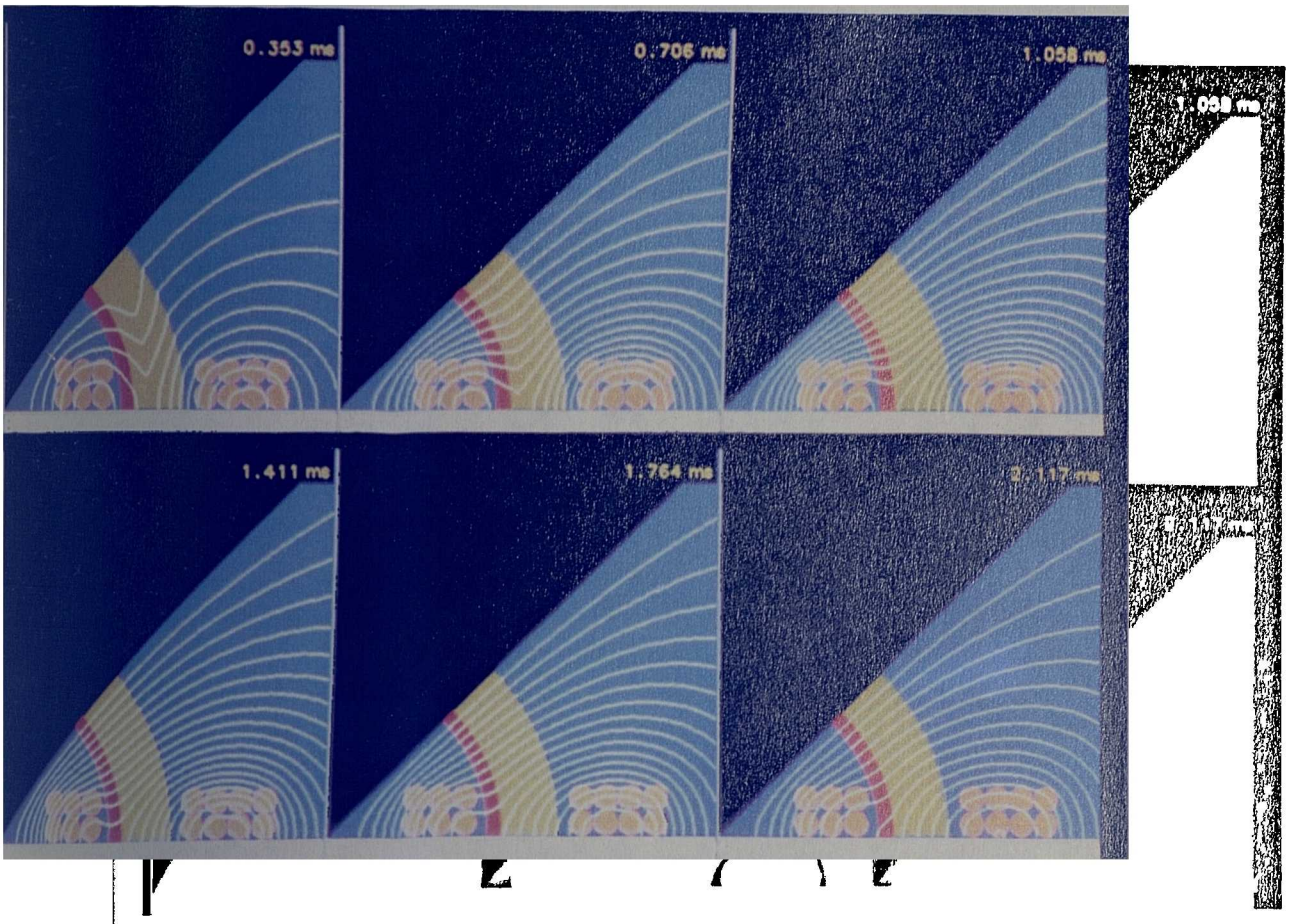

Fig. 4.49 Predicted field distributions at selected instants during the magnetization

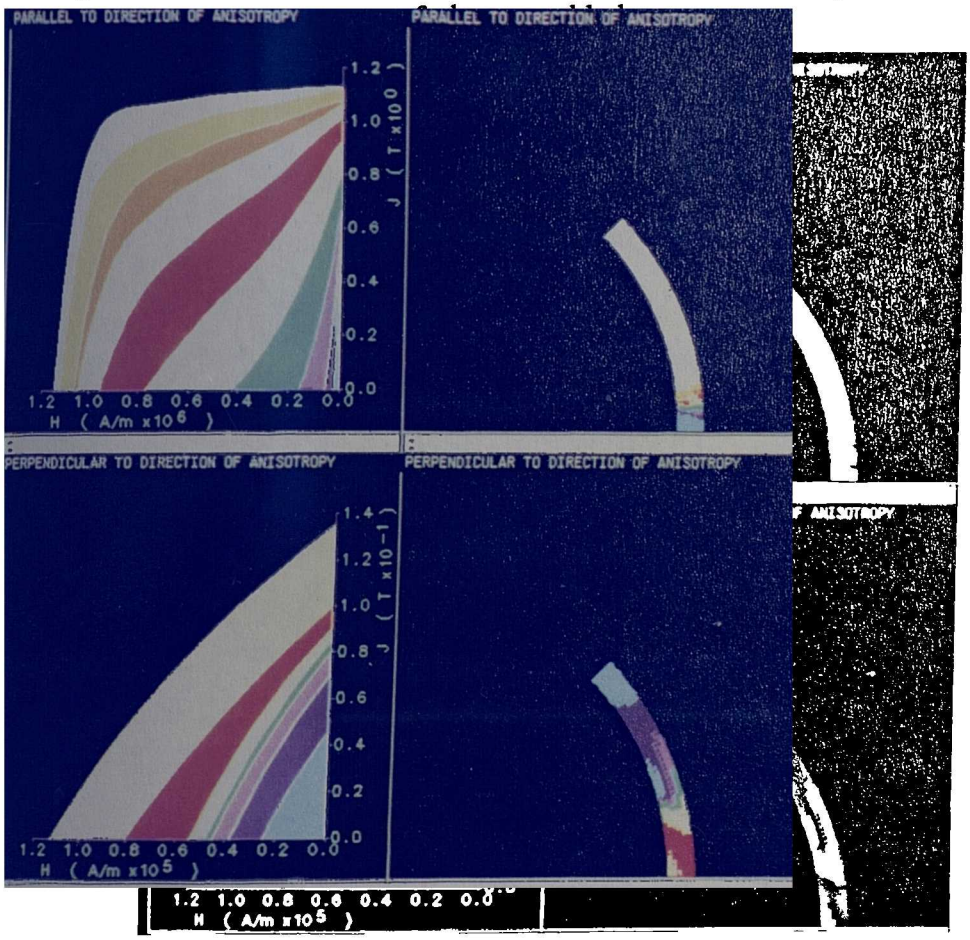

Fig. 4.50 Predicted distribution of demagnetization characteristics in the preferred radial and the non-preferred circumferential orientations following the decay of the magnetizing pulse.

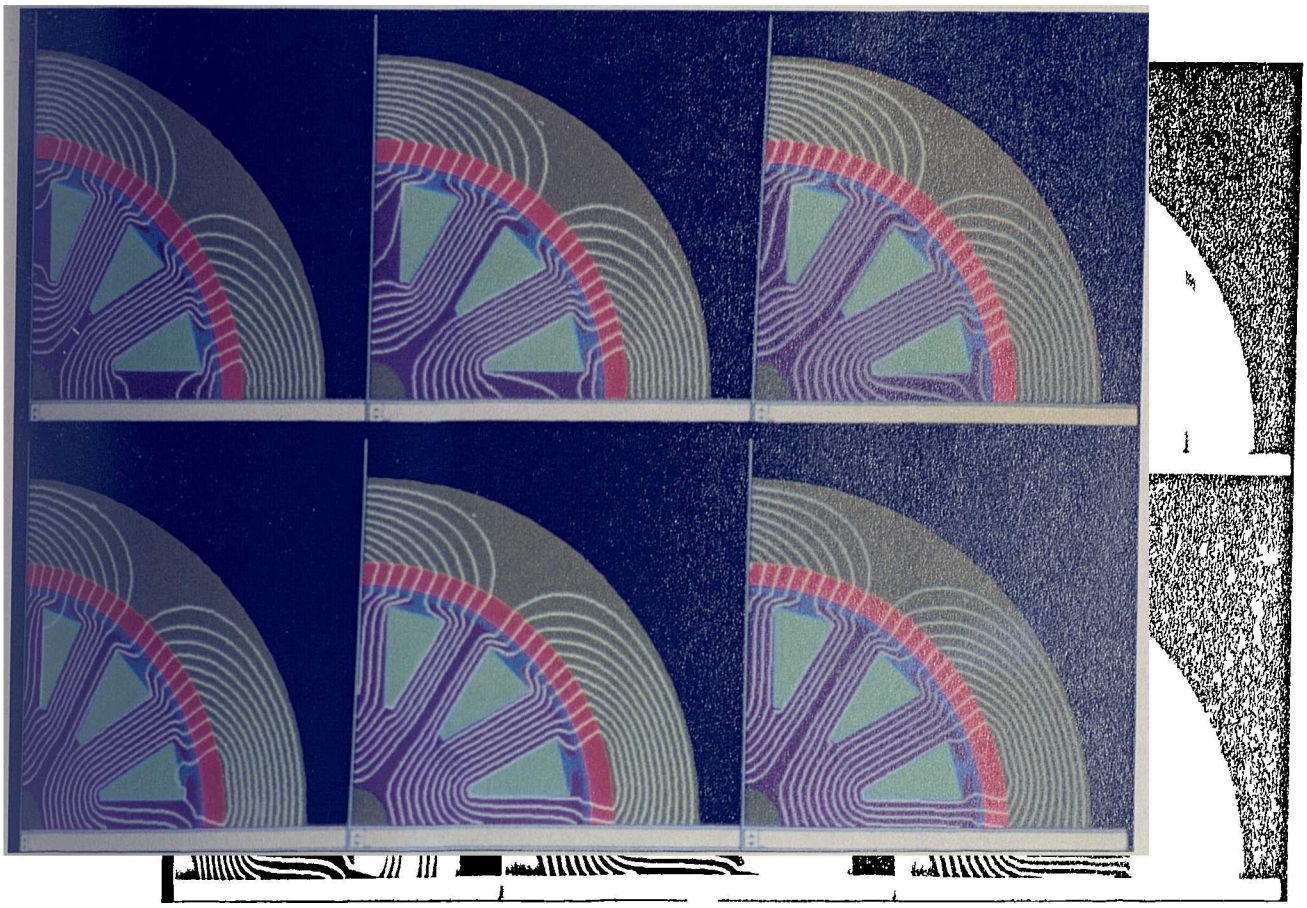

Fig. 4.51 Predicted static field distributions as the magnetized rotor is rotated in an assembled motor.

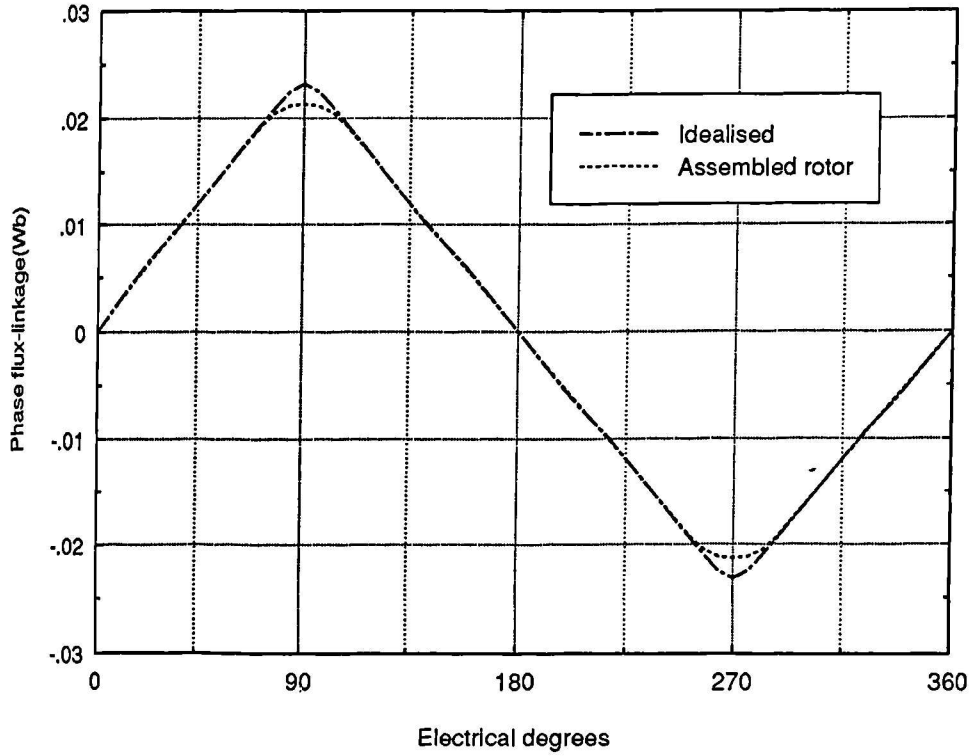

4.52 Predicted phase flux-linkage waveforms for the magnetized rotor and an idealised fully saturated magnet.

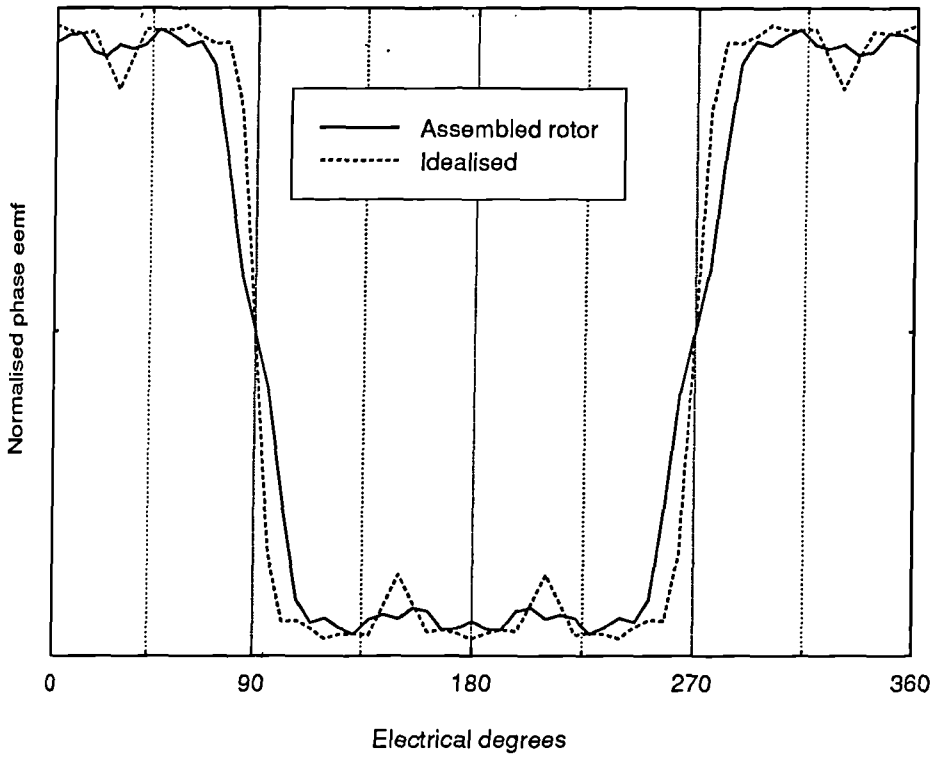

4.53 Predicted normalised phase induced emf waveforms for the magnetized rotor and an idealised fully saturated magnet.

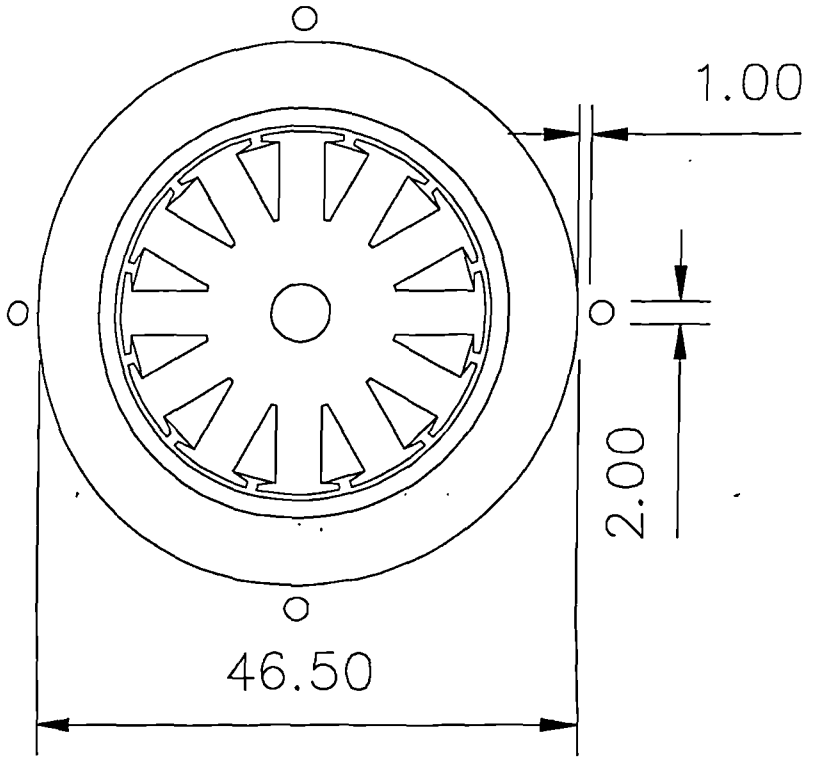

Fig. 4.54 Test fixture for assessing the applicability of the analytical field calculation method to post-assembly magnetization.

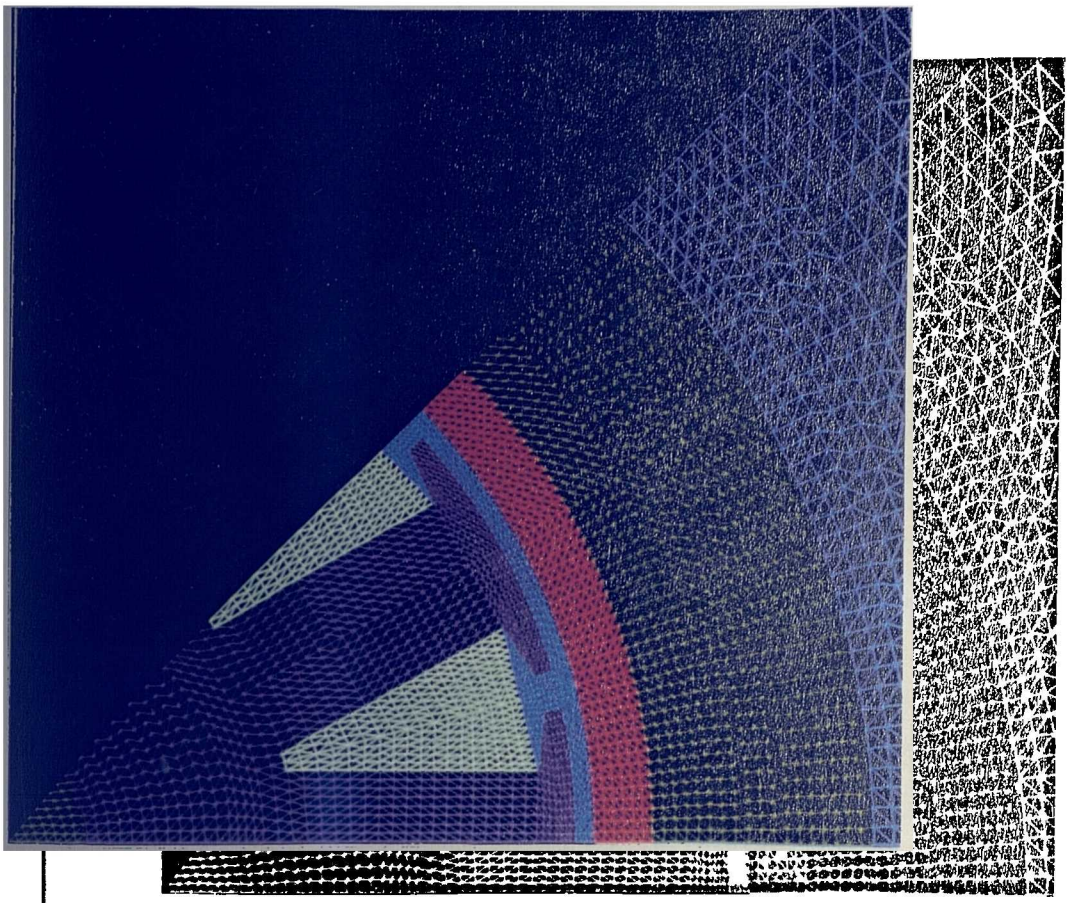

Fig 4.55. Close-up of the motor region of the finite element mesh utilised in the calculation of the static volume saturation versus mmf characteristic of the test fixture of fig 4.54.

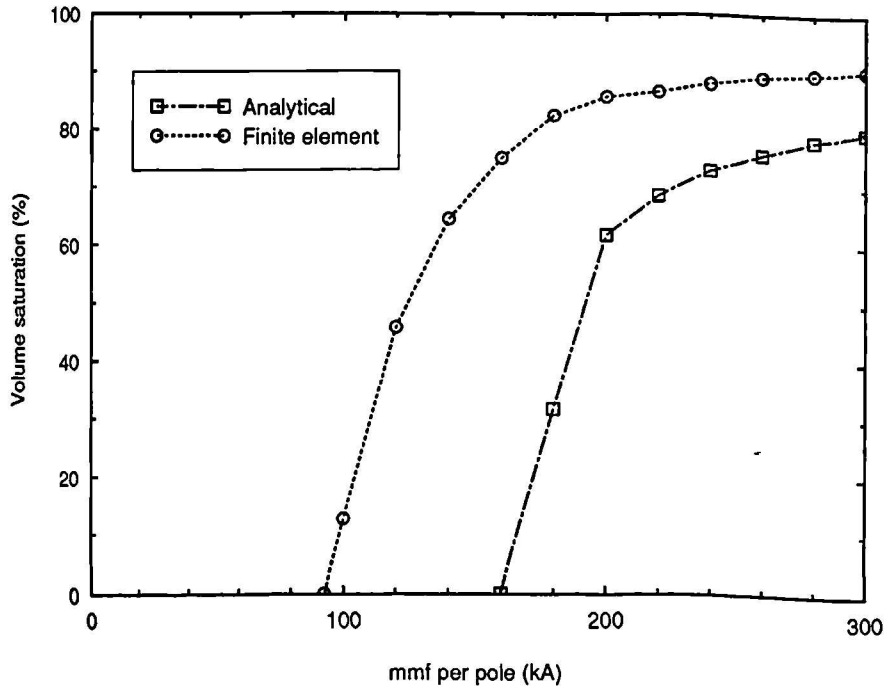

Fig. 4.56 Static volume saturation versus mmf characteristics predicted by both the analytical and non-linear finite element methods for the test fixture of fig 4.54.

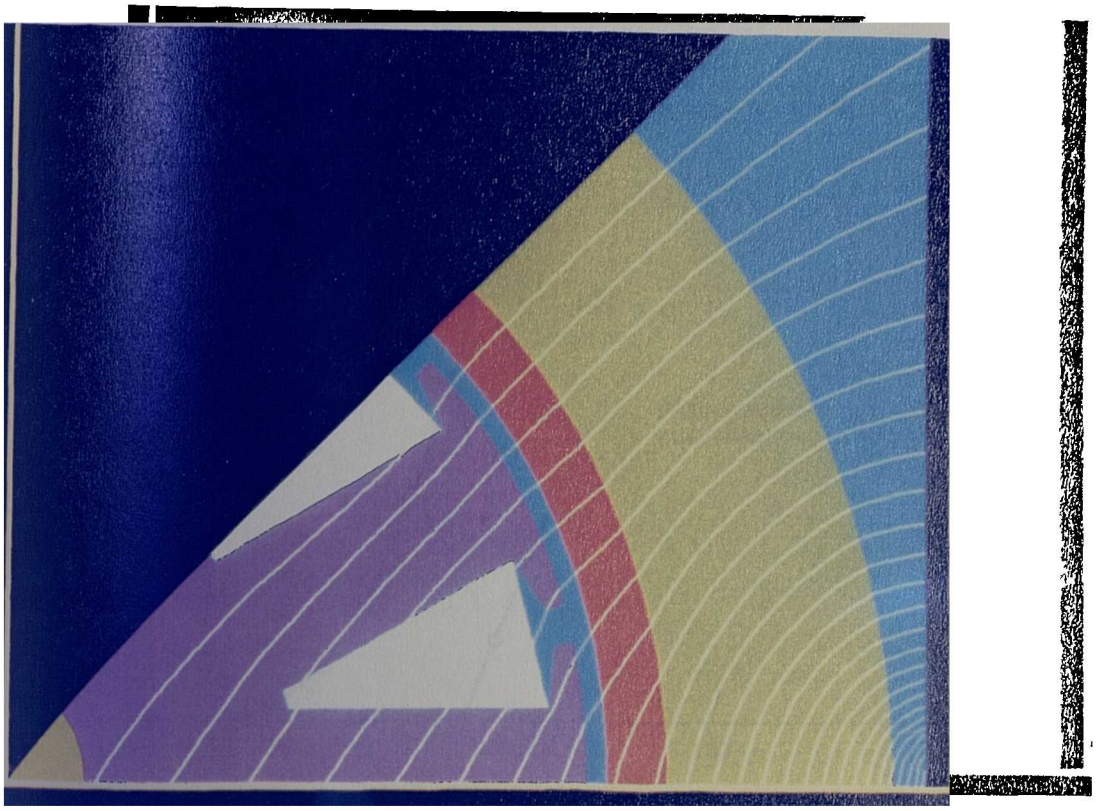

4.57 Predicted static field distribution for an applied mmf of 240kA per pole.

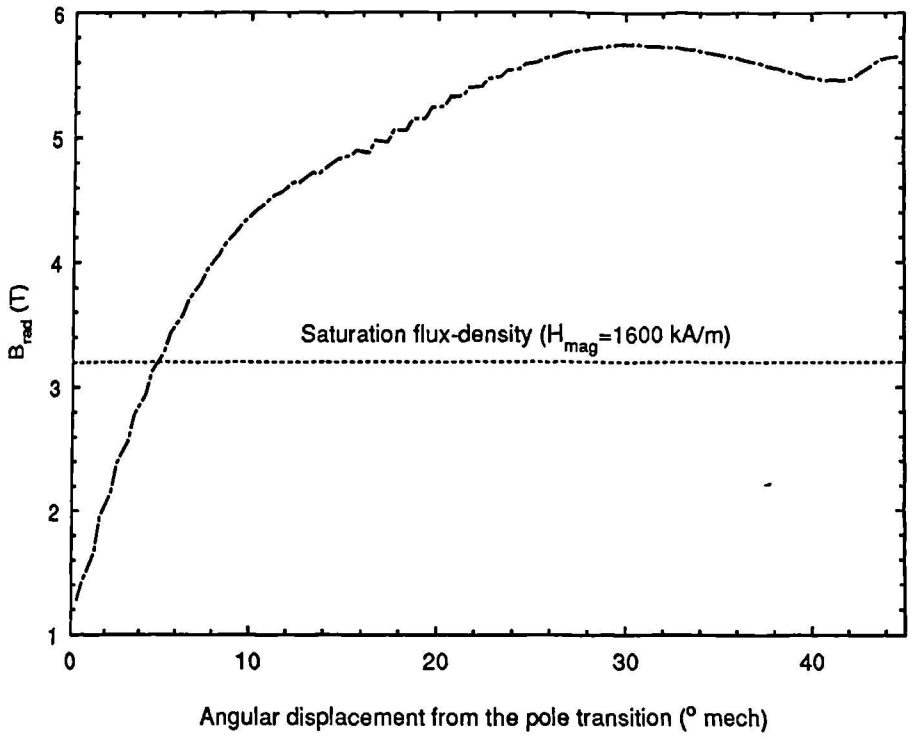

'edicted variation of the radial component of flux-density (B_{rad}) with
ıcement from the pole transition for an applied mmf of 240 kA per pole.

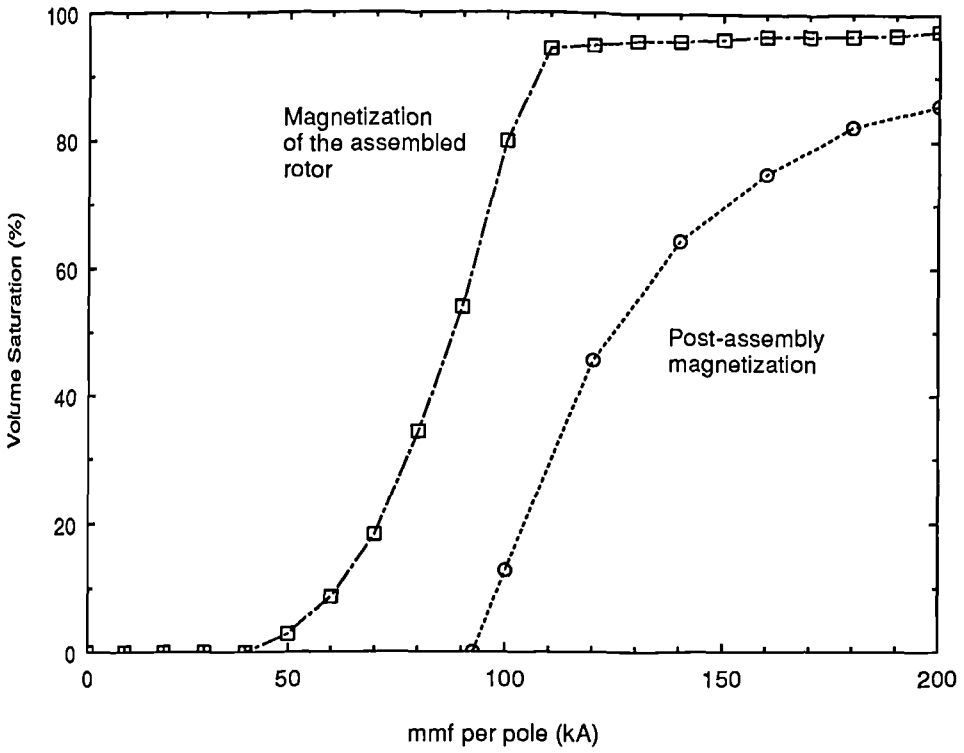

Fig. 4.59 Predicted static volume saturation versus mmf characteristics for the post assembly test fixture and the test fixture for the magnetization of the assembled rotor.

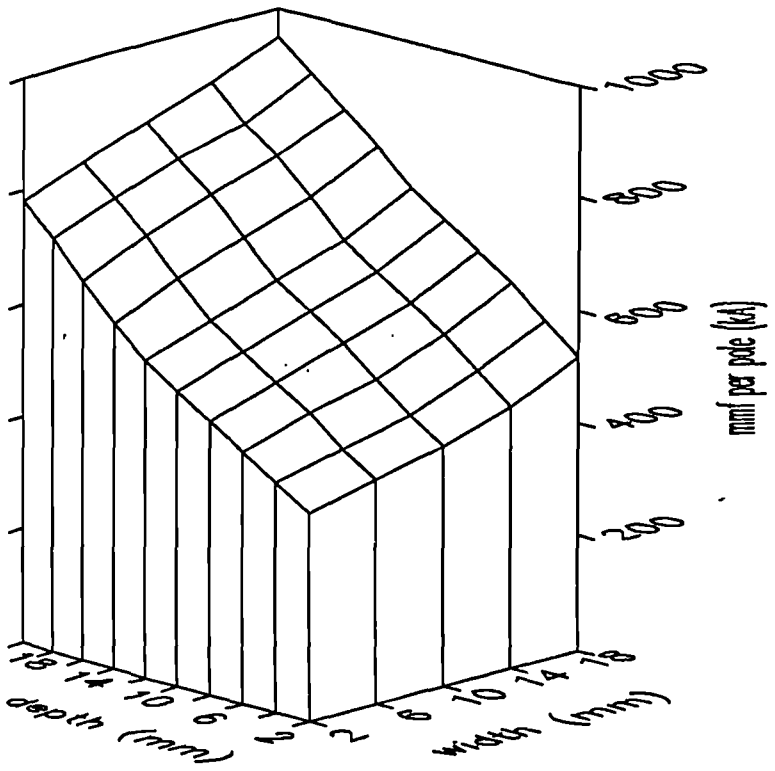

Fig. 4.60 Predicted static mmf required to achieve 70% volume saturation for a range of conductor bundle dimensions.

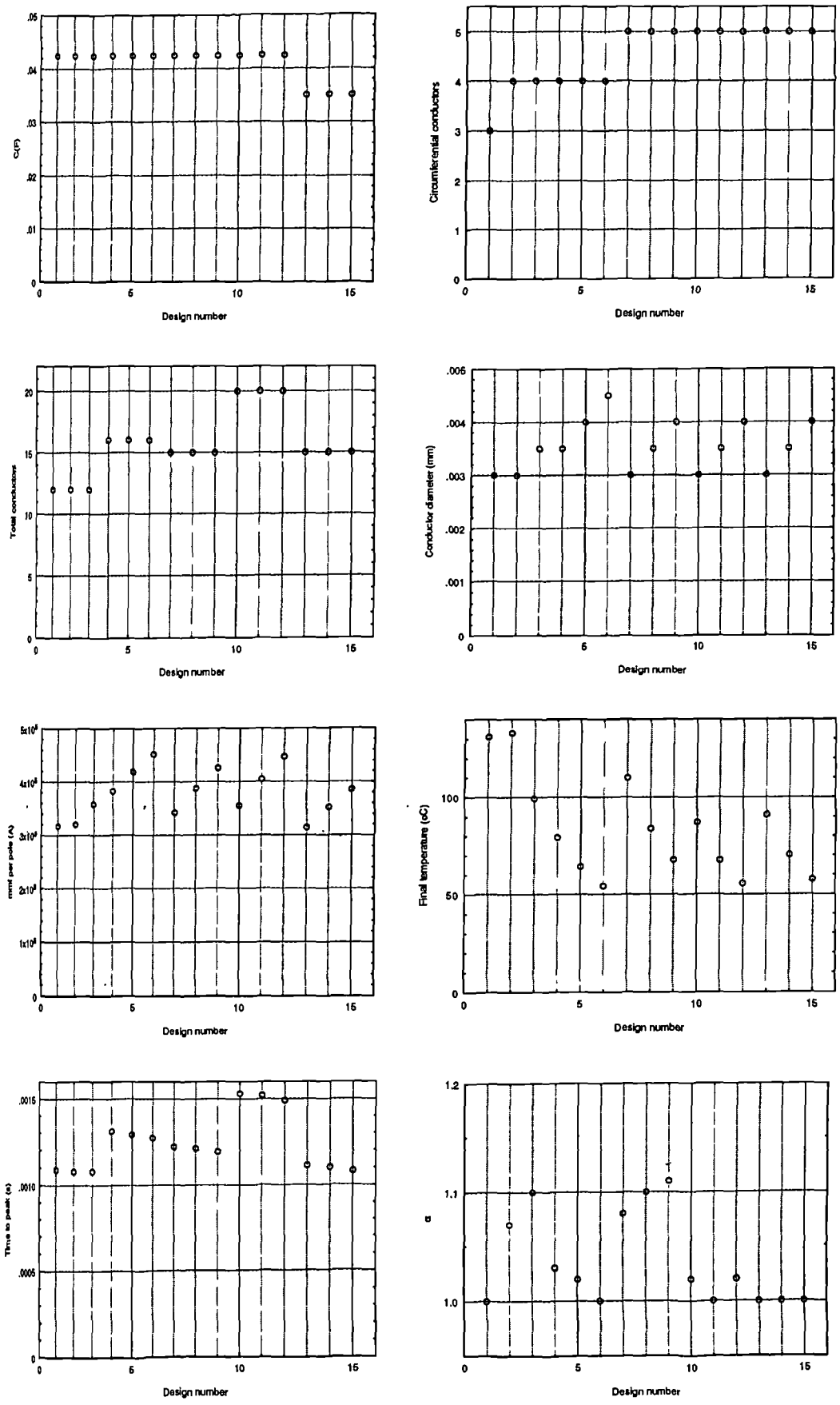

Fig. 4.61 Valid post-assembly fixture designs with axial lengths of 50mm. (V = 800V).

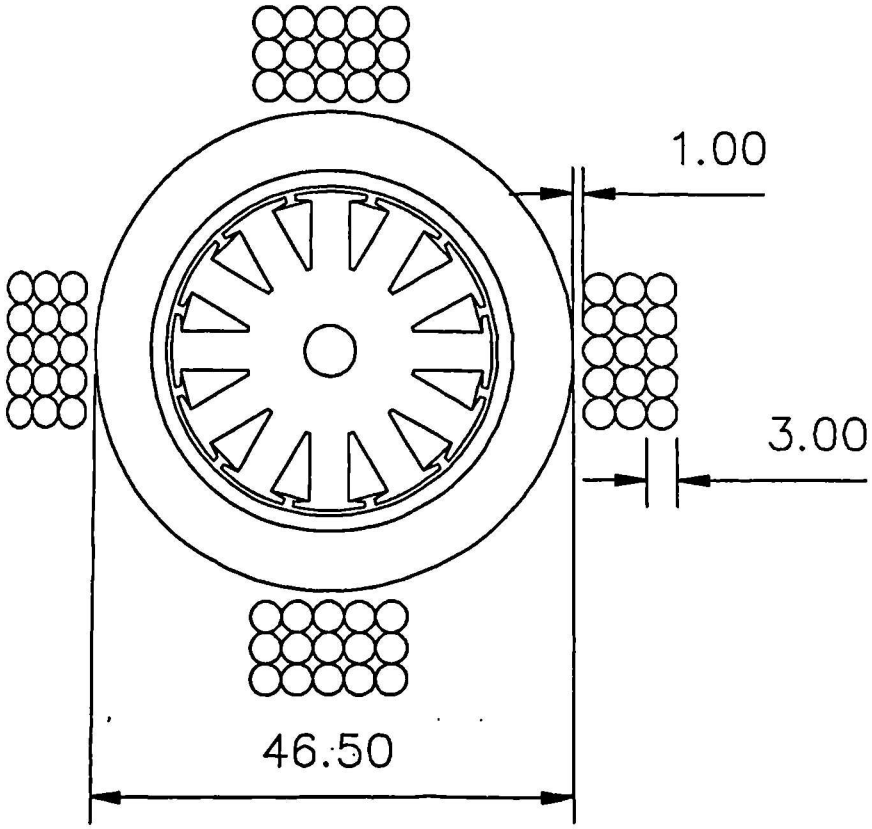

Fig. 4.62 Dimensions of fixture design No.7 selected for further analysis.

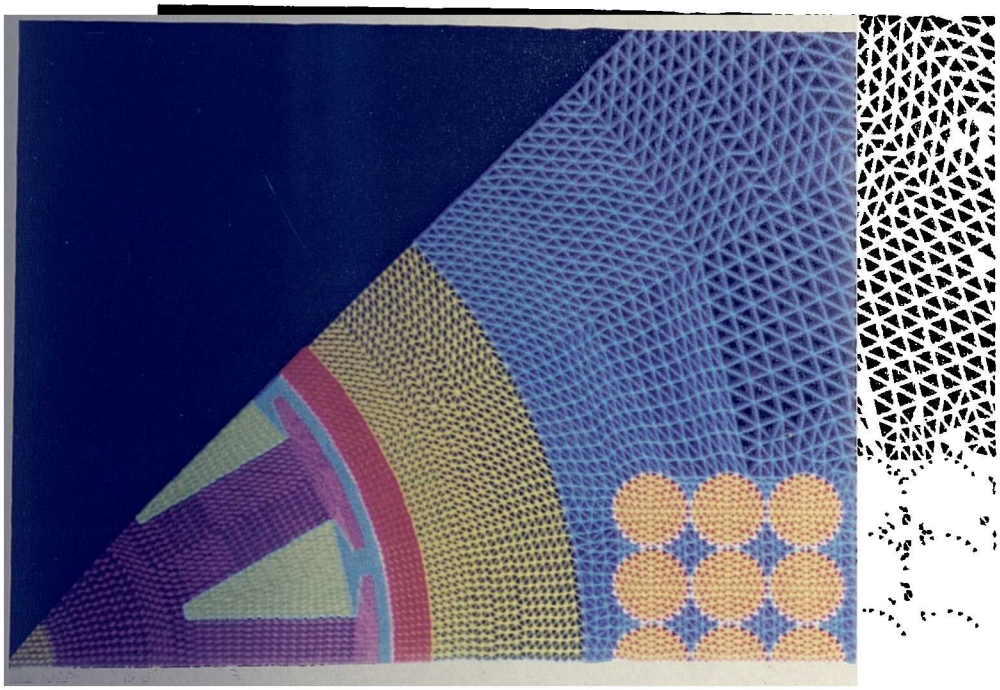

Fig. 4.63 Close-up of the motor region of the finite element mesh used in the dynamic simulation (Total number of nodes and elements 5208 and 10,094 respectively).

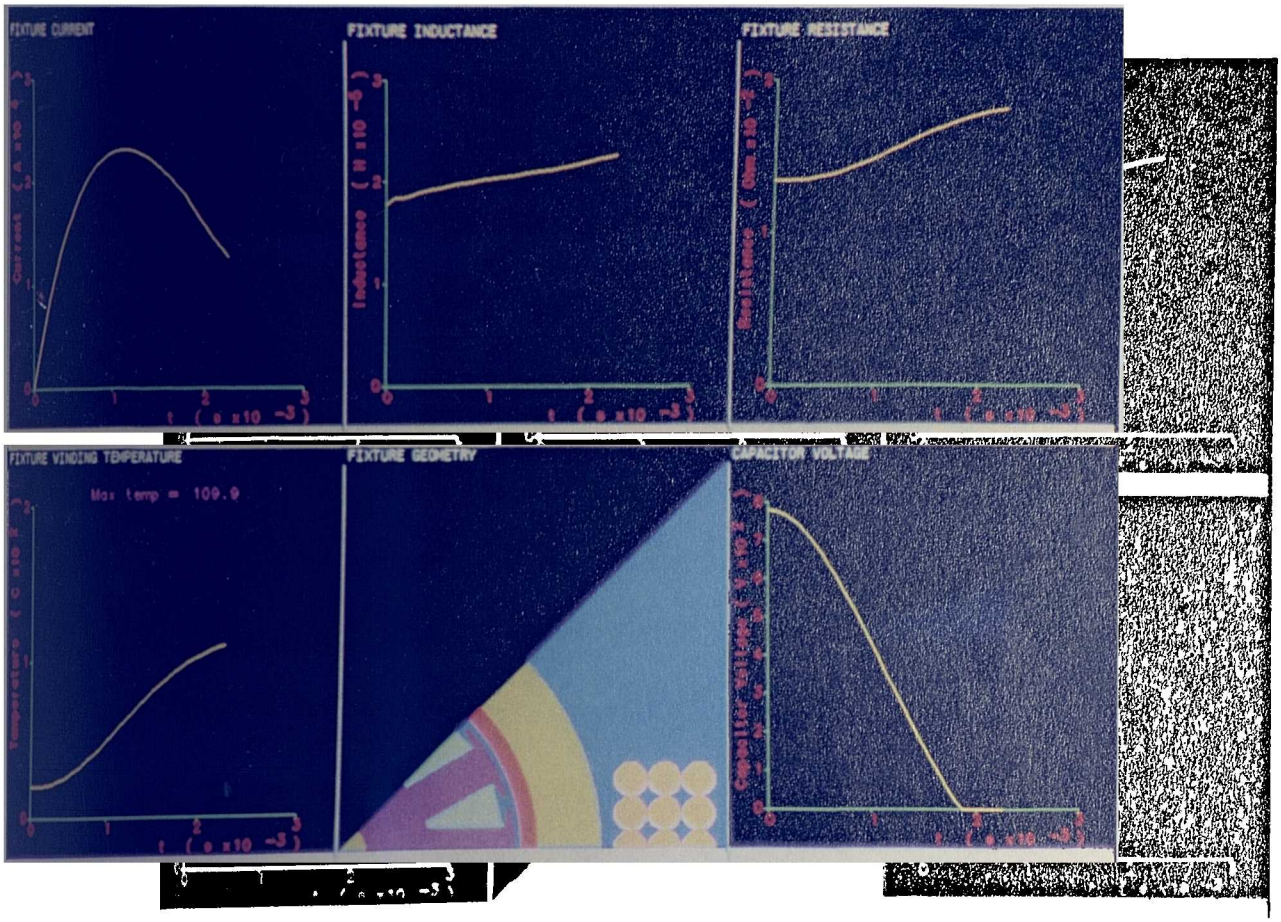

Fig. 4.64 Predicted varaiation in the electrical circuit parameters during the

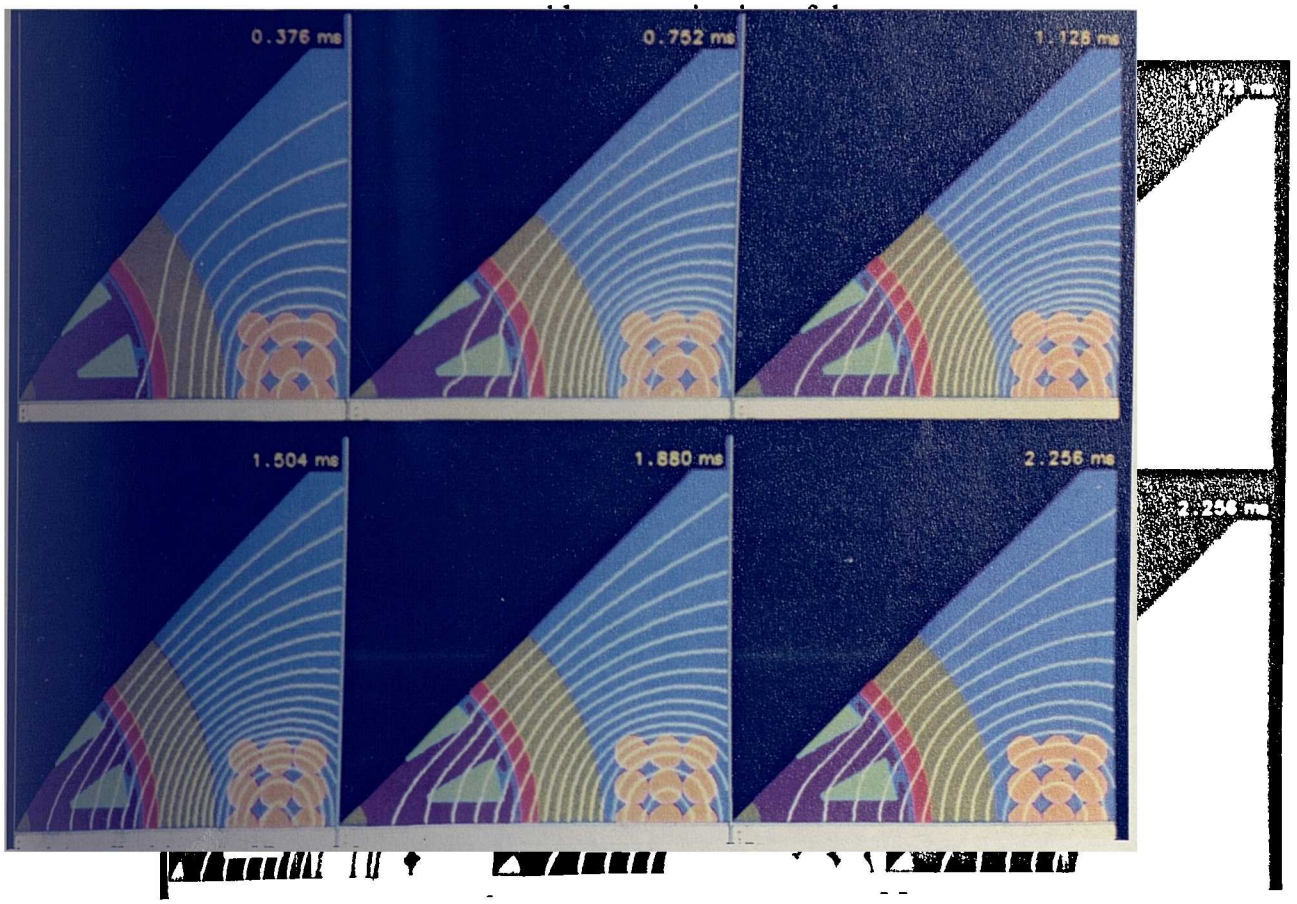

Fig. 4.65 Predicted transient field distributions at instants during the post-assembly magnetization of the motor.

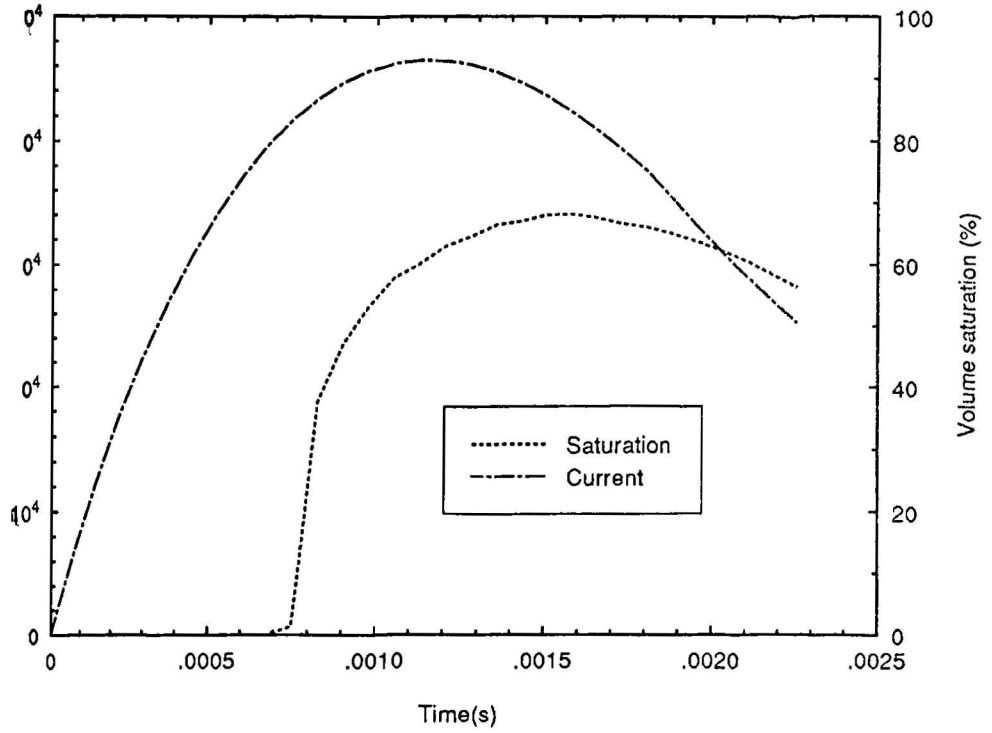

.66 Variation of the magnet volume saturation during the pulse, highlighting the significant effect of eddy-currents in the mild steel rotor.

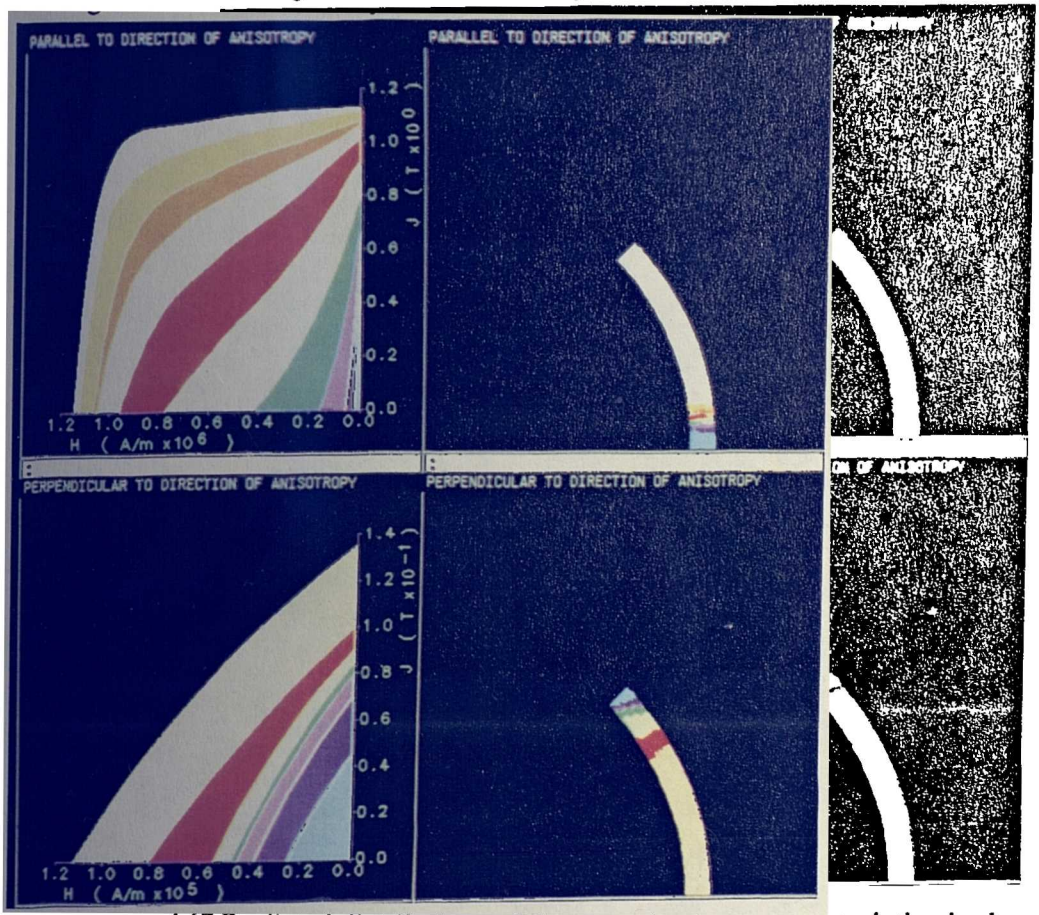

4.67 Predicted distribution of demagnetization characteristics in the magnet following the decay of the magnetizing impulse.

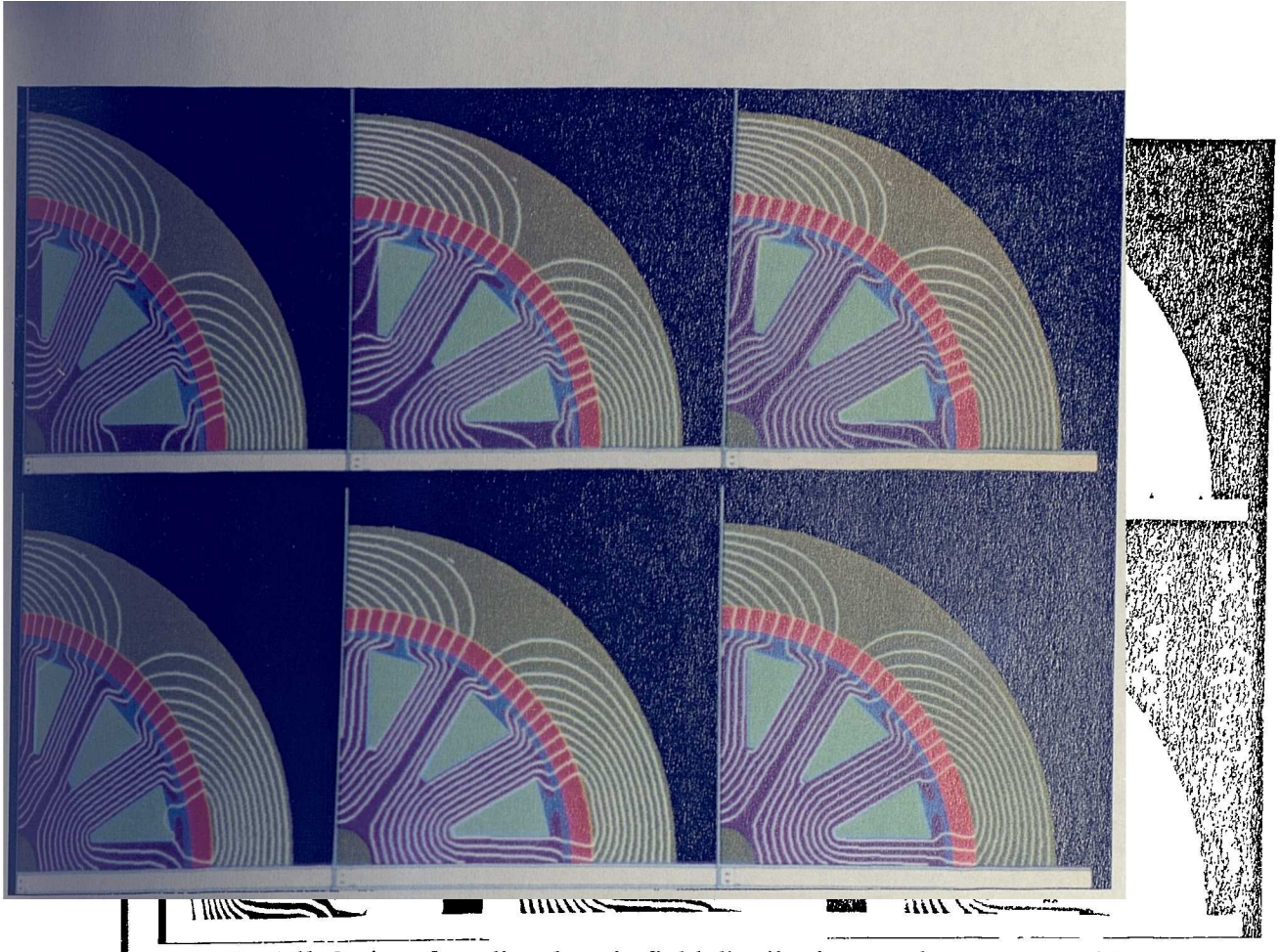

Fig. 4.68 Series of predicted static field distributions as the post-assembly magnetized motor is rotated.

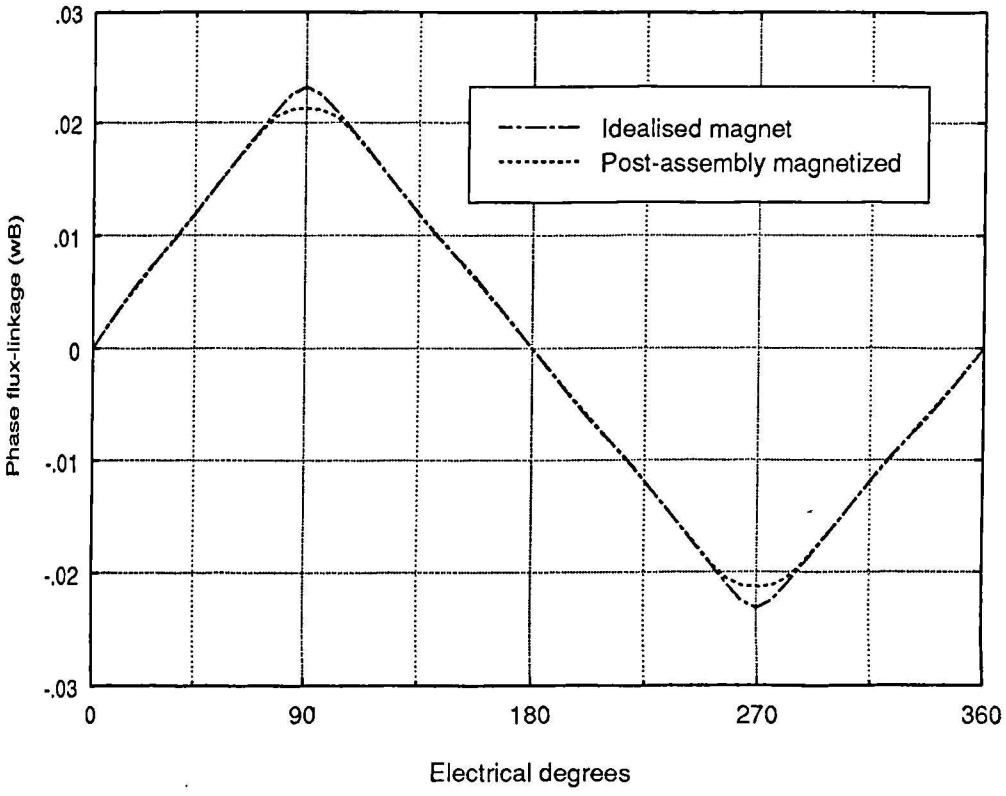

Fig. 4.69 Predicted phase flux-linkage waveforms for the post-assembly magnetized motor and an idealised fully saturated magnet.

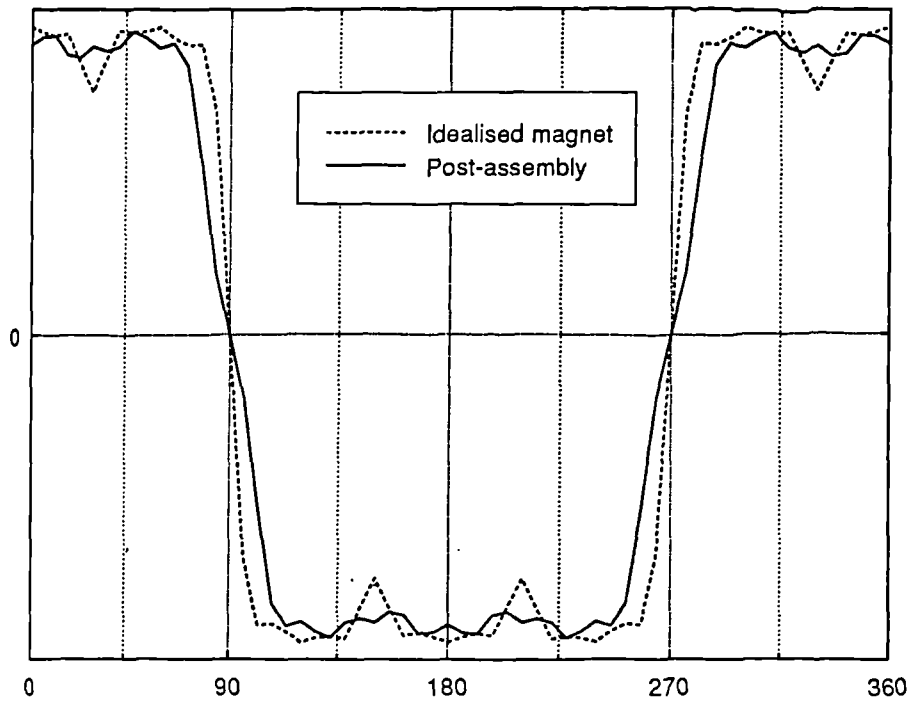

4.70 Predicted normalised phase induced emf waveforms for the post-assembly magnetized motor and an idealised fully saturated magnet.

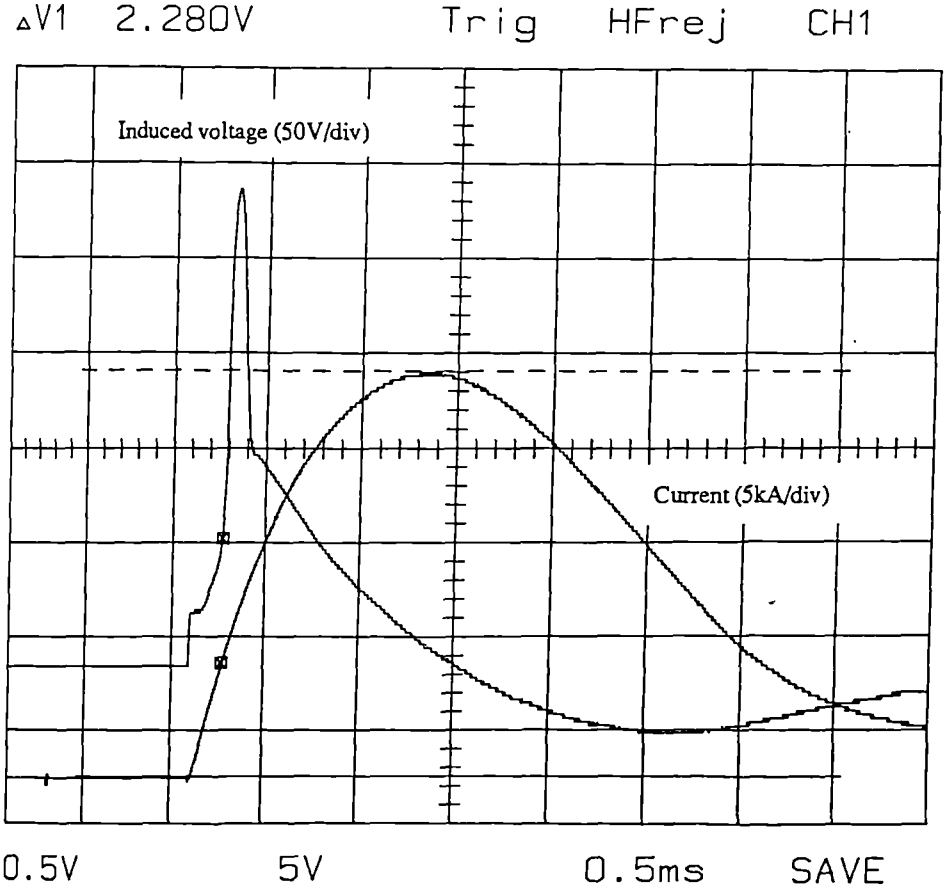

Fig. 4.71. Measured fixture current and voltage induced in one phase of the motor winding during the impulse period. (Current scaling 10kA /V).

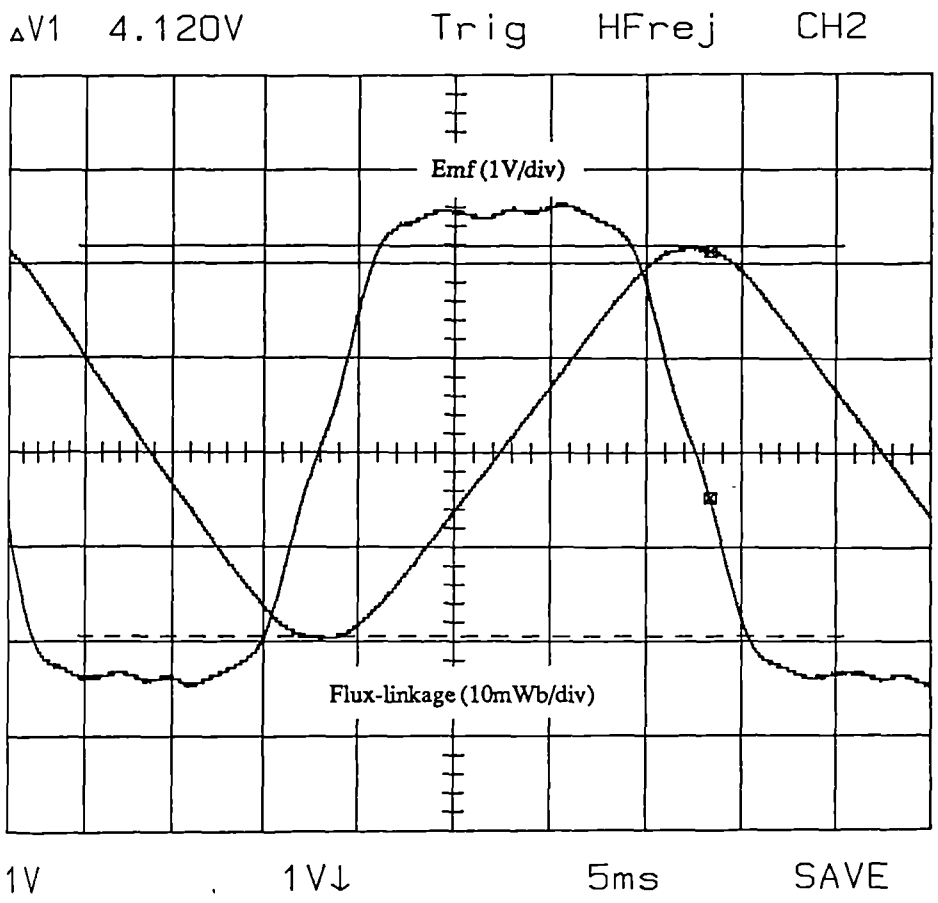

Fig. 4.72 Measured phase flux-linkage and induced emf at 800 rpm.

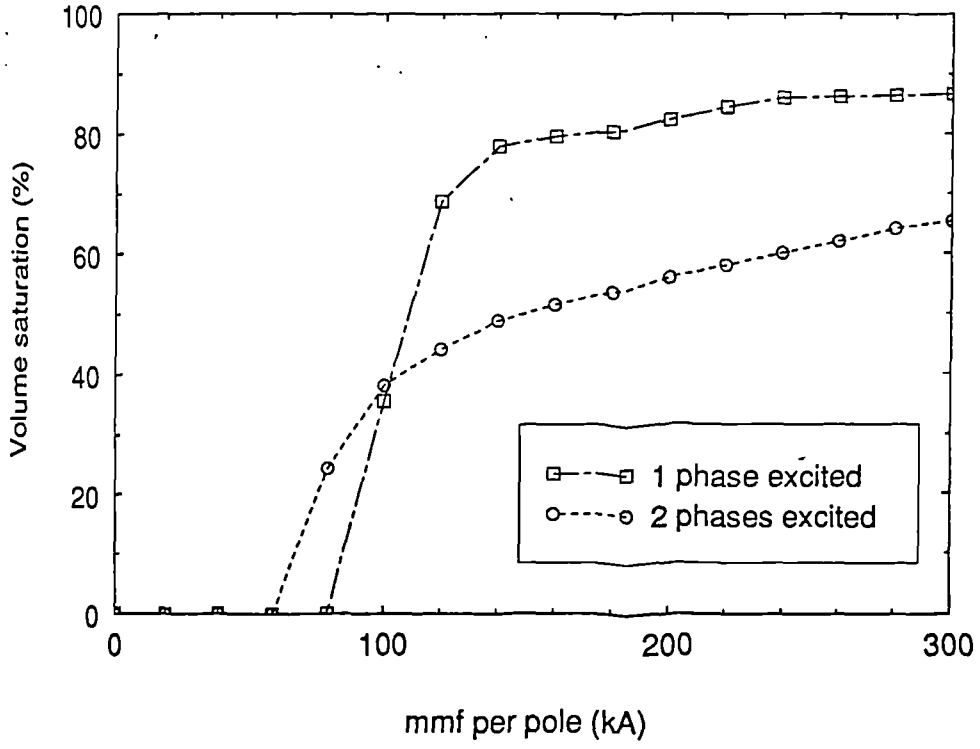

Fig. 4.73 Predicted static volume saturation versus mmf for the magnetization of the assembled motor using the motor windings.

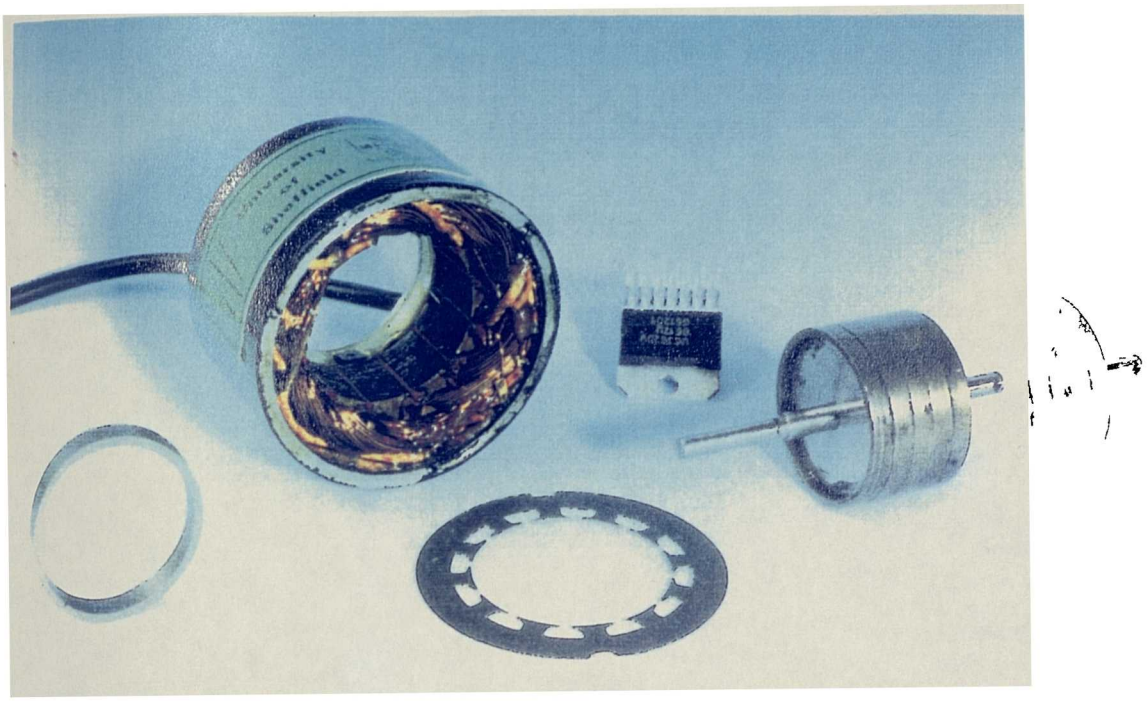

Fig. 4.74 Internal rotor brushless motor designed to the same performance specification as the motor of fig 4.1.

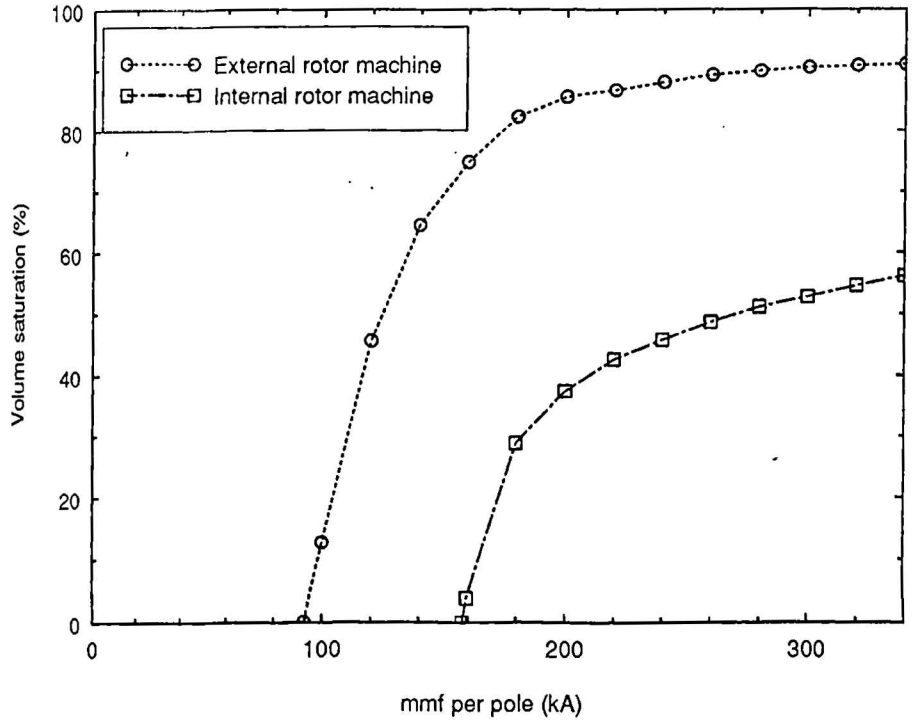

Fig. 4.75 Predicted static volume saturation versus mmf for the post-assembly magnetization of the internal rotor motor with a fixture having a single 2mm diameter conductor per pole located 1mm from the motor casing.

Component Magnetized	Magnetizer stored energy (kJ)	Volume Saturation (%)	Peak motor open-circuit phase flux-linkage (mWb)	Emf "flat top" width (^{o} elec)
Magnet ring alone	2.0	93.5	22.9	156
Assembled rotor-single sided fixture, short duration pulse	2.0	31.5	21.7	148
Assembled rotor-double sided fixture, long duration pulse	9.5	71.3	21.6	140
Fully assembled motor	14.2	68.0	21.3	140
Idealised magnet	-	100	23.2	158

Fig. 4.76 Summary of predicted performance for magnets magnetized at various stages during the production of the motor.

CHAPTER 5

MAGNETIZATION OF A POLYMER BONDED NdFeB MAGNET RING

5.1 INTRODUCTION

Polymer bonded forms of isotropic NdFeB magnets are an attractive alternative to sintered NdFeB magnets in many applications, where they offer intermediate performance between sintered ferrite and rare-earth materials. Although there is continued development of anisotropic grades of bonded NdFeB, the isotropic grades based on General Motors Magnaquench powder are the dominant technology at present. Recent estimates indicate that approximately 100 million electric motors employing bonded NdFeB magnets were produced during 1991, predominantly for use in office automation equipment, computer peripherals and consumer electronics [5.1]. Thus, the multipole magnetization of isotropic bonded NdFeB is an important consideration in a comprehensive CAD system, particularly since it raises a number of issues which are not directly relevant to the magnetization of anisotropic materials.

In isotropic materials, the magnetization produced in the material is parallel to the applied magnetizing field. Hence, any deviation of the magnetizing field from the desired orientation will result in a corresponding deviation in the resultant remanent magnetism. This places additional constraints on the design of multipole fixtures since particular attention must be paid to the conformance of the magnetizing field to the required magnetization direction. Radial-field magnetization of an annular ring magnet, for example, is best achieved by a small volume winding placed directly on the surface of the magnet. An increased winding volume in either the radial or circumferential direction or an increase in its distance from the magnet surface will have a detrimental effect on the radial alignment of the remanent magnetism. The optimal radial-field

fixture designs for isotropic materials, in terms of the level of radial alignment, therefore tend to have a low number of small cross-sectional area conductors, despite the relative electrical inefficiency of such designs. Additional factors which must be considered in designing a fixture for magnetizing a multipole bonded magnet compared to anisotropic materials have been investigated by a case study on the magnetization of a 4-pole rotor for a double airgap moving magnet brushless d.c machine.

5.2 DOUBLE AIRGAP BRUSHLESS D.C MACHINE.

The double airgap brushless d.c machine is shown in fig 5.1. The rotor consists of an isotropic bonded NdFeB ring (axial length 16.5 mm, inner diameter 27.5mm and outer diameter 33mm) which is connected to the motor shaft by a thin aluminium end-cap. This rotor construction in which the laminated rotor core remains stationary, has a much lower inertia than a conventional rotor, and hence is suited to applications requiring rapid acceleration. The decrease in rotor inertia is, however, gained at the expense of penalties in other aspects of performance:

1) The total airgap length is twice that of a conventional machine for the same mechanical clearance, resulting in a reduction in magnetic loading and hence specific torque and efficiency. The increased airgap does, however, have the beneficial effect of reducing the motor inductance, which can be useful at high speed [5.2].

2) In a conventional brushless d.c motor the rotor core is exposed to an almost constant field, with a small alternating component due to the modulating effect of the slot openings of the stator. The core is, therefore, a source of negligible iron loss and can be constructed from a solid soft magnetic material. However, the stationary core of the double airgap motor is exposed to an alternating field, and is, therefore, a source of iron loss per unit mass comparable to that in the stator core (although the stator contains regions in which the loss is increased greatly by the presence of rotating rather than

alternating fields). Therefore, the alternating field in the rotor core of a double airgap machine reduces the efficency of the machine and requires that the rotor core be constructed from a laminated material.

The double airgap construction, in which mechanical considerations are of paramount importance, highlights the advantages of bonded materials compared to sintered materials despite their reduced magnetic properties. The use of a single piece radially anisotropic magnet for this application is not feasible since the aspect ratio of the rotor is such that the aligning field which could be achieved during pressing would show a significant deviation from the required radial orientation. The rotor would, therefore, have to be constructed from a series of short axial length rings, in each of which a reasonable degree of radial anisotropy could be achieved. This multi-component rotor structure would require sleeving and reinforcement at the ends of the rotor to ensure sufficient mechanical strength. The additional sleeving would necessarily require an increase in the total effective airgap length thus reducing any benefits in the magnetic loading of the motor which can be derived from the higher magnetic properties of anisotropic materials.

The motor design strategy and the relative merits of alternative motor topologies are discussed in [5.3], as are the details of a previous attempt to magnetize the rotor using a single turn 2mm diameter conductor serpentine magnetizing fixture and a 40μF,8000V magnetizer. The measured emf constant which was achieved was only 23% of the value predicted at the initial design stage using analytical design equations and assuming magnetization to saturation.

5.3 MAGNETIZING REQUIREMENTS.

The permanent magnet is an isotropic polymer bonded NdFeB ring produced by I.G Technologies Ltd using powder derived from General Motors rapidly quenched

ribbon. The 2nd quadrant demagnetization characteristic of this grade of material were measured by I.G Technologies Ltd, and is shown in fig 5.2. The dependance of the intrinsic demagnetization characteristic on the applied magnetizing field was not supplied, and since no samples suitable for measurement were available, the required saturating field strength was set to 2300 kA/m, by reference to fig 1.14 of chapter 1. The motor was designed to operate from a 3-phase inverter in which a 120^{o} nominally square wave current is applied. Thus to ensure maximum torque per amp and hence efficiency, a trapezoidal back-emf waveform is required with a minimum 120^{o} electrical flat-top. This condition is best met by a radial magnetization of the magnet ring, which results in an approximately rectangular magnet mmf waveform.

5.4 DESIGN CONSTRAINTS.

The fixture windings on both the inner and outer sections of a double-sided fixture are separated from the magnet by a non-magnetic and non-conducting thin wall which can be machined from laminated composite tubes e.g Tufnol, or formed by wrapping epxoy resin soaked stranded fibreglass around the fixture formers. The principal role of these walls is to provide mechanical strength and hence a high degree of structural integrity to the fixture so as to prevent damage to the magnet during the magnetizing pulse, particularly for the section of the fixture within the bore of the magnet ring in which the force is directed outwards against the wall. These walls should be as thin as possible since the achievable degree of radial alignment of the magnetizing field is crtically dependant on the separation of the conductors from the magnet surface.

The calculated minimum wall thickness based on the worst case estimate discussed in Appendix C for a stranded glass fibre construction was 0.23mm. Since this is a worst case, the minimum practically realisable wall thickness of 0.5mm was deemed to be adequate. Although this is a somewhat arbitrary specification, its implication on the durability of the fixture can only be assessed by testing the constructed

fixture. This experimental information can subsequently provide empirical data for future design studies.

In isotropic materials the fixture end-windings can induce a significant multipole axial magnetization as well as distorting the radial magnetization. This axial magnetization can subsequently cause problems with axial vibration because of the rotating axial field produced by the motor end-windings. The problem would be aggravated in this case since the motor has a low inertia rotor. Therefore the electrical design of the fixture was directed towards maximising the axial length, and hence minimising the axial magnetization, without compromising significantly the achievable level of radial saturation. The other constraints applied to the design were a maximum final temperature of 200°C from a 20°C ambient, and a maximum peak current of 30kA.

5.5 FIXTURE TOPOLOGY

There are three possible topologies of radial multipole magnetizing fixtures which can be used to magnetize the magnet ring prior to assembly of the rotor, viz single-sided internal,single-sided external and double-sided fixtures. For this application, a double-sided fixture is the preferred topology because it results in a better radial alignment of the magnetizing field, since the presence of fixture conductors on both sides of the magnet tends to reduce the circumferential flux in the pole transition regions. This tendency to prevent circumferential flux from passing through the magnet does, however, limit the volume of magnet which can be magnetized to saturation with practical levels of magnetizing field to less than 100% since the pole transition region between the conductors is only exposed to a small field resulting in a weakly magnetized zone. The level of saturation achieved for a given current density, and hence thermal performance, is higher for a double sided fixture than for single sided fixtures since the mmf source can be located closer to the magnet. Increasing the volume of the conductor bundle at each pole increases the size of the weakly magnetized zone and

reduces the degree of radial alignment over the entire pole.

5.6 CALCULATION OF MAGNETIZING MMF.

The relative permeability of isotropic bonded NdFeB, derived from the its initial magnetization characteristic, is shown in fig 5.3. It is low over the entire magnetization curve, particularly at the magnetizing field strength required for saturation (approximately 2300 kA/m). The low relative permeability, the absence of a preferred direction of magnetiztion and the short magnet length suggest that the analytical field calculation method for estimating the required magnetizing mmf is ideally suited to this case. To confirm this suitability, the percentage volume saturation versus mmf per pole for the double sided fixture of fig 5.4 was calculated by both the magnetostatic non-linear finite element method and the analytical method.

The field distribution calculated by the non-linear finite element method for an mmf of 150kA is shown in fig 5.5. It demonstrates that the tendency for magnetizing flux to pass circumferentially through the pole transition region is small. Hence a large proportion of the magnetizing flux follows a long path in which the modifying effect of the non-linear magnet material is minimal. This results in excellent agreement between the percentage volume saturation versus mmf per pole calculated by both methods as shown in fig 5.6. Hence the analytical method was selected for use in the subsequent electrical design. Increasing the winding dirstibution tends to improve the agreement between the analytical and finte element methods due to the decrease in the influence of the magnet on the global reluctance of the magnetic circuit .

5.7 ELECTRICAL DESIGN

The requirement for a radially aligned field is best served when the circumferential dimension of the conductor bundle at each pole is small. Therefore, the design was focussed intially on double sided fixtures with only one conductor per pole in the

circumferential direction. In incrementing the number of conductors at each pole during the design procedure, a symmetrical distribution of conductors on each side of the magnet ring was enforced whenever space made this possible.

There are a number of factors which make a low capacitance/high voltage magnetizer the preferred magnetizer for this application, viz:

1) The highest degree of radial alignment is achieved with a fixture having a minimum winding circumferential dimension, which in turn is achieved by using a high current density and a small conductor cross-sectional area. In order to achieve the high current densitiy without excessive dissipation, the pulse duration should be short, a condition best served by a low capacitance/high voltage magnetizer unit.

2) The low bulk eletrical conductivity of the magnet (5.5×10^4 Sm^{-1} c.f 7.0×10^5 Sm^{-1} for sintered NdFeB) is such that eddy-current effects will be negligble even for very short pulse lengths (<100μs rise time). The pulses produced by the low values of capacitance available viz. 150,300 and 450μF, even under the worst case condition of a short-circuit, produce pulses which are likely to be of sufficient duration to ensure almost complete penetration of the magnetizing field.

3) The compact winding dictated by the requirement for a high degree of radial alignment will necessarily involve some compromise in the electrical efficiency of the fixture. Thus the internal impedance of the magnetizer should be minimised since the scope for impedance matching may well be limited.

The design strategy adopted was to calculate the performance of a range of fixtures connected to the available values of capacitance, viz 150,300 and 450 μF, at an intial voltage of 3000V. For each value of capacitance the following variables were incremented:

1) Conductor diameter, from 0.5mm to 3mm in 0.5mm increments.

2) Axial length of the fixture, from 35mm to 50mm in 5mm increments.

3) Number of conductors on each side of the magnet, from 1 to 10 subject to space limitations inside the magnet ring.

For a capacitance of 150μF at an intial voltage of 3000V the fixture parameters which produce the maximum percentage saturation for a range of fixture axial lengths are shown in fig 5.7. The predicted percentage volume saturation is extremely low since there is insufficient stored energy to produce the required magnetizing mmf, and hence the use of the lowest available capacitance, although attractive from the point of view of fixture energy dissipation, is not feasible.

Increasing the capacitance to 300μF improves the maximum percentage volume saturation for each of the axial lengths, as shown in fig 5.8. However, even for an axial length of 35mm, the percentage volume saturation is limited to 78.8%. For the fixtures of fig 5.8 the limiting factor on the performance is the maximum capacitor voltage of 3000V, since in terms of the thermal constraint there is scope for increasing the current in these fixtures to achieve saturation levels in excess of 90%.

A further increase in the capacitance to 450μF results in a large number of fixtures which produce levels of saturation in excess of 85%, with a maximum percentage volume saturation of 91.6%. The parameters of the 39 designs which produce a volume saturation greater than 85% whilst also meeting the constraints outlined earlier are shown in fig 5.9. Of the 39 designs, 18 are forced to have unsymmetrical winding distributions due to the limited space available inside the magnet ring. The number of possible designs which produce a saturation of greater than 85% decrease with an increasing fixture axial length, with no suitable designs for axial lengths greater than

45mm.

No valid fixture designs based on 1mm diameter conductors produced saturation levels of greater than 85%. Although certain fixtures with 1mm diameter conductors produce sufficient current to achieve levels of saturation in excess of 90%, the pulse duration produced by the capacitance of 450 μF results in excessive dissipation and temperature rise. The highest level of saturation for a given axial length is achieved with fixtures containing 1.5mm diameter conductors(designs 1,22 and 34), albeit at the expense of having the largest temperature rises. These fixtures correspond to the most compact winding arrangements which were analysed and did not violate the electrical and thermal constraints. The reduction in the highest percentage volume saturation for an increasing axial length is minimal, a reduction from 91.6% (design no.1) to 90% (design no. 34) for an increse in axial length from 35 to 45mm. This implies that a 45mm long fixture, with its reduced end-winding coupling and axial magnetization, can be employed with minmal dilution of the magnet performance.

The limit on the percentage volume saturation of approximately 90% is determined by the inherent field distribution of the double sided topology, in which the region between the conductors is exposed to a field which is small compared to the field intensity near the centre of the pole. An increase above approximately 90% can only be achieved by a large incremental increase in the fixture mmf. Even if this could be achieved without violating the thermal constraints, the magnetization in the interpole region will have poor radial alignment. The radial magnetization could also be improved by reducing the conductor diameter, an option which is not feasible in this case because of the thermal constraints.

The most electrically efficient designs in fig 5.9, i.e those which produce the largest mmf from a given capacitor stored energy, are based around fixtures having a

large number of 2.5mm diameter conductors per pole e.g design 33 which produces an mmf of 261 kA from 11 conductors per pole. These fixtures also result in the lowest temperature rise for a given stored energy because of the large volume of copper in which the energy is dissipated. However, the increase in electrical efficiency which is achieved in such large conductor volume fixtures does not compensate for the fact that an increased mmf is required to produce a given level of saturation, due to the average position of the conductors being further from the magnet. Therefore, these fixtures produce a lower level of saturation than less electrically efficient and more compact windings despite their increased mmf capability.

The predicted percentage volume saturation values shown in fig 5.9 do not indicate the orientation of the resultant magnetization. However, the analytically predicted field distributions can be used to calculate the departure of the alignment between the applied magnetizing field and the required radial direction of magnetization. Fig 5.10 shows histograms of the distribution of the alignment of the saturated volume of the magnet for selected fixtures. Of the fixtures analysed in fig 5.10 the best alignment is obtained with design 34, which has 4 1.5mm diameter conductors per pole on each side of the magnet. In this case almost all the 90.0% of the magnet volume which is saturated is aligned within 4.5^{o} of the radial direction. Fixtures 37 and 39 which have the same conductor arrangement and axial length but conductor diameters of 2mm and 2.5mm respectively have a reduced degree of alignment as well as lower total saturated volumes of 88.0% and 85.4% respectively.

The fixture with 1.5 mm diameter conductors which produces the lowest temperature rise whilst still meeting the specified performance criteria is design 25, which has 7 conductors on each side of the magnet. However, whilst the conductor bundle has the same circumferential width as design 34, its increased radial dimension has a deliterious effect on the alignment with only 46.9% of the magnet volume being both

saturated and aligned within 4.5° of the radial direction compared to 77.0% for fixture 34. A similar but more pronounced effect occurs for the lowest temperature rise designs for both 2mm and 2.5mm conductor diameters, i.e designs 21 and 15 respectively. Thus, in terms of achieving the highest degree of magnetization, as regards both radial alignment and overall level of saturation whilst also maximising the fixture axial length, of the fixtures scanned in the electrical phase stage, fixture 34 is the optimal design. Although its temperature rise is significantly larger than that of the majority of fixture designs in fig 5.9, its steady-state cycle time for a given cooling arrangement is determined by the stored energy, which is the same for all the fixtures.

The inference of an optimum in such multicriteria scanning design is influenced by the scanning increments which are used. Therefore, having established a likely optimum in design 34 by scanning in 0.5mm increments of conductor diameter a more refined discretization of the design space around this optimum was investigated. The temperature rise of design 34 is close to the temperature limit of 200°C, and therefore there is little scope to reduce the conductor diameter without violating the temperature constraint. A fixture with the same winding layout as design 34 but having 1.4mm diameter conductors produces a temperature rise of 188°C when connected to a capacitance of 450μF at 3000V, and a percentage volume saturation level of 89.0%. This slightly reduced level of saturation is due to the improved percentage saturation per unit mmf of the smaller conductor diameter not compensating for the reduction in the electrical efficiency and hence lower mmf. Increasing the conductor diameter to 1.6mm has negligible effect on the total level saturation but gives a reduced radial orientation of the magnetizing field.

Thus, on the basis of static analysis techniques, fixture 34, which has 4 conductors of 1.5 mm diameter on each side of the magnet, is the optimal design, albeit a rather shallow optimum with little reduction in performance for small variations of conductor

diameter either side of 1.5mm.

5.8 DYNAMIC SIMULATION.

Although this particular case study is ideally suited to static analytical methods, a non-linear finite element dynamic simulation of design 34 was performed to confirm the negligible effect of eddy currents in preventing the level of saturation predicted at the static design stage from being realised. A dynamic simulation also provides a demagnetization characteristic for each finite element in the magnet for use in subsequent magnetostatic field calculations of the performance of the magnet ring in the motor. The predicted variation in the electrical circuit parameters, fig 5.11, shows a small eddy-current screening effect reducing the fixture inductance during the initial stages of the pulse, and resulting in a higher current of 24.2kA than the 23.4kA predicted at the analytical design stage. The predicted transient field distributions of fig 5.12 demonstrate the high degree of radial alignment which is achieved over the bulk of the magnet and the minimal effect of eddy currents on the field distribution at the peak of the current pulse, i.e at 63μs.

The maximum flux densities achieved throughout the magnet volume are shown in fig 5.13, and highlights the difficulty in achieving saturation in the remaining 7.3% of the magnet volume which is exposed to a relatively low circumferential field component. The predicted percentage volume of magnet exposed to a magnetizing field strength in excess of 2300 kA/m is 92.7%. This slight increase compared to the analytically calculated value of 90% can be attributed to the slightly higher current, and the different discretization of points at which the level of saturation is assessed, the percentage volume saturation being calculated from the field level calculated at the centroids of the triangular elements in the magnet whereas a regular grid of points was used in the analytical calculation.

5.9 CALCULATION OF MAGNET PERFORMANCE

The distribution of the demagnetization characteristics and the orientation of the magnetization within the magnet following the decay of the magnetizing pulse were obtained from the results of the preceeding dynamic simulation. These were subsequently utilised in a series of magnetostatic finite element calculations to predict the flux-linkage versus rotor position waveform for the assembled motor.

Unfortunately, data regarding the dependancy of the demagnetization curve on the level of applied magnetizing field was not available for the particular grade of bonded NdFeB. However, for the purpose of modelling the effect of partial magnetization, the demagnetization characteristic corresponding to a given magnetizing field was obtained by simply scaling according to the measured characteristics for the grade of isotropic NdFeB shown earlier in fig 1.12. This scaling of the curve was based on the ratio of the properties of the fully saturated curve of fig 1.12 to the fully saturated curve of the motor ring material. This approach is likely to be reasonably accurate since both grades of magnet are based on the same isotropic NdFeB powder, and the magnet properties are essentially dependant upon the ratio of the polymer contents, the effect of which is largely independant of the magnetizing field.

In order to calculate the motor stator winding flux-linkage from a two-dimensional finite element field solution an effective axial length must specified. The magnet ring is bonded into a 1mm recess in the aluminium end-cap as shown in fig 5.1. This end-cap has a 0.5mm clearance from the end of the stationary rotor core, and hence the total rotor magnet axial length located within the lamination stack is 15mm. No account was taken of the 1.5mm magnet overhang in the calculation of the motor flux-linkage since the complex geometry in double airgap machines is unsuitable for the existing analytical techniques[5.4] which are themselves necessarily based on simplifying assumptions even for single airgap machines. However the underestimate

of the flux-linkage produced by neglecting the 10% magnet overhang is compensated for to a degree by the inherent overesimation of the parameters of finite length regions by the two dimensional finite element method.

The calculated field distributions for the simulated magnet as well as an idealised magnet, which is assumed to be fully magnetized throughout its volume in a radial direction, are shown in figs 5.14 and 5.15. The corresponding variations in the stator winding flux-linkage with rotor position calculated are shown in fig 5.16. Despite the lower volume saturation volume of the simulated magnet compared to the 100% saturation of the idealised magnet, its predicted flux-linkage is marginally higher for all rotor angles, with the peak flux-linkage being 3% greater.

This superior performance can be attributed to the fact that the non-radial magnetization of the pole transition regions increases the coupling of the magnet flux with the stator winding. In the case of the idealised radially magnetized magnet, the orientation of the field in the pole transition region is less favourable for linking with the stator winding. A close up of the pole transition regions of both the idealised and partially magnetized magnet are shown in figs 5.17 and 5.18 for the rotor position corresponding to the peak flux-linkage, i.e 30^{o} on the scale of fig 5.16. They illustrate the fact that the pole transition regions produce useful flux-linkage in the simulated magnet, but no useful flux-linkage in the idealised magnet.

Although the idealised magnet produces a lower winding flux-linkage, as expected it produces a higher total flux per pole than the simulated magnet, viz 7.54×10^{-5} Wb and 6.86×10^{-5} Wb respectively. The total flux per pole being calculated from the vector potential at a point on the pole transition axis at the mean radius of the magnet. The flux-linkage waveforms of fig 5.16 were numerically differentiated to produce the normalised induced emf waveforms of fig 5.19. The induced emf waveform for the

simulated magnet has the required 120^{o} flat-top and an average magnitude which is equal to that produced by the idealised magnet. However, it has an increased harmonic content compared to the induced emf produced by the idealised magnet.

5.10 FEASIBILITY OF POST-ASSEMBLY MAGNETIZATION

The problems encountered in achieving radial magnetization in isotropic materials are aggravated in post-assembly magnetization when the fixture conductors are necessarily more remote from the magnet. The percentage volume saturation versus mmf characteristic of fig 5.20 calculated by a non-linear finite element method for a $1mm^2$ conductor located 0.5mm from the motor casing, indicates that in order to achieve the same level of saturation as that achieved with the double sided fixture used for magnetizing the rotor alone requires an mmf of 350kA per pole. Clearly, this is impractical for a concentrated winding. A much larger distributed winding would be required in order to meet the thermal constraints. In turn this would subsequently require an increased mmf, and lead to a degradation in the radial alignment of the magnetizing field. However, even for the concentrated winding, which is a best case in terms of the quality of alignment between the magnetizing field and the radial direction, the alignment is very poor, as shown by the predicted field distribution of fig 5.21 and the histogram of fig 5.22. This is a direct consequence of the large distance between the magnet and the fixture conductors. Therefore for this case, in which a radial magnetization was specified, post-assembly magnetization is not feasible.

5.11 EXPERIMENTAL RESULTS.

The measured and predicted electrical circuit parameters of the constructed fixture are in good agreement, as shown in fig 5.23. The measured fixture inductance includes the contribution of the connection leads which was estimated to be $0.1\mu H$ by a measurement on a set of dummy leads having the same dimensions. The agreement

between the measured current waveform of fig 5.24 and the predicted waveform of fig 5.11 is within the acceptable error bounds.

The induced emf per phase of the assembled motor was measured by driving the motor at 2000rpm using a slotless, axial-field, brushed permanent magnet motor connected to a large inertia flywheel so as to eliminate speed ripple produced by the cogging torque of the double airgap motor. Elimination of the speed ripple in the measured emf is important for comparison with normalised predicted emf which is calculated as a function of position and hence implicitly assumes constant speed.

The measured waveforms of induced emf and flux-linkage (which was derived by analogue integration of the induced emf) shown in fig 5.25 exhibit a high degree of symmetry. The measured and predicted flux-linkage waveforms, fig 5.25 and fig 5.16 respectively, show excellent agreement in both magnitude and form. However, the agreement in the magnitude should be considered in the context of the simplifications applied in the selection of the effective axial length of the finite element region. The predicted and measured induced emf waveforms of figs 5.25 and 5.17 respectively again show excellent agreement, particularly with regard to the additional harmonic component content compared to induced emf waveform from the idealised magnet.

As regards the robustness of the fixture, the retaining wall on the internal winding former showed signs of surface cracking at each pole transition after a number of pulses. It is concluded therefore, that with the constructional techniques and materials employed a 0.5mm wall thickness would be insufficent to ensure long term strutural integrity, and an increase in the thickness to at least 1mm would be required. Alternatively, the mechanical strength could be improved by using an improved resin and stronger binding materials such as kevlar filaments or carbon fibre which are often used in very high field solenoids i.e >40T [5.5]. Encapsulation under vacuum would also be

beneficial since in the case of thin walled structures a single entrapped air bubble can be a significant fraction of the wall thickness and hence produce a marked change in the mechanical strength.

Figs 5.26 and 5.27 show the predicted effects of increasing the retaining wall thickness on the electrical circuit parameters, the saturation level and radial alignment. The benefits of a thin wall in terms of maximising the radially orientated saturated volume are clearly demonstrated. However, the selection of a wall thickness for a production fixture will inevitably be a compromise between electromagnetic and the mechanical considerations, with due account of cost and availability of materials and construction techniques, and the projected lifetime and duty cycle of the fixture, which are in turn related to the number of the motors to be produced.

5.12 CONCLUSIONS

This case study has demonstrated the utility and validated the accuracy of the analytically based design/analysis procedures, as well as the fact that an accurate prediction of device performance can be obtained with detailed finite element analysis. In addition, the following general points regarding the magnetization of isotropic bonded materials have been demonstrated during this case study:

1) For the magnetization of bonded magnets, in which induced eddy-currents and hence a minimum pulse duration are not significant considerations, a higher voltage magnetizer than the 3kV unit available would be useful.

2) A compact and electrically inefficient winding design often produces the optimal level of saturation in isotropic materials, particularly when the specification includes a required orientation for the remanent magnetism.

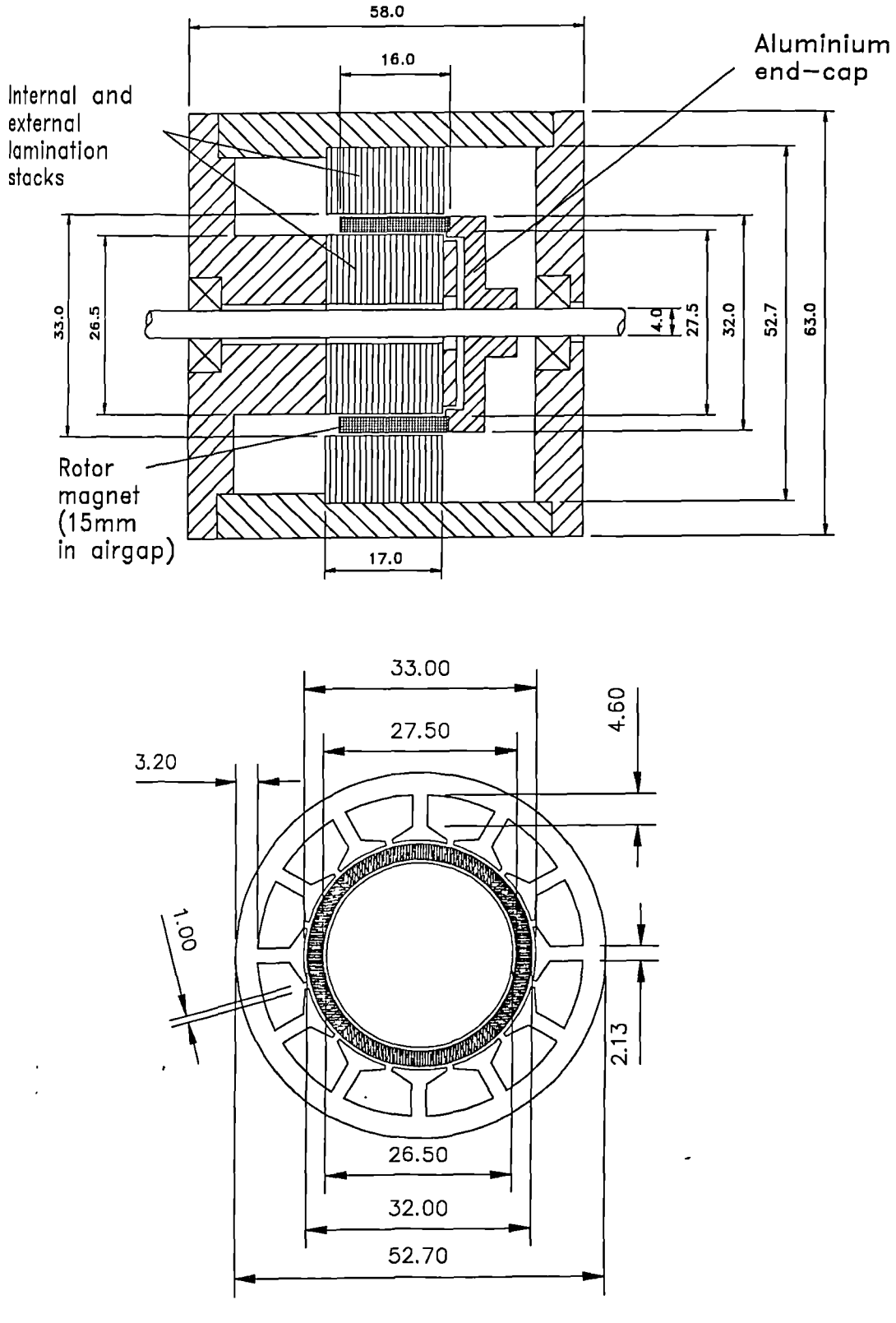

Fig. 5.1 Double airgap brushless dc motor.

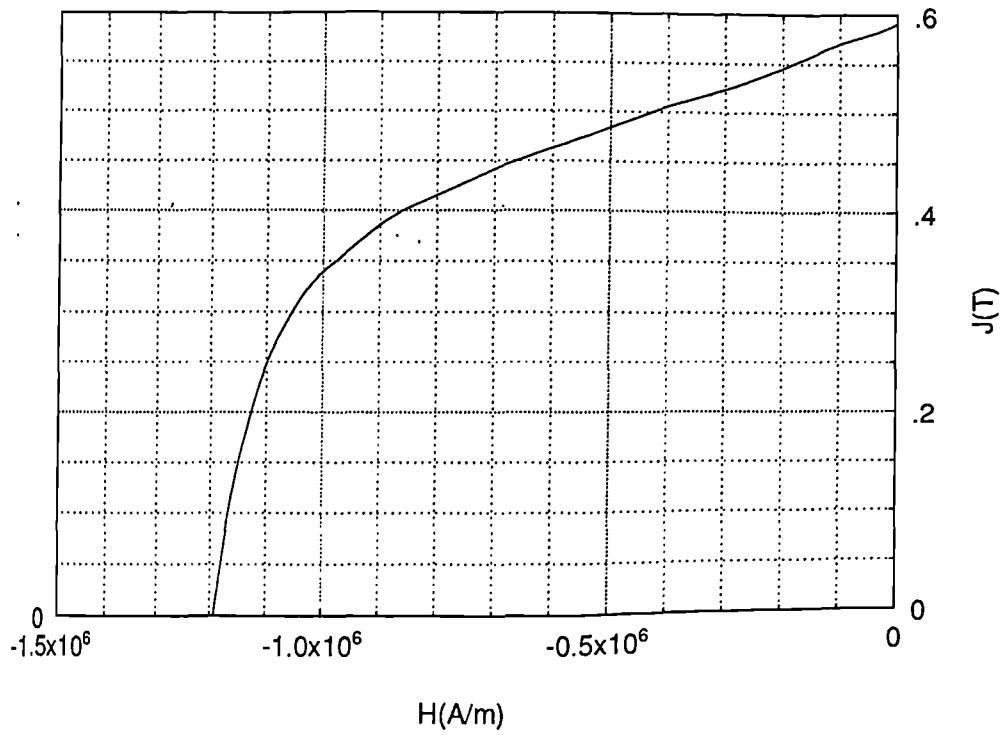

Fig. 5.2 Room temperature intrinsic demagnetization characteristic for IG bonded NdFeB (measurd by IG Technologies).

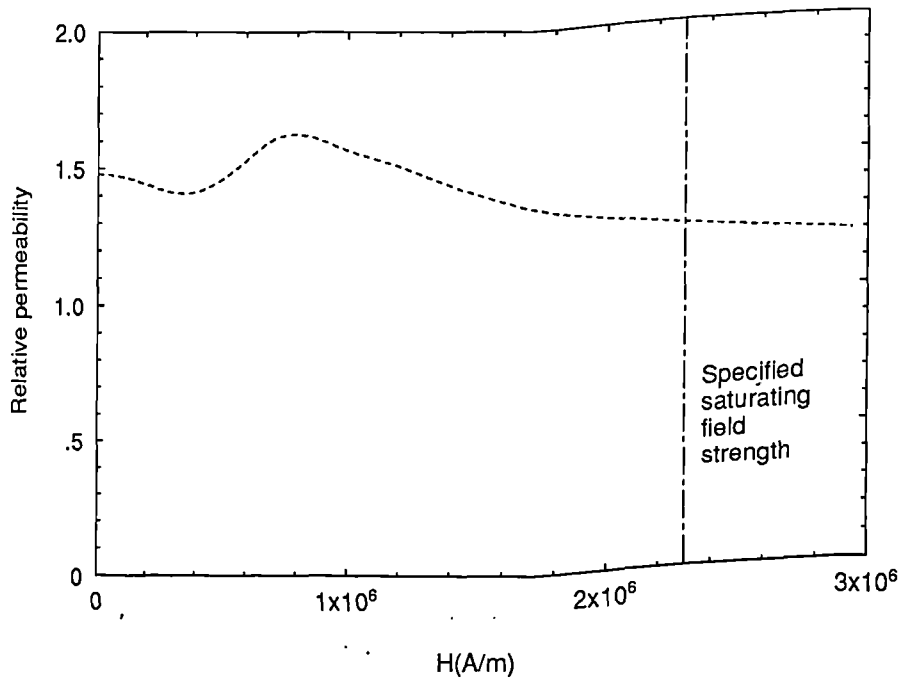

Fig. 5.3 Variation of the initial magnetization curve permeability for IG bonded NdFeB (derived from the initial magnetization curve measured by IG Technologies).

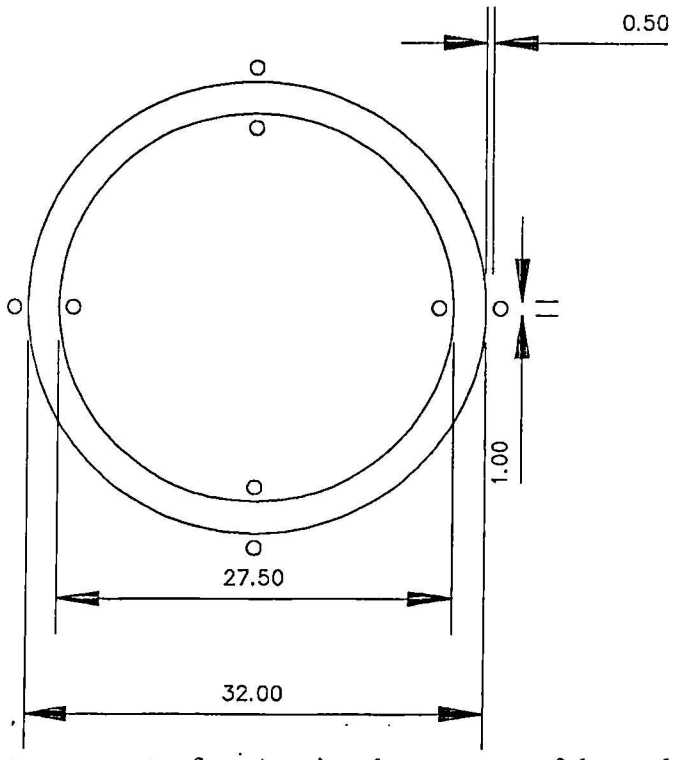

Fig. 5.4 Fixture geometry for assessing the accuracy of the analytical field calculation method.

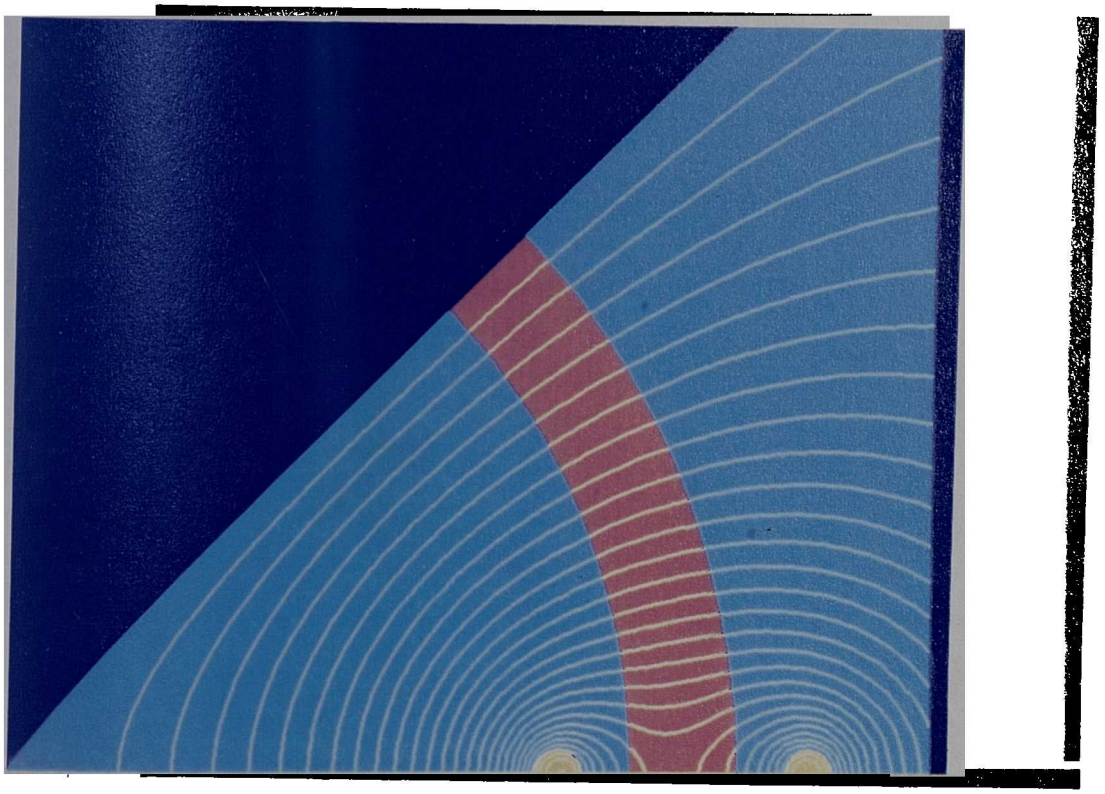

Fig. 5.5 Finite element predicted static field distribution for an mmf of 150 kA per pole.

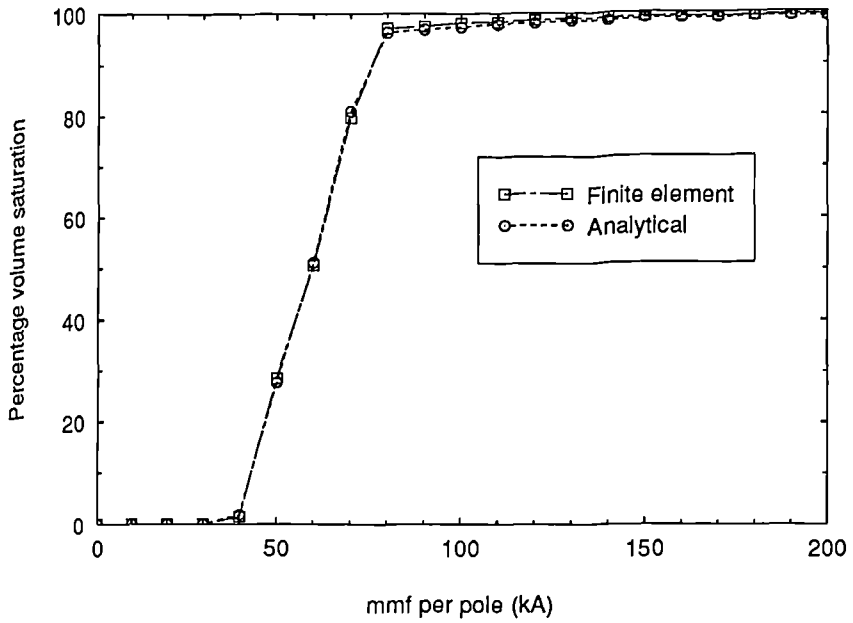

Fig. 5.6 Comparison of analytical and finite element volume saturation versus applied mmf characteristic.

Axial length (mm)	No. of conductors		diameter (mm)	Temperature rise (^{o}C)	Peak current (kA)	Volume saturation (%)	Time to peak (μs)
	inner	outer					
35	5	5	1.0	177	16.3	7.4	32.3
40	4	4	1.0	165	15.6	2.6	33.5
45	3	3	1.0	156	15.0	1.7	35.0

Fig. 5.7 Optimal fixture designs for C=150μF

Axial length (mm)	No. of conductors		diameter (mm)	Temperature rise (^{o}C)	Peak current (kA)	Volume saturation (%)	Time to peak (μs)
	inner	outer					
35	5	5	1.5	102	18.5	78.8	58.4
40	4	4	1.5	114	20.5	69.1	52.9
45	4	4	1.5	107	19.7	57.4	54.2

Fig. 5.8 Optimal fixture designs for C=300μF

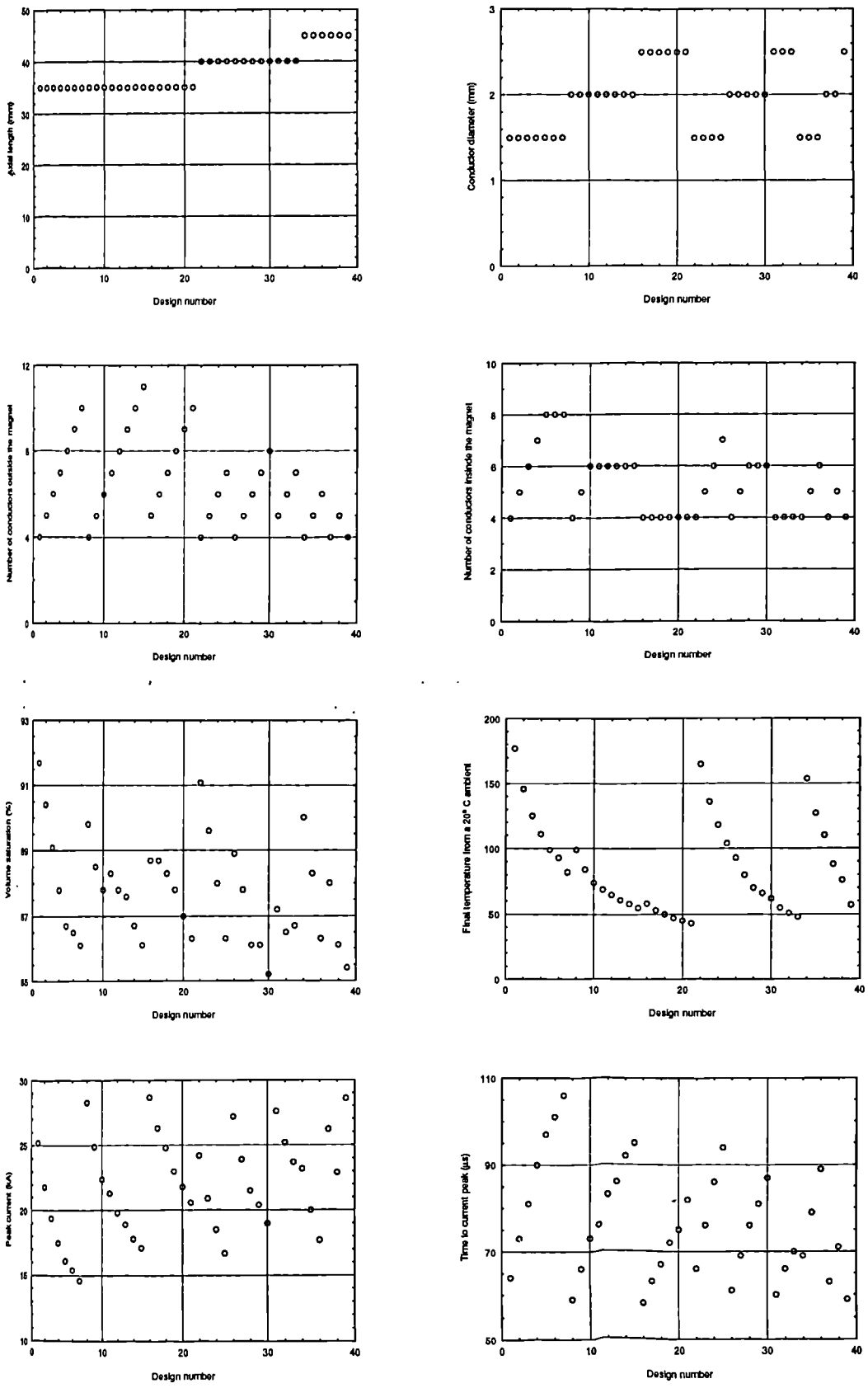

Fig. 5.9 Valid double-sided fixture designs for C=450μF , Vo = 3000V.

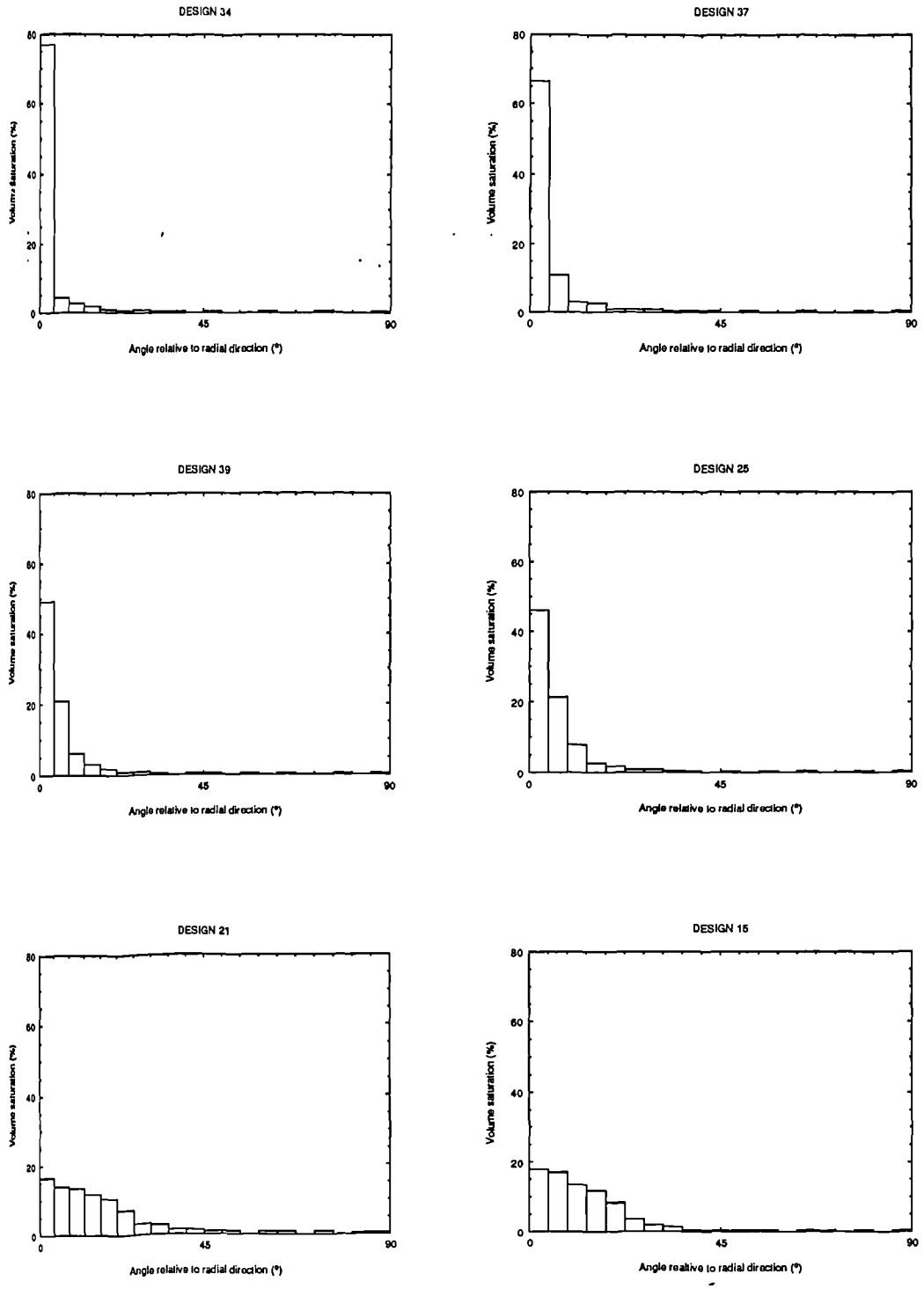

Fig. 5.10 Comparison of the radial alignment of the saturated magnet volume (>2300 kA/m) for a range of fixture designs.

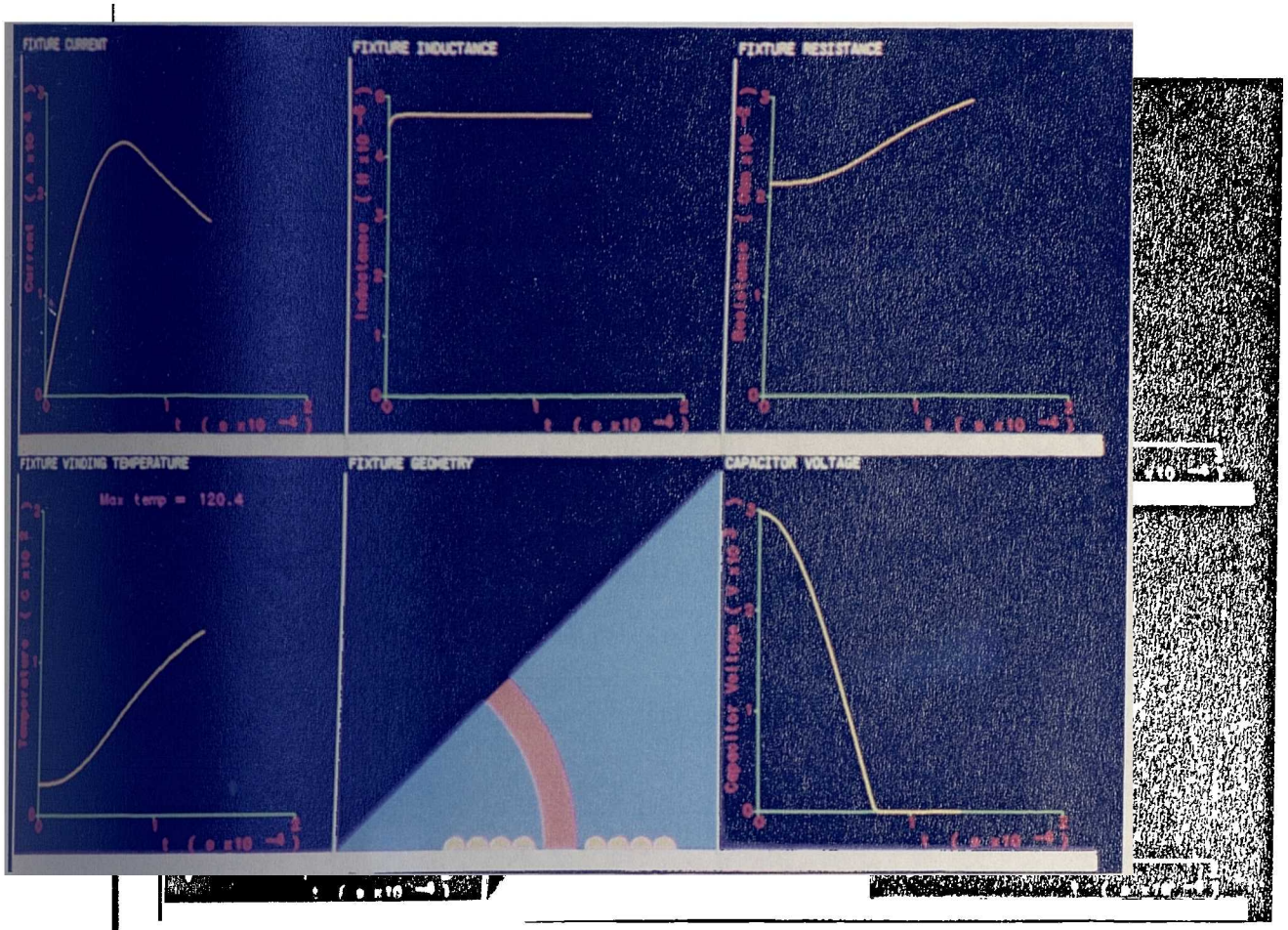

5.11 Predicted variation in electrical circuit parameters during the magnetizing pulse.

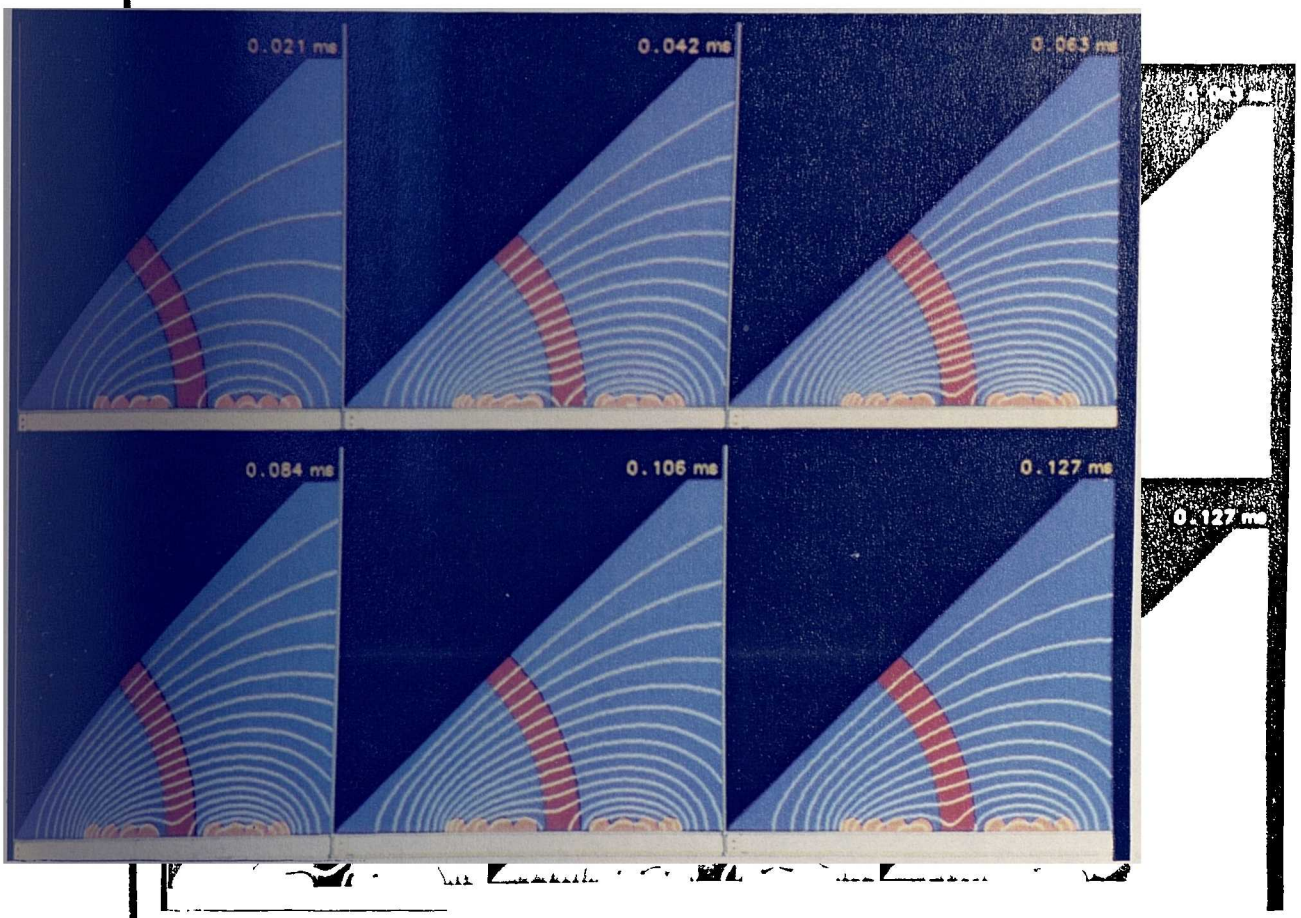

Fig. 5.12 Predicted transient field distributions during the magnetizing pulse.

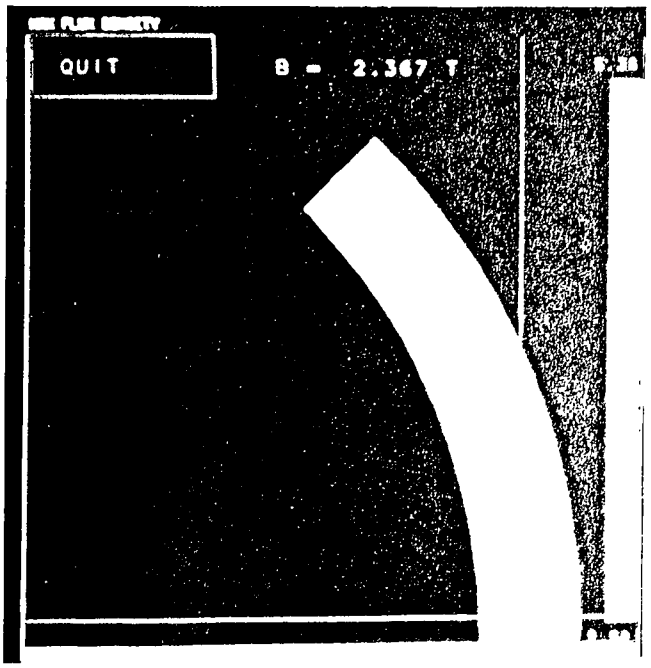

5.13 Predicted maximum flux density in each element of the magnet.

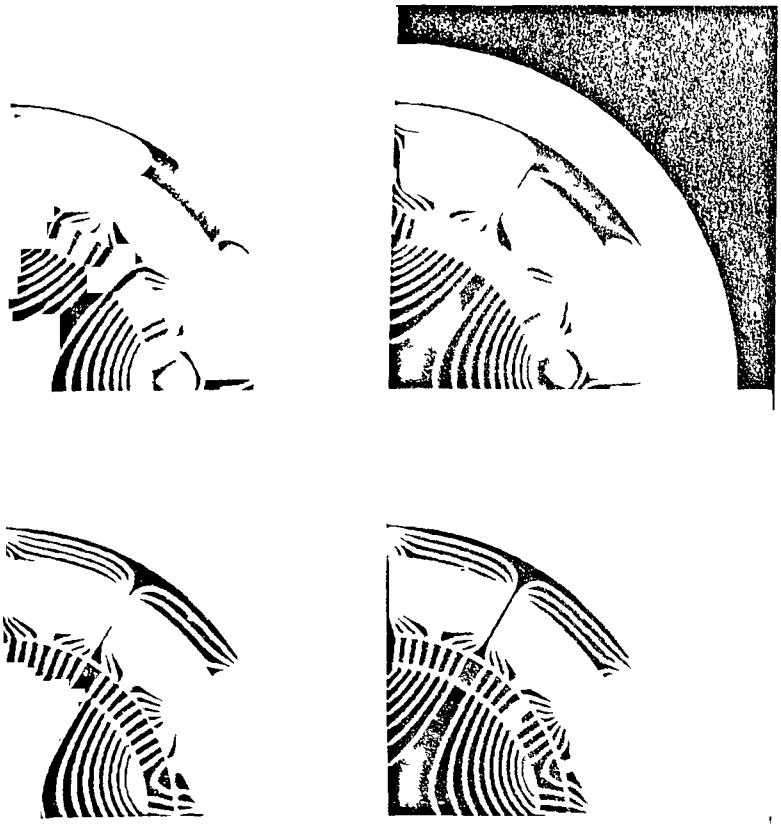

redicted static field distributions as the simulated magnet is rotated in an assembled motor.

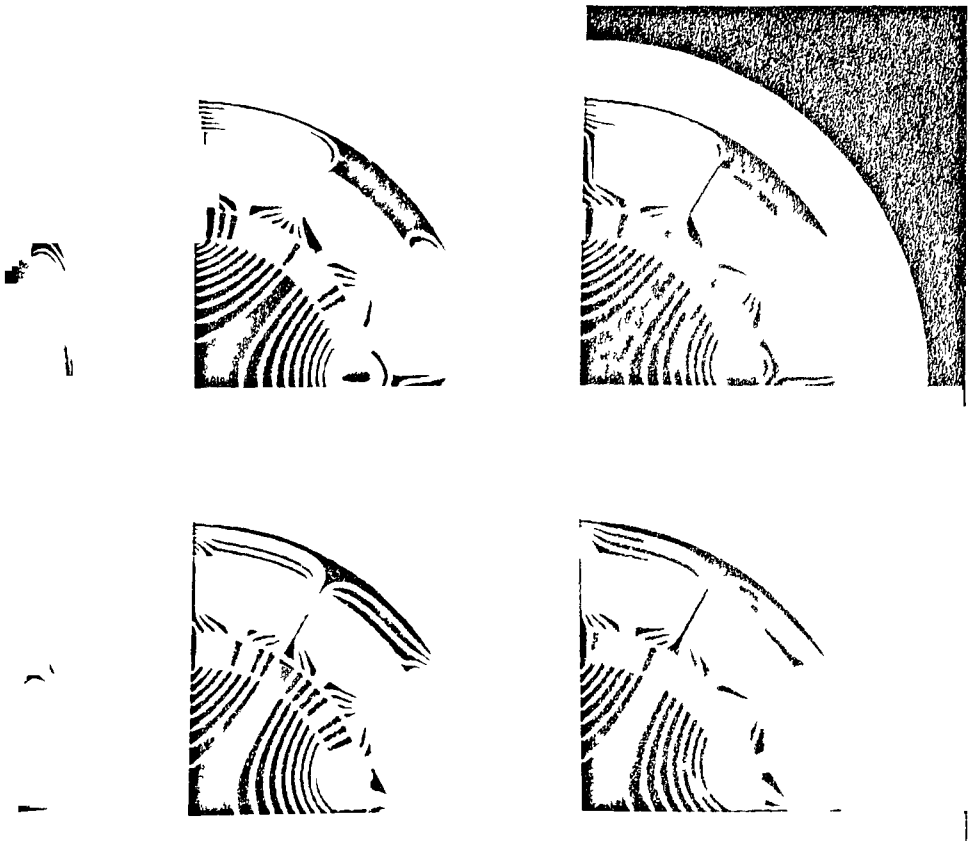

Fig. 5.15 Predicted static field distributions as the idealised magnet is rotated in an assembled motor .

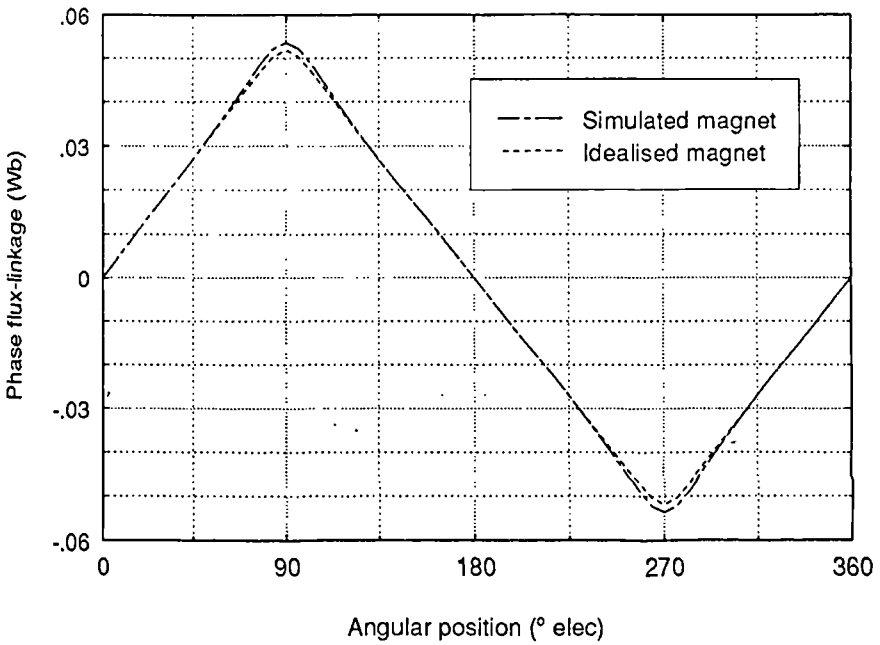

Fig. 5.16 Predicted flux-linkage waveforms.

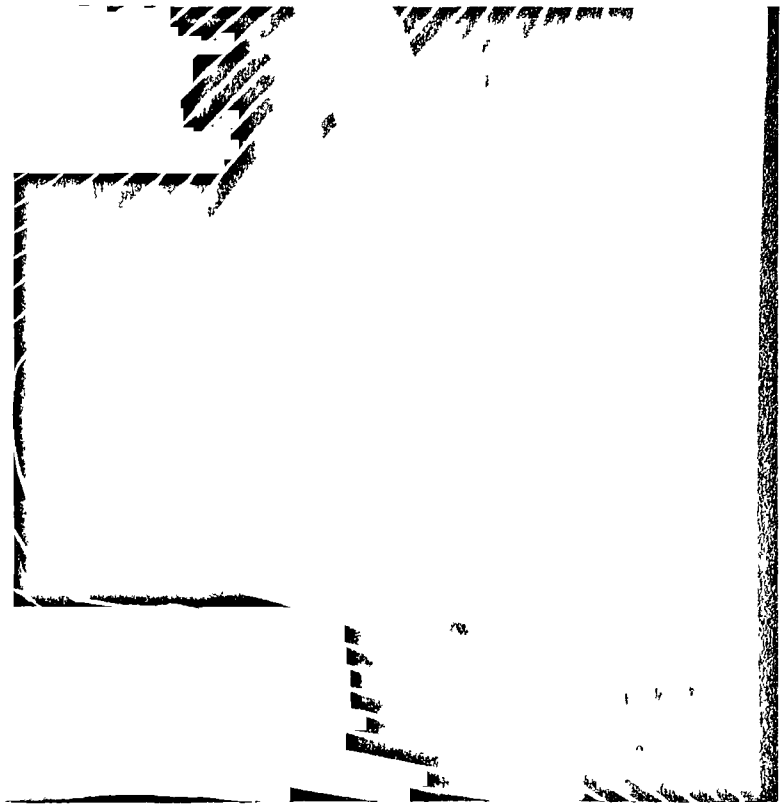

Fig. 5.17 Close up of the predicted field distribution near the pole transition for the simulated magnet (Increments in equipotential contours 5 times smaller than in fig 5.14)

Fig. 5.18 Close up of the predicted field distribution near the pole transition for the idealised magnet (Increments in equipotential contours 5 times smaller than in fig 5.15)

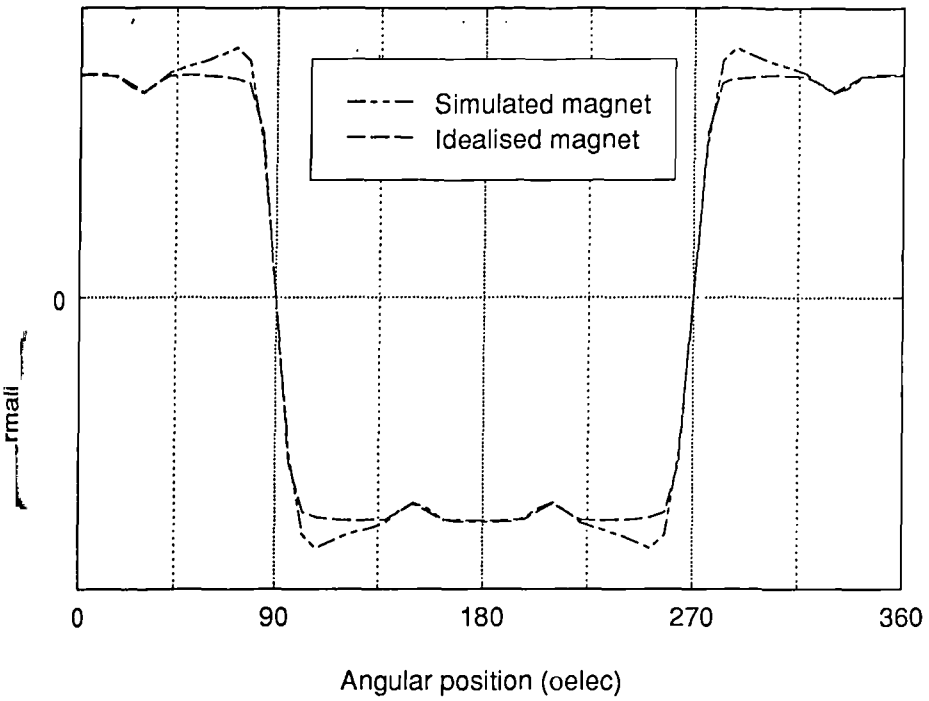

Fig. 5.19 Predicted induced phase emf waveforms

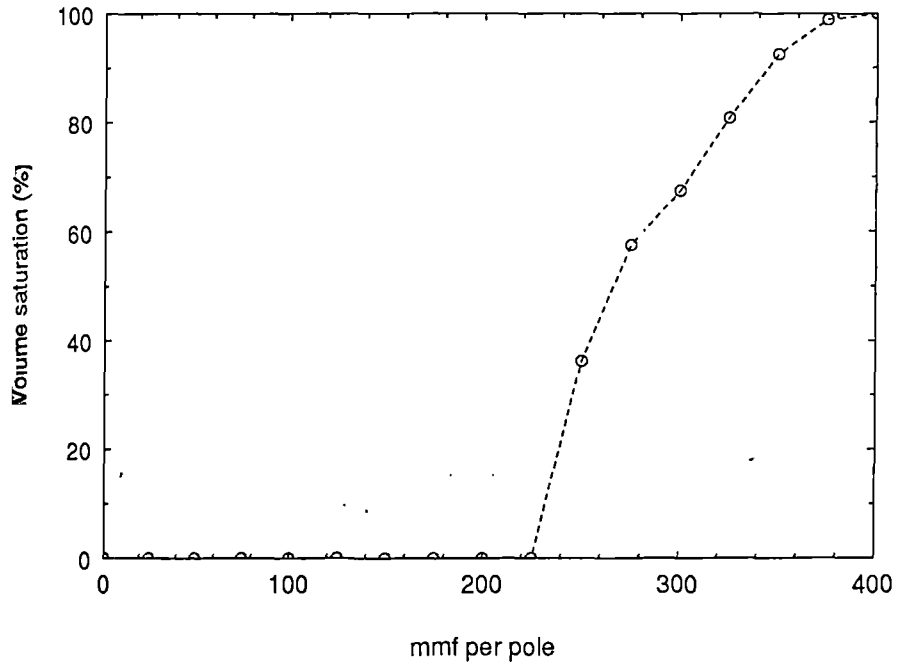

ɔntage volume saturation versus mmf per pole for a post-assembly mag-
xture with a $1mm^2$ conductor located 0.5mm from the motor casing.

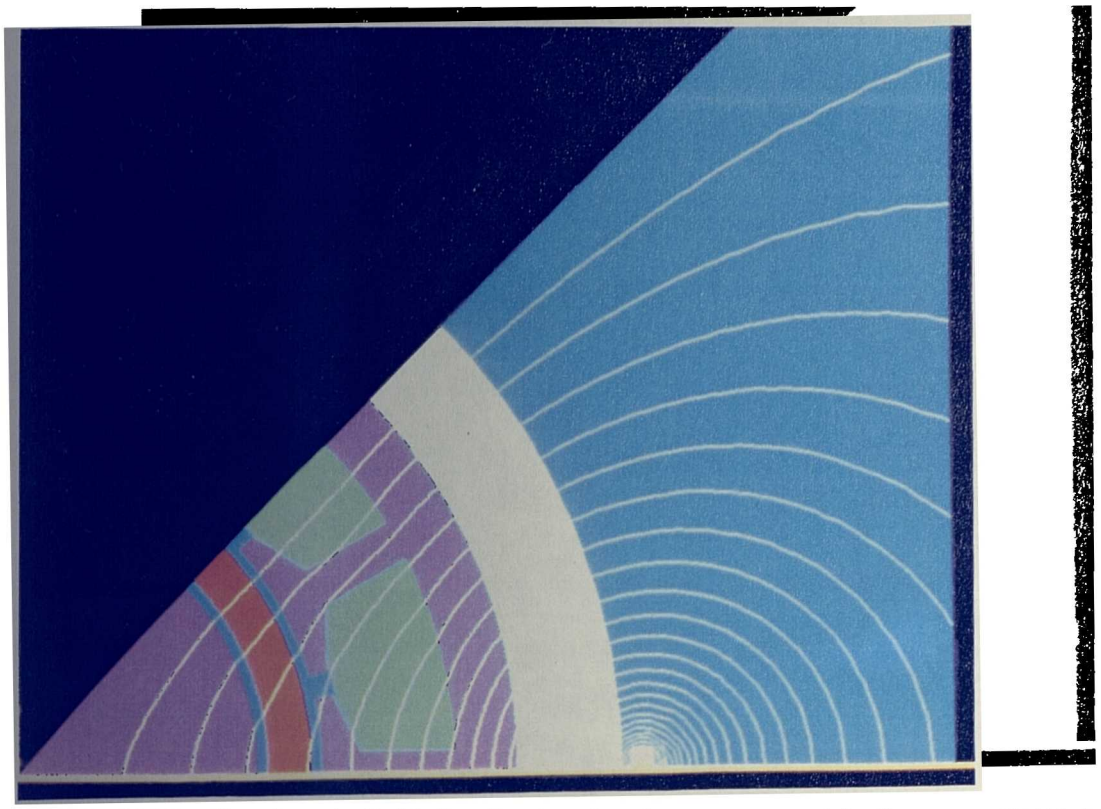

Fig. 5.21 Predicted static field distribution for the post-assembly fixture at 325 kA/m

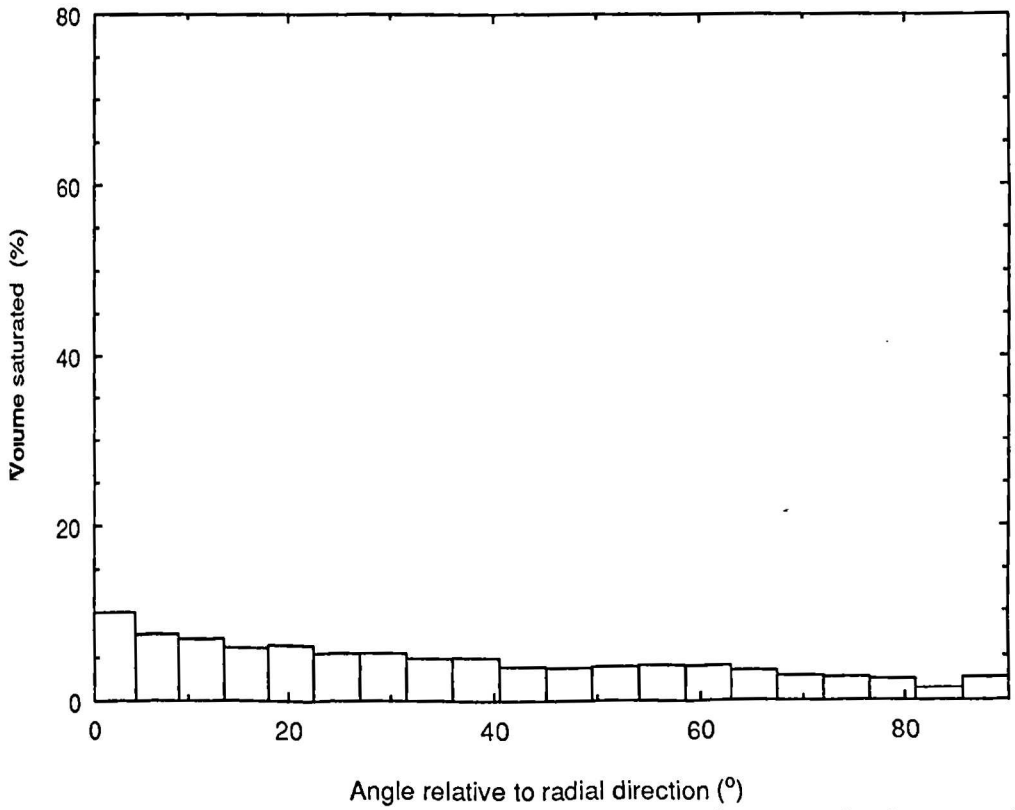

22 Distribution of radial alignment in the post-assembly magnetized magnet for a fixture mmf of 325 kA per pole

	Predicted		Measured	Measuring method
	Linear Analytical	Dynamic Simulation		
Fixture resistance ($m\Omega$)	21.3	Variable	22.5	Cambridge Precision Decade Bridge
Fixture inductance (μH)	4.31	Variable	4.46 (@1kHz)	Marconi TF1313 AC bridge (¼% accuracy)
Peak current (kA)	23.4	24.2	24.0	Current transformer and DSO (resolution approx 1% of peak)
Time to peak (μs)	69.0	66.0 ± 2.7 time step	66.2	

Fig. 5.23 Comparison of predicted and measured parameters for the prototype fixture.

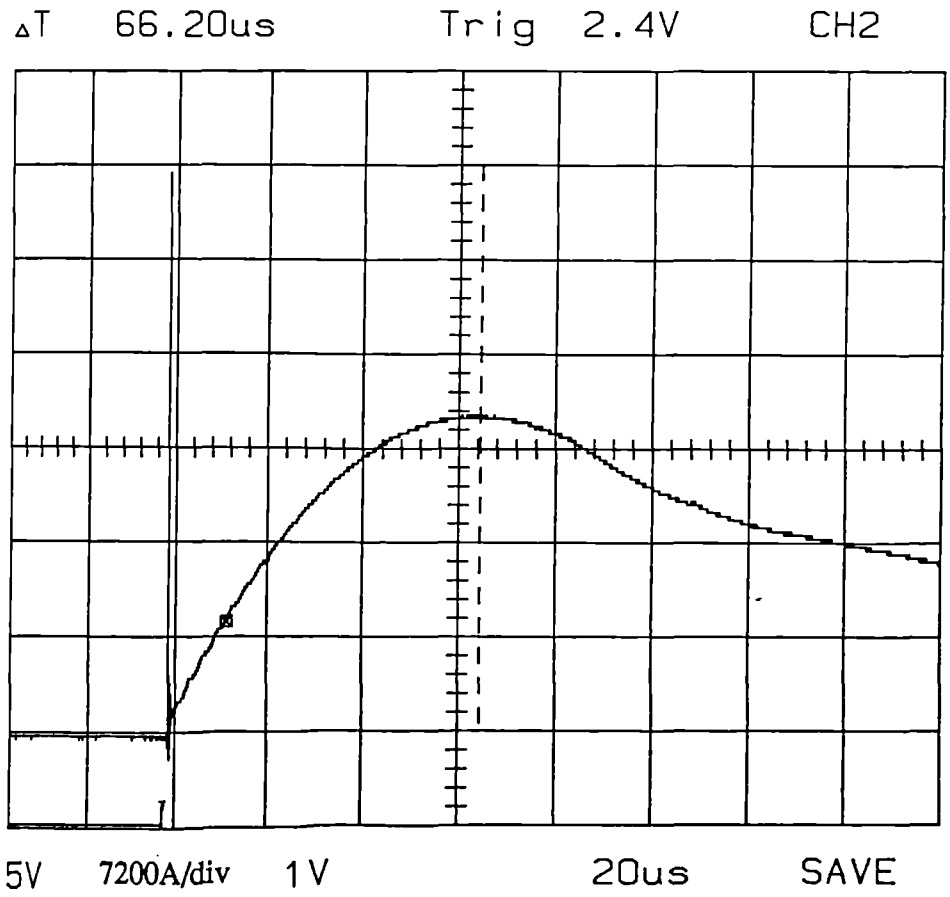

Fig. 5.24 Measured fixture current waveform.

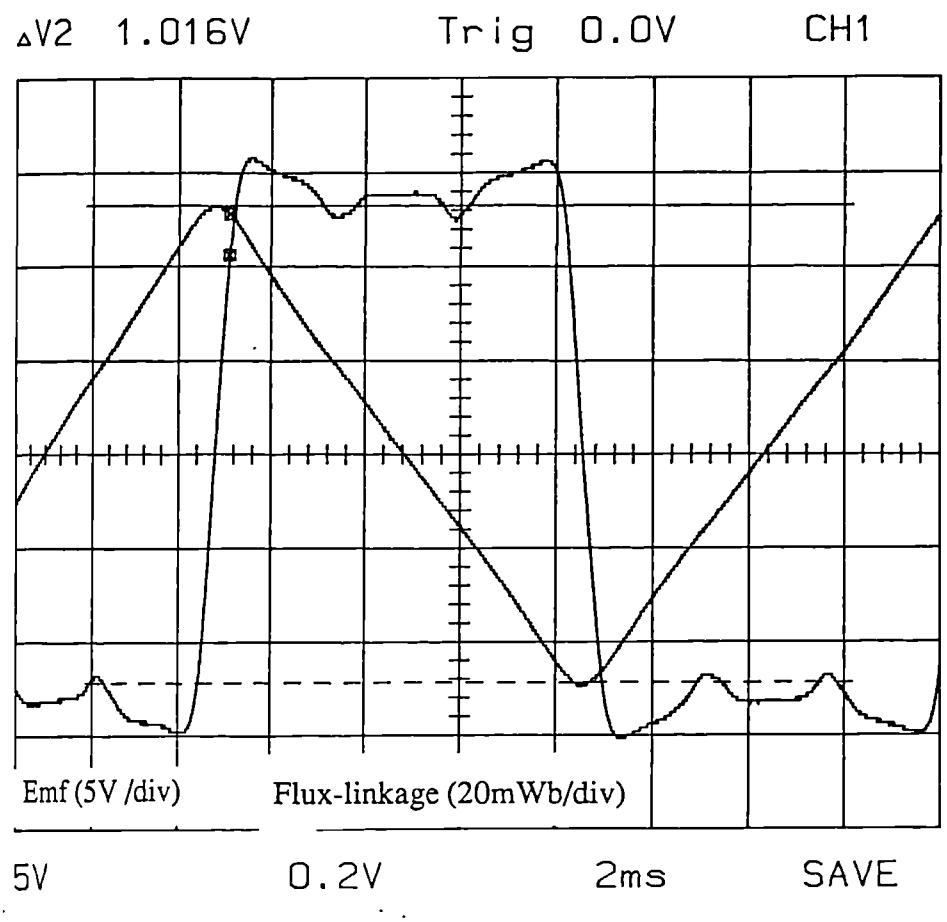

Fig. 5.25 Measured flux-linkage and induced emf waveforms.

Gap (mm)	Inductance (μH)	Resistance ($m\Omega$)	Peak current (kA)	Volume saturation (%)
0.5	4.31	21.3	23.4	90.0
1.0	4.12	21.3	23.7	85.5
1.5	3.95	21.4	24.1	73.9
2.0	3.79	21.4	24.4	52.2
2.5	2.73	21.5	24.8	20.4

Fig. 5.26 Predicted sensitivity of the electrical circuit parameters and the volume saturation to the gap between the magnet surface and the fixture windings.

Gap (mm)	Percentage of the magnet volume saturated and aligned within 4.5^{o} of the radial direction
0.5	77.5
1.0	70.0
1.5	59.4
2.0	45.8
2.5	19.5

Fig. 5.27 Predicted effect of the gap between the magnet surface and the fixture winding on the radial alignment of the magnetizing field.

CHAPTER 6

MAGNETIZATION OF A 32 POLE AXIALLY ANISOTROPIC MAGNET RING.

6.1 INTRODUCTION

Axially anisotropic sintered NdFeB ring magnets are finding numerous applications in electromagnetic devices e.g axial-field brushless motors, disc stepper motors, loudspeakers and compact disc focussing systems. They are easier and more economical to produce than radially anisotropic rings for the reasons discussed in chapter 4. The standard stock list of Philips Components Southport Ltd[6.1], which although not exhaustive is representative of most magnet producers product range, contains a much wider range of axially anisotropic rings and solid discs than other magnet shapes for radial field machines, i.e arc segments and radially anisotropic rings.

Axial-field machines are generally employed in environments in which there are space constraints, and hence they can often justify the increased cost of rare-earth magnets which afford advantages in terms of the power to volume ratio compared to less expensive materials, e.g bonded and sintered ferrite. As a result axial-field machines are likely to remain a major sector in the rare-earth brushless machine market. Hence, the magnetization of axially anisotropic magnet rings is an important consideration in the development of a comprehensive CAD methodology for multipole magnetizing fixtures.

6.2 FIXTURE TOPOLOGIES.

Schematics of typical single and double sided fixtures for magnetizing axial multipole magnet rings are shown in fig 6.1. As with radial field fixtures, a double sided topology produces inherently better alignment between the magnetizing field and

the material preferred direction and allows the location of a given total mmf at half the effective distance from the magnet for the same current density. A single sided fixture is not as suitable for magnetization of an axially anisotropic ring, and is generally limited to post-assembly or sub-assembly level magnetization where geometrical considerations preclude the use of a double sided fixture. The single sided topology is also useful in cases where the required magnetization is not completely axial, e.g a "self-shielding" magnetization distribution such as that of fig 1.21.

The field patterns produced by the fixtures in fig 6.1 are highly three dimensional, i.e there is a significant variation in all directions. However, by taking a section through one pole of a double sided fixture, such as that of fig 6.2, it is possible to obtain a two-dimensional approximation which can be used as the basis for a design synthesis. The validity of representing the geometry of a magnet pole by one having parallel sides can be assessed initially from equations (6.1) and (6.2), from which the approximation is best when the pole number is high and the ratio of the inner to outer radii is close to unity. The two-dimensional section is taken through the outer periphery since this is a worst case in terms of the magnitude of the flux density produced by the fixture winding, although other considerations, such as the alignment of the field with the material preferred direction may require an additional analysis at the inner periphery.

$$\frac{AB}{CD} = \frac{r_o}{r_i} \rightarrow 1 \quad \text{for a good approximation in pole width} \tag{6.1}$$

$$\frac{\text{arc } AB}{AB} = \frac{2\Pi/p}{\sin 2\Pi/p} \rightarrow 1 \quad \text{when p is large} \tag{6.2}$$

where the points A,B,C and D are as defined in fig 6.2

In order to assess the applicability of using a two-dimensional analysis in such

cases, a fixture was designed to magnetize a 32-pole axially anisotropic sintered NdFeB magnet for use in the prototype two-phase axial-field generator of fig 6.3. The high pole number and the dimensions of the magnet, which are shown in fig 6.4, suggest that on the basis of the preceeding simplified analysis it is reasonable to employ a two dimensional analysis. The generator produces an output power of 120 mW at 5.6V for powering the electronics on a "smart-diskette" which has applications in computer security and data encryption [6.2].

The diskette is compatible with a conventional 3.5 inch 3000 rpm floppy disc drive, and the on-board electronics communicate with the host-computer via the usual disc drive read/write head and a magnetic transducer inside the diskette. The mechanical input power to the generator is supplied by the motor of the host disk drive. In order to accomodate the generator within the available space envelope, high specification magnetic materials were utilised viz. sintered NdFeB magnet ring and ROTELLOY50 nickel cobalt laminations. The permanent magnet material is Philips Components RES270 sintered NdFeB which was supplied with a Nickel coating to afford a degree of corrosion protection. The two-dimensional models at both the inner and outer peripheries are shown in fig 6.5.

There is negligible armature reaction and temperature rise in this device [6.3]. Therefore, the full squareness of the intrinsic hysteresis loop is not necessarily required. However, the required generator flux-linkage produced by the magnet was calculated at the initial design stage assuming an idealised fully saturated magnet. Therefore, in order to achieve the exacting performance specification, the flux-linkage produced by the magnetized multipole magnet cannot be significantly lower than that produced by an idealised fully magnetized magnet.

6.3 DIMENSIONAL CONSTRAINTS

Prior to the electromagnetic and electrical design of the fixture a number of factors had to be considered in order to constrain the design of the fixture so that it could be realised in practice. The clearance between the magnet and the closest conductor should be minimised to improve the alignment between the material preferred direction of magnetization and the applied magnetizing field. The electromagnetic forces acting on the conductors in such double sided topologies act in a direction away from the magnet and into the bulk of the fixture former, which is not dimensionally constrained and hence can be dimensioned to withstand the forces with a large margin of safety. Thus the insulating material placed between the conductors and the magnet does not have onerous mechanical load imposed on it, and its principal role is to provide electrical insulation.

Since the fixture was to be designed for operation from a 3kV capacitor-discharge unit, the worst case voltage stress, neglecting the voltage drop in the internal impedance, is 3000V across the 2 layers of insulation which separate the two sides of the fixture, since negligible insulation is provided by the electrically conductive magnet. The high temperature rises which are inevitable in such fine pole-pitch fixtures necessitate that the insulation also provides a degree of thermal insulation and heat capacity, so as to prevent the magnet from being exposed to a temperature rise which is sufficient to initiate irreversible demagnetization during the period in which it is being removed from the fixture. A suitable insulation material is 0.05mm thick Nomex 411, which has a manufacturers specified maximum electrical stress capability of 30 KV/mm and a continuous temperature rating of 200°C. Allowing for the enamel coating of the conductors, this leads to an minimum effective clearance between the magnet and the nearest conductors of the fixture winding of 0.1mm.

The length of the fixture conductors in the radial direction should be selected so

as to minimise distortion of the magnet poles by the fixture end-windings. In the design of serpentine wound fixtures for magnetizing multipole radial-field magnets there is no space constraint on the fixture axial length and its selection is based on a compromise between considerations of end effects and the fixture impedance. However, the fixture topology for a multipole axial-field magnet, fig 6.1, imposes a limit on the extent to which the conductors can be extended beyond the magnet inner radius. The fixture former is constructed from an insulating material in which radial slots are cut to locate the conductors, fig 6.6, and the inner end-windings are formed by bending the conductor around the slot former. Imposing a limit that a fixture conductor cannot be formed into an end-winding with a radius of curvature less than its own radius without distorting the cross section and stressing the insulation , a limit based on experiments with test windings, leads to the specification of a minimum inner radius, R_{min}, for each conductor diameter. The magnet ring inner radius of 14mm sets the limit for the maximum value of R_{min} and hence the maximum allowable conductor cross-section which can be accomodated, 1.3 mm in this case.

A symmetrical extension of the windings at the inner and outer radius of the magnet, as shown in fig 6.7, is desirable in order to prevent excessive asymmetrical end-effect distortion. Hence, the maximum length of the conductors in the radial direction for a given fixture conductor cross-section can be stipulated. The minimum former inner radius for a range of insulated conductor dimensions, up to the limit imposed by the magnet inner radius are also shown in fig 6.7. The following electrical circuit design constraints were also applied :

i) The ignitron switch ratings impose a maximum magnetizer current of 30kA

ii) The maximum temperature, which was governed by the thermal specification of the conductor enamel insulation and the Nomex insulation layer, was set at $200^{o}C$.

iii) The maximum initial capacitor voltage is 3000V.

iv) The available magnetizer capacitance values are 150,300 and 450 μF.

6.4 SELECTION OF THE STATIC FIELD CALCULATION METHOD

The magnetic properties which can be achieved in axially anisotropic rings show no dilution from those of anisotropic rectangular blocks since they are pressed and aligned in a field of the same configuration, generally by die-pressing with a ferromagnetic punch, although the rings could also be machined from isostatically pressed material. In order to assess whether the linear analytical model is sufficiently accurate to predict the level of saturation produced in the magnet for a given fixture mmf, a test fixture with 1 layer of 0.6mm diameter conductors situated 0.1mm from the surface of the magnet was analysed by both non-linear finite element analysis and the linear analytical method. The dimensions were selected to be an extreme case in terms of the proportion of the total magnetic circuit which is occupied by the non-linear magnet. The finite element mesh was based on a uniform discretization of 0.05mm in the magnet and in the region surrounding the conductors, so as to obtain a resolution of approximately 0.1% in predicting the percentage volume saturation. The open boundary of the region was positioned at 14mm from the magnet surface, resulting in the total number of elements and nodes being 6347 and 3303 respectively.

To ensure that any differences between the results from analytical and finite element methods are not due to discretization effects, the same finite element mesh was also used for a linear finite element solution with the region normally occupied by the magnet being defined as non-magnetic. Although the effect of discretization is problem dependant, the linear system will be indicative of effects in the non-linear model. The linear finite element solution will also give an indication as to whether the line current

representation used in the analytical model is a good representation of the distributed current in the conductors, an important consideration given that the conductors extend over a large fraction of the pole pitch.

The close agreement shown in fig 6.8 between results from the linear finite element and analytical methods, confirms the minimal role of discretization in causing any difference between results from the analytical and non-linear finite element methods and the validity of using a analytical technique based on line currents rather than a more complex distributed current. Fig 6.8 also demonstrates that the presence of the magnet, being anisotropic and permeable, leads to a higher percentage volume saturation being predicted by the non-linear model than by the linear analytical solution. The difference is significant, particularly in the mmf required to achieve in the vicinity of 80-90% volume saturation. This, therefore, precludes the use of the analytical method for this particular problem despite its advantages in terms of computation time etc. Thus, for this case a series of non-linear finite element solutions is required so as to accurately predict the required fixture magnetizing mmf since the non-linear magnet forms a significant fraction of the magnetizing flux path, particularly for 1 layer windings.

6.5 CALCULATION OF THE MMF REQUIRED FOR SATURATION OF THE MAGNET

In fine pole pitch magnetization, thermal considerations dictate that the conductors necessarily extend over a large fraction of the pole pitch, so their individual geometry will affect the field distribution, particularly with regard to its alignment with the preferred axis of magnetization. Thus, the approach whereby a conductor block, representing an unspecified number of turns, is used to determine an mmf specification and its dependance on the winding distribution is not readily applicable. However, the design space is very constrained by the small pole pitch, and hence there are a smaller

number of possible conductor dimensions and layouts than in less constrained problems. Therefore, it is feasible in this case to model each of the possible conductor arrangements, albeit at discrete practical conductor dimensions within the possible range.

For each conductor arrangement the current in each individual conductor was increased in 2.5 kA steps up to the 30kA limit of the available magnetizer, and for each value of current the percentage magnet volume in which the applied magnetizing field strength in the preferred direction exceeded 1600 kA/m was calculated. The results of a series of non-linear finite element solutions for 1,2 and 3 layer windings with conductor diameters in the range 0.6-1.3mm are shown in fig 6.9. The use of additional layers, although greatly increasing the mmf per pole for a given current, does not lead to the magnet being exposed to a proportionate increase in magnetizing field, since the additional layers are located further from the magnet to be magnetized. The limiting value of the saturated volume, i.e the value at the current limit of the magnetizer, increases with decreasing conductor dimensions due to the better alignment with the magnet preferred direction and the reduced distance of the current from the magnet surface. The field distribution of fig 6.10 demonstrates that the magnet region directly adjacent to the conductor is the most difficult to saturate in the preferred direction. The maximum achievable saturation is approximately 93%, for a 3 layer winding of 0.6mm conductors, this limit being due to the inherent difficulty in producing a field distribution which is well aligned with the magnet orientation. Reducing the threshold for saturation to 1200 kA/m, increases the maximum saturated volume for this fixture to 95%.

6.6 ELECTRICAL DESIGN.

A high voltage/low capacitance magnetizer is best suited to this application due to a number of factors:

1) The fixture resistance to inductance ratio and hence the damping of a fixture/magnetizer system reduces with an increasing number of fixture turns since the inductance scales approximately with the square of the turns whilst the resistance increases approximately in direct proportion to the number of turns. Thus, in a fixture which is not geometrically constrained the system can be made highly underdamped, and hence electrically very efficient in transferring the stored energy of the capacitor bank to stored energy in the magnetic field, by using a high number of turns with a large cross-sectional area. However, in fine pole-pitch fixtures the small conductor cross-section and the low number of turns per pole which can be accomodated in the limited space result in the fixture impedance having a significant resistive component with little scope for flexibility in improving the damping. Thus to ensure that the fixture/magnetizer combination has the minimum damping, the magnetizer capacitance should be as low as possible .

2) The low number of turns in fine pole-pitch magnetizing fixtures results in low fixture impedances. To obtain a reasonable degree of impedance matching the internal impedance of the magnetizer should be as small as possible, a condition best met by using oil filled or paper-foil high voltage capacitors rather than low voltage electrolytic capacitors.

3) The small cross-sectional area of the conductors and the high currents required to achieve useful levels of saturation, result in the temperature rise being the limiting factor on the fixture performance. Thus, to obtain the maximum peak current for a given temperature rise the pulse length should be as short as possible, a requirement best met by a low capacitance/high voltage magnetizer.

4) In an air-cored fixture, the absence of iron and the small dimensions of the magnet ring to be magnetized are unlikely to result in eddy-currents preventing full penetration

of the magnetizing field into the magnet, and therefore a short pulse duration can be utilised.

Having established the mmf requirement and selected the low capacitance\high voltage magnetizer, the fixture electrical parameters can be selected in order to realise the highest levels of saturation for minimal energy dissipation. Given the conductor diameter, the number of conductors per pole and the maximum limit for the radial extension beyond the magnet, the inductance and resistance of the fixture can be calculated by the analytical methods of Appendix A. The performance of the fixture with a specified capacitance and initial voltage can then be calculated using an electric circuit simulation to determine the peak current and the fixture temperature rise. For such a thermal constraint dominated problem a useful design startegy is to calculate the maximum peak current that can achieved from a given value of capacitance for the limiting temperature rise. This peak current can be subsequently related to a percentage volume saturation by reference to fig 6.9.

The results from an extensive scanning of the design space are shown in fig 6.11, which contains the fixture parameters and their predicted performance for designs which satisfied the performance constraints. The radial length of the fixture conductors for each design was set to the maximum allowable for the conductor diameter. The majority of fixture and capacitance combinations are limited by the imposed temperature limit of 200^{o}C, and their performance was calculated by an iterative process in which the initial capacitor voltage was modified until the limiting temperature rise was achieved. For certain fixture and capacitance combinations, operation at full voltage does not cause the temperature to exceed 200^{o}C, and for these, the performance is shown for operation at the upper voltage limit of 3kV for the magnetizer.

For a given capacitance and number of conductor layers there is a local optimum

in the percentage saturation, e.g for designs 1 to 8, which have a capacitance of 150μF and a 1 layer winding there is an optimum at design number 5. In all cases this local optimum occurs with a conductor diameter which corresponds to the transition between thermally and voltage limited designs, e.g designs 5,15 etc. The number of designs for a given capacitance whose performance is constrained by the voltage limit rather than the thermal limit increases as the number of layers is increased due to the larger copper volume in which the stored energy is dissipated. Thus, the local optimum gradually moves towards smaller conductor diameters as the number of layers increases, design 16 being the only for which the performance is limited by the maximum current contraint.

The use of 0.6mm and 0.7mm diameter conductors, although attractive in terms of the level of saturation achieved for a given current, as previously shown in fig 6.9, is not feasible because the excessive dissipation in such fixtures limits the attainable currents to levels where high saturation levels are not achieved. For a given stored energy, a higher level of saturation is achieved with a capacitance of 150μF rather than with 300μF, albeit with a reduced pulse duration. Of the 48 fixtures analysed, only 11 produced a level of saturation in excess of 80%, a maximum of 82.5% being achieved with design 36 with a stored energy of 1323 J. However, the best compromise in terms of the level of saturation for a given stored energy, is design no.5 which achieves 80.7% volume saturation for a stored energy of 588J. The use of a single layer winding, such as in design no.5, also has the benefit of having an increased electrical insulation reliability, which is an important consideration given the relatively large temperature rise.

The calculation of similar tables of results for radial conductor lengths less than the maximum values of fig 6.7 indicate that no significant improvement can be achieved in the performance of the fixtures which are limited by the temperature rise. There is

a slight increase in the peak current that can be conducted for a given temperature rise since the inductance is lower and hence the pulse is shorter. However, the effect on the total inductance of reducing the radial length (length l_r of fig 6.7) from its maximum to the limit determined by the magnet dimensions is small for fixtures producing useful levels of saturation and the improvement in performance does not outweigh the disadvantage of the increased influence of the end-windings on the field uniformity.

Therefore, at this stage of the design process the apparent optimal fixture design is No.5. However, other considerations require analysis before a firm conclusion can be drawn. The extreme electrical conditions necessary to achieve saturation of such fine pole-pitch structures are highlighted by the predicted peak power dissipation in the fixture of 18.04MW and the average heating rate of 4.2×10^6 °C/s.

6.7 DYNAMIC SIMULATION

A consequence of selecting fixture No.5 is the very short current rise time of 18.2μs, which could lead to eddy-currents being induced in the magnet and preventing field penetration to an extent where the magnetostatic finite element calculations used in the initial stages of design are no longer representative of the magnetization process. This possibility was investigated by performing a transient finite element simulation, applying the two-dimensional finite element model at the outer periphery of the magnet ring. The peak current and percentage volume saturation predicted from the dynamic and static simulations are in good agreement, fig 6.12, indicating that in this case eddy currents do not in fact produce a significant modifying effect on the final level of saturation achieved by the fixture. Indeed, the dynamic simulation predicts a slightly higher peak current and a subsequent higher level of saturation, which can be attributed to the screening effect and the subsequent reduction in fixture inductance during the initial stages of the magnetizing pulse.

Although the field distribution is affected by induced eddy-currents during the initial stages of the transient, as evidenced by the small variation in the fixture inductance, the eddy-current effects are not sufficient to prevent an essentially quasi-static field distribution at the peak of the current pulse. Thus, on the basis of the results of the dynamic simulation, which in a magnet of such a short axial length will tend to overestimate the effect of eddy-currents, there is no significant departure from the statically predicted levels of saturation.

6.8 INNER PERIPHERY MODEL

The selection of fixture 5 was based on the level of percentage saturation predicted from a two-dimensional finite element model applied at the outer periphery of the magnet ring. Whereas this is a worst case in terms of the average flux density over the pole pitch for a given fixture current, the effect of mis-alignment between the magnetizing field and the magnet preferred direction will vary with the radius. In order to assess this, a two-dimensional finite element analysis was also undertaken at the inner periphery of the magnet. The lower percentage saturation for a given current predicted at the inner periphery compared to the outer periphery, fig 6.13, demonstrates that the problem of achieving alignment between the magnet preferred direction and the applied magnetizing field is aggravated at the inner periphery since the conductor extends over a larger fraction of the pole pitch. However, the actual cross-section of each pole which is not saturated at the current limit of the magnetizer is highest at the outer periphery, i.e 0.752 mm^2 as opposed to 0.735 mm^2 at the inner periphery. This confirms that in terms of the subsequent performance of the magnetized magnet, the outer periphery model is indeed the worst case.

6.9 IRON CORED FIXTURE.

A schematic of a slotted double sided iron-cored fixture is shown in fig 6.14. From a practical point of view the major drawback of using iron in such small structures is the difficulty in maintaining the integrity of the electrical insulation. In double sided fixture topologies the use of iron also raises practical problems associated with the removal of the magnet from the fixture following magnetization because of the large attractive forces [6.4]. Therefore, the use of iron is only worthwhile if it offers a significant advantage in terms of the level of achievable saturation for a given stored energy.

The role of the iron in slotted fixtures is primarily to reduce the reluctance of the magnetizing flux path. The thickness of the back-iron iron is not constrained, and can therefore be dimensioned to operate at a flux density below the saturation flux density of the iron, thus offering a low reluctance path. This reduction in reluctance is most effective for fixtures having single layer windings for which the back-iron reluctance is a maximum proprtion of the total magnetic circuit reluctance.The dimensions of the iron teeth are limited by the pole pitch and the conductor diameter, and hence they are usually forced to operate well beyond saturation when the permeability is greatly reduced.

The percentage volume saturation versus fixture current for a slotted iron-cored version of fixture design No.5, as calculated from a series of non-linear finite element magnetostatic field solutions, is shown in fig 6.15. This shows that, on the basis of the static calculations, a benefit can be derived from the use of an iron core. The predicted magnetostatic field distributions of figs 6.16 and 6.17 show that the higher permeability of the teeth although heavily saturated, result in a better alignment of the magnetizing field compared to the previous air-cored fixture.

This improved alignment results in the geometrically limiting percentage saturation, i.e the level of saturation beyond which the incremental increase with applied mmf is greatly reduced, being higher than for the corresponding air-cored fixture. However, this apparent benefit of using an iron core has neglected the time dependancy of the field distribution, an important consideration given the very short pulse length. Therefore, a dynamic simulation was undertaken to assess the role of eddy-currents in the solid iron core. The series of predicted field distributions during the magnetizing pulse, fig 6,18, clearly show the effect of eddy currents which inhibit the penetration of the magnetizing field into the back-iron. However, penetration of the magnetizing field across the full width of a magnet pole arc is not prevented.

Thus, the principal benefit of the iron which was to reduce the reluctance of the magnetic circuit is greatly diminshed under dynamic conditions to an extent where the fixture performance is actually worse than that of the corresponding air-cored fixture, the percentage volume saturation levels being 78.2% and 81.5% respectively. However, as discussed in chapter 3, the two-dimensional model tends to overestimate eddy current effects, particularly in structures with short active lengths such as in this case. Nevertheless, the use of a solid iron core with the additional practical drawbacks discussed above is not a viable option in this case. However, a laminated strip wound ring, in which radial slots for locating the conductors could be machined after the strip is wound, could be used to reduce the influence of eddy currents. Unfortunately, however, the mechanical strength of a strip wound core, which is critical in preserving its shape during the pulse and hence the integrity of the electrical insulation, is greatly reduced compared to a solid construction.

6.10 EXPERIMENTAL RESULTS.

The inductance of the fixture of fig 6.19 without the magnet in place was measured as 0.54 μH at 10kHz using a Marconi T1313 A.C inductance bridge. The measured inductance includes the contribution of the connecting leads, which were each 60mm long, a minimum imposed by the separation of the magnetizer terminals. The inductance of these connection leads was estimated to be 0.09 μH from a measurement of the inductance of a set of dummy connection leads of the same dimensions. The measured inductance of the fixture alone can, therefore, be estimated to be 0.45 μH which is in excellent agreement with the analytically predicted value of 0.463 μH. The significant fraction of the fixture inductance which is contributed by the connection leads,approximately 15%, would lead to a siginifcant degradation from the performance predicted in the design stage if it was additional to the impedance of the fixture and the magnetizer. However, the connecting lead inductance was effectively included in the magnetizer internal impedance since this was measured with the magnetizer terminals short-circuited by a set of connection leads of the same dimensions as those used for the constructed fixture.

The analytically calculated fixture resistance of 22.1 $m\Omega$ is in excellent agreement with the measured value of 23.4 $m\Omega$. Similarly, the measured current waveform of fig 6.20 agrees well with that predicted by both the dynamic finite element simulation and the linear electrical circuit simulation. The measured rise time of 18μs is sufficiently short that the non-ideal turn on of the ignitron is noticeable in the measured waveform. The agreement between the measured and predicted current waveforms also indicate that despite the very short pulse duration, skin-effect in the fixture conductors themselves, which is neglected in the simulation, appears to have minimal effect on the impedance of the constructed fixture.

The preceeding design stage was aimed at maximising the volume of magnet

which is exposed to a magnetizing field in excess of 1600 kA/m in the preferred direction, albeit with a certain compromise in fixture selection so as to reduce the required stored energy. However, for sintered NdFeB which has a nucleation controlled coercivity mechanism, a large fraction of the saturation remanence of the magnet is developed for much lower magnetizing fields. Hence, the subsequent flux-linkage with the coils of the generator is not likely to be very senstive to the applied magnetizing field provided it is beyond a certain minimum, since the magnetic circuit of the generator has a relatively low-reluctance. Fig 6.21 shows the measured variation in the flux-linkage per turn of the generator coil, as the magnet was magnetized with increasing values of capacitor voltage up to the designed voltage level of 2800V.

The flux per pole was measured by integrating the output voltage of the generator coil and normalising this measured value by the number of coil turns and the number of poles. The magnet ring was thermally demagnetized at 320^{o}C for 5 minutes between successive magnetizations. As is clearly demonstrated the flux linkage is largely insensitive to the initial capacitor voltage. Indeed the degree of overdesign in the fixture for this application is highlighted by fig 6.22 which shows the variation in flux-linkage as a function of the energy dissipated in the fixture, a parameter which is important for production engineering considerations such as cycle time and cooling system cost.

The measured data of fig 6.21 is not very useful in assessing the accuracy of the design methodology since there is only a small variation in the measured flux linkage for the wide range of predicted volume saturation levels shown in fig 6.23. Additionally, the performance of the generator is limited by local saturation and leakage, a full analysis of which is not possible with two-dimensional modelling techniques due to the complex three dimensional geometry of the generator. For such a complex magnetic circuit the levelling off of the flux-linkage versus initial capacitor voltage characteristic of fig 6.22 cannot be attributed solely to a levelling off in the volume of the magnet

saturation. Therefore, since the principal aim of the case study was to validate the design method for multipole axial-field ring magnets, an experimental assessment method was required in which there was both a significant change in magnet flux per pole for an increasing capacitor voltage and which had a geometry which could be modelled approximately in two-dimensions.

The magnet operating condition which is most sensitive to the squareness of the intrinsic characteristic, with the exception of the application of an external demagnetizing field, is under an open-circuit. Therefore, the flux produced by the magnet when working in a magnetic open-circuit was measured by the single turn printed circuit search coil of fig 6.24. The printed circuit construction can be produced to a much higher dimensional tolerance than a wound search coil and is less distibuted since etched copper tracks can be made finer than wire diameters which can be readily handled. However as a result of its inherent single layer construction, the printed search coil suffers from a relatively low signal to noise ratio. Hence, it was constructed to measure the total flux produced by 16 pole pairs. As a consequence, it gives no information as regards the uniformity of the individual poles. In order to insulate the coil from the magnet a 0.1mm sheet of insulating polyester film was placed between the magnet and the search coil. The magnet ring was rotated whilst maintaining a rubbing contact with the film by a slotless axial-field brushed d.c motor with zero cogging torque. The magnet ring was located 40mm from the motor so as to ensure negligible coupling effects from the from motor iron and permanent magnet.

The variation in the flux per pole measured 0.1 mm above the magnet surface after magnetization at an increasing level of capacitor voltage is shown in fig 6.25. As expected there is a larger sensitivity to the level of magnetization than exhibited by the flux-linkage of the assembled generator coil. Oscilloscope traces of the measured open-circuit flux-linkage waveform for capacitor voltages of 1200V and 2800V are

shown in figs 6.26 and 6.27.

Dynamic simulations were undertaken for the various initial capacitor voltages used in the experimental performance assessments above. The resulting predicted distributions of the intrinsic demagnetization characteristics over half a pole pitch are shown in fig 6.28. These distributions of intrinsic demagnetization characteritics were then utilised in a series of magnetostatic field solutions to predict the maximum open-circuit flux produced by the magnet for the various capacitor initial voltages. The predicted field distributions over half a pole of the magnet at the inner and outer peripheries are shown in figs 6.29 and 6.30. Also shown in figs 6.29 and 6.30 are the predicted field distributions at the inner and outer peripheries of an idealised fully saturated magnet.

Applying a linear interpolation between the results of the field calculations at the inner and outer peripheries, the predicted average flux per pole 0.1mm above the magnet is given by:

$$\psi = \frac{(A_{outer} + A_{inner})\,(R_O - R_i)}{2} \qquad (6.3)$$

where

A_{outer} = Vector potential of the node located 0.1mm above the magnet surface at the pole transition in the section taken through the outer periphery.

A_{inner} = Vector potential of the node located 0.1mm above the magnet surface at the pole transition in the section taken through the inner periphery.

R_0 = Magnet ring outer radius.

R_i = Magnet ring inner radius

Comparisons of the measured flux per pole and values calculated using equation (6.3) are shown in fig 6.31. There is excellent agreement, particularly for the higher capacitor voltages, bearing in mind the inherent measuring limitations, such as the limited resolution of the storage oscilloscope (0.4% of full scale) and the uncertainty in the exact clearance between the magnet and the search coil. However, for the 1200V case the error increase to 6%, a contributory factor being the method of interpolating between the inner and outer periphery values to obtain the flux per pole.

The dependance of the predicted flux-linkage on the capacitor voltage is different for the inner and outer periphery as demonstrated in fig 6.31. Hence, the interpolation method, which assumes a linear variation in flux-linkage along the radius of the ring, introduces an additional error to that inherent in the idealised two-dimensional approximation. However, this interploation, which is based entirely on known dimensions, cannot be improved in a rigorous general way without recourse to a three-dimensional analysis.

The use of so called "field-sensitive paper", although giving only a qualitative display of the degree of the magnetization pattern does provide a useful guide in this case. The visible field patterns produced by the magnet under an open-circuit condition, after magnetization at capacitor voltages of 2800V and 1200V , figs 6.32 and 6.33, clearly demonstrate that sharper pole transition result from the higher level of saturation achieved with 2800V.

6.11 CONCLUSIONS.

A methodology for designing multipole axial-field magnetizing fixtures has been shown to give good agreement with measured parameters, albeit for a case which is

reasonably well suited to the approximate two-dimensional analysis method utilised. The case study also demonstrates that the performance of a complete device can be relatively insensitive to the degree of magnet saturation providing it is above a certain minimum. It would be useful in this case to assess the sensitivity of the device performance to the degree of magnet saturation during the design synthesis rather than experimentally following the construction of a prototype fixture.

However, in the case of the axial-field generator considered in this chapter, the complex three-dimensional geometry which contains numerous leakage paths and regions of local saturation cannot be satisfactorily assessed, particularly as the peformance of the generator has been shown to be dependant on numerous constructional factors [6.5].

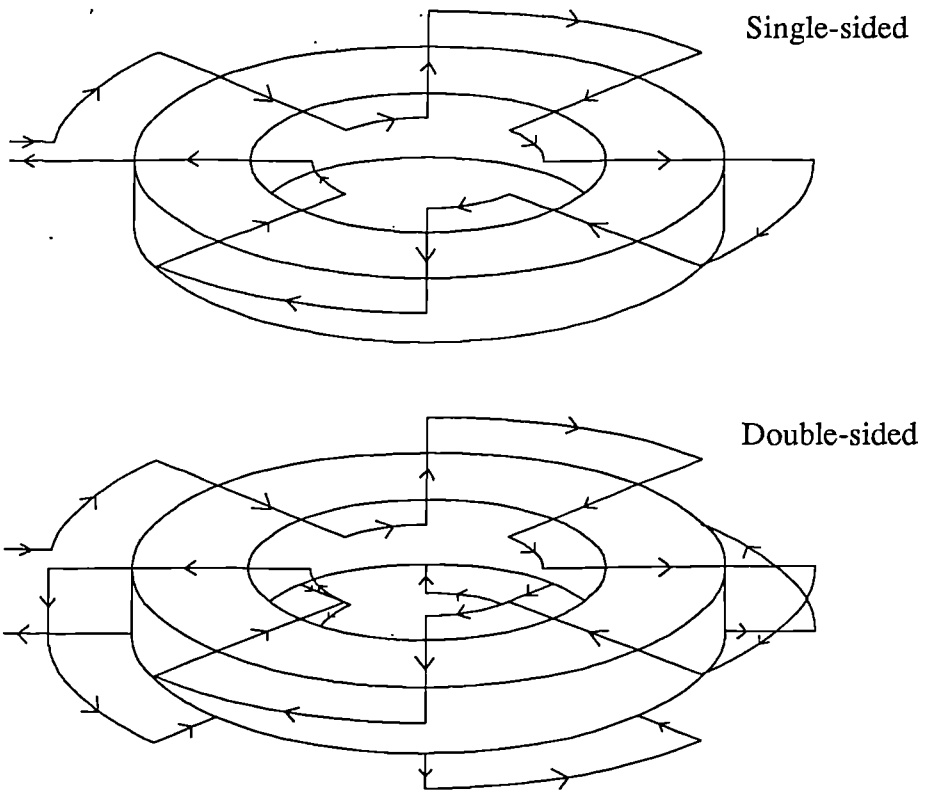

Fig. 6.1 Schematics of typical single and double sided fixtures for the magnetization of an axial multipole magnet.

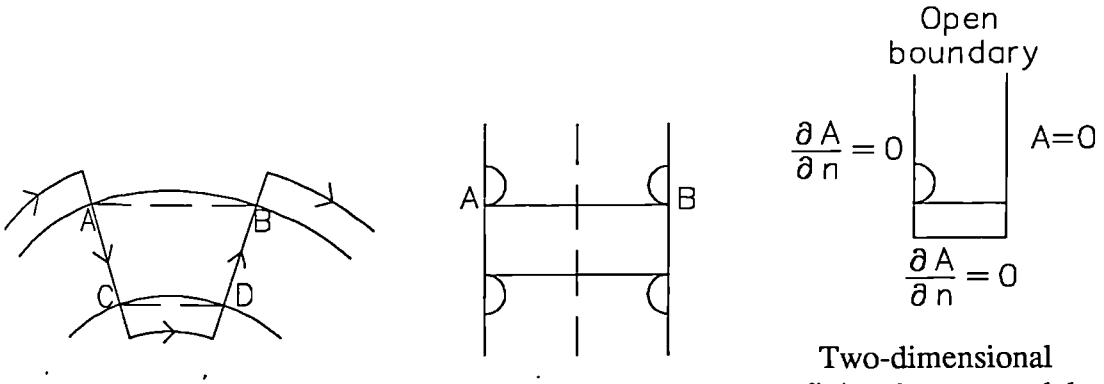

Plan view of 1 pole

Two-dimensional section through the outer periphery

Two-dimensional finite element model with boundary conditions for a vector potential formulation

Fig. 6.2 Two dimensional model for an axial multipole magnetizing fixture.

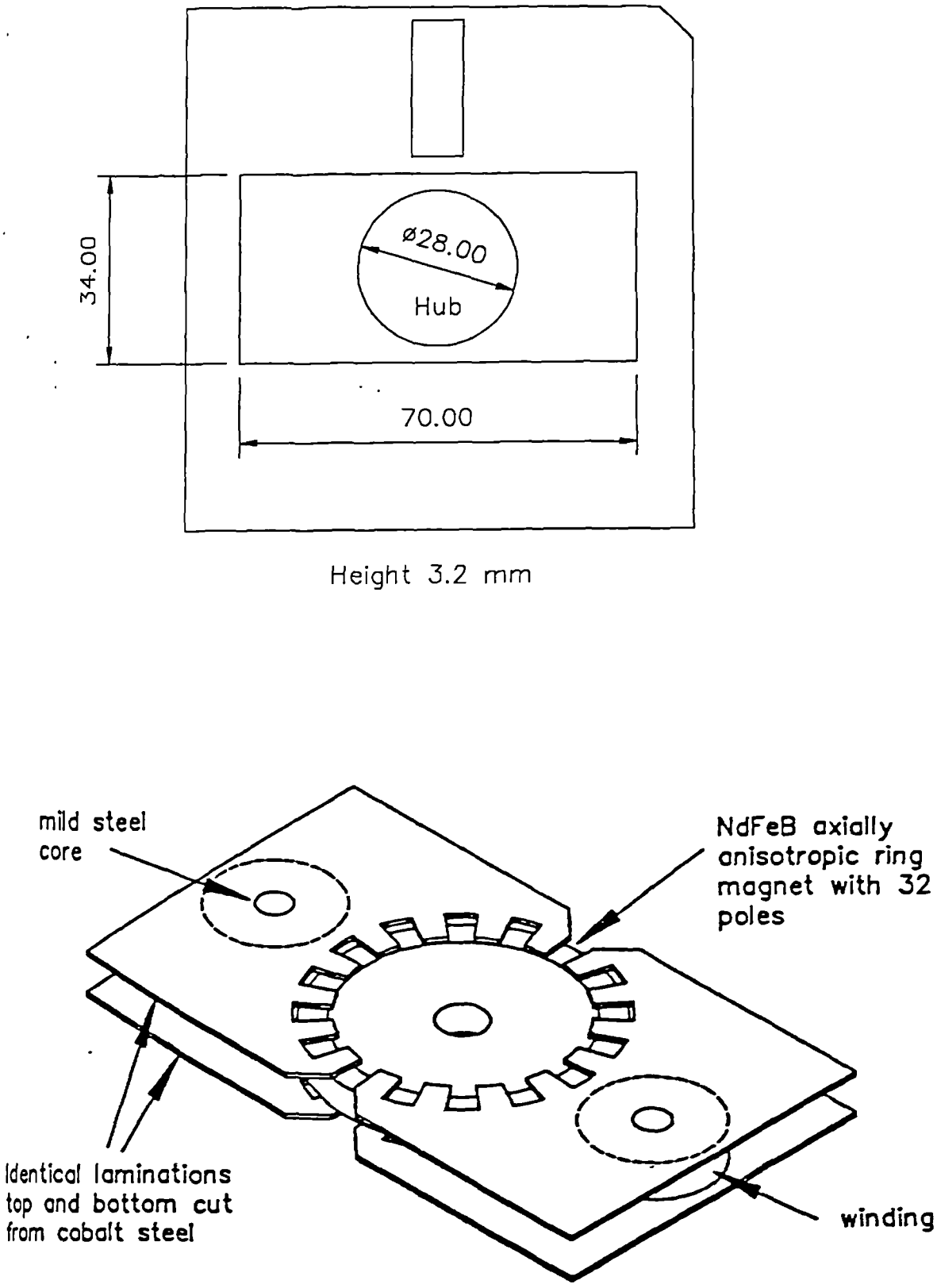

Fig. 6.3 Smart diskette dimensions and generator topology.

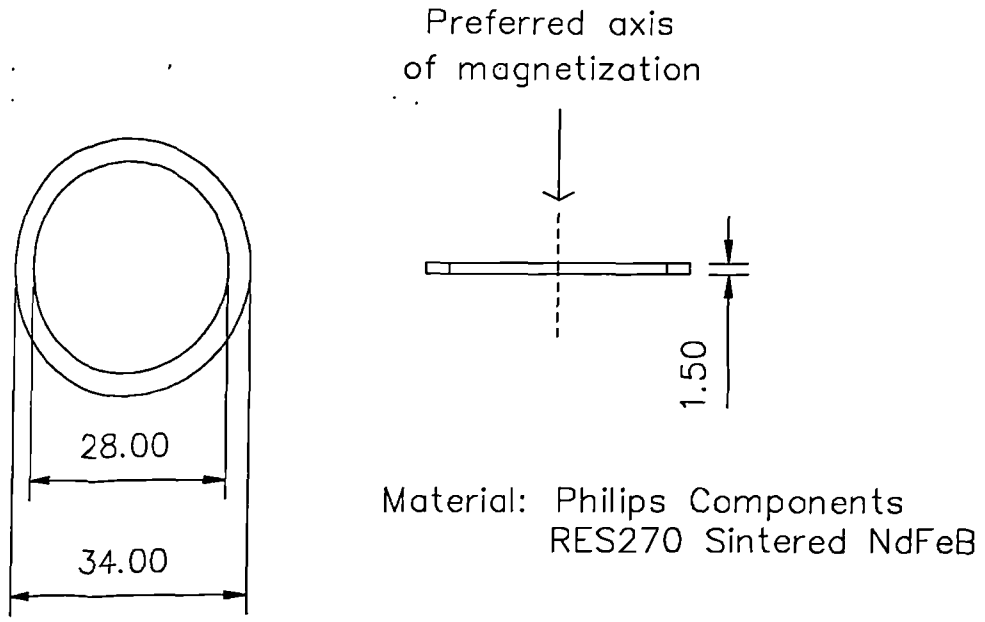

Fig. 6.4 Magnet ring dimensions. (Philips Components RES270 sintered NdFeB).

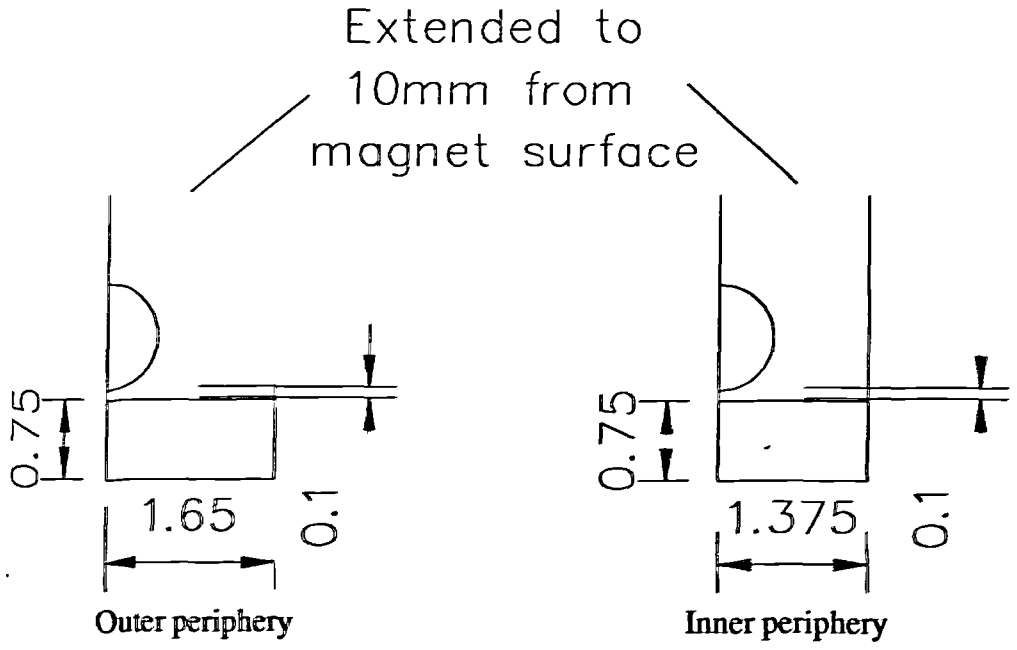

Fig. 6.5 Two-dimensional models at the outer and inner periphery of the ring magnet of fig 6.4

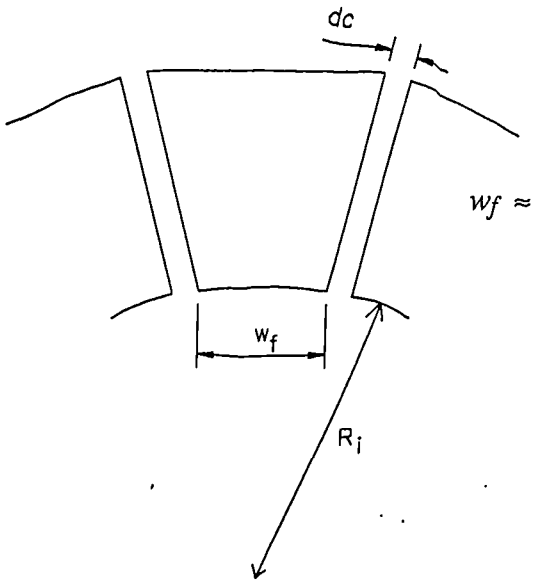

$$wf \approx \frac{2\Pi R_i}{p} - d_c$$ for a high pole number

for $w_f = d_c$:

$$R_{i_{min}} = \frac{pd_c}{\Pi}$$

p poles
d_c = Conductor diameter (including insulation)

Fig. 6.6 Calculation of the minimum former inner radius for a conductor bending radius equal to the radius of its cross section.

Conductor copper diameter (mm)	Conductor overall diameter (mm)	Minimum fixture former inner radius (mm)
0.6	0.68	6.9
0.7	0.78	7.9
0.8	0.88	9.0
0.9	0.98	10.0
1.0	1.08	11.0
1.1	1.18	12.0
1.2	1.28	13.0
1.3	1.38	14.0

Fig. 6.7 Calculated minimum former inner radius for a range of conductor diameters.

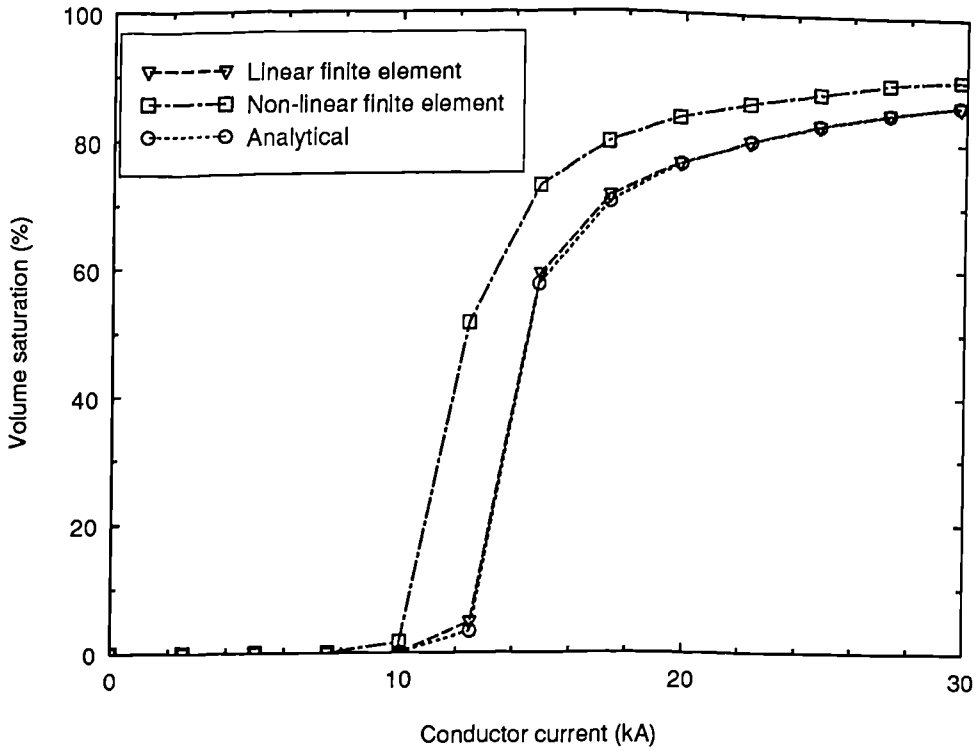

Fig. 6.8 Comparison of the volume saturation versus conductor current predicted by alternative techniques for a 0.6 mm diameter conductor, single layer, double sided fixture.

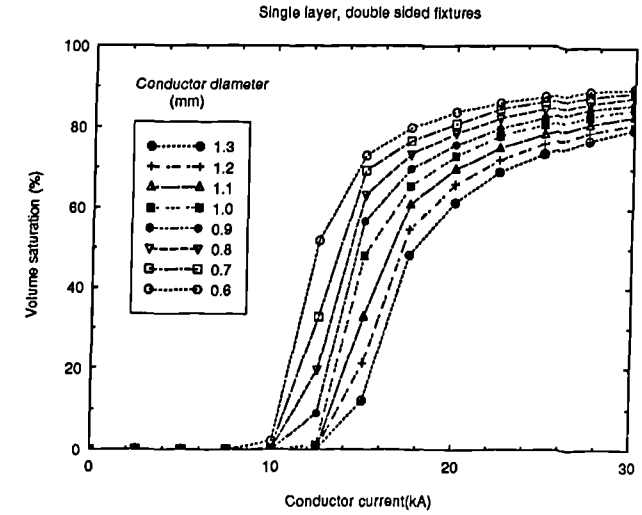

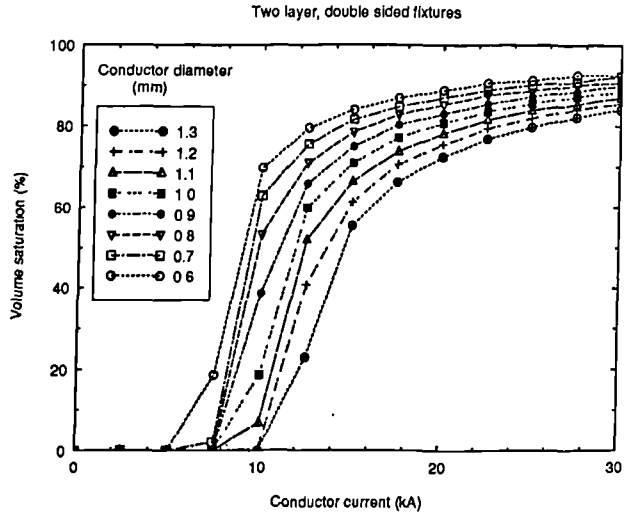

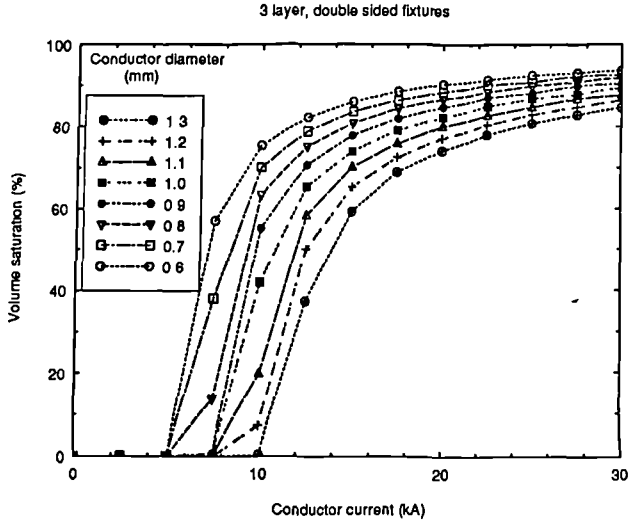

6.9 Finite element predicted volume saturation versus conductor current for 1,2 and 3 layer double sided fixtures.

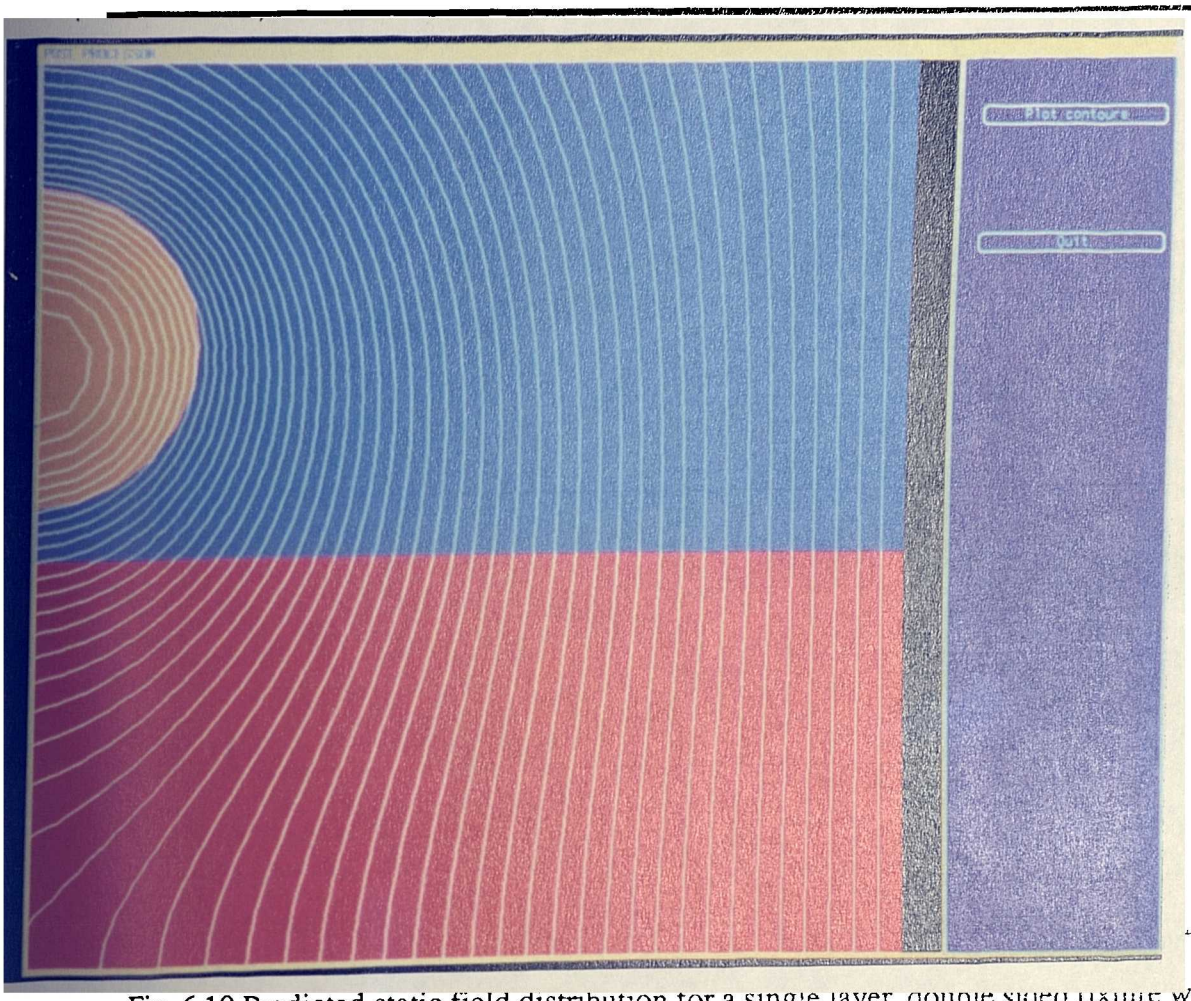

Fig. 6.10 Predicted static field distribution for a single layer, double sided fixture with a 0.6mm diameter condutor carrying 30kA.

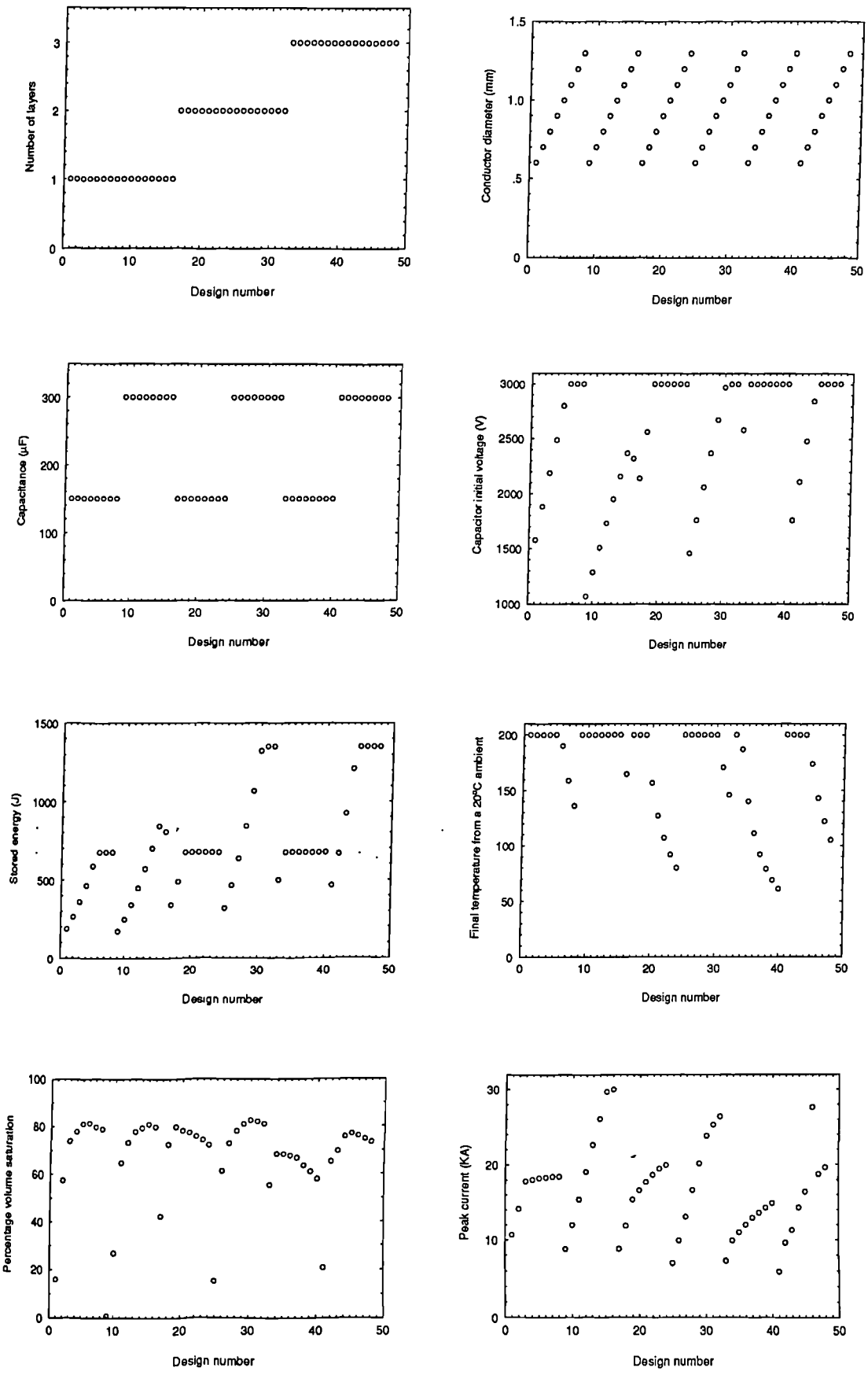

Fig. 6.11 Results of electrical scanning design.

	Peak Current (kA)	Percentage volume saturation (> 1600kA/m)
Dynamic Simulation	26.05	81.5%
Magnetostatic non-linear finite element field calculation and a linear electrical simulation	25.20	81.0%

Fig. 6.12 Comparison between dynamic and static simulations for fixture design No. 5.

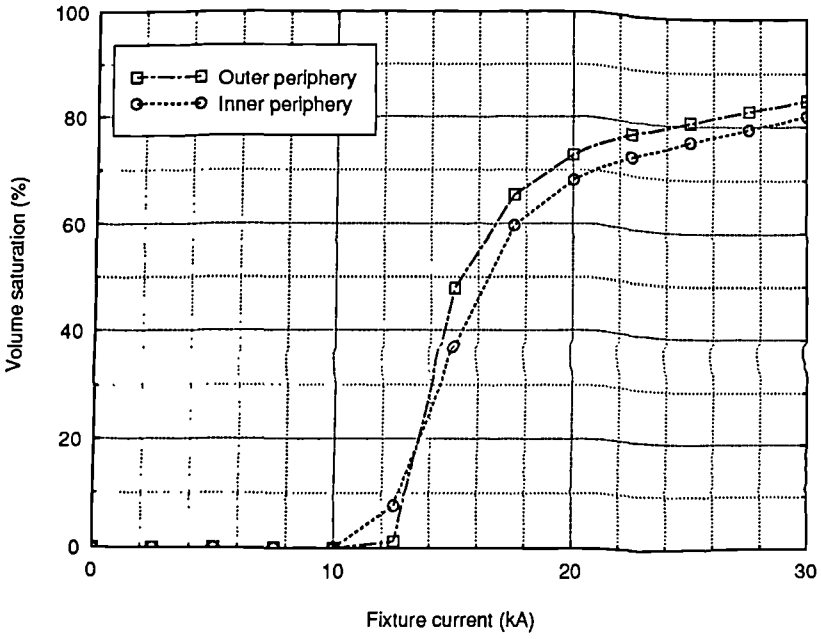

Fig. 6.13 Finite element predicted percentage volume saturation versus fixture current for the inner and outer periphery models.

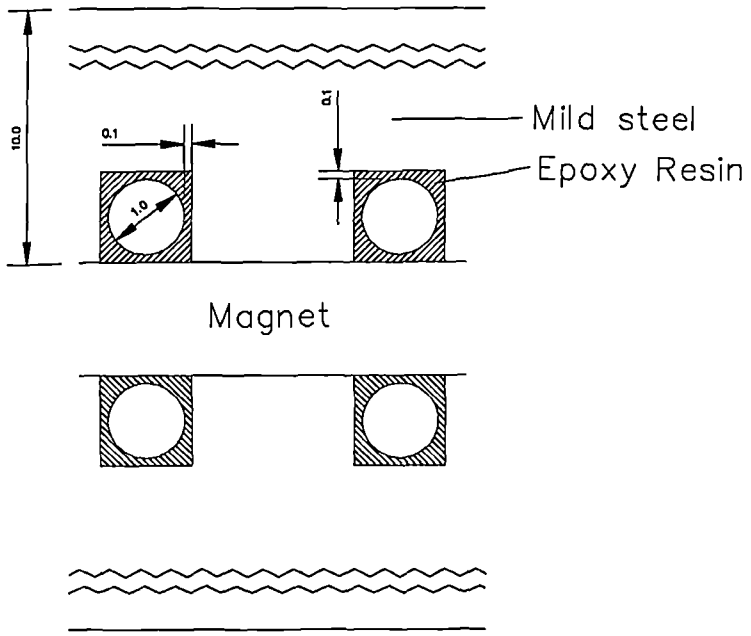

Fig. 6.14 Two-dimensional model of an iron cored version of fixture design No. 5

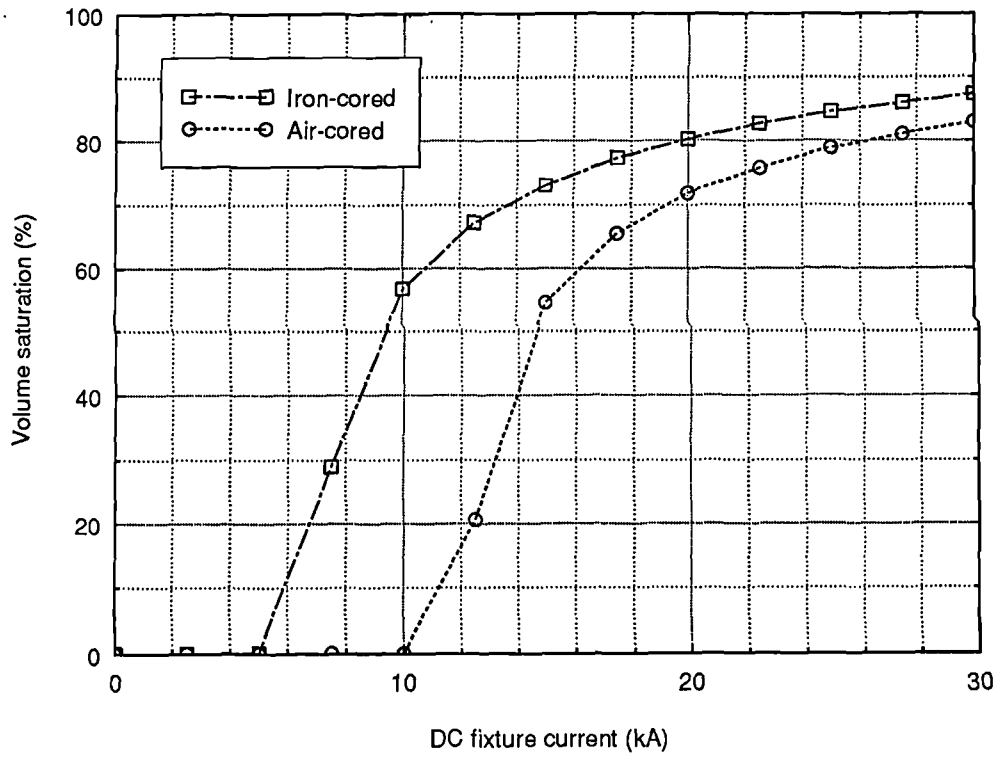

Fig. 6.15 Comparison of the static volume saturation versus fixture current characteristic of iron-cored and air-cored versions of fixture design No. 5.

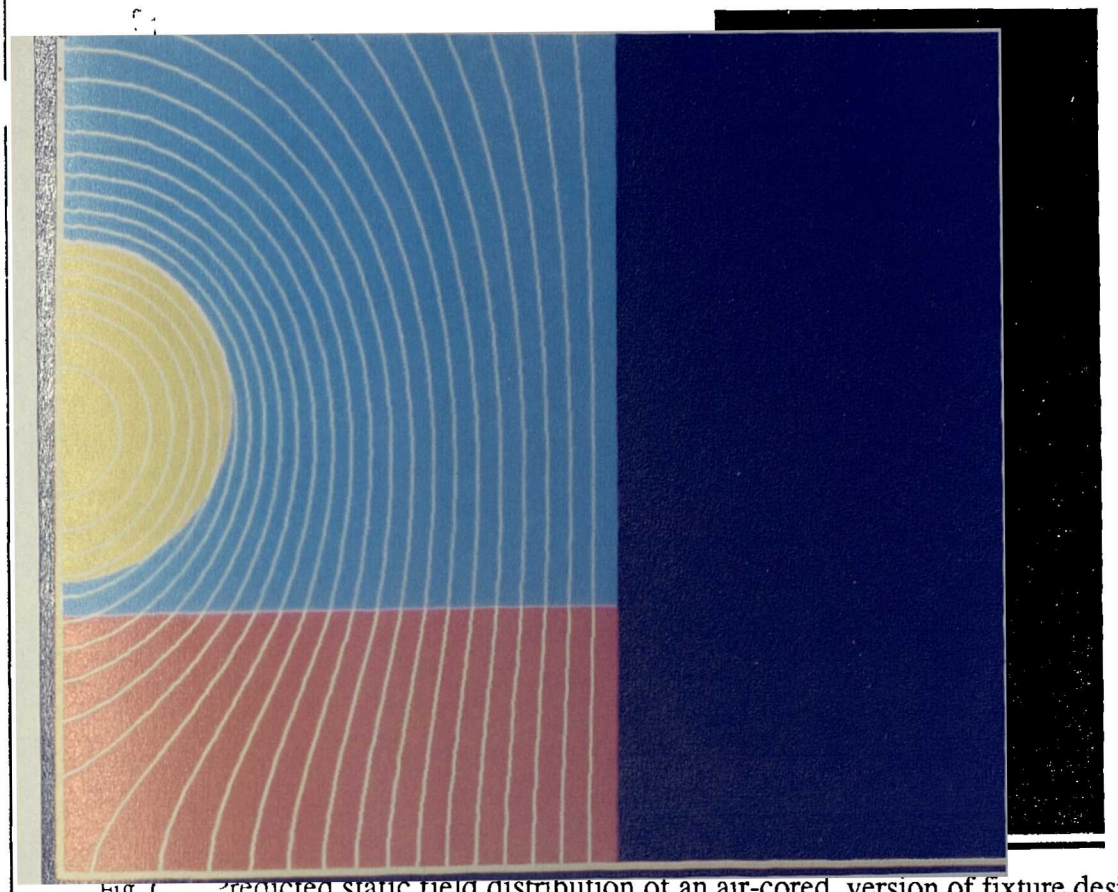

Fig. 6 Predicted static field distribution of an air-cored version of fixture design No.5 with a fixture current of 26.0kA
(Equipotential contour increments = 5×10^{-4} Wb/m)

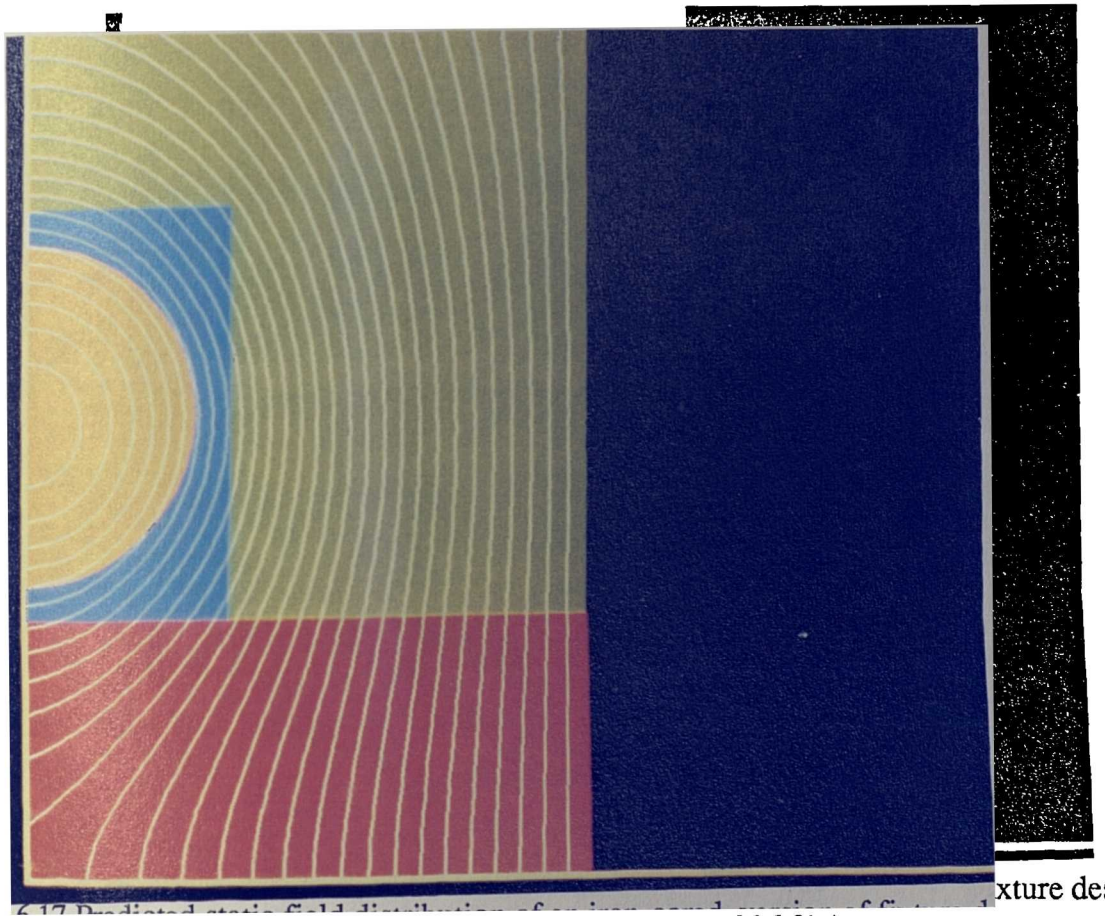

6.17 Predicted static field distribution of an iron-cored version of fixture design No.5 with a fixture current of 26.0kA.
(Equipotential contour increments = 5×10^{-4} Wb/m)

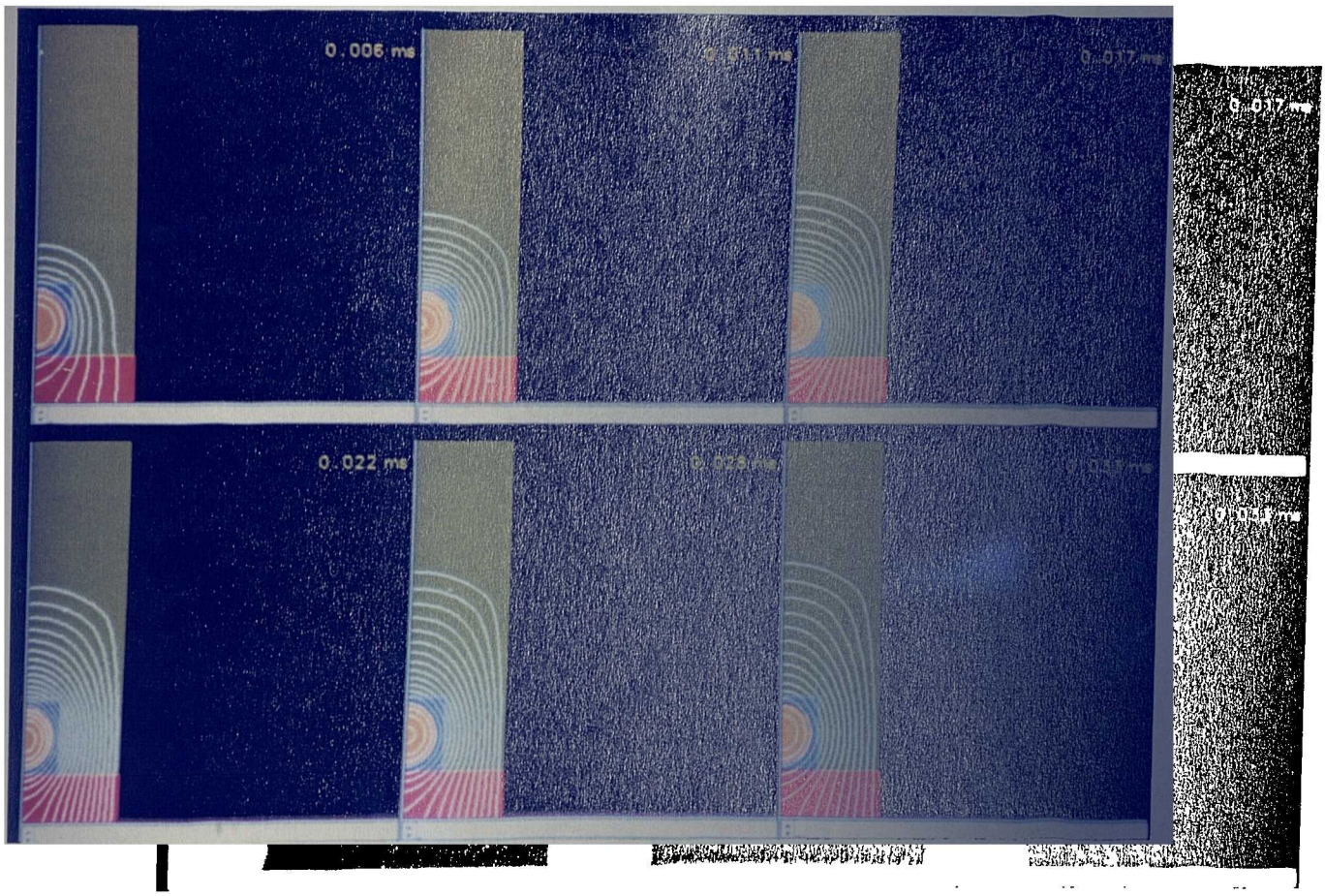

Fig. 6.18 Predicted transient field distributions during the magnetizing pulse, highlighitng the problems in penetrating the fixture back-iron.

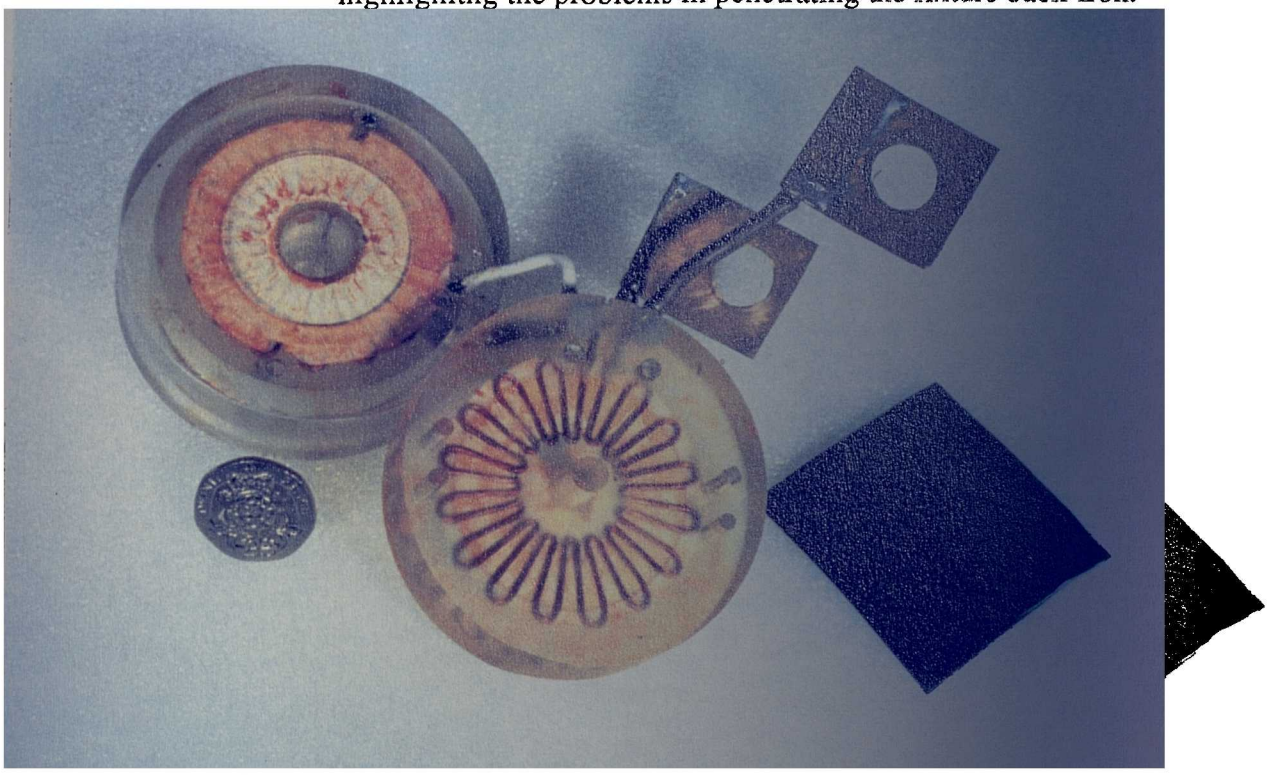

Fig. 6.19 Experimental fixture.

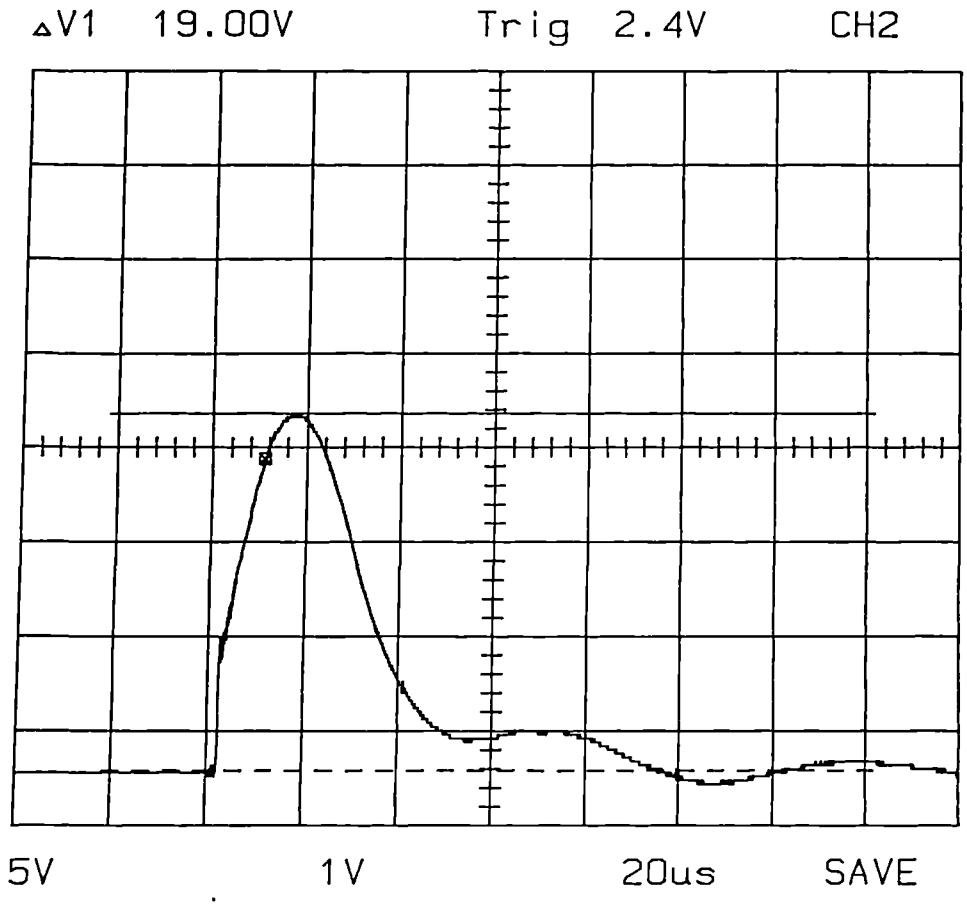

Fig. 6.20 Measured current waveform for C = 150μF and V = 2800V (Scale factor: 1440A / V).

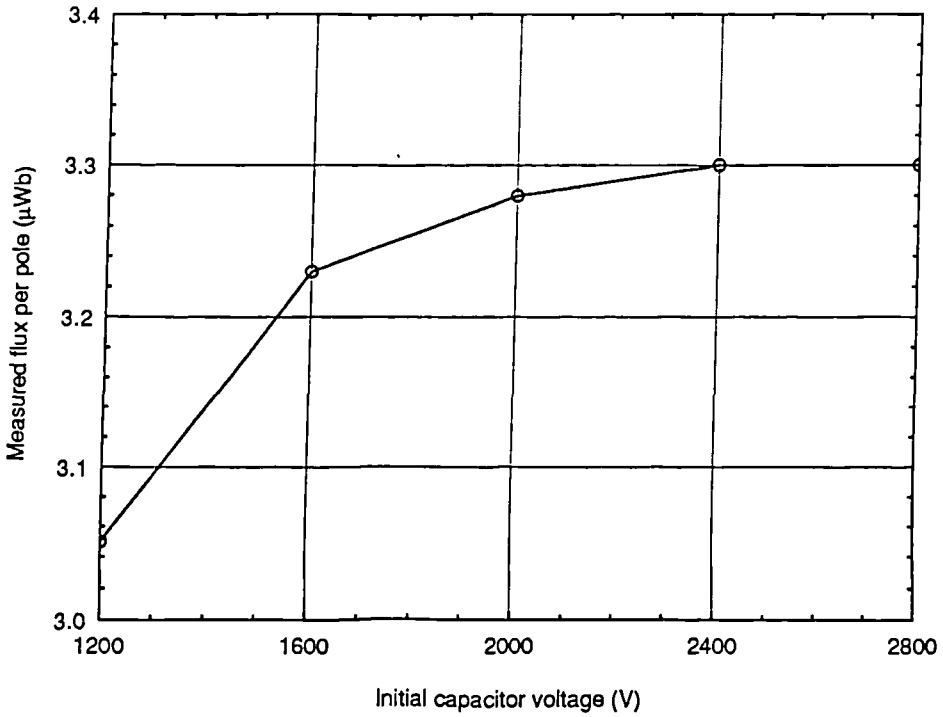

FIg. 6.21 Measured generator flux per pole for a range of initial magnetizer capacitor voltages up to the designed level of 2800V.

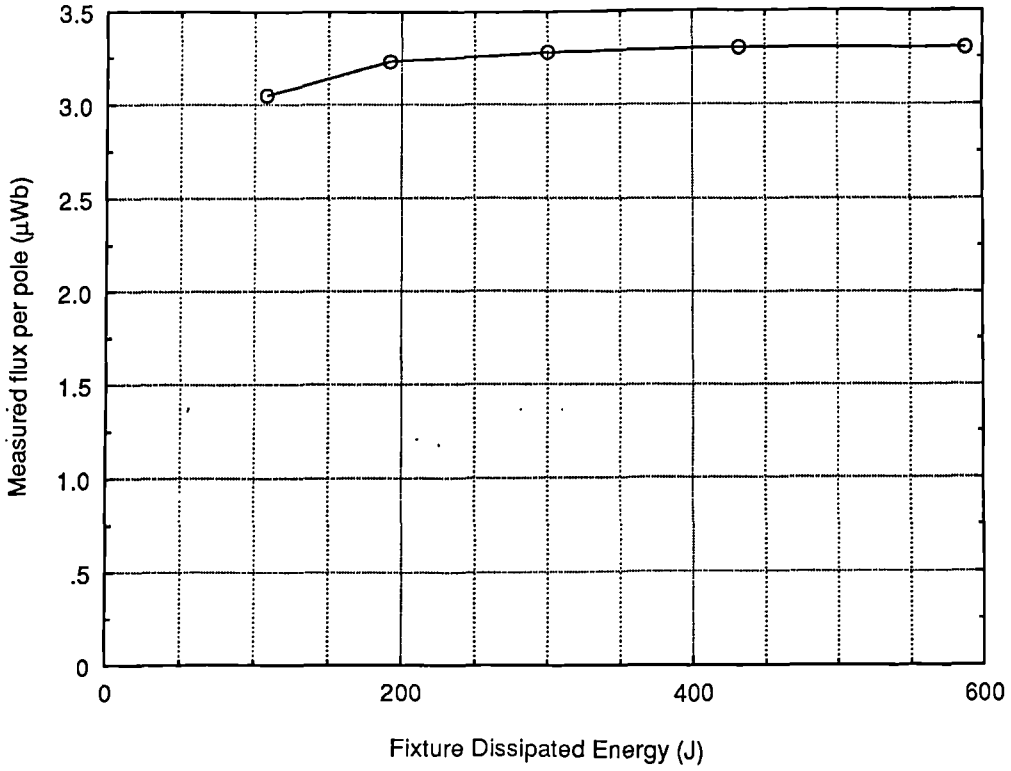

Fig. 6.22 Variation of the measured generator flux-linkage with the energy dissipated in the fixture.

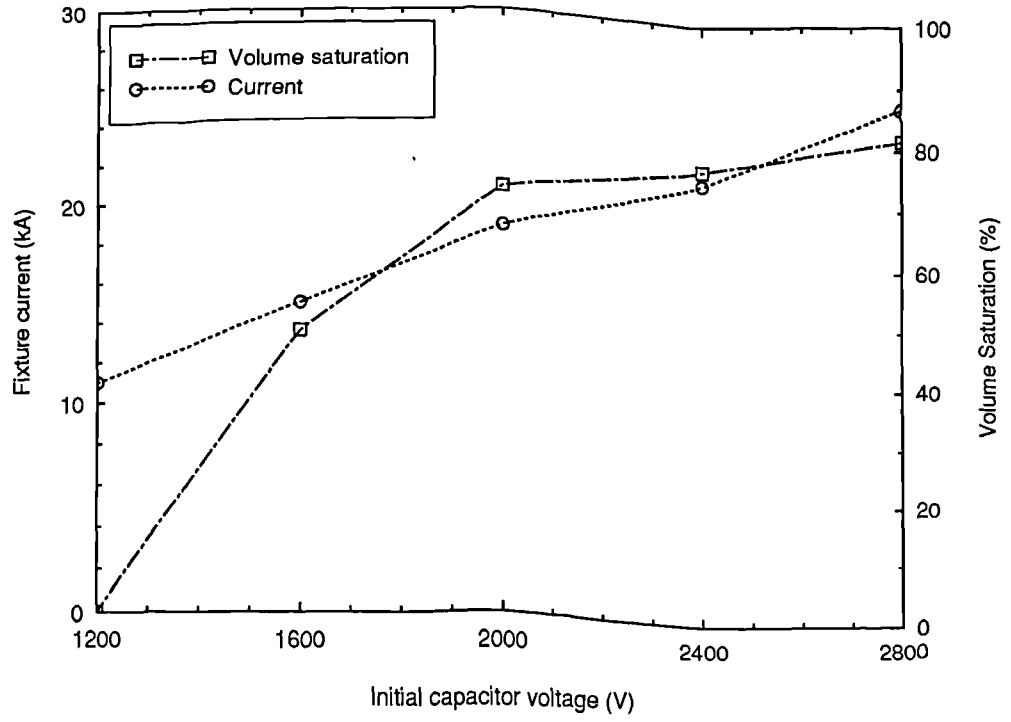

Fig. 6.23 Predicted peak current and resulting volume saturation for a range of initial capacitor voltages.

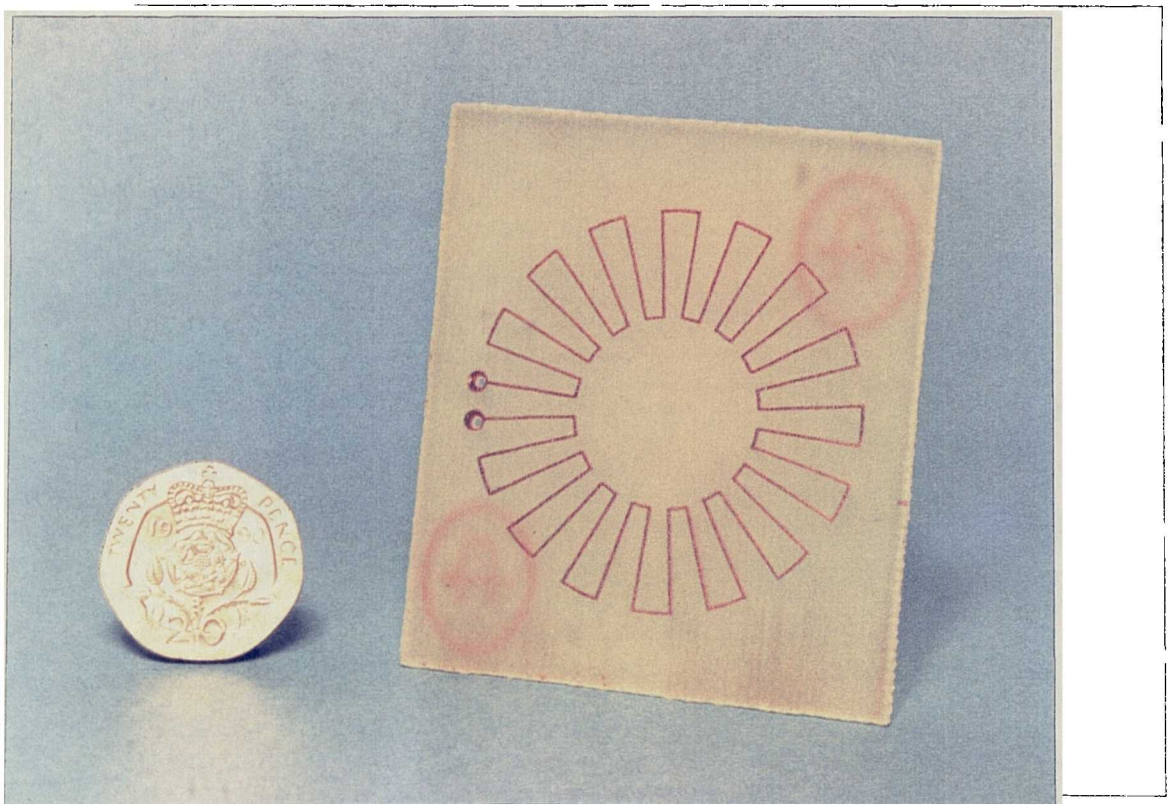

Fig. 6.24 Printed circuit search coil.

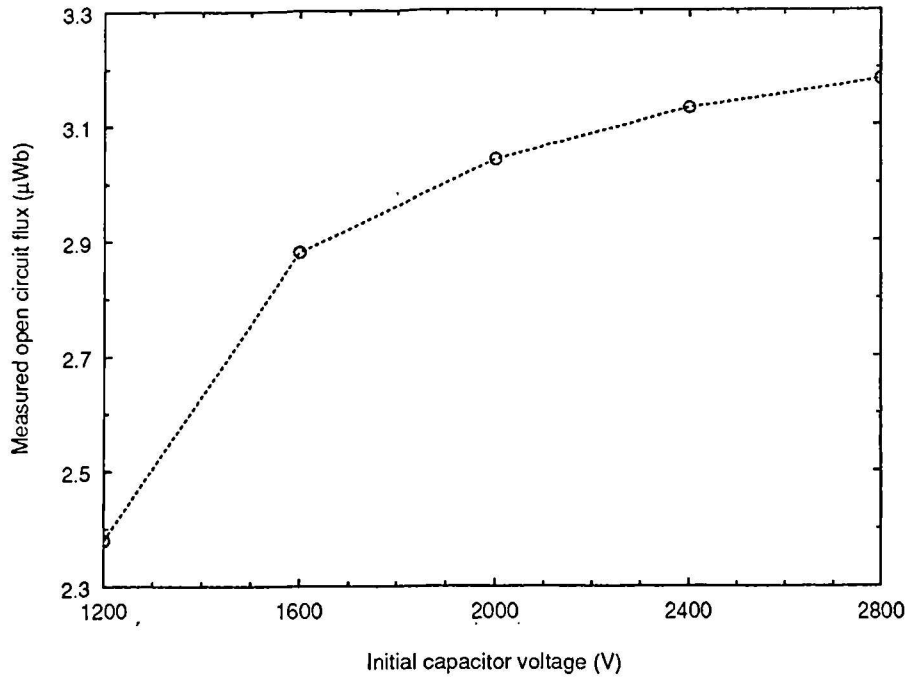

Fig. 6.25 Variation of the measured open-circuit flux 0.1mm above the magnet surface with the initial capacitor voltage.

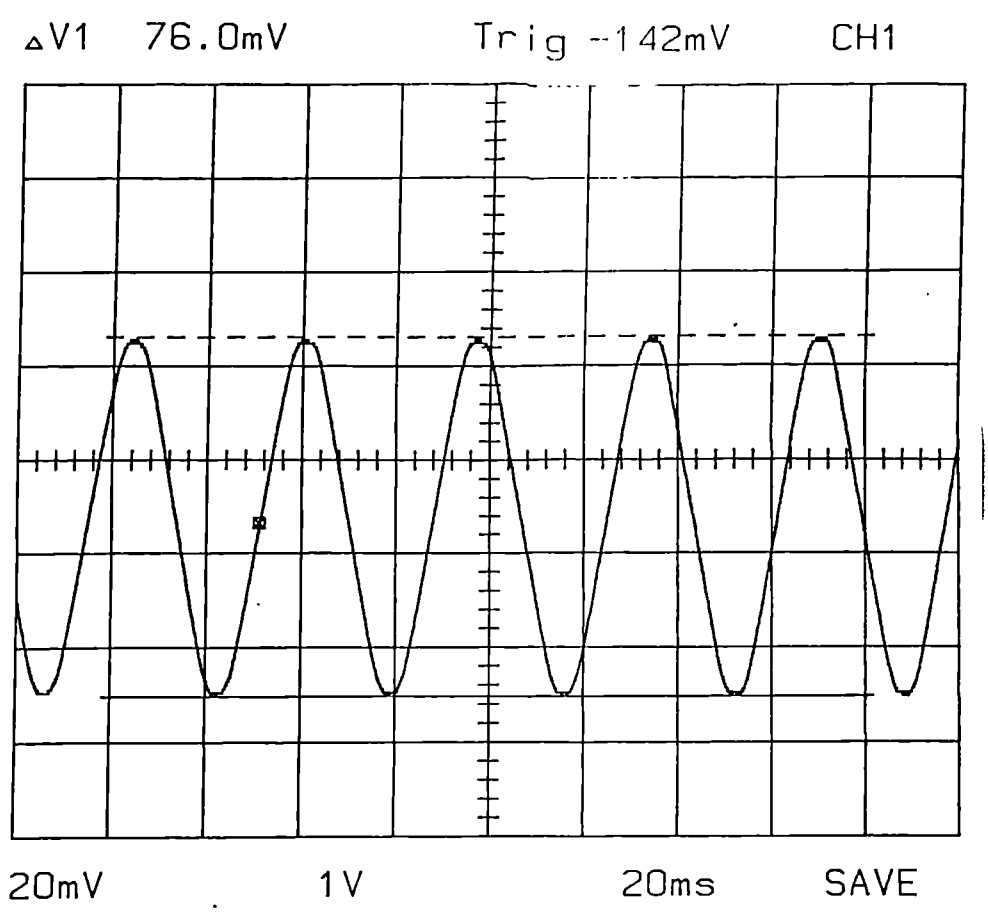

Fig. 6.26 Open circuit flux-linkage measured by the search coil of fig. 6.24 for a magnet magnetized with an initial capacitor voltage of 1200V.

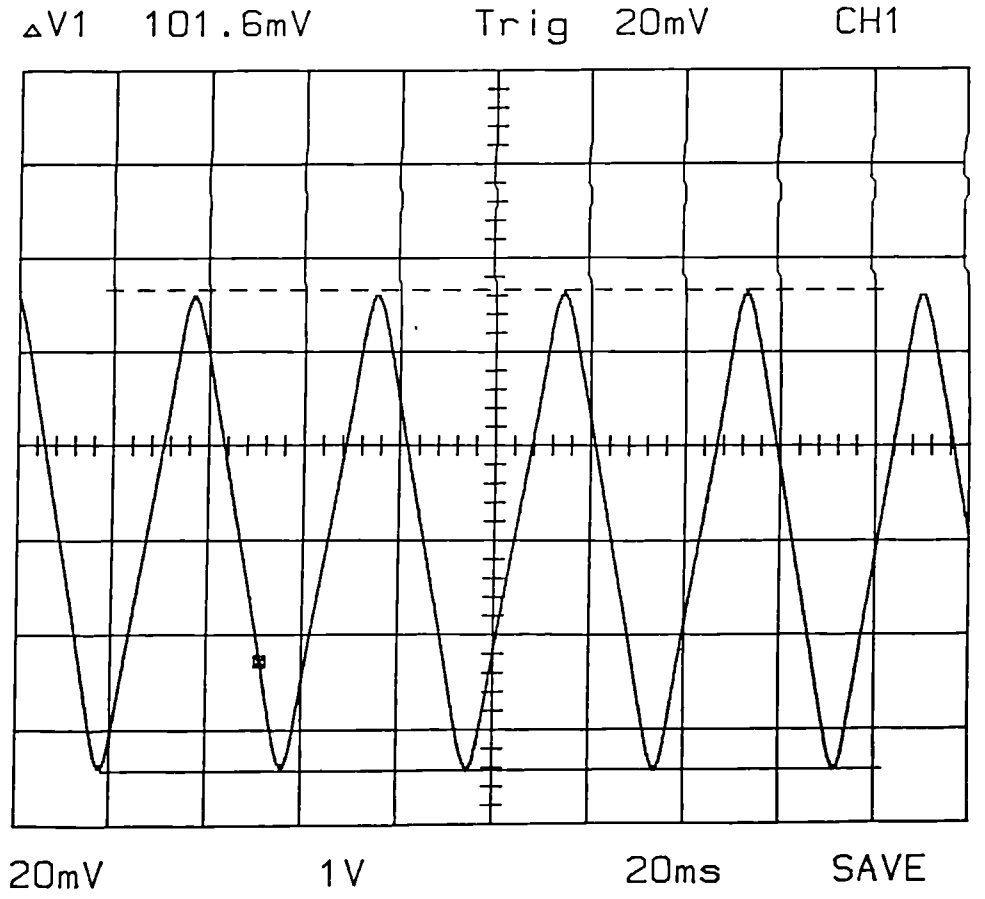

Fig. 6.27 Open circuit flux-linkage measured by the search coil of fig. 6.24 for a magnet magnetized with an initial capacitor voltage of 2800V.

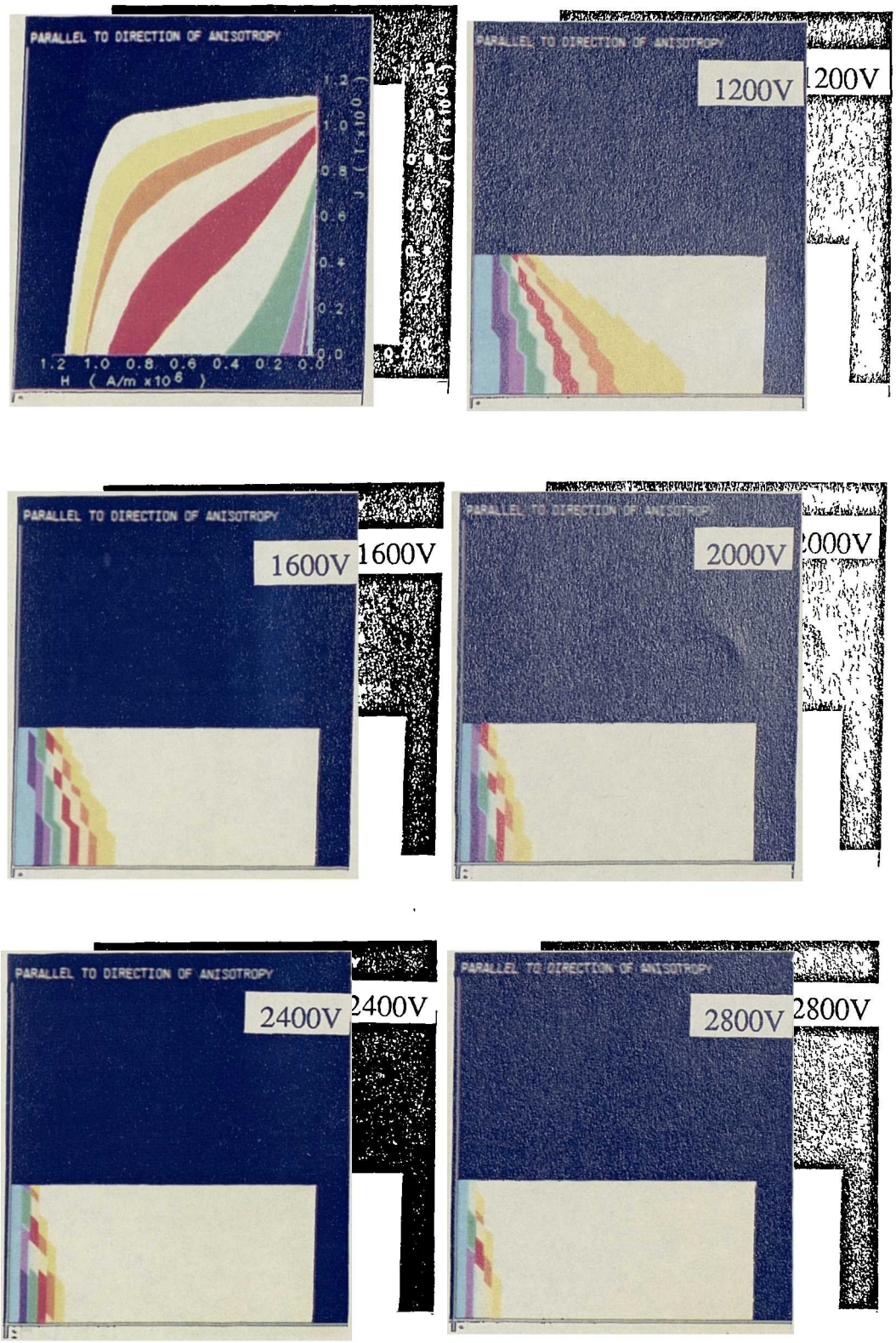

Fig. 6.28 Predicted distributions of intrinsic demagnetization characteristics over half a pole for a range of initial capacitor voltages.

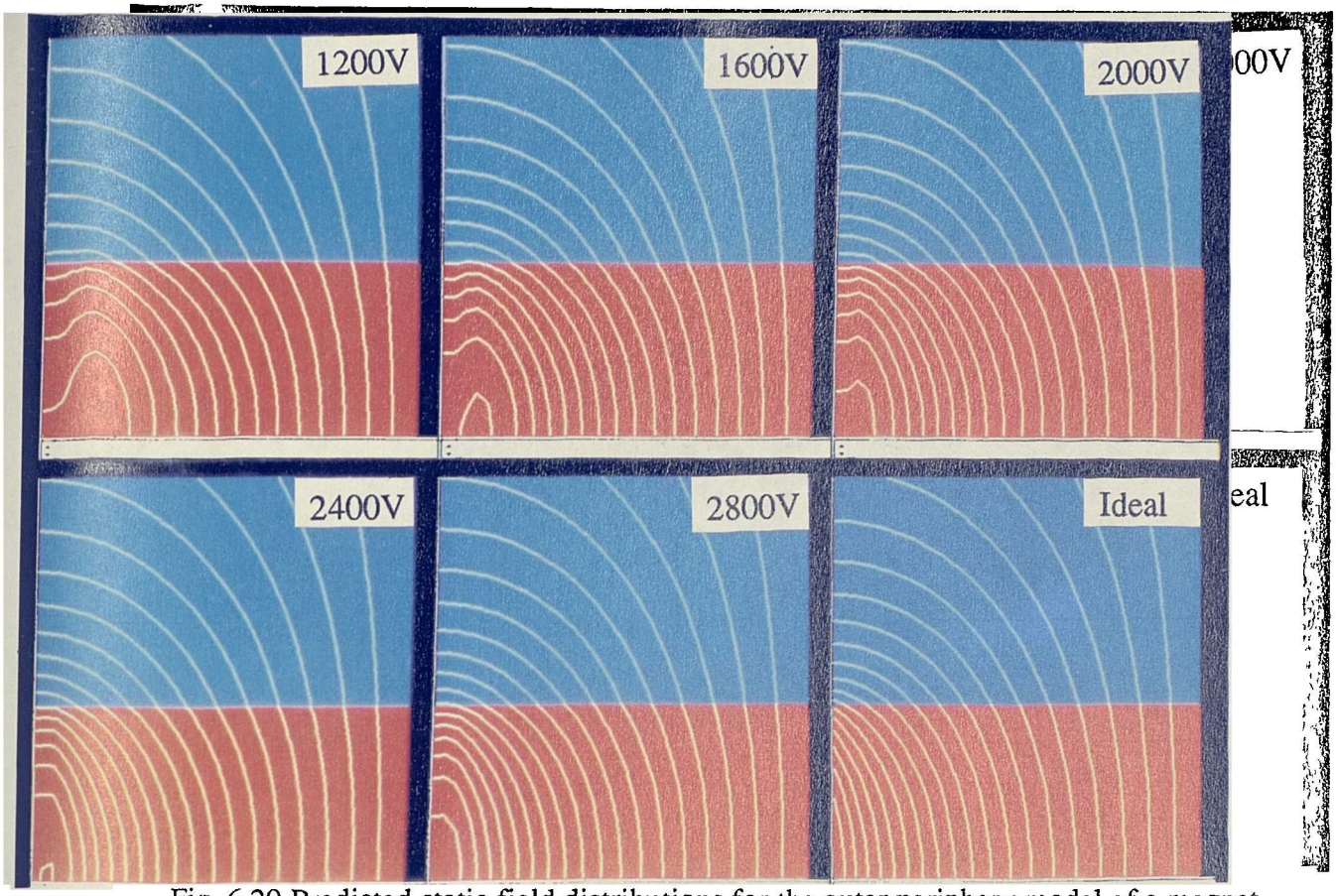

Fig. 6.29 Predicted static field distributions for the outer periphery model of a magnet ring magnetized with a range of capacitor voltages and an idelaised fully saturated magnet (Consistent potential contours throughout the field distributions).

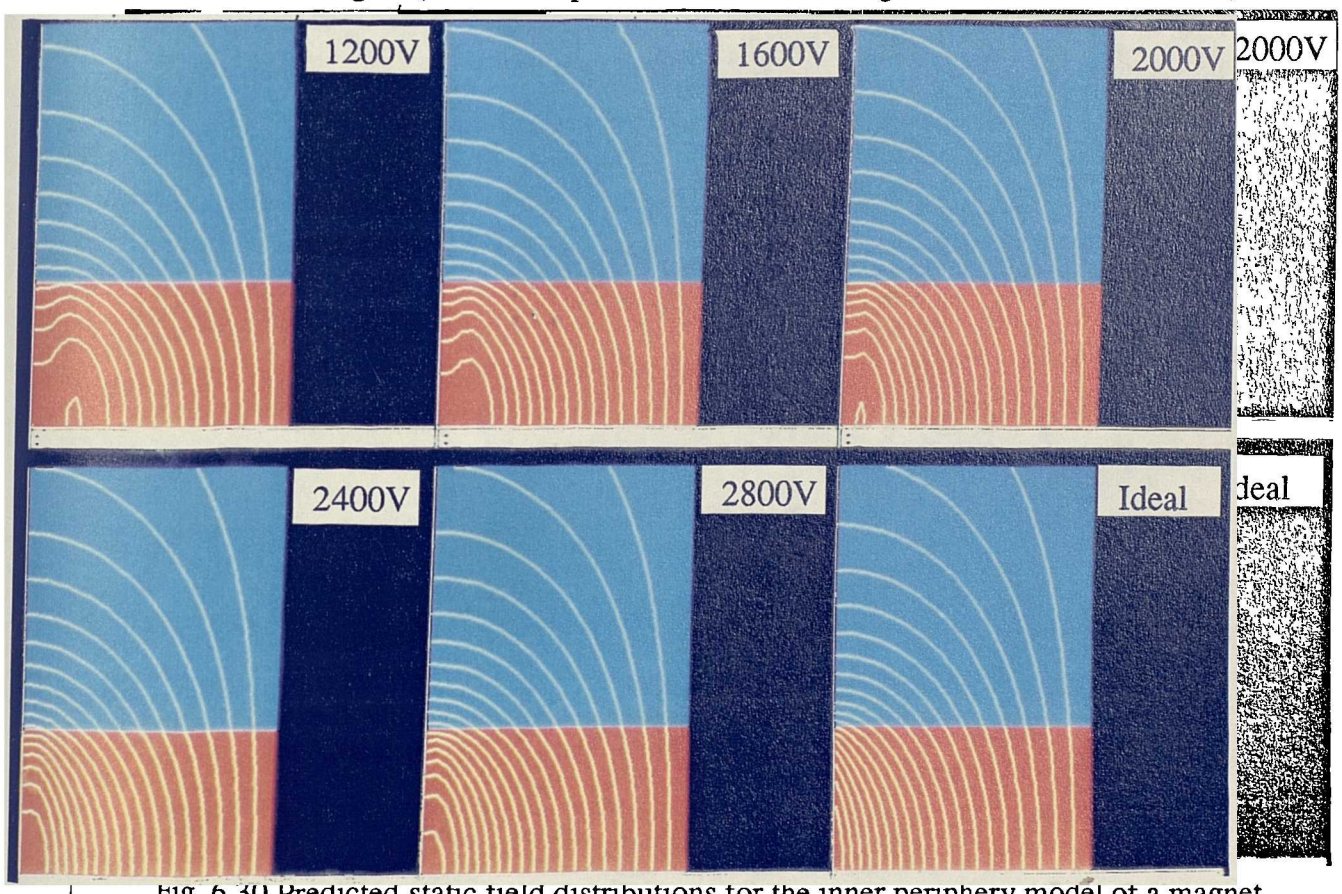

Fig. 6.30 Predicted static field distributions for the inner periphery model of a magnet ring magnetized with a range of capacitor voltages and an idelaised fully saturated magnet (Consistent potential contours throughout the field distributions).

Initial Capacitor Voltage (V)	Outer periphery node potential (10^{-4}Wb/m)	Inner periphery node potential (10^{-4}Wb/m)	Predicted average flux per pole (μWb)	Measured flux per pole (μWb)	*Inner potential* / *Outer potential*
Idealised Magnet	6.06	5.26	3.40	--	0.867
2800	5.71	4.92	3.19	3.18	0.862
2400	5.65	4.85	3.15	3.13	0.858
2000	5.54	4.75	3.09	3.04	0.857
1600	5.30	4.51	2.94	2.88	0.850
1200	4.61	3.88	2.54	2.38	0.841

Fig. 6.31Comparison of the predicted and measured open-circuit flux 0.1mm above the magnet surface.

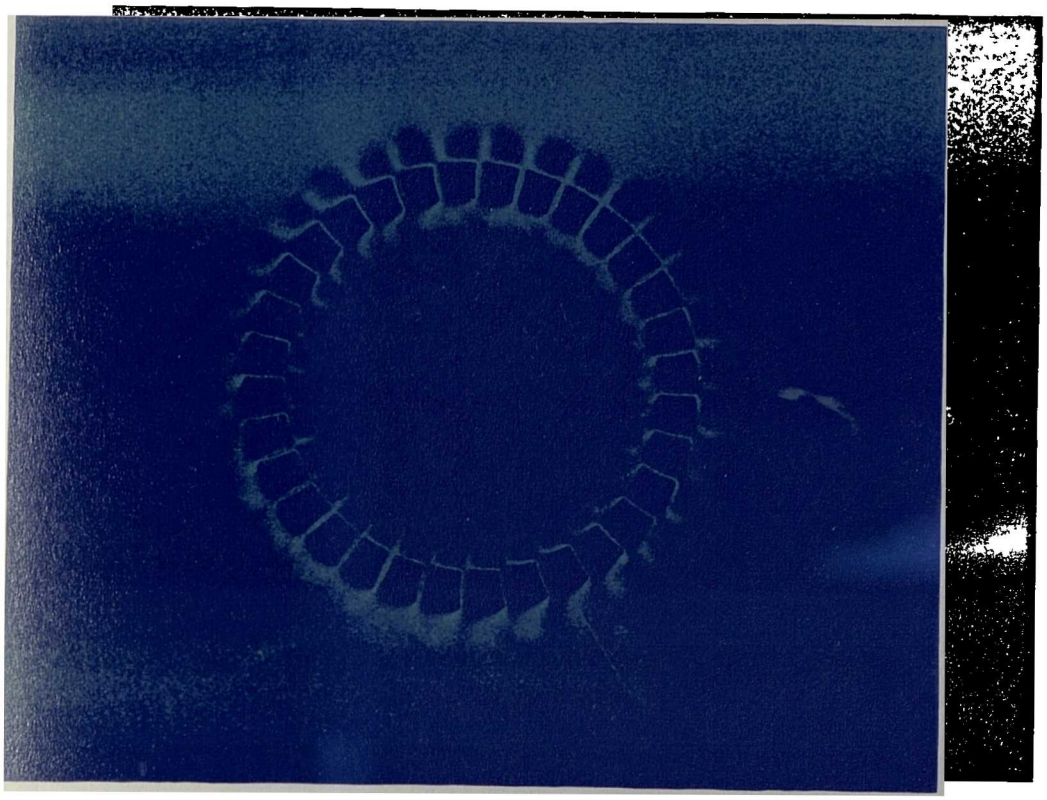

Fig. .32. Multipole pattern shown by "field sensitive paper" for a magnet magnetized with an initial capacitor voltage of 2800V.

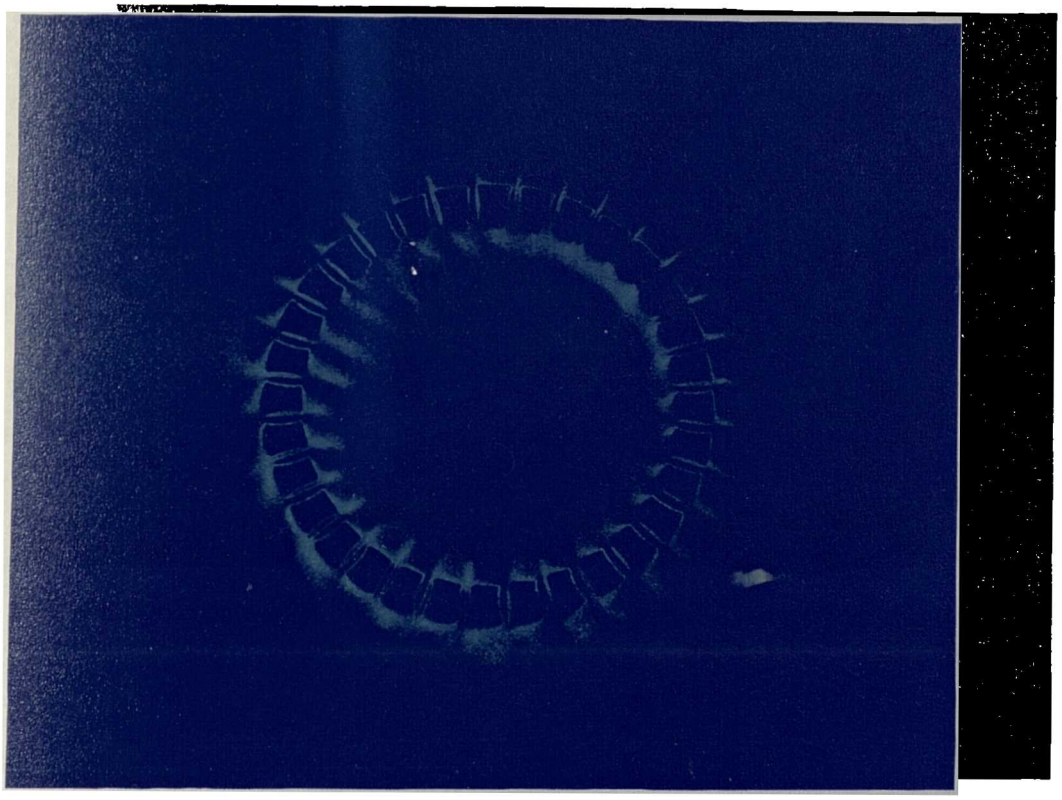

Fig. 6.33. Multipole pattern shown by "field sensitive paper" for a magnet magnetized with an initial capacitor voltage of 1200V.

CHAPTER 7

CONCLUSIONS

The cost effective and efficient magnetization of permanent magnet components is a key enabling technology in the manufacture of permanent magnet machines. However, although the preferred option in manufacture is multipole magnetization, either at the sub-component or post-assembly levels, the results presented in the thesis demonstrate that the convenience of multipole magnetization is usually achieved at the expense of an inevitable dilution in the magnet performance. Therefore, in order to minimise the dilution in properties and ensure maximum utilisation of the relatively expensive permanent magnet material, accurate design and analysis to establish optimal fixture designs is essential. The design methodology developed in this thesis has been shown to yield accurate predictions of both fixture performance and subsequent operation of the magnetized magnet in a number of diverse problems, ranging from the magnetization of a fine-pole pitch axial-field pattern to the post-assembly multipole magnetization of a radial field brushless motor. The accuracy and reliabilty of the methodology demonstrated in the case studies allows an informed decision to be made as to the viability of magnetizing a given multipole magnet without recourse to expensive and time consuming trial and error prototyping.

The analytical calculation techniques employed, although necessarily based on a number of simplifying approximations, have been shown to give reliable performance predictions in suitable problem environments, such as when magnetizing a multipole magnet prior to its incoropoartion into a device or sub-assembly. However, environments which involve the magnetization of a sub-component or a complete device containing significant regions of iron usually necessitate the use of numerically more intensive non-linear finite element techniques.

An important feature of the design methodology is the facility to model the behaviour of a non-uniformly magnetized magnet in an assembled device. This facility is essential in order to judge the performance of a given fixture/magetizer design, since the relationship between the material properties and the motor performance is usually problem dependant. Indeed, it has been demonstrated that the performance of some devices is extremely tolerant to a failure to fully magnetize a magnet and thereby not fully realise the maximum magnetic properties.

Although the methodology follows a systematic approach, it still provides considerable flexibilty to tailor the design synthesis to the particular nature of a problem. This is most apparent in the design of the 32-pole axial fixture described in chapter 6. The small pole-pitch results in rather extreme conditions, particularly in terms of the temperature rise in the necessarily small cross-section conductors and the large fraction of the pole-pitch occupied by the indiviual magnetizing conductors. Therefore, rather than adopt the simple scanning design utilised in less constrained environments, the electrical simulation stage was used to iteratively design the fixtures to a given temperature limit.

The role of eddy-currents induced in conducting regions during the impulse period has been thoroughly investigated. The dynamic simulation technique enables the effect of eddy currents to be quantified, and has been validated both experimentally and by comparison with results from a standard benchmark test, and has shown a reasonble degree of correlation over a wide range of time constant and field levels. The results of the various dynamic simulations which have been undertaken demonstrate that in the multipole magnetization of the magnets alone, the electrical conductivity and permeability of both sintered and bonded forms of rare-earth magnets is sufficiently

low to prevent any discernable reduction in volume saturation compared to that predicted under static conditions.

Problems with induced eddy-currents can, however, arise in the magnetization of sub-assemblies or complete assembled devices containing regions of solid iron, as was discussed in chapter 4. In such cases, there can be considerable reduction in the saturation level compared to that predicted under a static condition, thus highlighting the utility of the dynamic simulation technique.

The case studies have shown that the magnetization of isotropic NdFeB is considerably more demanding than that of anisotropic NdFeB, both in terms of the magnitude of the magnetizing field, and the control which must be exercised over the conformance of the magnetizing field to the required orientation of the remanent magnetism. In the case studies described in chapters 4 and 6, which are concerned with the magnetization of anisotropic sintered NdFeB, the limiting factor which prevents a fully saturated multipole magnet from being realised is the poor field alignment in the pole transition region. The problem of achieving a high degree of alignment between the magnetizing field and the material preferred orientation is aggravated in the magnetization of fine pole-pitch patterns where thermal considerations dictate that the conductors necessarily extend over a significant fraction of the pole pitch.

The study of the merits of alternative strategies for the magnetization of an external rotor brushless d.c motor equipped with a radially anisotropic magnet has demonstrated the feasibility of post-assembly magnetization, albeit at the expense of a large increase in the magnetizer energy from that required to magnetize either the multipole magnet ring alone or the assembled rotor. Results from the case study also demonstrate that the sub-assembly and post-assembly magnetization also reduces the peak flux-linkage of the motor, with a corresponding narrowing of the flat-top of the

nominally trapezoidal motor phase emf. Although post-assembly magnetization of a motor equipped with isotropic bonded NdFeB was not feasible due to the specified requirement for radial magnetization, such a technique may be useful in the magnetization of motors with a diametrically magnetized two pole isotropic rotor.

In summary, the study has demonstrated that multipole magnetization can be realised even in onerous conditions, such as post-assembly magnetization. However, ultimately, the feasibility of multipole magnetization in a production environment will be governed by the production volumes, because of the large expense involved in designing and constructing a specific multipole magnetizing fixture.

Scope for Future work.

The electromagnetic design methodology and analysis is presently based entirely on two-dimensional analyses. The approximations implicit in such analyses limits the applicability of the software in the design of multipole axial magnetizing fixtures. Whilst, the case study of chapter 6 was well suited to two-dimensional analysis, in general there is a requirement to cater for ring magnets with low pole numbers. Therefore, the extension of the analysis to cater for three dimensionsal fields, particularly the analytical field calculations, would add further utility and scope to the design methodology. The extension of the static and dynamic finite element calculations to three dimensions and the incorporation of adaptive meshing would also improve the utility of the design methodology, albeit being computationally much more demanding.

In the design of a magnetizing fixture for a production environment, the thermal and mechanical aspects of the design are very important. An important consideration in assessing the viability of a given fixture for a production environment is the minimum cycle time. Although re-charging of the capacitors imposes a minimum cycle time, the principle limiting factor is usually the period required to remove the dissipated

energy from the fixture conductors. However, in order to maximise the through-put of a fixture, a far more detailed consideration of the construction with regard to producing the optimal arrangement of cooling ducts is required. Therefore, the thermal modelling of fixtures incorporating forced cooling ducts, by either finite element or lumped parameter methods merits further investigation in order to optimise heat transfer from the fixture windings.

APPENDIX A

CALCULATION OF THE INDUCTANCE AND RESISTANCE OF A MULTIPOLE AXIAL MAGNETIZING FIXTURE.

The layout of conductors in one side of typical multipole axial magnetizing fixtures with both low and high pole numbers are shown in fig A.1. For fixtures with a low pole number, there is a significant curvature in the end-windings, and the components of self and mutual inductance associated with the each end-winding conductor must be calculated with due account of this curvature. However, for high pole number fixtures, such as the fixture which forms the basis of the case study of chapter 5, the short end windings can be regarded as approximating to straight filaments for the purpose of calculating the fixture inductance. In such cases, the inductance of the fixture can be estimated by a summation of all the components of self and mutual inductance of elementary straight filaments in a similar manner to the radial field fixtures discussed in section 2.11.

Neglecting the curvature of the end-windings, the total-self inductance of high pole number double sided fixture, with p poles and N_l conductors per pole per side, is given by:

$$L_{self} = 2\,p\,N_l\,(\,L_{rad} + L_{ew}\,) \qquad (1)$$

The self-inductance of the elementary radial and end-winding conductors, L_{rad} and L_{ew} respectively, are given by standard analytical formulae for finite length straight conductors:

$$L_{rad} = 2x10^{-7}\,(r_o - r_i)\,\log_e[\frac{2\,(r_o - r_i)}{d_c} - \frac{3}{4}] \qquad (2)$$

$$L_{ew} = 2x10^{-7} \left(\frac{\pi r_o}{p} \log_e \left[\frac{2\pi r_o}{pd_c} - \frac{3}{4} \right] + \frac{\pi r_i}{p} \log_e \left[\frac{2\pi r_i}{pd_c} - \frac{3}{4} \right] \right) \quad (3)$$

where

d_c = Conductor cross-section diameter.

r_i = Inner radius of the radial conductor position (as defined in fig. A.1).

r_o = Outer radius of the radial conductor position (as defined in fig. A.1).

The components of mutual inductance associated with a given conductor are greatly simplified because of the inherent symmetry of the fixture layout. For each of the radially orientated conductors, the mutual components with all the other radially orientated conductors on the same side of the fixture sum to zero. The only net component of mutual coupling for each of the radially orientated conductor bundles located at each pole is with the corresponding conductor bundle on the other side of the magnet. Thus the model for the calculation of the mutual coupling per pole between radially orientated conductors reduces to that of fig A.2

Assuming that a given end-winding is at right angles to its two associated radially orientated conductors, a valid assumption for a high pole number, the model for calculating the mutual coupling for each pole pair can be reduced to that of fig. A.3. For a fixture which has a multiple of 2 conductors per pole per side, the end-windings can be arranged as shown in fig.A.1, such that the net coupling between any given radial conductor and the end-windings, approximately sum to zero, neglecting practical effects such as the stacking of alternate end-windings etc. The mutual inductance between two elementary filaments, i and j, in the models of figs. A.2 and A.3 is given

by the standard analytical formula for two straight conductors:

$$M_{ij} = 2x10^{-7}\ l_{ax}\left(\ \log_e\left(\frac{l_{ax}}{S_{ij}}\right)+\sqrt{1+\frac{l_{ax}^2}{S_{ij}^2}}-\sqrt{1+\frac{S_{ij}^2}{l_{ax}^2}}+\frac{S_{ij}}{l_{ax}}\right) \qquad (4)$$

where

l_{ax} = Conductor axial length.

S_{ij} = Distance between conductors i and j.

For a winding on either side of the magnet consisting of a single turn, the inherent asymmetry results in a net-mutual coupling between each radial conductor and the fixture end-winding. However, in high pole number fixtures this can generally be neglected since the end-winding conductors in which the small asymmetry is a significant factor, i.e those close to the radial conductor under consideration, are almost at right angles to the radial direction, whilst for those end-winding conductors that are more favourably aligned, the asymmetry is small in relation to their displacement from the radial conductor under consideration.

The total contribution of the mutual inductance components to the fixture inductance is therefore given by:

$$M_{total} = p\left(M_{rad}+\frac{M_{ew}}{2}\right) \qquad (5)$$

where M_{rad} and M_{ew} are calculated from the simplified models of figs A.2 and A.3.

The net fixture inductance is therefore given by:

$$L_{fix} = L_{self} + M_{total} \qquad (6)$$

The resistance at 20°C of a double sided fixture with p poles and Nl conductors per pole per side is given by:

$$R = \frac{2\,\rho_{Cu}\,p\,N_l\,\left[\,(r_o - r_i) + \frac{\pi r_o}{2p} + \frac{\pi r_i}{2p}\,\right]}{A_c} \qquad (7)$$

where

ρ_{Cu} = Resistivity of copper at 20°C.

A_c = Cross-sectional area of each conductor.

In fixture with a high pole number, such as that in the case study of chapter 5, the cross-sectional area of each individual conductor is comparable with the pole-pitch and there is considerable difficulty in realising the ideal end-winding form shown in fig. A1. For such cases, a better estimate of the resistance realised in practice can be achieved by assuming that the end-windings form a semi-circle in passing from one pole to the next as shown in fig.A.4. The resistance of a double sided fixture with this end-winding model is given approximately by:

$$R = \frac{2\,\rho_{Cu}\,p\,N_l\,\left[\,(r_o - r_i) + \frac{\pi^2 r_o}{4p} + \frac{\pi^2 r_i}{4p}\,\right]}{A_c} \qquad (8)$$

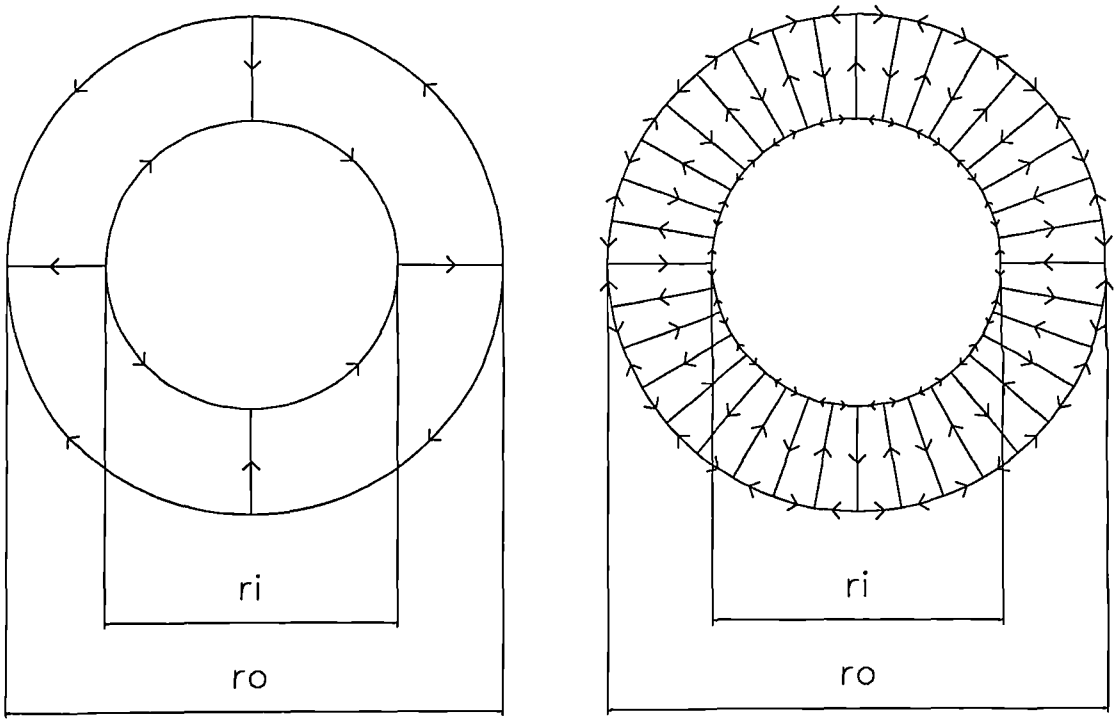

Fig. A.1 Conductor layouts for typical axial field multipole magnetizing fixtures.

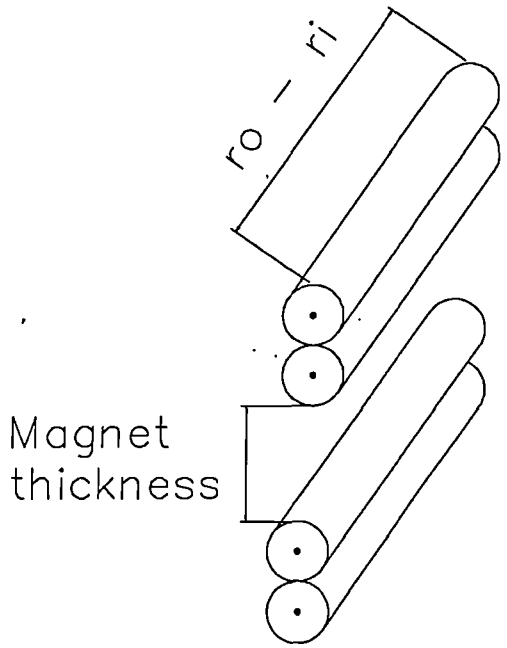

Fig. A.2 Simplified model for the calculation of mutual inductance per pole for the radially orientated conductors in a fixture with 2 turns per pole per side.

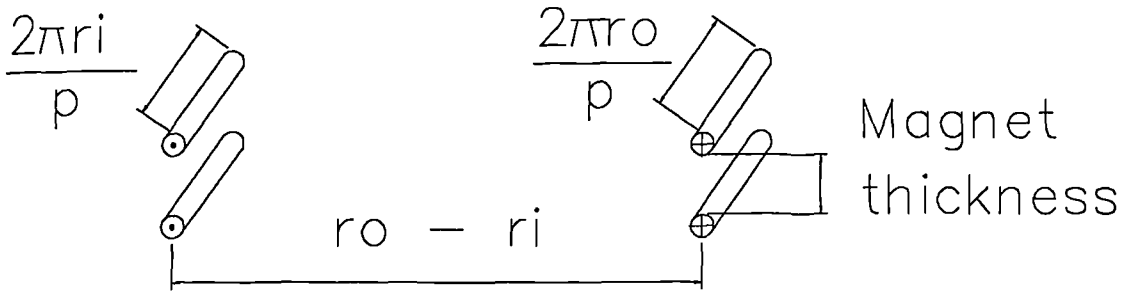

Fig. A.3. Simplified model for the calculation of mutual inductance per pole pair for the end-winding conductors of a fixture with 2 turns per pole per side.

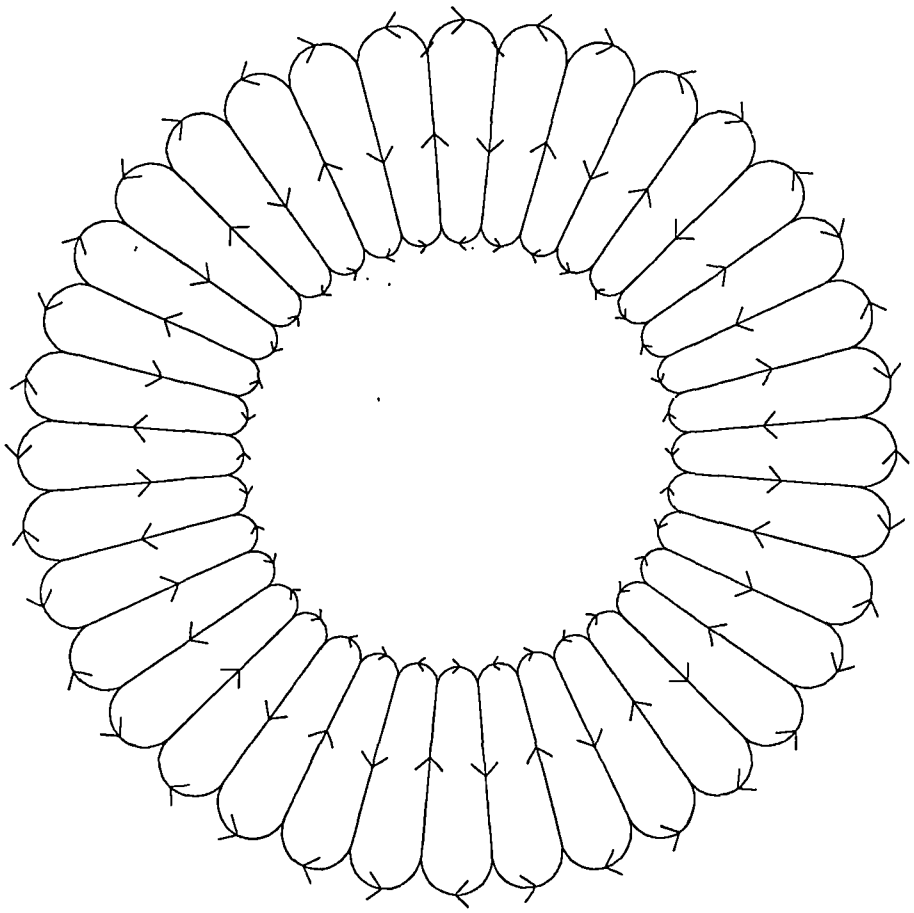

Fig. A.4 36 pole axial magnetizing fixture with semi-circular end-windings.

APPENDIX B

FINITE ELEMENT FORMULATIONS.

The vector potential forms of three governing electromagnetic field equations utilised at various stages during the design synthesis are given in (1a) (1b) and (1c):

Magnetostatic- externally driven current, no magnetized magnets (utilised in the calculation of static mmf required for saturation of the magnet).

$$\frac{\partial}{\partial x}\left(\nu_y \frac{\partial A}{\partial x}\right) + \frac{\partial}{\partial y}\left(\nu_x \frac{\partial A}{\partial x}\right) = -J_z \qquad (1a)$$

Transient diffusion equation (utilised in the dynamic simulation of the impulse magnetizing process).

$$\frac{\partial}{\partial x}\left(\nu_y \frac{\partial A}{\partial x}\right) + \frac{\partial}{\partial y}\left(\nu_x \frac{\partial A}{\partial x}\right) = -J_z + \sigma \frac{\partial A}{\partial t} + \sigma \frac{\partial \Phi}{\partial z} \qquad (1b)$$

Magnetostatic- externally driven current, magnetized magnets (utilised in the calculation of the static performance of the magnetized magnet).

$$\frac{\partial}{\partial x}\left(\nu_y \frac{\partial A}{\partial x}\right) + \frac{\partial}{\partial y}\left(\nu_x \frac{\partial A}{\partial x}\right) = -J_z + \frac{\partial M_x}{\partial y} - \frac{\partial M_y}{\partial x} \qquad (1c)$$

where

A = z direction component of vector potential.

J_z = Externally driven current density.

ν_x = Reluctivity in the x direction.

ν_y = Reluctivity in the y direction.

Φ = Electrical scalar potential.

M_x = x direction component of permanent magnet magnetization.

M_y = y direction component of permanent magnet magnetization.

The electical scalar potential term can be eliminated as discussed in chapter 3. The solution of the resulting equations can be realised by the application of variational principles. In this approach a functional is formed, the minimisation of which results in the governing field equations whilst also satisfying the imposed boundary conditions. For many problems, the functional is associated with the energy in the problem domain. The corresponding functionals for the governing equations above are given in (2a) (2b) and (2c):

$$F = \int_{\Omega} [\ \nu_y\ (\frac{\partial A}{\partial x})^2 + \nu_x\ (\frac{\partial A}{\partial y})^2 - 2\,J_z\,A\ ]\ d\Omega \qquad (2a)$$

$$F = \int_{\Omega} [\ \nu_y\ (\frac{\partial A}{\partial x})^2 + \nu_x\ (\frac{\partial A}{\partial y})^2 - 2\,J_z\,A + 2\,\sigma\frac{\partial A}{\partial t}\ ]\ d\Omega \qquad (2b)$$

$$F = \int_{\Omega} [\ \nu_y\ (\frac{\partial A}{\partial x})^2 + \nu_x\ (\frac{\partial A}{\partial y})^2 - 2\,J_z\,A - M_x\frac{\partial A}{\partial y} + M_y\frac{\partial A}{\partial x}\ ]\ d\Omega \qquad (2c)$$

To facilitate the minimisation of the functionals the problem domain is divided into a number of coupled elements in each of which simplifying approximations are made with regard to the variation of the field. The implementation used in the design synthesis is based on first order triangular elements, the general form of which is shown

in fig. (B.1). The vector potential within each element varies accoding to equation (3):

$$A = a + bx + cy \tag{3}$$

where a,b and c are unknown constants.

The constants a,b and c can be related to the potentials at each of nodes, i.e A_i, A_j and A_k :

$$A_i = a + bx_i + cy_i \tag{4a}$$

$$A_j = a + bx_j + cy_j \tag{4b}$$

$$A_k = a + bx_k + cy_k \tag{4c}$$

Hence the constants can be obatined as:

$$a = \frac{A_i (x_j y_k - x_k y_j) + A_j (x_k y_i - x_i y_k) + A_k (x_i y_j - x_j y_i)}{2\Delta} \tag{5a}$$

$$b = \frac{A_i (y_j - y_k) + A_i (y_k - y_i) + A_i (y_i - y_j)}{2\Delta} \tag{5b}$$

$$c = \frac{A_i (x_k - x_j) + A_j (x_i - x_k) + A_k (x_j - x_i)}{2\Delta} \tag{5c}$$

where

Δ is the area of the triangular element.

Hence, the variation of the potential within the element can be written as:

$$A = N_i A_i + N_j A_j + N_k A_k = \sum_{l=i,j,k} N_l A_l \tag{6}$$

where Ni, Nj and Nk are the shape functions of the elements and are given by:

$$N_l = \frac{a_l + b_l x + c_l y}{2\Delta} \tag{7}$$

The functionals of equations (2a), (2b) and (2c) can be minimised by differentiating with respect to A_i and equating to zero. The three differentials corresponding to equations (2a), (2b) and (2c) are given, with appropriate substitution for the shape functions defined above, by (8a), (8b) and (8c) respectively:

$$\frac{\partial F}{\partial A_i} = \int_\Omega \left(\frac{\nu_y b_i}{2\Delta} \sum_{l=i,j,k} \frac{b_l A_l}{2\Delta} + \frac{\nu_x c_i}{2\Delta} \sum_{l=i,j,k} \frac{c_l A_l}{2\Delta} - J_z \frac{(a_i + b_i x + c_i y)}{2\Delta} \right) d\Omega = 0 \tag{8a}$$

$$\frac{\partial F}{\partial A_i} = \int_\Omega \left[\frac{\nu_y b_i}{2\Delta} \sum_{l=i,j,k} \frac{b_l A_l}{2\Delta} + \frac{\nu_x c_i}{2\Delta} \sum_{l=i,j,k} \frac{c_l A_l}{2\Delta} - J_z \frac{(a_i + b_i x + c_i y)}{2\Delta} + \sigma \frac{\partial}{\partial A_i} \left(\frac{\partial A}{\partial t} \right) \right] d\Omega \tag{8b}$$

$$\frac{\partial F}{\partial A_i} = \int_\Omega \left(\frac{\nu_y b_i}{2\Delta} \sum_{l=i,j,k} \frac{b_l A_l}{2\Delta} + \frac{\nu_x c_i}{2\Delta} \sum_{l=i,j,k} \frac{c_l A_l}{2\Delta} - J_z \frac{(a_i + b_i x + c_i y)}{2\Delta} - \frac{M_x c_i}{2\Delta} + \frac{M_y b_i}{2\Delta} \right) d\Omega \tag{8c}$$

Integrating (8a), (8b) and (8c) over the area of the element yields (9a), (9b) and (9c) respectively:

$$\frac{\partial F}{\partial A_i} = \frac{\nu_y}{4\Delta} \sum_{l=i,j,k} b_i b_l A_l + \frac{\nu_x}{4\Delta} \sum_{l=i,j,k} c_i c_l A_l - \frac{J_z \Delta}{3} = 0 \tag{9a}$$

$$\frac{\partial F}{\partial A_i} = \frac{\nu_y}{4\Delta} \sum_{l=i,j,k} b_i b_l A_l + \frac{\nu_x}{4\Delta} \sum_{l=i,j,k} c_i c_l A_l - \frac{J_z \Delta}{3} + \sigma \sum_{l=i,j,k} \frac{\Delta}{12} (1 + \delta_{il}) \frac{\partial A}{\partial t} = 0 \tag{9b}$$

$$\frac{\partial F}{\partial A_i} = \frac{\nu_y}{4\Delta} \sum_{l=i,j,k} b_i b_l A_l + \frac{\nu_x}{4\Delta} \sum_{l=i,j,k} c_i c_l A_l - \frac{J_z \Delta}{3} - \frac{M_x c_i}{2} + \frac{M_y b_i}{2} = 0 \tag{9c}$$

where δ_{il} =1 if i= 1 or δ_{il} =0 if i≠ 1

To obtain the solution of equatino (9b) at discrete time steps, the time derivative term is replaced by a linear backward difference approximation, as dicussed in chapter3. The time derivative term then becomes:

$$\frac{\partial A}{\partial t} = \frac{\Delta A}{\Delta t} \tag{10}$$

The minimisation procedure for each element described above is performed for all the elements in the domain to obtain a global minima of the functional. The solution of equations (9a), (9b) and (9c) is realised by a non-linear Newton-Raphson technique. To enable such a technique to be used, equations (9a), (9b) and (9c) are further differentiated:

$$\frac{\partial^2 F}{\partial A_i \partial A_j} = \frac{1}{4\Delta} \left[b_i b_j \left(\nu_y + B_y \frac{\partial \nu_y}{\partial B_y} \right) + c_i c_j \left(\nu_x + B_x \frac{\partial \nu_x}{\partial B_x} \right) \right] \tag{11a}$$

$$\frac{\partial^2 F}{\partial A_i \partial A_j} = \frac{1}{4\Delta} \left[b_i b_j \left(\nu_y + B_y \frac{\partial \nu_y}{\partial B_y} \right) + c_i c_j \left(\nu_x + B_x \frac{\partial \nu_x}{\partial B_x} \right) \right] + \frac{\sigma \Delta}{12} (1 + \delta_{ij}) \frac{1}{\Delta t} \tag{11b}$$

$$\frac{\partial^2 F}{\partial A_i \partial A_j} = \frac{1}{4\Delta} \left[b_i b_j \left(\nu_y + B_y \frac{\partial \nu_y}{\partial B_y} \right) + c_i c_j \left(\nu_x + B_x \frac{\partial \nu_x}{\partial B_x} \right) - c_i c_j \frac{\partial M_x}{\partial B_x} - b_i b_j \frac{\partial M_y}{\partial B_y} \right] \tag{11c}$$

where the components of flux-density B_x and B_y are given by:

$$B_x = \sum_{l=i,j,k} \frac{c_l A_l}{2\Delta} \tag{12a}$$

$$B_y = -\sum_{l=i,j,k} \frac{b_l A_l}{2\Delta} \tag{12b}$$

For the iterative Newton-Raphson technique, in which the permeability of the non-linear materials is adjusted at each iteration, the matrix eqution to be solved for each element has the form shown in equation (13):

$$[G] \quad [D] = [g] \tag{13}$$

where

[G] Represents the Netwon-Raphson coefficent matrix containing the second derivatives of the functional.

[D] Represents the corrections made to the node potentials at each iteration.

[S] Represents the first derivatives of the functional.

The global matrix formed by the series of elemental matrices is generally very sparse and is inverted using a modified Gaussian elimination technique optimized in terms of computational speed and memory storage for banded sparse matrices. The finite element solution package which forms the core of the CAD methodology has

been implemented in C for execution on SUN Unix workstations.

Inertia or mass lumping:

In the previously derived functional derivatives for each element the inertia term, i.e the term associated with the eddy-current flow, was distributed over the entire element area. However, it has been noted by a number of authors that this can in certain circumstances cause physically unreasonable phenomena to be predicted during the initial stages of a transient as discussed in section 3.9. To rectify such instabilities, the inertia term can be lumped at each node of the element. The consistent inertia matrix for the element, i.e the matrix in which the inertia is distributed across the element consistently with the distribution of the stiffness terms, and the corresponding lumped inertia matrix are given by (13a) and (13b) respectively:

$$\textit{Consistent Element Inertia} = \begin{pmatrix} 1/6 & 1/12 & 1/12 \\ 1/12 & 1/6 & 1/12 \\ 1/12 & 1/12 & 1/6 \end{pmatrix} \begin{pmatrix} \frac{\partial A_i}{\partial t} \\ \frac{\partial A_j}{\partial t} \\ \frac{\partial A_k}{\partial t} \end{pmatrix} \qquad (13a)$$

$$\textit{Lumped Element Inertia} = \begin{pmatrix} 1/3 & 0 & 0 \\ 0 & 1/3 & 0 \\ 0 & 0 & 1/3 \end{pmatrix} \begin{pmatrix} \frac{\partial A_i}{\partial t} \\ \frac{\partial A_j}{\partial t} \\ \frac{\partial A_k}{\partial t} \end{pmatrix} \qquad (13b)$$

The effect of lumping the inertia matrix on the predicted field distributions is discussed in the experimental validation of chapter 3.

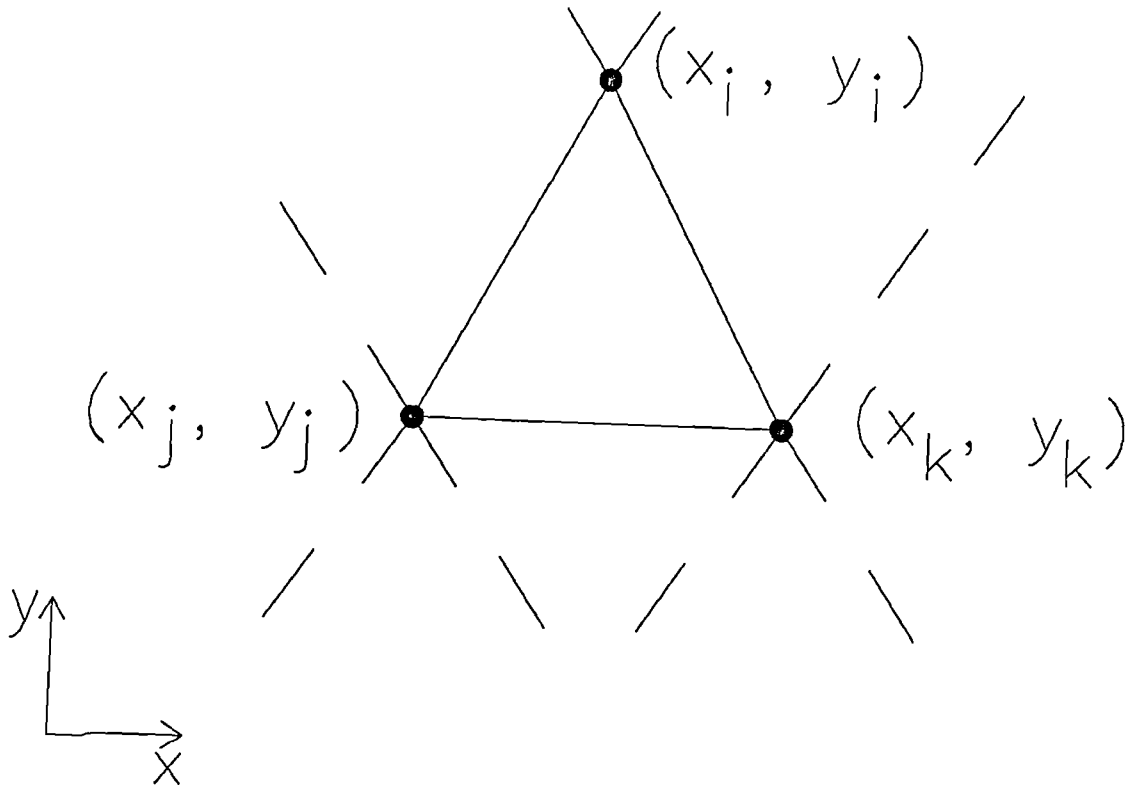

Fig. B.1 General form of a 1st order triangular finite element.

APPENDIX C

CALCULATION OF ELECTROMAGNETIC FORCE IN A RADIAL FIELD MAGNETIZING FIXTURE.

The fixture components which restrain the conductors of a magnetizing fixture are exposed to intense mechanical loads during the impulse period. Whereas most regions can be almost arbitrarily dimensioned in terms of their effect on the electromagnetic performance of the fixture, the thickness of the protective layer between the conductors and the magnet surface plays a critical role in determining the level of magnet saturation achieved for a given peak current.

Although as discussed in chapter 2 there is little merit in comparing candidate designs in terms of the force exerted on the protective layer, it is nevertheless useful to get a worst case estimate of the minimum usable wall thickness prior to the initiation of extensive electromagnetic design.

Single sided fixtures inherently exert a higher mechnical load on the protective layer since in a double sided fixture there is a tendency for the internal and external conductor bundles to repel each other away from the protective layer. A cross-section through a single sided 4-pole radial field magnetizing fixture is shown in fig C.1. From the definition of the Ampere, the force per unit length between two infinitely long straight conductors is given by:

$$F = \frac{\mu_o I_1 I_2}{2 \pi s} \qquad (1)$$

where s is the distance between the two conductors.

It can be seen that there is no net radial force acting outwards on a conductor bundle due to the other bundles of the fixture, since for any of the conductor bundles of the 4 pole fixture of fig C.1:

$$F_{rad} = \frac{\mu_o I^2}{2\pi}\left(\frac{1}{2r_o} - \frac{\cos \pi/4}{r_o\sqrt{2}} - \frac{\cos \pi/4}{r_o\sqrt{2}}\right) < 0 \qquad (2)$$

Hence the radial force to which the protective layer is exposed is due to the repulsive forces between the individual conductors which form the conductor bundle at each pole. In a fixture with a single conductor per pole, the conductor can be regarded as a large number of mechanically connected parallel filaments, carrying current of the same polarity, which attempt to repel each other. The repulsive forces between these elemental filaments act radially outwards and are opposed by internal stresses in the solid conductor. The surrounding fixture structure is not exposed to an onerous mechanical load, since the field levels generally encountered in pulsed magnetization are insufficient to overcome the ultimate tensile stress capability of copper. Disintegration of a solid copper conductors is however a consideration in very high field pulsed solenoids, e.g 60T coils used in fundamental materials research. In the case where there are a number of individual conductors located at each pole, the forces generated within each conductor are again borne largely by internal stresses, whereas the force on a conductor due the other conductors of the bundle is exerted on the fixture former and the protective layer.

Further sub-division of a conductor bundle inherently increases the proportion of the repulsive force which must be borne by the protective layer which serperates the magnet from the fixture conductors. Therefore, the worst case in terms of the force exerted on the fixture structure occurs when the bundle has non internal stress capability, i.e the conductor bundle is formed from an infinite number of mechanically

unconnected filamemts.

Representing the cross-section of a conductor bundle by the circular model of fig.C.2, the pressure exerted on the protective layer can be estimated. At a radius r, the magnetic field strength H is given by Amperes law:

$$\int H\, dl = J \pi r^2 \tag{3}$$

$$H = \frac{J r}{2} \tag{4}$$

The force per unit axial length acting radially outwards on the shaded elementary area is given by:

$$f = \mu_o H J r dr\, d\Theta \tag{5}$$

Therefore the total force per unit axial length directed radially outwards is given by :

$$F = \mu o\, H J \int_0^{2\pi} \int_0^{r_o} r\ dr\, d\Theta \tag{6}$$

Substituting for H from (4) yields:

$$F = \frac{\mu_o J^2}{2} \int_0^{2\pi} \int_0^{r_o} r^2\ dr\, d\Theta \tag{7}$$

$$F = \frac{\mu_o \pi J^2 r_o^3}{3} \tag{8}$$

Since there are no internal stresses opposing the electromagnetic force, the radial pressure per unit length acting on the circumference of the bundle is:

$$P = \frac{F}{2\pi r_o} = \frac{\mu_o J^2 r_o^2}{6} \qquad (9)$$

For a given mmf, the pressure is a worst case when the conductor radius is small. By specifying a conductor diameter equal to that used in the test problem to determine the accuracy of the analytical field calculation, an estimate of the required wall thickness for the predicted current density required for saturation can be obtained in terms of the continuous safe tensile stress of the wall material.

This worst case estimate, must be treated with extreme caution for a number of practical reasons:

a) The tensile stress of composites fabricated in-situ, e.g wrapping epoxy resin soaked stranded fibre glass around the former will generally be lower and less consistent than fabricated pre-components, e.g DURAVER-E laminated glass-fibre tubes manufactured by ISOLA Werke AG which have a minimum guaranteed continuous tensile stress of 200 MN/m^2.

b) In practice the major problems in maintaining the structural integrity of the fixture are related the transitional regions between the axial regions of the conductors and the end-windings. The conductor layout in this region is complex and dependant on the quality of the construction.

c) There is a lower limit on the practically realisable wall thickness, which is approximately 0.5mm for an in-situ wound stranded glass fibre/epoxy resin construction.

Ultimately despite the utility of the calculation outlined above, the selection of wall thickness will remain somewhat empirical with due account of previous construction experience.

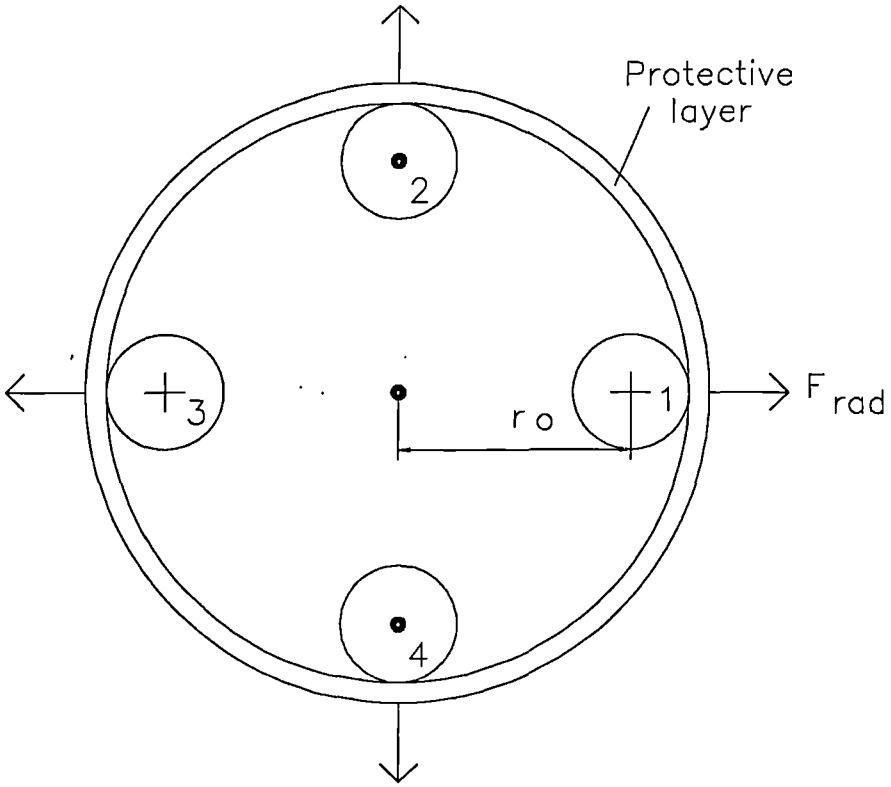

Fig. C.1 Cross-section through a 4-pole, internal single sided, radial field magnetizing fixture

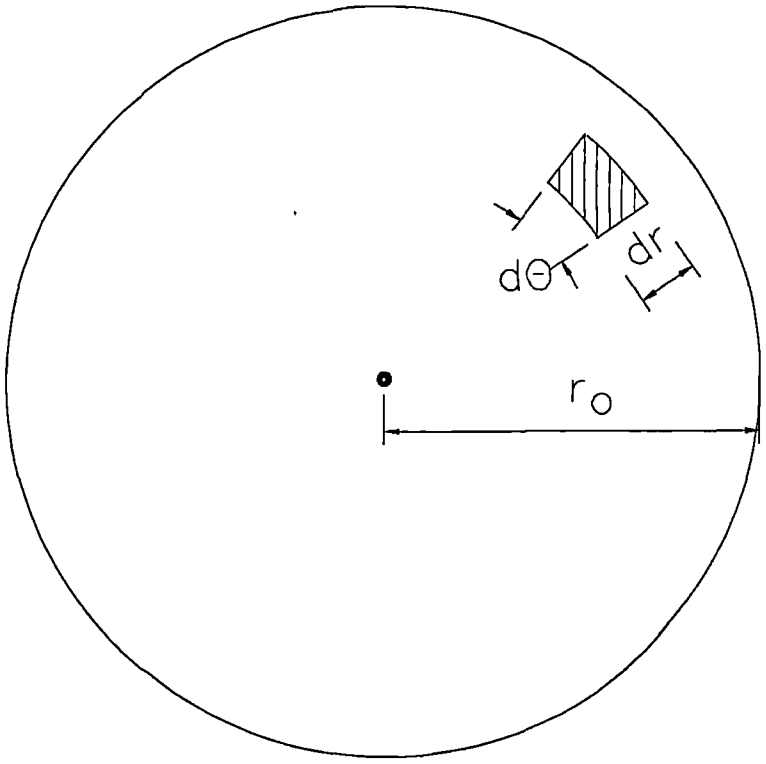

Fig. C.2 Circular,model of a conductor bundle for the calculation of surface pressure.

REFERENCES

CHAPTER 1

[1.1] A.C Nyce, "State of The Industry", Proceedings of the Gorham Advanced Materials Institute Permanent Magnet Design Short-Course and Exhibition, Rosemont Illinois. May 31-June 3, 1992.

[1.2] W. Ervens "Comparison of Properties of NdFeB and SmCo Permanent Magnets", Proceedings of the Commission of the European Communities Workshop on NdFeB Permanent Magnets - Their Present and Future Applications, Brussels. 25th October 1984 pp. 111-122.

[1.3] J. Bell, "Future Products in Bonded Rare Earth Magnets",IBC Conference on Rare-Earth Permanent Magnets and Ultra High Saturation/Low Loss Materials, London, March 1992.

[1.4] R.J Parker, "Advances in Permanent Magnetism", John Wiley and Sons 1990.

[1.5] K. Sparwasser,"Technical and Commercial Status of NdFeB Magnets", IBC Conference on Rare-Earth Permanent Magnets and Ultra High Saturation/Low Loss Materials, London, March 1992.

[1.6] T. Takeshita, "Preparation of NdFeB Anisotropic Magnet Powders Produced by HDDR Process and Bonded Magnets made from them", Proceedings of the Gorham Advanced Materials Institute Technical Conference and Exhibition on Reassessing the Business Oppurtunities, Markets And Technology for Neodymium-Iron-Boron Permanent Magnets, Orlando, Florida, Feb. 16-18. 1992

[1.7] E.Rozendaal, "Corrosion Resistance and Thermal Stability Improvement by Alloy and Process Optimisation", IBC Conference on Rare-Earth Permanent Magnets and

Ultra High Saturation/Low Loss Materials, London, March 1992.

[1.8] P. Mitchell,"Corrosion Protection of NdFeB Magnets", IEEE Transactions on Magnetics,VOL 26, No.5, Sept 1990,pp 1930-1932.

[1.9] M. Sagawa, P. Tenaud, F. Vial, K. Hiraga, "High Coercivity NdFeB Sintered Magnet Containing Vanadium with New Microstructure", IEEE Transactions on Magnetics,VOL 26, No.5, Sept 1990, pp 1957-1959.

[1.10] H. Kirchmayr, "Determination of the Anisotropy Field by the Singular Point Detection Method",Chapter 18, Supermagnets-Hard Magnetic Materials, Kluwer Academic 1991.

[1.11] F.E Pinkerton and D.J Van Wingerden, "Magnetization Process in Rapidly Solidified Neodymium-Iron-Boron Permanent Magnet Materials", J. Appl. Phys. 60 (10); November 1986, pp 3685-3690.

[1.12] J. Ormerod, "Processing and Physical Metallurgy of NdFeB and Other R.E Magnets", Proceedings of the Commission of the European Communities Workshop on NdFeB Permanent Magnets - Their Present and Future Applications, Brussels. 25th October 1984 pp. 69-92.

[1.13] L. Schultz, "Preparation and Properties of Mechanically Alloyed NdFeB Magnets", Chapter 23, Supermagnets-Hard Magnetic Materials, Kluwer Academic 1991.

[1.14] I.R Harris, "NdFeB Type Magnets - Scientific and Technological Developments", IBC Conference on Rare-Earth Permanent Magnets and Ultra High Saturation/Low Loss Materials, London, March 1992.

[1.15] T. Shimoda, K. Akioka, O. Kobzyashi, T. Yamaagami and A. Arai,"Current Situation in Development of Hot-Rolled R-Fe-B Magnets", Vol.1 Proceedings Of The

Eleventh International Workshop on Rare-Earth Magnets and their Applications, Pittsburgh, Oct. 1990. pp 17-28.

[1.16] Y. Bogatin, M. Robinson, J. Ormerod, "Water Milling and Gas Passivation Method for Production of Corrosion Resistant NdFeB-N/C powder and magnets", Journal of Applied Physics, Vol.70, No.10, Part II, Nov. 1991, pp 6594-6596.

[1.17] A.J Ward, "The Development and Implementation of Commercially Viable Processing Techniques for Neodymium Iron Boron Magnets", Concerted European Action on Magnets (CEAM) final report for the period Oct 1985-Sept. 1988, pp463-480.

[1.18] I.R Harris, P.J Mc.Guiness, "Hydrogen: Its Use in the Processing of NdFeB-Type Magnets and in the Characterization of NdFeB-Type Alloys and Magnets", Vol.1 Proceedings Of The Eleventh International Workshop on Rare-Earth Magnets and their Applications, Pittsburgh, Oct. 1990. pp 29-48.

[1.19] G.W Jewell, D. Howe, T.S Birch, "Capacitor Discharge Magnetization of Fine Pole-Pitch Rare-Earth Magnets", Proceedings 25th Universities Power Engineering Conference, Aberdeen, 12-14 Sept. 1990, pp 581-584.

[1.20] J.F Herbst "Structural Characteristics and Rapid Solidification of $Nd_2Fe_{14}B$ Type Permanent Magnet Materials", Chapter 5, Supermagnets-Hard Magnetic Materials, Kluwer Academic 1991.

[1.21] S.Tanaka, "Materials: What are the Prospects",IEEE Transactions on Magnetics, VOL 27, No.2, March 1991.

[1.22] "Magnetic Chargers - MC Range", Sales Literature, Hirst Magnetic Instruments Ltd.

[1.23] "Impulse Magnetizer - Types IM-MA-C and IM-MS-SC", Sales Literature, Magnet-Physik Dr. Steingrover GmbH.

[1.24] "High Pulsed Magnetic Fields Laboratory at MASPEC Institue", Proceedings of CEAM2 Topical Meeting on High Magnetic Field Techniques for Hard Magnetic Materials, Istituto MASPEC del CNR, Parma (Italy). 22-23 March 1991.

[1.25] "Ceramo High Temperature Wire", Technical Bulletin 38, Franco Corradi, Milan, Italy.

CHAPTER 2

[2.1] J.K Lee and E. Furlani, "The Optimization of Multipole Magnetizing Fixtures for High-Energy Magnets", J.Appl.Phys, 67, (3), 1 Feb 1990, pp 1570-1575.

[2.2] J.K Lee, "The Analysis of a Magnetizing Fixture for a Multipole NdFeB Magnet", IEEE Transactions on Magnetics, VOL 24, No.5, Sept 1988, pp 2166-2171.

[2.3] V.I Astapov and I. Ovchinnikov, "Magnetization of Permanent-Magnet Components of Electric-Machine Rotors", Electrotekhnika, Vol 59, No.2, 1988, pp 54-57.

[2.4] L.Chang, T.R Eastham, G.E Dawson, "In-Situ Magnetization of NdFeB Magnets for Permanent Magnet Machines",IEEE Transactions on Magnetics, VOL27, No.5, Sept 1991.

[2.5] T. Nakata and N. Takahashi, "Numerical Analysis of Transient Magnetic Field in a Capacitor-Discharge Magnetizer". IEEE Transactions on Magnetics,VOL MAG-22,No.5, Sept 1986.

[2.6] G.P Widdowson, D. Howe, P.R Evison, "Computer Aided Design Optimization of Rare-Earth Permanent Magnet Actuators", Proceedings of The IEE International

Conference on Computational Electromagnetics, Sept.1991, pp 90-93.

[2.7] D. Lowther, C.M Saldanha, "A Frame-Based System for the Design of Electromagnetic Devices", IEEE Transactions on Magnetics, VOL MAG-22(5), pp 814-816.

[2.8] B. Istfan, S.J Salon, "Inverse Nonlinear Finite Element Problems with Local and Global Constraints", IEEE Transactions on Magnetics, Vol 24. No.6, Nov 1988, pp 2568-2572.

[2.9] G.R Slemon, "Design of Permanent Magnet AC Motors for Variable Speed Drives", Chapter 3, IEEE Industry Applications Society Tutorial Course TH0408-05, Performance and Design of Permanent Magnet AC Motor Drives, Sept 1991.

[2.10] P. Hammond, "Electromagnetism for Engineers", 3rd Edition, Pergamon Press 1986.

[2.11] W.F Low, "The Computation of Magnetostatic Fields in Permanent Magnet Devices", PhD Thesis, University of Sheffield, Oct. 1985.

[2.12] D. Staton, "CAD of Permanent Magnet DC Motors for Industrial Drives", PhD Thesis, University of Sheffield, Aug. 1988.

[2.13] F.W Grover, "Inductance Calculations - Working Formulas and Tables", Reprinted by The Instruments Society of America, 1982.

[2.14] A. Abdel-Razek, J.L Coulomb, M. Feliachi and J.C Sabonnadiere, "The calculation of electromagnetic torque in saturated electrical machines within combined numerical and analytical solutions of the field equation", IEEE Transactions on Magnetics, VOL MAG-17, No.6, pp 3250-3252.

[2.15] D. Rodger, H.C Lai, P.J Leonard, "Coupled Elements for Problems Involving Movement", IEEE Transactions on Magnetics, VOL26, No.2, pp 548-549.

[2.16] I.A Tsukerman,"Overlapping Finite-Elements for Problems with Movement", Paper AQ05 - Digests of the International Magnetics Conference, St. Louis Missouri, April 1992.

[2.17] T.A Nyamusa, N.A Demerdash, "Integrated Nonlinear Magnetic Field-Network of an Electronically Commutated P.M Motor System Under Normal Operation", IEEE Transactions on Energy Conversion, Vol. EC-2, No.1 March 1987, pp 77-85.

CHAPTER 3

[3.1] T.Nakata, N.Takahashi and K.Fujiwara, "Physical Meaning of gradΦ in Eddy Current Analysis using Magnetic Vector Potentials", IEE Transactions on Magnetics, Vol.24, No.1, Jan 1988.

[3.2] W.F Low, "The Computation of Magnetostatic Fields in Permanent Magnet Devices", PhD Thesis, University of Sheffield, Oct. 1985.

[3.3] T. Nakata and Y. Kawase," Numerical Analysis of Non-Linear Transient Magnetic Field Using the Finite Element Method", Electrical Engineering in Japan, Vol. 104, 1984, pp 81-85.

[3.4] C.R.I Emson, "Methods for the solution of open-boundary electromagnetic-field problems", IEE Proceedings, Vol 135,Pt.A,No.3, March 1988, pp 151-158.

[3.5] E.Rank, C.Katz, H.Werner,"On the Importance of the Discrete Maximum Principle in Transient Analysis using Finite Element Methods", International Journal for Numerical Methods in Engineering, Vol.19, 1983, pp 1771-1782.

[3.6] P.J Leonard, D.Rodger, "Some aspects of two- and three-dimensional transient-eddy-current modelling using finite elements and single-step time-marching algorithms", IEE Proceedings, Vol 135, Pt.A, No.3, March 1988, pp 159-166.

[3.7] W. Press, B.P Flannery, S.A Teukolsky, W.T Vetterling, "Numerical Recipes in C - The Art of Scientific Computing", 1988, Cambridge University Press.

[3.8] C.H Quah," Magnetisation of multi-polar permanent magnet rotors for miniature synchronous motors", M.Eng Thesis, University of Sheffield 1981.

[3.9] R. Boll, "Soft Magnetic Materials - Fundamentals, Alloys, Properties, Products, Applications", Vacuumschmelze Handbook, Heyden and Son Ltd. 1979.

[3.10] A. de Beer, S.J Polak, A.J.H Wachters, J. van Welij, "MAGGY Materials Library" Mathematical Software User's Documentation 2nd edition, Vol 3. Philips Corporate CAD Centre.

[3.11] G.F.T Widger, "Represntation of magnetisation curves over extensive range by rational-fraction approximations", Proc. IEE, Vol. 116, No.1, Jan 1969.

[3.12] G.H Tan, "Design of a permanent magnet air-turbo generator", PhD Thesis, University of Sheffield. 1980.

[3.13] T. Tarnhuvud, K. Reichert, J. Skoczylas, "Problem-Orientated Adaptive Mesh-Generation for Accurate Finite-Element Calculation", IEE Transactions on Magnetics, Vol.26, No.2, March 1990.

[3.14] A.G Jack, J.W Finch, J.P Wright, "Adaptive Mesh Generation Applied to Switched-Reluctance Motor Design", IEEE Transactions on Industry Applications, Vol.28, No.2 March 1992.

[3.15] K. Davey, "The FELIX Cylinder Problem (International Eddy-Current Workshop Problem 1)", The Internatioinal Journal for Computation and Mathematics in Electrical and Electronic Engineering, Vol 7, Nos.1 and 2,1988,pp11-27.

[3.16] L.R Turner, G.R Gunderson, M.J Knott, D.G McGhee, W.F Praeg, R.B Wehrle, "Results from the FELIX experiments on electromagnetic effects in hollow cylinders", IEEE Transactions on Magnetics, VOL MAG-21, No.6, Nov 1985.

CHAPTER 5

[5.1] K. Sparwasser,"Technical and Commercial Status of NdFeB Magnets",IBC Conference on Rare-Earth Permanent Magnets and Ultra High Saturation/Low Loss Materials, London, March 1992.

[5.2] Y.P Liu, D.Howe, T.S Birch and D.M.H Matthews, "Dynamic Modelling and Performance Prediction of Brushless Permanent Magnet Drive System", IEE 4th Int. Conf. on Electrical Machines and Drives, 1989, 95-99.

[5.3] R.J Lavender, "Design of a Permanent Magnet Brushless D.C Motor using a Radial NdFeB Magnet Ring", Final year project report, University of Sheffield 1989.

[5.4] P.R Evison, "Magnet Overhang in ERONI Motors", Report No.4, CEC BRITE-EURAM Project No. P-2380-5, Mathematical Modelling, Computer Aided Synthesis and Optimisation of Permanent Magnet Excited Brushless Motor Drives and Actuators Taking into Account Advanced Materials and Technology.

[5.5] G. Heremans, F. Herlach, L. Van Bockstal, J.Witters and I. Lefever, "High Performance Coils for Pulsed Magnets", IEEE Transactions on Magnetics, Vol.28, No.1, Jan 1992.

CHAPTER6

[6.1] "Permanent Magnets", Philips Components Data Handbook C16 and Supplement.

[6.2] M.K Jenkins, G.W Jewell, K. Harmer, D.Howe, "Micro-Generator for Smart Diskette", Proceedings 12th International Workshop on Rare-Earth Magnets and Their Application, Canberra, Australia, July 12-15, 1992.

[6.3] K. Harmer, "Development of SMART Diskette Internal Power Generator", Final year project report, University of Sheffield 1991.

[6.4] E.M.H Kamerbeck, A.J.C Van der Bost, J. Koornel, "Magnetising Multipole NdFeB Magnets", Philips Research Laboratories, Proceedings Concerted European Action on Magnets (CEAM) Final Report, 1988, pp 673-686.

[6.5] M.K Jenkins, "Design of a miniature generator for a Smartdiskette", Research Report, University of Sheffield, Jan 1992.